New insight into the interaction of light with tailored and photofunctional materials:

the role of (dis-)order, periodicity and symmetry

Kumulative Dissertation
zur Erlangung des Grades
eines Doktors der Naturwissenschaften

von

Björn Bourdon

genehmigt vom Fachbereich Physik der

UNIVERSITÄT OSNABRÜCK

Osnabrück, im Januar 2020

Erstgutachter:	Prof. Dr. Mirco Imlau
Zweitgutachter:	Prof. Dr. Joachim Wollschläger

Tag der Einreichung: 14. Januar 2020

Contents

1 Introduction

In 1865, James C. Maxwell succeeded in unifying the theory of electricity and magnetism and laid the foundation for our understanding of light as an electromagnetic wave [1]. Its interaction with charged particles in the matter, mainly bound electrons, is commonly called light-matter interaction (LMI). A vivid depiction is carried out along the Lorentz-oscillator model – a damped harmonic oscillator – where the electrons are assumed to be bound to the nucleus by springs [2, 3]. The applied electric field then leads to an oscillating displacement of the charge carriers thereby inducing a dipole moment and, thus, a polarization. Via the *Clausius-Mossotti-relation*, the microscopic dipole moment is further related to the macroscopic permittivity, i.e., to the absorption coefficient and refractive index [4]. Correspondingly, light-matter interaction can be experimentally observed by analyzing the transmitted light of an incident electromagnetic wave which offers direct access to the absorption coefficient. Since the permittivity is in general wavelength/frequency dependent, utilizing white light allows for determining the absorption spectrum and, thus, characteristic absorption bands. This is the fundamental principle of spectroscopy. The refractive index can then be deduced by applying the Kramers-Kronig relation [5, 6]. Further details are described in chapter 2.

However, these principles are not only limited to analyze transitions from the ground state. In addition, they can be transferred to the investigations of already excited atoms or molecules which opens the field of transient absorption spectroscopy. If the excited states are in turn generated by light, the technique is called light-induced transient absorption (spectroscopy). Typically, excitation is carried out by ns-pump pulses while the decay dynamics, i.e., transport, recombination and relaxation of transient states with characteristic lifetimes in the microsecond to second time domain are probed by continuous wave (cw) lasers [7–13]. However, clock frequencies in the Gigahertz-regime limit the electronic time resolution to the ns-time domain. Thus, new techniques are required to measure even faster processes.

One well-established method for investigating light-matter interactions in the picosecond (ps) to femtosecond (fs) time domain (or even faster) is ultrafast spectroscopy or pump-probe spectroscopy [14–18]. Here, an ultrashort pump pulse transfers the molecules/atoms etc. into their excited states. The response of the system is interrogated by a time-delayed probe pulse. Subsequently, the respective time delay is varied and the corresponding transient absorption is measured for each delay. If these obtained value-pairs are plotted against each other, the dynamics of the light-matter interaction after excitation can be analyzed. This allows to study physical processes in the solid state continuum on the ultrashort time scale after exposure to single fs-laser pulses [19, 20]. The high temporal resolution further enables the analysis of structural changes and transition states in chemical reactions (called *femtochemistry* [21]) established by Ahmed H. Zewail and honored with the Nobel Prize in chemistry in 1999 [22, 23].

These techniques have in common that the light-matter interaction and temporal dynamics are essentially investigated on the basis of absorption changes while refractive index changes remain mainly hidden. For this purpose, holographic measuring principles are commonly applied which were first observed and described by the Hungarian scientist Gabor in 1948 [24]. A detailed description is given by the coupled-wave theory of Kogelnik [25]: two spatially and temporally synchronized, coherent light waves create a sinusoidal intensity/interference pattern within the sample which is subsequently transferred into a periodic modulation of the absorption coefficient and/or refractive index. These modulations are called elementary holographic gratings and are responsible for the appearance of diffraction phenomena. Analyzing the diffraction efficiency development of an additionally applied laser beam then provides direct access to the amplitudes of the holographic gratings, i.e., to the light-induced absorption and refractive index changes related to excited states. Correspondingly, the photophysical and photochemical mechanisms of the light-matter interaction as well as characteristic properties of the investigated systems can be deduced by performing these techniques as a function of experimental parameters, i.e., intensity, photon energy, light polarization, sample composition etc. According to reference [26], photo-induced mechanisms such as photon absorption and emission or vibration relaxation refer to photophysical processes since the chemical structure is maintained. Contrary, photochemical processes like isomerization result in a change of the chemical structure.

Within this thesis, the photophysical and photochemical processes of the light-matter interaction are investigated in tailored and photofunctional materials that strongly differ in their optical and structural properties. This includes photoswitchable ruthenium sulfoxide molecules embedded into the solid-state polymer polydimethylsiloxan (PDMS [27]) where LMI is related to the excitation of metastable states [28–33]. Furthermore, congruently melted, nominally undoped and iron-doped lithium niobate crystals of different doping concentration are studied in which transient polaronic or excitonic states are generated [12, 34–41]. This thesis is dedicated to the elucidation of the individual coupling mechanisms which are examined in particular by the principle of holographic grating recording and light-induced transient spectroscopy within chapter 3. Additionally, the impact of structural parameters on the light-matter/-surface interaction is studied as a function of pulse parameters by investigating diffraction phenomena arising from the interaction with an artificially, periodically structured surface-relief grating. A cross-system comparison presented in chapter 4 exhibits similar phenomena of the light-matter interaction in the investigated tailored and photofunctional materials, i.e., the determined absorption and refractive index changes are in the same order of magnitude, although the underlying photophysical and photochemical processes differ significantly. By relating these results to a single-crystalline reference holographic medium, a considerable influence of the internal/intrinsic structure and orientation of the photo-induced metastable and transient states is deduced for the formation of macroscopic refractive index changes while local absorption and microscopic refractive index alterations are unaffected. The developed results are finally summarized in chapter 5.

2 Fundamental principles

2.1 Linear optics

2.1.1 Lorentz-oscillator model

The description of the Lorentz-oscillator model will be given along reference [2,3,42]. An applied electric field $\mathbf{E}$ results in a net displacement $\mathbf{r}$ of positive and negative charges which induces a dipole moment $\mathbf{p}$ and, thus, a polarization $\mathbf{P}$. However, in case of an electromagnetic wave of frequency ω, the applied electric field is alternating which forces the induced dipoles to oscillate around their equilibrium position with the same frequency. The dipoles in turn radiate an electromagnetic wave with frequency ω. This process is repeated from dipole to dipole so that the initial wave ultimately propagates through the material.

The dynamics of the oscillating dipoles are described in a first approximation by the model of a damped harmonic oscillator where the electrons are assumed to be bounded to the nucleus via springs. The corresponding one-dimensional equation of motion is defined by

$$\frac{d^2\mathbf{r}(t)}{dt^2} + 2\gamma\frac{d\mathbf{r}(t)}{dt} + \omega_0\mathbf{r}(t) = -\frac{e}{m}\mathbf{E}(t), \tag{2.1}$$

with the displacement $\mathbf{r}(t)$, time t, damping γ, resonance frequency ω_0, electron charge e and electron mass m. For the sake of simplicity, the applied electric field of amplitude $\mathbf{E}_0$ and frequency ω is given by $\mathbf{E}(t) = \mathbf{E}_0\exp(-i\omega t)$. Substituting this expression into the equation of motion results in the solution

$$\mathbf{r}(t) = -\frac{e}{m}\frac{1}{\omega_0^2 - \omega^2 - i\gamma\omega}\mathbf{E}_0\exp(-i\omega t) \tag{2.2}$$

and the induced atomic dipole moment $\mathbf{p}(t) = -e\mathbf{r}(t)$

$$\mathbf{p}(t) = -\frac{e^2}{m}\frac{1}{\omega_0^2 - \omega^2 - i\gamma\omega}\mathbf{E}_0\exp(-i\omega t). \tag{2.3}$$

The microscopic dipole moment $\mathbf{p}$ is furthermore proportional to the local electric field $\mathbf{E}_{\text{loc}}$:

$$\mathbf{p} = \alpha\mathbf{E}_{\text{loc}}, \tag{2.4}$$

with the polarizability α. The sum of all induced dipole moments then defines the macroscopic polarization $\mathbf{P}$:

$$\mathbf{P} = N\mathbf{p} = N\alpha\mathbf{E}_{\mathrm{loc}}, \tag{2.5}$$

$$\mathbf{P} = \epsilon_0\chi\mathbf{E} = \epsilon_0(\epsilon_{\mathrm{r}} - 1)\mathbf{E}, \tag{2.6}$$

where N is the number density of atoms/molecules, ϵ_0 is the vacuum permittivity and $\mathbf{E}$ describes at first an arbitrary external electric field. Correspondingly, the polarization $\mathbf{P}$ can be derived by the macroscopic susceptibility χ and the macroscopic dielectric constant ϵ_{r}, respectively.

In general, the local electric field is the sum of the external electric field $\mathbf{E}$ and the polarization charge field (Lorentz field) $\mathbf{P}_{\mathrm{L}} = \mathbf{P}/3\epsilon_0$, where $\mathbf{P}$ is given by Eq. 2.5. By equating the right hand side of Eq. 2.5 and Eq. 2.6 and substituting the local electric field by the above defined expression, the microscopic polarizability α can be linked to the macroscopic dielectric constant ϵ_{r} which is known as Clausius-Mossotti-relation [4]:

$$\frac{\epsilon_{\mathrm{r}} - 1}{\epsilon_{\mathrm{r}} + 2} = \frac{N}{3\epsilon_0}\alpha \qquad \Leftrightarrow \qquad \epsilon_{\mathrm{r}} = 1 + \frac{3N\alpha}{3\epsilon_0 - N\alpha} = 1 + \chi. \tag{2.7}$$

Additionally, the dielectric constant is linked to the microscopic, frequency dependent dipole moment via Eq. 2.5 and Eq. 2.6 which can be obtained from a Fourier transformation of Eq. 2.3. By inserting and transforming the appropriate equations, $\epsilon_{\mathrm{r}}(\omega)$ can be derived to

$$\epsilon_{\mathrm{r}}(\omega) = 1 + \frac{Ne^2}{\epsilon_0 m}\frac{1}{\omega_0^2 - \omega^2 - i\gamma\omega}. \tag{2.8}$$

Separating the complex expression of the dielectric permittivity into its real and imaginary part $\epsilon_{\mathrm{r}}'(\omega)$ and $\epsilon_{\mathrm{r}}''(\omega)$, respectively, gives rise to the definition of a complex refractive index $N(\omega)$:

$$\epsilon_{\mathrm{r}}(\omega) = \epsilon_{\mathrm{r}}'(\omega) + i\epsilon_{\mathrm{r}}''(\omega), \tag{2.9}$$

$$\begin{aligned} &= \frac{1}{\mu_{\mathrm{r}}}\left[n(\omega) + i\kappa(\omega)\right]^2, \\ &= \frac{1}{\mu_{\mathrm{r}}}N(\omega)^2, \end{aligned} \tag{2.10}$$

with the permeability μ_{r}. Correspondingly, the real part of $N(\omega)$ is described by the refractive index $n(\omega)$ which is related to the real part of $\epsilon_{\mathrm{r}}(\omega)$. The imaginary part of $N(\omega)$ linked to the imaginary part of $\epsilon_{\mathrm{r}}(\omega)$ is given by the extinction coefficient $\kappa(\omega)$ which is correlated to the absorption coefficient $\alpha(\omega)$ via

$$\kappa(\omega) = \alpha(\omega)c/(2\omega), \tag{2.11}$$

where c is the speed of light.

2.1.2 Kramers-Kronig relation

Light propagating through a material experiences the dispersion of the refractive index $n(\omega)$ known for instance from the wavelength dependent angular distribution of polychromatic light on a prism. A mathematical description of $n(\omega)$ is known for a large number of materials and is described by Sellmeier equations [43]. As described above, the refractive index is in general complex and can be defined according to Eq. 2.10. The real and imaginary part of the complex refractive index are affiliated with each other via the Kramers-Kronig relation [5, 6]:

$$n(\omega) = 1 + \frac{2}{\pi}\mathrm{CH}\int_0^\infty \frac{\omega'\kappa(\omega')}{\omega'^2 - \omega^2} d\omega', \tag{2.12}$$

$$\kappa(\omega) = -\frac{2\omega}{\pi}\mathrm{CH}\int_0^\infty \frac{n(\omega') - 1}{\omega'^2 - \omega^2} d\omega', \tag{2.13}$$

where CH is the Cauchy principal value. Combining Eq. 2.11 - Eq. 2.13 enables the calculation of the refractive index $n(\omega)$ by measuring the absorption spectrum $\alpha(\omega)$ and vice versa.

2.1.3 Linear absorption

In the field of linear optics, optical charge carrier excitation is performed by a one-photon absorption (1PA) from the ground into a higher electronic state if the light frequency is resonant with the spectral dependence of $N(\omega)$. The intensity development of the incident light wave while propagating through a medium of thickness z and absorption coefficient α is given by

$$\frac{dI}{dz} = -\alpha I, \tag{2.14}$$

$$I(z) = I_0 \exp\left(-\alpha z\right). \tag{2.15}$$

The solution of the differential equation results in the transmitted intensity $I(z)$ (Eq 2.15) which is known from Beer's law with the incident intensity I_0.

2.2 Nonlinear optics

2.2.1 Parametric frequency conversion

The description of nonlinear optics and the nonlinear polarization, respectively, will be given along references [44–47]. As previously described, the polarization $\mathbf{P}$ depends linearly on the electric field $\mathbf{E}$ in the framework of linear optics, i.e., for moderate light intensities/electric fields (cf. Eq. 2.6). However, strong electric fields in the range of

$E = 10^{12}\,\mathrm{V/m}$ result in additional, nonlinear terms. Thus, the polarization is developed mathematically by a power series over $\mathbf{E}$ [45,46]:

$$\mathbf{P} = \epsilon_0 \sum_n \chi^{(n)} \mathbf{E}^n = \epsilon_0 \left(\chi^{(1)} \mathbf{E} + \chi^{(2)} \mathbf{E}^2 + \chi^{(3)} \mathbf{E}^3 + ... \right), \tag{2.16}$$

where $\chi^{(n)}$ now describes the n-th order tensorial dielectric susceptibility. In most practical cases, higher order tensors ($n > 2$) can be simplified by utilizing appropriate material symmetries (Neumann principle) [48]. For an applied electric field $\mathbf{E}(t) = \mathbf{E}_0 \cos(\omega t)$ with frequency ω, the first three components of the polarization are given by:

$$\mathbf{P}^{(1)}(t) = \epsilon_0 \chi^{(1)} \mathbf{E}_0 \cos(\omega t), \tag{2.17}$$

$$\mathbf{P}^{(2)}(t) = \frac{1}{2} \epsilon_0 \chi^{(2)} \mathbf{E}_0^2 + \frac{1}{2} \epsilon_0 \chi^{(2)} \mathbf{E}_0^2 \cos(2\omega t), \tag{2.18}$$

$$\mathbf{P}^{(3)}(t) = \frac{1}{4} \epsilon_0 \chi^{(3)} \mathbf{E}_0^3 \cos(3\omega t) + \frac{3}{4} \epsilon_0 \chi^{(3)} \mathbf{E}_0^3 \cos(\omega t). \tag{2.19}$$

Here, $\mathbf{P}^{(1)}(t)$ describes the linear material response, thus, oscillating with the frequency ω of the fundamental wave. However, higher order terms give rise to additional frequency components which is called frequency conversion. For example, the second order susceptibility $\chi^{(2)}$ results in a frequency-independent term (optical rectification) and a frequency-doubled component known as the generation of the second harmonic wave (SHG). Correspondingly, $\chi^{(3)}$ leads to a frequency tripling (third harmonic generation, THG) and a term with the fundamental frequency which is linked to the nonlinear refractive index [44,46].

In a more general case, applying two input fields $\mathbf{E}_1(t,\omega_1)$ and $\mathbf{E}_2(t,\omega_2)$ with different frequencies $\omega_1 \neq \omega_2$ gives rise to further frequency conversion processes like sum frequency (SFG, $\omega_3 = \omega_1 + \omega_2$) and difference frequency (DFG, $\omega_3 = |\omega_1 - \omega_2|$) [3,45,49]. Thus, SHG is a special case of SFG with $\omega_1 = \omega_2$. Similar calculations can be performed for higher orders ($n > 3$) which are not further considered. The frequency conversion processes related to the second order susceptibility are visualized in Fig. 2.1. In contrast to real atomic electronic states, the intermediate levels are regarded as virtual states, i.e., there is no absorption of the incident light wave and, subsequently, no energy is transferred into the nonlinear material. In more detail, virtual states are assumed to be present only during the conversion process. Since the quantum state of the system is therefore not changed and the frequency conversion is instantaneous, it is a so-called parametric process. Thus, the aforementioned process has to be distinguished from multi-photon absorption, e.g., cascaded one-photon absorption or two-photon or three-photon absorption, where electrons are transferred non-instantaneously or nearly instantaneously from an initial into a final state [50].

Apart from energy conservation, the conservation of momentum has to be considered to ensure high conversion efficiencies [2,46,49]. However, light waves of distinct frequencies feature different phase velocities within the material arising from refractive

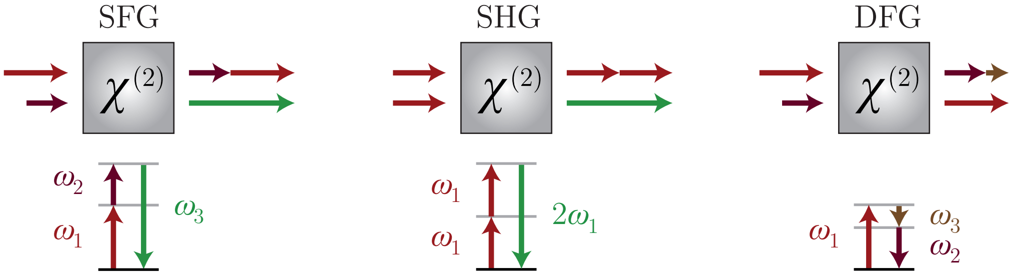

Figure 2.1 – Geometry of second order $\chi^{(2)}$ nonlinear frequency conversion processes (top) and corresponding energy scheme (bottom) according to reference [50]. The excitation ground state is marked in black while intermediate levels are shown as gray lines. SFG: two waves with frequencies ω_1 and ω_2 lead to a third wave with frequency $\omega_3 = \omega_1 + \omega_2$. SHG: two identical waves with frequency ω_1 gives rise to a frequency-doubled wave $2\omega_1$. DFG: a third wave with frequency ω_3 results from the difference of two incident waves with distinct frequencies ω_1 and ω_2.

index dispersion $n(\omega)$ which in general leads to a phase mismatch between the fundamental and continuously generated converted frequencies. On the example of the above presented sum frequency generation, the conservation of momentum considering the mutual phase shift Δk can be expressed by

$$k_{\omega_1} = k_{\omega_2} + k_{\omega_3} + \Delta k \qquad \Leftrightarrow \qquad \Delta k = k_{\omega_1} - (k_{\omega_2} + k_{\omega_3}) \tag{2.20}$$

where $k_\mathrm{i} = n_\mathrm{i}\omega_\mathrm{i}/c$ are the respective wave vectors. Typically, the phase mismatch is eliminated by utilizing birefringent materials where the refractive index becomes orientation dependent or periodically poled nonlinear optical materials [46, 47].

Nonlinear optical frequency conversion processes are used in particular in the field of optical parametric amplification [44, 49]. Here, a weak seed wave of frequency ω_2 is amplified by a strong pump wave of frequency $\omega_1 = \omega_2 + \omega_3$ (three wave mixing). Inside the nonlinear medium, the pump wave is converted into two waves, one with seed frequency ω_2 which is then called signal wave and a residual one with frequency ω_3 (difference frequency of ω_1 and ω_2) called idler wave. By satisfying the phase matching condition (Eq. 2.20), frequency conversion in combination with optical parametric amplification allows for generating frequencies continuously from the ultraviolet (UV), over the visible (VIS) to the near-infrared (NIR) and mid-infrared (MIR) spectral range.

2.2.2 Nonlinear refractive index

Linear electro-optic effect

Another special case of the polarization $\mathbf{P}^{(2)}(t)$ occurs when an electromagnetic wave of frequency ω_1 interacts with an electric field $\mathbf{E}^{\mathrm{dc}}$ of frequency $\omega_2 = 0$ (dc: direct charge).

Then, the first two orders of the polarization $\mathbf{P}(t)$ can be written as [51]

$$\mathbf{P}^{(1)}(t) = \epsilon_0\chi^{(1)}\mathbf{E}_0\cos(\omega t) + \epsilon_0\chi^{(1)}\mathbf{E}^{\mathrm{dc}}, \tag{2.21}$$

$$\mathbf{P}^{(2)}(t) = 2\epsilon_0\chi^{(2)}\mathbf{E}_0\cos(\omega t)\mathbf{E}_{\mathrm{dc}}. \tag{2.22}$$

As a consequence, two polarization terms with frequency ω arise. The corresponding polarization component $\mathbf{P}(\omega)$ is thus given by

$$\mathbf{P}(\omega) = \epsilon_0 \underbrace{\left(\chi^{(1)} + 2\chi^{(2)}\mathbf{E}^{\mathrm{dc}}\right)}_{\chi_{\mathrm{eff}}} \mathbf{E}(\omega). \tag{2.23}$$

The comparison to the linear polarization 2.6 allows to define an effective susceptibility χ_{eff} which depends on both $\chi^{(1)}$ and $\chi^{(2)}$. Besides, the susceptibility is related to the refractive index n by

$$n(E^{\mathrm{dc}}) = \sqrt{1+\chi_{\mathrm{eff}}} = \sqrt{1+\chi^{(1)}+2\chi^{(2)}E^{\mathrm{dc}}}, \tag{2.24}$$

$$\begin{aligned} n(E^{\mathrm{dc}}) &\approx n_0 + \frac{\chi^{(2)}}{n_0}E^{\mathrm{dc}} \\ &= n_0 + n_1 E^{\mathrm{dc}}. \end{aligned} \tag{2.25}$$

The Taylor approximation of the square root around the $\chi^{(2)}$-contribution yields the electric field dependent refractive index $n(E^{\mathrm{dc}})$ (Eq. 2.25), where E^{dc} is the strength of the electric field of frequency $\omega_2 = 0$. Accordingly, the refractive index can be described by the linear refractive index n_0 and an electric field dependent contribution given by the product of E^{dc} and the nonlinear refractive index n_1. Due to the proportionality to E^{dc}, this effect is called linear electro-optic effect or Pockels effect [46, 51]. Note that the nonlinear index of refractive is given by $\chi^{(2)}$, thus being a second-order, nonlinear optical process. Consequently, this effect can only be observed in non-centrosymmetric crystals [46,51,52].

Quadratic electro-optic effect

Apart from the linear polarization $\mathbf{P}^{(1)}(t)$ (Eq. 2.6), an additional term with the fundamental light frequency ω arises from the third order nonlinear polarization $\mathbf{P}^{(3)}(t)$ (Eq. 2.19) which can be summarized to

$$\mathbf{P}(\omega) = \epsilon_0 \underbrace{\left(\chi^{(1)} + \frac{3}{4}\chi^{(3)}\mathbf{E}_0^2\right)}_{\chi_{\mathrm{eff}}} \mathbf{E}(\omega). \tag{2.26}$$

Similar to the previous section, an effective susceptibility can be defined. Here, the Taylor approximation of the square root around the $\chi^{(3)}$-contribution in combination with the transition from the electric field to the intensity $I_0 = 1/2\epsilon_0 c n E_0^2$ (again only the strength of the electric field is considered) yields an intensity dependent refractive index $n(I)$ (Eq. 2.28):

$$n(E_0) = \sqrt{1+\chi_{\text{eff}}} = \sqrt{1+\chi^{(1)}+\frac{3}{4}\chi^{(3)}E_0^2}, \tag{2.27}$$

$$\begin{aligned} n(I) &\approx n_0 + \frac{3}{4n_0^2\epsilon_0 c}\chi^{(3)}I \\ &\quad n_0 + n_2 I. \end{aligned} \tag{2.28}$$

As a consequence, the refractive index can be described by the linear refractive index n_0 and an intensity dependent contribution given by the product of I and the nonlinear refractive index n_2 [53]. Since $n(I)$ is proportional to the intensity and thereby to the square of the electric field, this effect is called quadratic electro-optic effect or Kerr-effect [3, 45, 54]. Furthermore, n_2 is proportional to the third order susceptibility $\chi^{(3)}$ [46, 52, 55] and can therefore be detected in centrosymmetric as well as non-centrosymmetric crystals. Besides, this material parameter leads to nonlinear effects like self-phase modulation or self-focusing by applying intensive laser pulses [3, 56, 57]. Both mechanisms are utilized in modern wavelength tuneable fs-laser systems. Self-phase modulation is typically applied to generate a white-light continuum within an optical parametric amplifier which serves as seed-pulse for the nonlinear frequency mixing process (cf. section 2.1.1). Self-focusing on the other hand is exploited within the fs-pulse generation: the transversal beam profile $I(x,y)$ of an incident laser induces a radial change of the refractive index $n(I)$ resulting in a so-called refractive index lens or Kerr-lens [58–60].

2.2.3 Nonlinear Absorption

As previously described, high light intensities in the range of several GW/cm^2 give rise to the nonlinear index of refraction n_2 (Eq. 2.28). As a consequence of the complex refractive index (Eq. 2.10), the nonlinear index of refraction $n(I)$ is correlated to a nonlinear extinction coefficient $\kappa_{\text{NL}}(I)$ via

$$N(I) = \underbrace{n_0 + n_2 I}_{n_{\text{NL}}(I)} + i\underbrace{(\kappa_0 + \kappa_2 I)}_{\kappa_{\text{NL}}(I)}, \tag{2.29}$$

$$= \underbrace{n_0 + i\kappa_0}_{n_{\text{L}}} + \underbrace{(n_2 + i\kappa_2)I}_{n_{\text{NL}}(I)}. \tag{2.30}$$

For the sake of clarity, the frequency dependence is omitted here. By rearranging Eq. 2.29 it becomes obvious that the complex refraction index $N(I)$ consists of the complex linear and nonlinear, intensity dependent refractive index n_{L} and $n_{\text{NL}}(I)$, respectively

(Eq. 2.30). Accordingly and together with Eq. 2.11, the nonlinear extinction coefficient $\kappa_{\mathrm{NL}}(I)$ can be described by the linear and nonlinear absorption coefficient α_0 and βI:

$$\kappa_{\mathrm{NL}}(I) = \kappa_0 + \kappa_2 I = \frac{c}{2\omega}\underbrace{(\alpha_0 + \beta I)}_{\alpha_{\mathrm{NL}}}, \tag{2.31}$$

where β is called nonlinear absorption coefficient. Since n_2 and β are correlated with each other via the Kramers-Kronig relation, β is related to the imaginary part of the third order susceptibility $\chi^{(3)}$ [52, 55, 61], therefore, being a material parameter as well.

Subsequently, the differential equation Eq. 2.14 has to be adapted to high light intensities including the nonlinear absorption coefficient $\alpha_{\mathrm{NL}} = \alpha_0 + \beta I$:

$$\frac{dI}{dz} = -\alpha I - \beta I^2, \tag{2.32}$$

$$I(z) = \frac{\alpha I_0}{\alpha \exp(\alpha z) + \beta I_0 \left(\exp(\alpha z) - 1\right)}, \tag{2.33}$$

$$I(z) = \frac{I_0}{1 + \beta I_0 z}. \tag{2.34}$$

The additional term in Eq. 2.32 depends quadratically on the incident intensity I indicating that two photons are involved in the absorption process. Therefore, this excitation mechanism is called two-photon absorption (TPA) which was already postulated in 1931 [62] and experimentally verified in 1961 [63]. Consequently, the nonlinear absorption coefficient β is called two-photon absorption coefficient which is in the range of a few mm/GW to cm/GW for the nonlinear material lithium niobate [14, 18, 64]. The transmitted intensity $I(z)$ in case of both, a one-photon and two-photon absorption, respectively, is given by Eq. 2.33 while Eq. 2.34 only accounts for TPA.

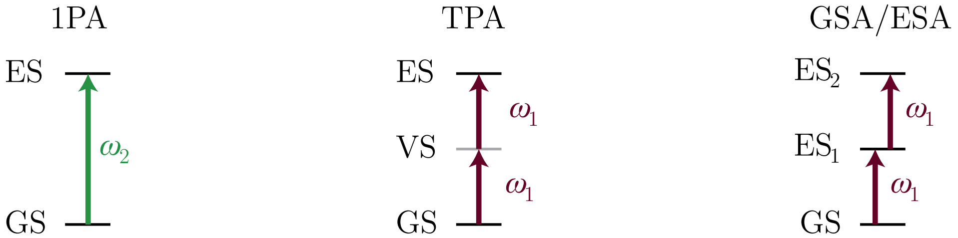

Figure 2.2 – Energy scheme depicting one-photon absorption (1PA), two-photon absorption (TPA) and sequential one-photon absorption, i.e., sequential ground state (GSA) and excitation state absorption (ESA) according to reference [50]. GS, VS and ES denote the ground state, virtual state and excited state, respectively.

Fig. 2.2 illustrates the different excitation mechanisms, i.e., one-photon absorption and two-photon absorption, on an energy scale. In contrast to the frequency conversion presented in section 2.1.1 now both, the initial/ground (GS) and final/excited state

(ES) are real electronic states while intermediate levels are still regarded as virtual states (VS). However, it is crucial that the two photons are absorbed simultaneously which distinguishes the TPA from sequential absorption upconversion [50] known for example from upconversion nanocrystals/nanoparticles (UCNPs) [65–67] and depicted in the right part of Fig. 2.2. Here, the ground state absorption (GSA) is followed by an excited state absorption (ESA) from ES_1 to ES_2.

2.3 Ultrashort laser pulses

Nonlinear processes as described in the previous section require large electric fields which are commonly provided by applying ultrashort laser pulses in the femtosecond time regime. Since higher order nonlinear processes are typically described by the intensity (proportional to the square of the electric field), a mathematical description of ultrashort laser pulses is mandatory which will be given along reference [47].

2.3.1 Intensity

Ultrashort laser pulses are characterized by their transversal $I(x,y)$ and temporal $I(t)$ intensity profile. The spatial profile is usually described by the product of two Gaussian functions

$$I(x,y) \propto \exp\left(-\frac{x^2}{R_\mathrm{x}^2}\right) \exp\left(-\frac{y^2}{R_\mathrm{y}^2}\right), \tag{2.35}$$

where $R_\mathrm{x,y}$ is the beam radius perpendicular to the direction of propagation, i.e., in x- and y-direction, respectively.

The time time-dependent electric field $E(t)$ of a pulse is characterized by an harmonic oscillation with frequency ω_0 and starting phase ϕ_0 multiplied by an envelope $A(t)$ which specifies the temporal shape, e.g., Gauss or Lorentz shape:

$$E(t) = A(t)\cos(\omega_0 t + \phi_0) = \frac{1}{2}\left(\tilde{E}(t) + \tilde{E}^*(t)\right), \tag{2.36}$$
$$\text{with} \quad \tilde{E}(t) = A(t)\exp\left[i(\omega_0 t + \phi_0)\right].$$

A more general expression is given according to the exponential notation of the cosine by the complex electric field $\tilde{E}(t)$ and its complex conjugate $\tilde{E}^*(t)$. As already briefly introduced in section 2.2.2, the square of this electric field yields the temporal intensity profile $I(t)$ of the pulse including the vacuum permittivity ϵ_0, speed of light c, and refractive index n:

$$I(t) = \frac{1}{2}\epsilon_0 c n \left|\tilde{E}(t)\right| = \frac{1}{2}\epsilon_0 c n A(t)^2. \tag{2.37}$$

Thus, considering both the temporal and transversal beam profile with equal beam radii R in x- and y-direction, respectively, results in the overall pulse intensity profile:

$$I(r,t) = I_0 \exp\left(-4 \cdot \ln(2)\frac{t^2}{\tau^2}\right) \exp\left(-\frac{r^2}{R^2}\right), \tag{2.38}$$

where τ describes the temporal full width at half maximum and R corresponds to the $1/e^2$ value of the intensity. The peak intensity I_0 is defined by

$$I_0 = 4\sqrt{\frac{\ln(2)}{\pi}}\frac{E_\mathrm{p}}{\pi R^2 \tau} = 4\sqrt{\frac{\ln(2)}{\pi}}\frac{\langle P\rangle}{\pi R^2 \tau f_\mathrm{rep}}, \tag{2.39}$$

with the pulse energy E_p. Additionally, I_0 can be described by considering the time-averaged power $\langle P\rangle$ in combination with the pulse repetition rate f_rep.

2.3.2 Dispersion

Ultrashort laser pulses of pulse duration τ cannot be treated as monochromatic laser sources but possess a spectral width $\Delta\omega$ arising from the energy-time uncertainty relation [44, 47]:

$$\tau\Delta\omega \geq 2\pi c_\mathrm{ps}. \tag{2.40}$$

This time-bandwidth-product is bounded below by its characteristic, pulse shape dependent numerical constant c_ps which is equal to 0.441 for a Gaussian temporal shape. Thus, a reduction of the pulse duration implies an increase of the spectral width and vice versa. If there is equality in Eq. 2.40, the pulse is called Fourier-limited. For instance, a fourier-limited pulse with a pulse duration of $\tau = 100\,\mathrm{fs}$ or $\tau = 8\,\mathrm{ns}$ features a spectral width of $\approx 4\,\mathrm{nm}$ or $\approx 0.05\,\mathrm{pm}$, respectively, therefore allowing to neglect the spectral broadening for pulse durations above the ps-time regime.

As a consequence of the refractive index dispersion [43], distinct frequencies will propagate with different phase velocities v_p within a medium:

$$v_\mathrm{p}(\omega) = \frac{c_0}{n(\omega)} = \frac{\omega}{k} \qquad \Leftrightarrow \qquad k = \frac{n(\omega)\omega}{c_0}. \tag{2.41}$$

Here, c_0 is the speed of light in vacuum, $\omega = 2\pi c/\lambda$ the light frequency and k the wave vector. Multiplication of the wave vector with the propagation length L defines the phase $\phi(\omega)$ of a complex electric field $\tilde{E}(\omega)$ in the frequency domain. Similar to the temporal domain, a spectral intensity $I(\omega)$ can be obtained:

$$\tilde{E}(\omega) = A(\omega)\exp\left[i\phi(\omega)\right], \tag{2.42}$$

$$I(\omega) \propto |\tilde{E}(\omega)| = A(\omega)^2, \tag{2.43}$$

with the envelope $A(\omega)$. Several physical parameters and relations can be obtained from the phase $\phi(\omega)$: a pulse with extended spectrum $\Delta\omega$ will travel through a medium with the group velocity v_{g} defined via the first derivative of $\phi(\omega)$:

$$v_{\mathrm{g}} = \frac{L}{T_{\mathrm{g}}} = \frac{L}{\phi'(\omega_0)} = \left(\frac{dk}{d\omega_0}\right)^{-1} = \frac{c_0}{n - \lambda_0 \frac{dn}{d\lambda_0}}, \tag{2.44}$$

where $\phi'(\omega_0)$, $dk/d\omega_0$ and $dn/d\lambda_0$ denote the derivative at the point of central frequency ω_0 and central wavelength λ_0, respectively. T_{g} is commonly called group delay. The dispersion of the individual frequency components (group velocity dispersion, abbr.: GVD) is given by the second derivative of the phase $\phi(\omega)$:

$$\mathrm{GVD} = \frac{\phi''(\omega_0)}{L} = \frac{d^2k}{d\omega^2} = \frac{d}{d\omega}\frac{1}{\nu_{\mathrm{g}}} = \frac{\lambda_0^3}{2\pi c_0^2}\frac{d^2n}{d\lambda_0^2}. \tag{2.45}$$

Multiplying Eq. 2.45 with the propagation length L leads to the dispersion of the group delay (GDD: group delay dispersion) which is equal to $\phi''(\omega_0)$.

In conclusion, even though the pulse propagates with the group velocity within the medium, different spectral components will travel with their respective phase velocities, thus, resulting in different time spans required to pass the medium (GDD). Hence, GDD leads in general (normal dispersion) to a broadening of the pulse duration (pulse stretching) illustrated in Fig. 2.3. If the Fourier-limited pulse duration τ_0 is known, the

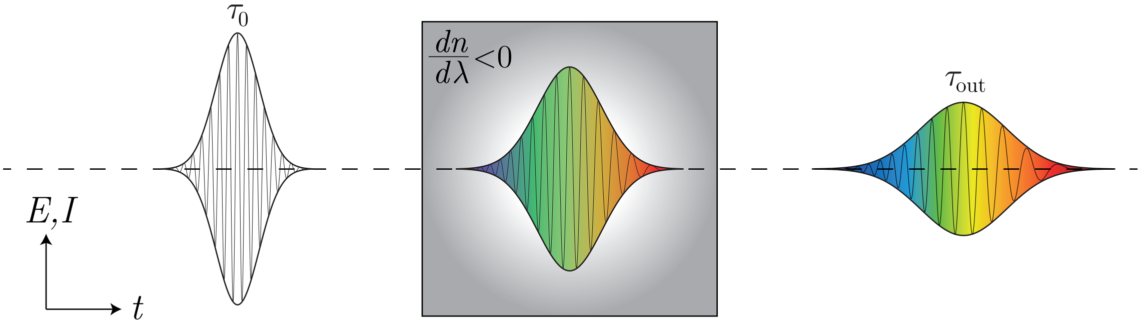

Figure 2.3 – Impact of dispersion on the spectral distribution of the spectral components of a broadband, ultrashort laser pulse with incident pulse duration τ_0. While propagating through the medium, the pulse experiences dispersion which results in a temporal broadening due to different phase velocities of the respective spectral components and, subsequently, in a reduced peak intensity according to Eq. 2.39. The pulse duration after the medium is expressed by τ_{out} (cf. Eq. 2.46). The oscillation within the pulse represents the temporal electric field $E(t)$ (cf. Eq. 2.36 and Eq. 2.48).

temporal pulse width at the output face of the material τ_{out} can be calculated via

$$\tau_{\mathrm{out}} = \sqrt{\tau_0^2 + \left(4\ln(2)\frac{\phi''(\omega_0)}{\tau_0}\right)^2}. \tag{2.46}$$

Thus, in case of a non-dispersive medium or a negligible spectral width of the incident light source, the group velocity dispersion, group delay dispersion and thereby the temporal broadening of the pulse duration are zero. The electromagnetic wave will then propagate with the group velocity which is equal to the phase velocity.

2.3.3 Chirp

After passing a normal dispersive medium, an initially Fourier-limited pulse will experience a broadening of its pulse duration due to group delay dispersion. Therefore, the phase of the temporal electric field (Eq. 2.36) is extended by an additional term

$$\phi(t) = \phi_0 + \frac{d\phi}{dt}(t-t_0) + \frac{1}{2}\frac{d^2\phi}{dt^2}(t-t_0)^2, \tag{2.47}$$

$$\phi(t) = \phi_0 + \omega_0(t-t_0) + \frac{1}{2}a(t-t_0)^2, \tag{2.48}$$

$$\omega(t) = \frac{d\phi(t)}{dt} = \omega_0 + a(t-t_0). \tag{2.49}$$

The first derivative of the phase $\phi(t)$ results in a current frequency $\omega(t)$ which depends linearly on the time $(t-t_0)$. This time dependent frequency distribution inside the pulse is called linear chirp and is determined by the chirp parameter

$$a = \frac{d\omega(t)}{dt} = \frac{\Delta\omega}{\tau}\sqrt{1-\left(\frac{\tau_0}{\tau}\right)^2}, \tag{2.50}$$

which can be deduced from the first derivative of $\omega(t)$ or the appropriate pulse parameters [68]. The temporal distribution of the frequency $\omega(t)$ (black dashed line) is illustrated in Fig. 2.4 with chirp parameter $a = 1.0 \cdot 10^{26}\,\mathrm{rad/s^2}$, pulse duration $\tau = 100\,\mathrm{fs}$ (FWHM) and spectral width $\Delta\omega \approx 3.0 \cdot 10^{13}\,\mathrm{rad/s}$ ($\Delta\lambda \approx 4\,\mathrm{nm}$). In addition the current wavelength $\lambda(t)$ is shown in green. The current frequency at the point $t = t_0$ corresponds to the central frequency (wavelength) $\omega_0 \approx 3.5 \cdot 10^{15}\,\mathrm{rad/s}$ ($\lambda_0 = 532\,\mathrm{nm}$). The time dependent electric field $E(t)$ with current phase according to Eq. 2.48 ($\phi_0 = 0$) is presented in the right part of Fig. 2.4. To visualize the effect of a linear chirp, the chirp parameter and, thereby, the spectral width are increased to $a = 1.0 \cdot 10^{28}\,\mathrm{rad/s^2}$ and $\Delta\omega \approx 3.0 \cdot 10^{15}\,\mathrm{rad/s}$ ($\Delta\lambda \approx 550\,\mathrm{nm}$) while the pulse duration of $\tau = 100\,\mathrm{fs}$ is maintained.

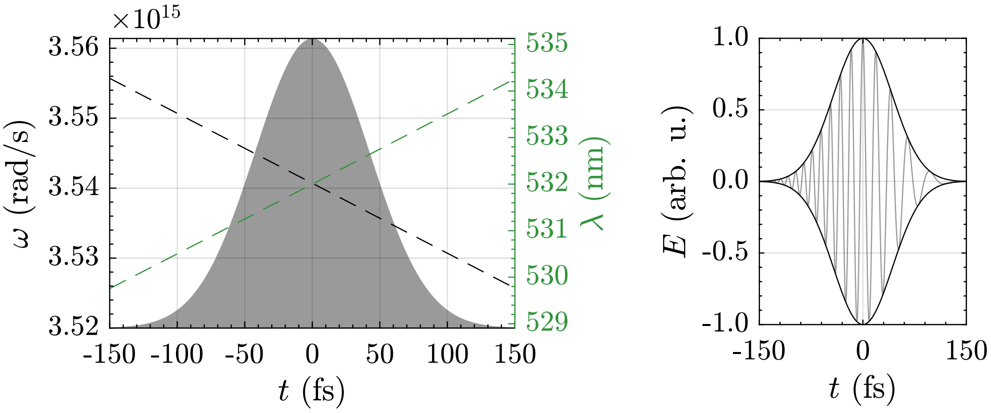

Figure 2.4 – **Left:** Temporal distribution of the frequency ω (black dashed line) and wavelength λ (green dashed line) of a linearly chirped pulse with a chirp parameter $a = 1.0 \cdot 10^{26}\,\mathrm{rad/s^2}$, $\tau = 100\,\mathrm{fs}$ (FWHM), $\omega_0 \approx 3.5 \cdot 10^{15}\,\mathrm{rad/s}$ ($\lambda_0 = 532\,\mathrm{nm}$) and spectral width $\Delta\omega \approx 3.0 \cdot 10^{13}\,\mathrm{rad/s}$ ($\Delta\lambda \approx 4\,\mathrm{nm}$). The temporal intensity profile is shown in gray. **Right:** Illustration of the development of the electric field E as a function of time with $a = 1.0 \cdot 10^{28}\,\mathrm{rad/s^2}$ and $\tau = 100\,\mathrm{fs}$ (FHWM). The spectral width is thereby increased to $\Delta\omega \approx 3.0 \cdot 10^{15}\,\mathrm{rad/s}$ ($\Delta\lambda \approx 550\,\mathrm{nm}$).

2.4 Holography

2.4.1 Holographic principle

The interference of two coherent light waves of equal polarization states commonly called reference (R) and signal (S) beam/wave with their respective electric fields

$$E_{\mathrm{R,S}}(\mathbf{r},t) \;=\; E^0_{\mathrm{R,S}} \exp\left[-i(\mathbf{k}_{\mathrm{R,S}}\mathbf{r} + \omega_{\mathrm{R,S}}t)\right], \tag{2.51}$$

where $E^0_{\mathrm{R,S}}$ is the amplitude, $\omega_{\mathrm{R,S}}$ the frequency and $\mathbf{k}_{\mathrm{R,S}}$ the wave vector of the reference and signal beam, respectively [25, 54, 69, 70] (cf. left part of Fig. 2.5) results in an cosinusoidal intensity modulation $I(\mathbf{r})$

$$I(\mathbf{r}) \;=\; |E_{\mathrm{R}}(\mathbf{r},t) + E_{\mathrm{S}}(\mathbf{r},t)|^2 = I_0 \cdot [1 + m \cdot \cos(\mathbf{K} \cdot r)], \tag{2.52}$$

$$\text{with} \quad m = \frac{2\sqrt{I_{\mathrm{R}} I_{\mathrm{S}}}}{I_{\mathrm{R}} + I_{\mathrm{S}}}, \quad I_0 \;=\; I_{\mathrm{R}} + I_{\mathrm{S}}.$$

Here, I_0 describes the total intensity and $m \in [0;1]$ is the modulation depth of the arising intensity pattern whose wave vector $\mathbf{K}$ can be derived via

$$\mathbf{K} = \mathbf{k}_{\mathrm{R}} - \mathbf{k}_{\mathrm{S}},\ |\mathbf{K}| = 2\pi\sqrt{\frac{1}{\lambda_{\mathrm{R}}^2} + \frac{1}{\lambda_{\mathrm{S}}^2} - \frac{2}{\lambda_{\mathrm{R}}\lambda_{\mathrm{S}}}\cos(2\theta)} = \frac{2\pi}{\Lambda}, \tag{2.53}$$

where $\lambda_{\mathrm{R,S}}$ is the wavelength of the reference and signal wave, respectively, and 2θ describes the total angle between both beams. The wave vector $\mathbf{K}$ can be associated to the wavelength Λ, commonly known as grating constant d.

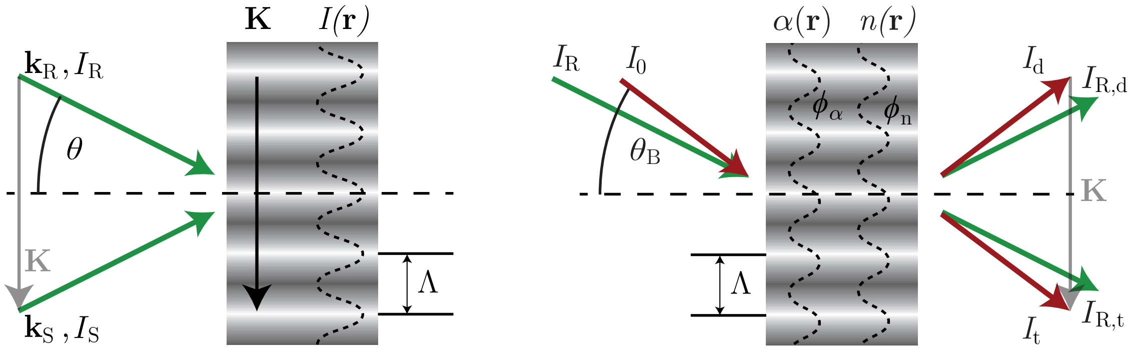

Figure 2.5 – **Left:** Principle of grating recording by two identical light waves according to [25, 68]. The interference of reference **R** and signal **S** beam impinging onto the sample under the angle θ results in a modulation of the intensity $I(\mathbf{r})$ (marked as gray shades areas) with the grating vector $\mathbf{K} = \mathbf{k}_{\mathrm{R}} - \mathbf{k}_{\mathrm{S}}$ and periodicity Λ. **Right:** Principle of grating read-out by the reference wave I_{R} and a third light wave with incident intensity I_0 and angle of incident θ_{B}. The intensity modulation of both writing beams can be transferred into an elementary holographic grating, i.e., a modulation of the absorption coefficient $\alpha(\mathbf{r})$ and/or refractive index $n(\mathbf{r})$ with a possible phase shift ϕ_α, ϕ_{n} in relation to $I(\mathbf{r})$, respectively. Diffraction on the grating results in a transmitted ($I_{\mathrm{R,t}}$ and I_{t}) and diffracted ($I_{\mathrm{R,d}}$ and I_{d}) light wave.

The intensity modulation can be transferred into a modulation of the absorption coefficient $\alpha(\mathbf{r})$ (absorption or amplitude grating) and/or refractive index $n(\mathbf{r})$ (refractive or phase grating) in photochromic and/or photorefractive materials [25, 71–75] (cf. right part of Fig. 2.5). These elementary, holographic gratings can be read-out by diffraction of either the reference wave when the signal wave is turned off or an additional beam (cf. right part of Fig. 2.5) which satisfies the first order Bragg-condition

$$2d\sin(\theta_{\mathrm{B}}) = \lambda \qquad \Leftrightarrow \qquad 2\Lambda\sin(\theta_{\mathrm{B}}) = \lambda, \tag{2.54}$$

where θ_{B} describes the angle of incidence related to the wavelength λ of the additional beam, commonly known as Bragg-angle. In the latter case, the efficiency of the diffraction process η can be determined by

$$\eta = \frac{I_{\mathrm{d}}}{I_0}, \tag{2.55}$$

$$\eta = \frac{I_{\mathrm{d}}}{I_{\mathrm{d}} + I_{\mathrm{t}}}, \tag{2.56}$$

where I_0 and I_{d} are the intensities of the incident and diffracted (first diffraction order) beam, respectively. If extinction losses, i.e., reflexion, absorption and scattering, are accounted for, Eq. 2.55 can by modified to Eq. 2.56, where I_t is the intensity of the transmitted (zeroth diffraction order) beam.

2.4.2 Coupled wave theory

In 1969, Kogelnik derived a coupled wave theory for the diffraction of light waves on elementary holographic volume gratings [25], i.e., a modulation of the refractive index Δn and/or absorption coefficient $\Delta\alpha$. A brief description will be given in the following along reference [25, 76]. The starting point is the wave equation inside the material for the wave Ψ:

$$\nabla^2\Psi + k^2\Psi = 0, \tag{2.57}$$

$$\text{with} \quad k^2 = \frac{\omega^2}{c^2}\epsilon + i\omega\mu\sigma, \quad \alpha = \frac{\mu c\sigma_0}{2\sqrt{\epsilon_0}}, \tag{2.58}$$

where μ is the magnetic permeability and σ describes the conductivity which is correlated to the absorption coefficient/average absorption constant α. The dielectric constant ϵ and conductivity σ are given by

$$\epsilon = \epsilon_0 + \epsilon_1\cos(\mathbf{Kr} + \phi_\mathrm{n}), \tag{2.59}$$

$$\sigma = \sigma_0 + \sigma_1\cos(\mathbf{Kr} + \phi_\alpha), \tag{2.60}$$

with the dielectric constant and conductivity modulation ϵ_1 and σ_1, respectively. The general solution for Eq. 2.57 is assumed to arise from the superposition of two equal waves referred to as reference and signal wave with their complex amplitudes $R(z)$ and $S(z)$ (electric fields) and wave vectors $\mathbf{k}_\mathrm{R,S}$ ($|\mathbf{k}_\mathrm{R,S}| = 2\pi/\lambda$)

$$\Psi = R(z)\exp(i\mathbf{k}_\mathrm{R}\mathbf{r}) + S(z)\exp(i\mathbf{k}_\mathrm{S}\mathbf{r}) \tag{2.61}$$

in combination with the Bragg condition Eq. 2.53 (cf. left part of Fig. 2.5). Here, θ is the angle of incidence inside the material. Investing additionally weak coupling ($d^2R/dz^2 \approx d^2S/dz^2 \approx 0$) results in the coupled wave equations for the reference R and signal S wave

$$\begin{aligned} \frac{dR}{dz} &= -\frac{1}{\cos\theta}(\alpha R - i\kappa_+ S), \\ \frac{dS}{dz} &= -\frac{1}{\cos\theta}(\alpha S - i\kappa_- R). \end{aligned} \tag{2.62}$$

The complex coupling parameters κ_+ and κ_- characterize the mutual energy transfer between the reference R and signal S wave and can be deduced from:

$$\begin{aligned} \kappa_+ &= \frac{1}{2}\left(\frac{\omega\Delta n}{c}\exp(i\phi_\mathrm{n}) + i\Delta\alpha\exp(i\phi_\alpha)\right) \\ &= \frac{\pi\Delta n}{\lambda}\exp(i\phi_\mathrm{n}) + i\frac{\Delta\alpha}{2}\exp(i\phi_\alpha), \end{aligned} \tag{2.63}$$

$$\begin{aligned}\kappa_- &= \frac{1}{2}\left(\frac{\omega\Delta n}{c}\exp(-i\phi_\mathrm{n}) + i\Delta\alpha\exp(-i\phi_\alpha)\right)\\ &= \frac{\pi\Delta n}{\lambda}\exp(-i\phi_\mathrm{n}) + i\frac{\Delta\alpha}{2}\exp(-i\phi_\alpha),\end{aligned} \tag{2.64}$$

where

$$\Delta n = \frac{\epsilon_1}{2\sqrt{\epsilon_0}} \qquad \text{and} \qquad \Delta\alpha = \frac{\mu c\sigma_1}{2\sqrt{\epsilon_0}} \tag{2.65}$$

are the amplitudes of the refractive index and absorption modulation (cf. Eq. 2.59, Eq. 2.60 and right part of Fig. 2.5), respectively.

Solving the coupled wave equations for the reference and signal wave enables the determination of the diffraction efficiency η. For simplicity, the grating is assumed to be unslanted, i.e., $\mathbf{K}$ is perpendicular to the surface normal, and read-out is performed under the Bragg-angle. Thereby, the diffraction efficiency for a pure refractive ($\Delta\alpha = \alpha_0 = 0$) and pure absorption grating ($\Delta n = 0$) can be determined via

$$\eta(\Delta\alpha = \alpha_0 = 0) = \sin^2\left(\frac{\pi\Delta n d_\mathrm{h}}{\lambda\cos\theta}\right), \tag{2.66}$$

$$\eta(\Delta n = 0) = \sinh^2\left(\frac{\Delta\alpha d_\mathrm{h}}{2\cos\theta}\right)\exp\left(-\frac{-2(\alpha_0+\Delta\alpha)d}{\cos\theta}\right), \tag{2.67}$$

where d_h describes the hologram thickness, α_0 the fundamental absorption for the wavelength λ and θ_B is the internal Bragg-angle. In case of pure absorption gratings, the maximum diffraction efficiency is limited to 3.7 % while values of up to 100 % are reached for pure refractive index gratings ($\Delta\alpha = 0$) [77]. However, average bulk absorption is not considered in case of a phase grating which is consistent if the diffraction efficiency is defined according to Eq. 2.56. Taking additional absorption losses into account results in the well known equation for the diffraction efficiency of mixed holographic gratings

$$\eta = \left[\sin^2\left(\frac{\pi\Delta n d_\mathrm{h}}{\lambda\cos\theta_\mathrm{B}}\right) + \sinh^2\left(\frac{\Delta\alpha d_\mathrm{h}}{2\cos\theta_\mathrm{B}}\right)\right]\exp\left(-\frac{2(\alpha_0+\Delta\alpha)d_\mathrm{h}}{\cos\theta_\mathrm{B}}\right). \tag{2.68}$$

Stationary energy transfer

According to Eq. 2.36, the electric field of the reference R and signal S wave can be described by

$$R = \sqrt{I_\mathrm{R}}\exp(-i\Psi_\mathrm{R}), \tag{2.69}$$

$$S = \sqrt{I_\mathrm{S}}\exp(-i\Psi_\mathrm{S}), \tag{2.70}$$

where $I_{\mathrm{R,S}}$ and $\Psi_{\mathrm{R,S}}$ are the respective intensities and phases. Inserting these expressions into the coupled wave equations Eq. 2.62 and comparing the imaginary and real terms result in the following set of equations:

$$\frac{dI_{\mathrm{R}}}{dz} = -\frac{\kappa_{+}^{\mathrm{im}}}{\cos\theta}\frac{4I_{\mathrm{R}}I_{\mathrm{S}}}{I_{\mathrm{R}}+I_{\mathrm{S}}} - \alpha_0 I_{\mathrm{R}}, \tag{2.71}$$

$$\frac{dI_{\mathrm{S}}}{dz} = -\frac{\kappa_{-}^{\mathrm{im}}}{\cos\theta}\frac{4I_{\mathrm{R}}I_{\mathrm{S}}}{I_{\mathrm{R}}+I_{\mathrm{S}}} - \alpha_0 I_{\mathrm{S}}, \tag{2.72}$$

$$\frac{d\Psi_{\mathrm{R}}}{dz} = -\frac{\kappa_{+}^{\mathrm{re}}}{\cos\theta}\frac{2I_{\mathrm{S}}}{I_{\mathrm{R}}+I_{\mathrm{S}}}, \tag{2.73}$$

$$\frac{d\Psi_{\mathrm{S}}}{dz} = -\frac{\kappa_{-}^{\mathrm{re}}}{\cos\theta}\frac{2I_{\mathrm{R}}}{I_{\mathrm{R}}+I_{\mathrm{S}}}. \tag{2.74}$$

Here, the exponents refer to the real (re) and imaginary part (im) of the coupling constants κ_+ and κ_-. These equations are derived for the stationary case, i.e., any time derivative reaches a value of zero [78]. Rearranging Eq. 2.71-2.74 to

$$\frac{d(I_{\mathrm{R}}+I_{\mathrm{S}})}{dz} = -\frac{4\Delta\alpha\ \cos\phi_{\alpha}}{\cos\theta}\frac{I_{\mathrm{R}}I_{\mathrm{S}}}{I_{\mathrm{R}}+I_{\mathrm{S}}} - \alpha_0 I_{\mathrm{R}} - \alpha_0 I_{\mathrm{S}}, \tag{2.75}$$

$$\frac{d(I_{\mathrm{R}}-I_{\mathrm{S}})}{dz} = \frac{8\pi\Delta n\ \sin\phi_{\mathrm{n}}}{\lambda\cos\theta}\frac{I_{\mathrm{R}}I_{\mathrm{S}}}{I_{\mathrm{R}}+I_{\mathrm{S}}} - \alpha_0 I_{\mathrm{R}} + \alpha_0 I_{\mathrm{S}}, \tag{2.76}$$

$$\frac{d(\Psi_{\mathrm{S}}-\Psi_{\mathrm{R}})}{dz} = 2\frac{\pi\Delta n\ \cos\phi_{\mathrm{n}}}{\lambda\ \cos\theta}\frac{I_{\mathrm{S}}-I_{\mathrm{R}}}{I_{\mathrm{R}}+I_{\mathrm{S}}} - \frac{\Delta\alpha\ \sin\phi_{\alpha}}{\cos\theta}, \tag{2.77}$$

$$\frac{d(\Psi_{\mathrm{S}}+\Psi_{\mathrm{R}})}{dz} = -2\frac{\pi\Delta n\ \cos\phi_{\mathrm{n}}}{\lambda\ \cos\theta} + \frac{\Delta\alpha\ \sin\phi_{\alpha}}{\cos\theta}\frac{I_{\mathrm{S}}-I_{\mathrm{R}}}{I_{\mathrm{R}}+I_{\mathrm{S}}}. \tag{2.78}$$

allow for formulating some fundamental properties of mixed holographic gratings where bulk absorption will not be considered $\alpha_0 = 0$:

- Energy conservation: energy conservation is expressed by Eq. 2.75 and is solely related to absorption. It is achieved for a phase shift of $\pi/2$ or in the absence of any modulation $\Delta\alpha$.
- Energy exchange: energy exchange is expressed by Eq. 2.76 and is only dependent on the refractive index modulation. It reaches the maximum for a phase shift of $\pi/2$ between the refractive index modulation and the intensity pattern. Thus, no energy is transferred in case of a local response ($\phi_{\mathrm{n}} = 0$).
- Phase shifting or phase coupling: even though a direct energy exchange (Eq. 2.76) is not possible in case of a local response ($\phi_{\mathrm{n}} = 0$), a transient energy transfer can occur by using different intensities of the reference and signal wave (the absorption modulation will be neglected in the following). This mechanism will be described within the next section.

Solving Eq. 2.71 and Eq. 2.72 leads to the intensity of the reference and signal wave as a function of propagation depth z [54, 69, 79] where the modulation of the absorption coefficient $\Delta\alpha$ is neglected (according to Eq. 2.77 $\Delta\alpha$ is not involved in the stationary energy transfer):

$$I_\mathrm{R} = I_\mathrm{R}(0)\frac{1+m^{-1}}{1+m^{-1}\ \exp(\gamma z)}\exp(-\alpha_0 z), \tag{2.79}$$

$$I_\mathrm{S} = I_\mathrm{S}(0)\frac{1+m^{-1}}{1+m^{-1}\ \exp(\gamma z)}\exp\left((\gamma-\alpha_0)z\right), \tag{2.80}$$

where $m = I_\mathrm{R}(0)/I_\mathrm{S}(0)$ is the intensity ratio of the input beams and γ is defined by Eq. 2.71 and Eq. 2.72 in combination with $\kappa_+^\mathrm{im}(\Delta\alpha = 0)$ to

$$\gamma = \frac{4\pi\Delta n}{\lambda\cos\theta}\sin\phi_\mathrm{n}. \tag{2.81}$$

Note that in the absence of any coupling ($\gamma = 0$), both intensities are given by Beer's law (Eq. 2.15). However, in the absence of absorption, I_S will increase with increasing z while I_R decreases, thus, energy is transferred from the reference into the signal wave provided $\Delta n > 0$. As previously mentioned, this coupling reaches a maximum for a phase shift of $\phi_\mathrm{n} = \pi/2$ of the refractive index grating with respect to the interference pattern. In conclusion, the signal beam will be amplified if the energy gain overcomes the absorption losses.

2.4.3 Dynamic gratings

Transient energy transfer

The phase coupling (cf. Eq. 2.77) represents a lateral shift of the intensity pattern as function of propagation depth z and thereby time t which is illustrated in Fig. 2.6 according to references [78, 80]. At time $t = 0$, there is no grating present ($\Delta n = 0$), thus, the interference pattern phase planes are parallel to the sample surface (Fig. 2.6 left). A further recording results in a build-up of the grating on which both beams are diffracted. Due to the different intensities and the phase shift of the diffracted wave, the superposition of the diffracted and transmitted wave leads to a phase shifted interference pattern with respect to the initial intensity modulation and, subsequently, in a phase shifted refractive index modulation. This self-diffraction process continuous with increasing propagation depth z resulting in a linear phase shift of the phase grating. However, due to the inertia of the material (characteristic relaxation time τ), the refractive index modulation lags behind the interference pattern (Fig. 2.6 middle). This inertia gives rise to a phase mismatch between the grating and the fringe pattern which is the origin of the energy transfer. In the steady state ($t \geq \tau$), the phase modulation catches up the interference pattern and the energy transfer vanishes. Hence, energy can be exchanged even in photorefractive media with a local response if the intensity of the reference and signal beam differ [81–85] and the exposure time is less than or equal to the relaxation time τ. This process is then called transient holography or transient energy transfer (TET) [78, 83, 85] where energy is always transferred from the strong into the weak wave [83, 85–87].

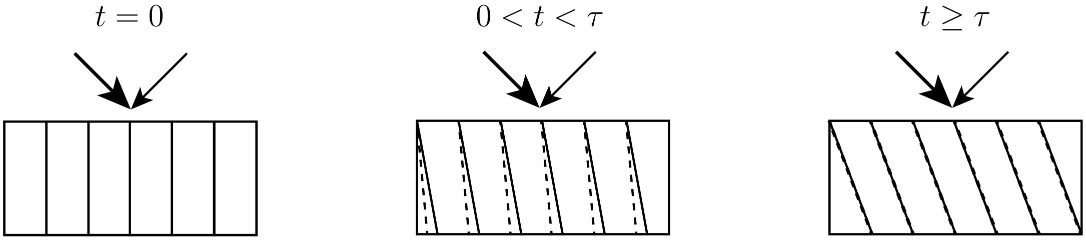

Figure 2.6 – Illustration of the transient energy transfer in photorefractive media with a local response $\phi_\mathrm{n} = 0$ according to references [78, 80]. Two beams of different intensities (highlighted by the thickness of the respective arrows) give rise to a tilt of the intensity modulation (lines) and, subsequently, the refractive index modulation Δn (dashed lines). The inertia of the material described by the decay time constant τ results in a phase shift of the interference pattern and index modulation which facilitates the energy exchange from the strong to the weak wave (see full text for further information).

Moving gratings

The aforementioned principle of holographic grating recording is usually referred to equal beams, i.e., equal wavelengths. However, using ultrashort laser pulses facilitates also the recording of elementary holographic gratings of significant contrast with different colors [17, 88]. In this case, the grating is not stationary but moves with the velocity

$$v = \frac{\Omega}{|\mathbf{K}|} = \frac{\omega_\mathrm{R} - \omega_\mathrm{S}}{|\mathbf{K}|} \tag{2.82}$$

along the slanted grating vector $\mathbf{K}$ (c.f Fig. 2.7) where Ω describes the frequency detuning between the reference and signal pulse of frequency $\omega_\mathrm{R,S}$, respectively. In case of a non-instantaneous material response, a phase shift of the interference pattern and the written holographic grating arises which enables energy transfer [69]. Here, the amplitude of the phase grating Δn is given by

$$\Delta n = \frac{\Delta n^{(0)}}{(1 + \Omega^2 \tau^2)^{1/2}}, \tag{2.83}$$

where τ is the decay time constant and $\Delta n^{(0)}$ is the phase modulation of the degenerated case $\Omega = 0$ derived in section 2.4.2. Thus, the amplitude of the refractive index modulation decreases with increasing grating velocity v, i.e., frequency detuning, and decay time τ.

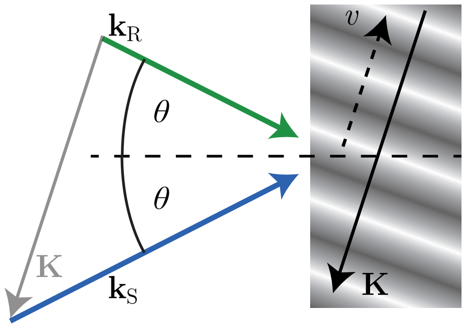

Figure 2.7 – Principle of grating recording by two laser pulses of different wavelengths. The frequency detuning of the signal $\mathbf{k}_\mathrm{S}$ and reference $\mathbf{k}_\mathrm{R}$ wave leads to a tilt of the grating which performs a lateral movement with the velocity v along the grating vector $\mathbf{K}$.

2.4.4 Holographic gain factor

A quantitative description of the energy transfer is given by the holographic gain factor Γ which is equal to γ (Eq. 2.81). As mentioned before, the energy transfer and thereby the holographic gain reaches its maximum if the phase shift between the intensity and refractive index modulation is equal to $\pi/2$. By using non-degenerated waves, the coupling constant/holographic gain factor depends again on the frequency detuning Ω and decay time τ:

$$\Gamma_\mathrm{nd} = \gamma_\mathrm{nd} = \frac{\gamma}{1+(\Omega\tau)^2}, \tag{2.84}$$

where γ is the coupling constant or holographic gain of the degenerated, i.e., stationary case. However, in media with a pronounced Kerr-effect (Kerr media) where the refractive index modulation is proportional to the electric field strength and not to the contrast of the interference pattern [54, 69], the gain factor is given by

$$\gamma^\mathrm{K}_\mathrm{nd} = \gamma^\mathrm{K}\frac{\Omega\tau}{1+(\Omega\tau)^2}. \tag{2.85}$$

Here, γ^K is again the gain factor in the event of degenerated waves.

2.4.5 Photorefractive effect

The photorefractive effect (PR-effect) describes in general the alteration of the refractive index by means of light exposure and was first observed by Ashkin in 1966 as a disruptive effect regarding the spatial beam profile [89]. The first model of the PR-effect was introduced by Chen [90, 91] where space charge fields induced by charge transport mechanisms result in refractive index changes Δn via the linear electro-optic effect (Pockels effect). The following description and equations will only account for electrons, however, similar considerations can be performed for positively charged electron holes. According to the original model of Chen [91] and the further developed Kuhktarev-Vinetskii-model [54, 78, 92], the material is assumed to contain electron donor impurities and electron traps, so called acceptor states. The photorefractive effect can be separated into four steps: (1) charge carrier excitation, (2) charge transport, (3) charge carrier trapping, and (4) refractive index modulation via the Pockels effect (cf. Fig. 2.8). The intensity pattern of two writing beams within the material gives rise to a periodically modulated charge carrier excitation from donor sites into the conduction band and, subsequently, in a periodic charge carrier density $N(\mathbf{r})$. Beside a recombination with the ionized donor site, a redistribution (charge transport) of the excited electrons from bright towards dark areas takes place which is characterized by the current density $j(\mathbf{r})$ and commonly attributed to three different processes [71, 93]: (i) unidirectional drift in an externally applied electric field ($j_{\mathrm{drift}}(\mathbf{r})$), (ii) diffusion due to a charge concentration gradient ($j_{\mathrm{diff}}(\mathbf{r})$), and (iii) charge transport arising from the photovoltaic effect ($j_{\mathrm{phv}}(\mathbf{r})$). Thus, the total current density is given by

$$j(\mathbf{r}) = j_{\mathrm{drift}}(\mathbf{r}) + j_{\mathrm{diff}}(\mathbf{r}) + j_{\mathrm{phv}}(\mathbf{r}), \tag{2.86}$$

with

$$j_{\mathrm{drift}}(\mathbf{r}) = (\sigma_{\mathrm{ph}} - \sigma_{\mathrm{d}})E(\mathbf{r}), \tag{2.87}$$

$$j_{\mathrm{diff}}(\mathbf{r}) = eD\nabla N(\mathbf{r}), \tag{2.88}$$

$$j_{\mathrm{phv,i}}(\mathbf{r}) = \frac{1}{2}(\beta_{\mathrm{ijk}}E_{\mathrm{j}}^{*}(\mathbf{r})E_{\mathrm{k}}(\mathbf{r}) + c.c.), \tag{2.89}$$

where σ_{ph} and σ_{d} is the photo- and dark conductivity of the material, respectively, $E(\mathbf{r})$ is the strength of an externally applied electric field, e is the electron charge, D is the diffusion tensor, and β_{ijk} is the photovoltaic tensor, where the indices j and k account for the orientation of the light polarization and i for the direction of the macroscopic current. $E_{\mathrm{j}}^{*}(\mathbf{r})$ and $E_{\mathrm{k}}(\mathbf{r})$ are the corresponding electric field components of the impinging light waves, respectively. Note that the complex conjugate of $E_{\mathrm{j}}^{*}(\mathbf{r})$ is incorporated. Trapping at acceptor sites occurs within the dark areas giving rise to a spatially modulated charge density ρ which is linked to the current density $j(\mathbf{r})$ via the continuity equation $\dot{\rho}(\mathbf{r}) + \nabla j(\mathbf{r}) = 0$. Via the Poisson's equation $\nabla E^{\mathrm{SC}}(\mathbf{r}) = \rho(\mathbf{r})/\epsilon$, where ϵ is the permittivity, $\rho(\mathbf{r})$ is linked to a spatially modulated electric field $\mathbf{E}^{\mathrm{SC}}(\mathbf{r})$ which is called space charge field. This internal electric field provokes a periodic modulation of the refractive index via the Pockels effect:

$$\Delta n(\mathbf{r})_{\mathrm{ij}} = \frac{1}{2}n^{3}r_{\mathrm{ijk}}E_{\mathrm{k}}^{\mathrm{SC}}(\mathbf{r}). \tag{2.90}$$

Here, n is the undisturbed refractive index, $E_{\mathrm{k}}^{\mathrm{SC}}(\mathbf{r})$ denotes the k-component of the electric space charge field $\mathbf{E}^{\mathrm{SC}}(\mathbf{r})$ and r_{ijk} describes the electro-optic tensor where the indices i and j account for the direction of the refractive index change and k corresponds to the orientation of the electric field. This tensor can be reduced to four elements by applying appropriate symmetry operations and combining the first to indices to a single

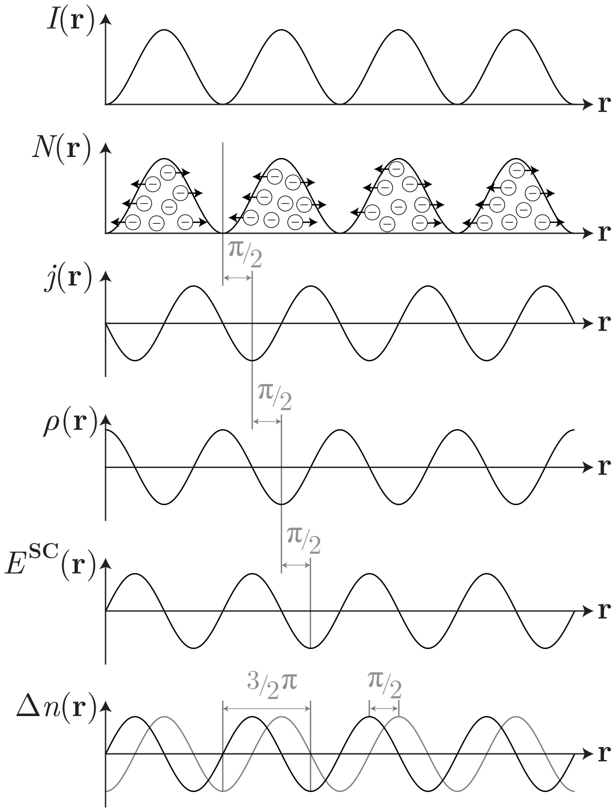

Figure 2.8 – Illustration of the photorefractive effect for a diffusion based charge transport. A sinusoidal intensity distribution $I(\mathbf{r})$ results in a modulated charge carrier density $N(\mathbf{r})$. Charge redistribution gives rise to the current density $j(\mathbf{r})$ which in turn leads to a modulated electric space charge field $E^{\mathrm{SC}}(\mathbf{r})$ via the charge density $\rho(\mathbf{r})$. Subsequently, a periodic refractive index change $\Delta n(\mathbf{r})$ is caused via the Pockels effect which is $\pi/2$ phase shifted (in total $3/2\pi$) with respect to the intensity modulation $I(\mathbf{r})$ (light gray).

index [48,69]. However, most frequently, only the $r_{13}\widehat{=}r_{\mathrm{xz}}$- and $r_{33}\widehat{=}r_{\mathrm{zz}}$-tensor element is used. Here, the x- and z-direction is perpendicular and parallel to the crystallographic c-axis, respectively.

In case of a diffusion based charge transport (cf. Fig. 2.8), the spatial modulation of the refractive index is $\pi/2$ phase shifted with respect to the intensity pattern of the recording waves, thus, enabling considerable charge transfer according to section 2.4.2.

Photogalvanic effect

The photogalvanic effect, often called (bulk) photovoltaic effect (BVPE) is known as the driving charge transport mechanism to initiate the photorefractive effect in iron-doped lithium niobate [71,72,94], where iron is incorporated as Fe^{2+} (electron donor) and Fe^{3+} (electron acceptor) [95,96]. It was first observed by Glass *et al.* [94], who discovered a steady short-circuit current j_{phv} when a crystal is exposed to uniform light illumination. Contrarily to the charge redistribution via diffusion, the excited charge carriers have a higher probability to travel along the crystallographic polar axis (c-axis), i.e., $+c$ direction, rather than in the opposite $-c$ direction. The reason for this is an asymmetric potential of the donor impurities (Fe^{2+}-center) [97]. As a consequence, a net macroscopic current arises which is orientated along the c-axis and characterized by the photovoltaic tensor β_{ijk} (Eq. 2.89). Similar symmetry operations as applied for the electro-optic tensor allow the reduction to four individual elements [48], where the indices j and k account for the orientation of the light polarization and i for the direction of the macroscopic current. Subsequently, the excited electrons can be trapped by deep Fe^{3+}-centers. Thereby, Fe^{3+} is reduced into Fe^{2+} which then serves as new donor state. However, a periodic intensity modulation will prevent from an optical re-excitation within dark areas, thus, terminating the photovoltaic current. This leads in turn to a steady-state electron distribution and, subsequently, to the development of a holographic grating via the photorefractive effect. In 2011, Schirmer *et al.* have proposed a microscopic model of the underlying charge transport taking the contribution of small polarons (see section 2.6.1) into account [98] which was further investigated by Vittadello *et al.* [99].

In comparison to a diffusion driven charge redistribution, the total phase shift between an intensity pattern and refractive index modulation will reach a value of π in case of the photovoltaic effect. Thus, the material exposes a local response, thereby preventing from the stationary energy transfer. However, considerably large electric space fields of several 10-100 kV/cm^2 [99, 100] ensure diffraction efficiencies of up to 100 % [100].

2.5 Photoswitchable molecules

Molecular switches are in general components whose physical or chemical properties are modified by changes of the environment. If this modification is triggered by light, the compounds are called photoswitchable molecules or optical switches. In this regard, the term switch/switching is referred to an isomerization of the molecule. In principle, two types of isomers with further sub-categories can be distinguished: (i) stereoisomers (spatial isomers) and (ii) constitutional (structural) isomers. The first reveal a spatial rearrangement of the atoms while the respective binding partners are preserved after the isomerization. One of the most prominent compounds is azobenzene (N-C=C-N) performing a trans→cis and cis→trans isomerization under UV- and VIS-light exposure, respectively [101–104]. However, the conformational geometry of constitutional isomers differ with respect to their binding partners as known for instance for the photorefractive sodium nitroprusside (SNP) [105, 106] or photochromic ruthenium sulfoxide compounds [28, 107]. The fundamental properties of photoswitchable molecules will be described briefly i.a. on the example of the photochromic transition metal compound $[\mathrm{Ru(bpy)_2(OSO)}]^+$, where bpy is 2,2'-bipyridine and OSO is the photoswitchable 2-methylsulfinylbenzoate-ligand [28, 29, 108]. It consists of two bpy-ligands which are bonded to the central ruthenium(II)-atom (Ru) by two N-Ru-single bounds each, where N is nitrogen. In its thermodynamic ground state (GS), the OSO-ligand is bonded to ruthenium via the sulfoxide-atom (S). Detailed information on the structure are given in references [28, 29, 108], appendix A.1 and the references therein. In the following, the compound will be abbreviated as OSO-complex.

Light-induced charge transfers

In general, transition metal compounds can be excited from their ground state into a higher electronic state (ES) by absorbing a photon of appropriate energy $E = h\nu = E_{\mathrm{ES}} - E_{\mathrm{GS}}$. This transition from an occupied into an empty molecule orbital can be achieved by four different electron transfers [109], where M indicates the metal atom, L a ligand, and $*$ an anti-bonding molecule orbital:

- Metal to ligand charge transfer (MLCT), i.e., a charge transfer from Mπ to Lπ^*.
- Ligand to metal charge transfer (LMCT), i.e., a charge transfer from Lπ to Mσ^*.
- Metal centered charge transfer (MC), i.e., an intra metal charge transfer from Mπ to Mσ^*.
- Ligand centered charge transfer (LC), i.e., an intra ligand charge transfer from Lπ to Lπ^*.

The energy difference of the involved molecule orbitals is related to specific absorption bands within the absorption spectrum of the ground state. For instance, the OSO-complex features a pronounced absorption band at 285 nm which is referred to a LC-transfer [109], while a second broad absorption band peaking at 396 nm is associated with a MLCT [28,29,108]. Subsequently, a photoexcited molecule can lower its energy by three unimolecular reactions which transfer the molecule either back into its original ground state or into another conformation/isomer [109]: (i) heat dissipation, (ii) luminescence, and (iii) a photochemical reaction. Apart from that, also bimolecular reactions [109] can lower the potential by performing an energy or electron transfer to a second molecule into account [110]. However, in comparison to the other three unimolecular reactions, bimolecular reactions are in general slow and require long-lived excited states in the range of ns [109]. Since the OSO-complex reveals lifetimes in the ps-time domain [29, 108], bimolecular reactions are not considered. In fact, the energy minimization by means of linkage isomerization via a photochemical reaction is the most important mechanism regarding constitutional isomers like SNP or the OSO-complex. Therefore, this process will be examined in more detail within the next section.

Photochemical reaction

The photochemical reaction of a photoswitchable molecule is associated to a linkage isomerization, i.e., a deactivation/decay into a metastable state MS. The energy level diagram including the total energy of the molecule in the ground and metastable state as well as the lowest excited states is illustrated in Fig. 2.9. The reaction coordinate represents the progress of the structural alteration of the molecule and is exemplarily shown for the OSO-compound. By absorbing a photon of sufficiently high energy $E = h\nu = E(\mathrm{GS}^*) - E(\mathrm{GS})$, the excited state GS* can be addressed by an electron transfer from the central metal atom to one of its bpy-ligands (MLCT) via a Frank-

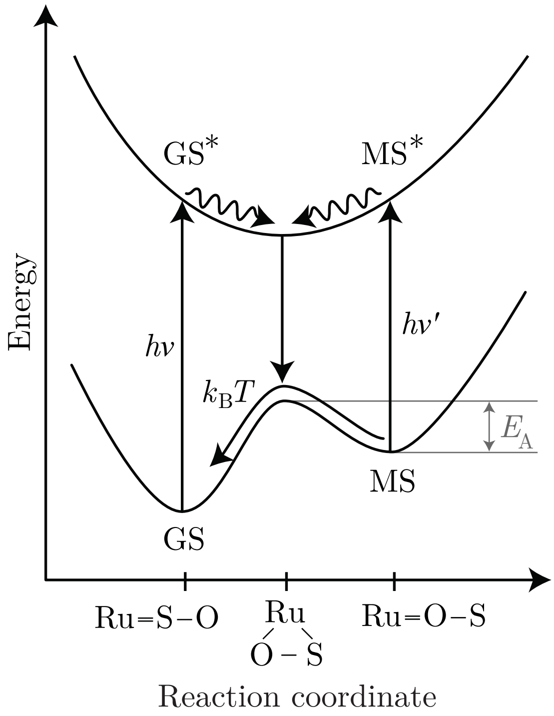

Figure 2.9 – Energy level diagram according to reference [31] depicting the transformation of a photoswitchable molecule from the ground state (GS) into the metastable MS via the excited ground state GS*. The corresponding structural change is characterized by the reaction coordinate on the example of the OSO-compound. A back isomerization into GS can be achieved either thermally (k_BT) or optically via MS* (not valid for the OSO-complex but e.g. for SNP [31]) by overcoming the energy barrier E_A.

Condon-transition [29,108]. Thus, the reaction coordinate is not changed. Subsequently, the molecule can lower its energy to the minimum of the excited state landscape by, e.g., vibrational relaxation typically within several femto- to picoseconds [29,111]. This transition results in a structurally changed intermediate state (see reaction coordinate). Starting from the local minimum, the molecule has two possible relaxation paths both accompanied by an alteration of the structure: (i) back into the original ground state (GS) and (ii) into a second electronic ground state MS [29,108]. Due to the elevated potential, this state is referred to a metastable state MS which is separated from the global ground state minimum by an energy barrier. As a result on the example of the OSO-complex, the molecule has performed a structural change from its S-bonded ground state via an SO-bonded intermediate state to the final O-bonded metastable state. However, the formation of MS strongly depends on the relative position of the excited state minimum and local ground state maximum with respect to the reaction coordinate [112] and exhibits a quantum yield of 0.45 in case of the OSO-compound [28,108].

A thermally activated transition from the metastable state back into the ground state is possible by overcoming the energy barrier. The temperature dependence of this reaction is characterized by Arrhenius law which enables the determination of the activation energy E_A. Typical values for the OSO-compound are in the range of $0.7-1.0\,\text{eV}$ resulting in metastable state lifetimes of $10^3 - 10^4\,\text{s}$ in solution [30] and $10^4 - 10^5\,\text{s}$ embedded into a solid-like polymer at room temperature [33]. Apart from this thermally activated reaction, Fig. 2.9 illustrates additionally an optical electron excitation by absorbing a photon of energy $E = h\nu' = E(\mathrm{MS}^*) - E(\mathrm{MS})$. In case of the OSO-compound, the electron is transferred from the O-bonded metastable state into an O-bonded excited state MS*. The molecule will return back into MS only via vibrational relaxations [29]. As a consequence, backswitching from MS to GS can only be triggered thermally but not optically. However, several photoswitchable molecules, e.g. SNP, allow for an optical back reaction. The excited molecule relaxes vibrationally from MS* to the local minimum of the excited state curve accompanied by a structural change. From here on, the further transformation corresponds to the processes described above. In conclusion, this type of photoswitchable transition metal compounds can perform an optically induced isomerization from the ground state into the metastable state and vice versa which offers great potential for write-read-erasure cycles in holographic storage [87,113]. Apart from that, the optical transition from MS to MS* can be utilized to dynamically probe the isomerization process.

Photorefractive and photochromic sensitivity

The photorefractive sensitivity of a material is a measure with respect to its optical susceptibility/sensitivity. It was introduced by Günter in 1982 [114] for photorefractive crystals and can be defined as amount of optical energy required to produce a certain (generally the maximum) change of the refractive index Δn:

$$S_{\Delta \mathrm{n}} = \frac{\Delta n}{Q} = \frac{\Delta n}{I\,t}, \tag{2.91}$$

$$S_{\Delta \mathrm{n}} = \frac{\Delta n}{I\,t\,c}. \tag{2.92}$$

The exposure Q is given by the product of light intensity I and exposure time t. The photorefractive sensitivity can be easily adapted to molecular compounds by additionally normalizing to the concentration c (Eq. 2.92). Accordingly, the photochromic sensitivity is applied for molecular compounds featuring pronounced absorption changes $\Delta\alpha$:

$$S_{\Delta \alpha} = \frac{\Delta \alpha}{I\,t\,c}. \tag{2.93}$$

2.6 Transient quasiparticles in lithium niobate

2.6.1 Lithium niobate

In the following section, the most important properties of lithium niobate (abbr.: LN) are summarized. The description is based mainly on references [48, 115], thus, further details about the crystallographic properties can be found therein.

Lithium niobate crystallizes in its solid form in a perovskite like structure, i.e., the structure can be described along the crystallographic *c*-axis by a chain of oxygen octahedra that form the valence band. One third each contains lithium (Li^+), niobium (Nb^{5+}) representing the conduction band or is left empty. One of the most prominent phases is the congruent phase in which the Li/Nb-ratio is about 0.94 [115–117]. However, the crystal reacts on the mismatch by the build-up of intrinsic defects, e.g., lithium vacancies (V_{Li}) or antisite-defects like niobium on a lithium-site (Nb_{Li}). The regular Nb-atoms form a trigonal sub-lattice with the lattice constants $a = 515\,pm$ and $c = 1386\,pm$. Perpendicular to the c-axis, the oxygen-ions are arranged in planes which are in a distorted hexagonal configuration along the *c*-axis.

Undoped, congruently melted lithium niobate is transparent over the VIS-spectral range and has a fundamental absorption starting around 3.8 eV-4.1 eV at room temperature [118]. However, the optical/crystal absorption properties can be tuned by embedding different doping atoms into the melt that occupy Li-sites, e.g., iron (Fe), copper (Cu) or manganese (Mn) to increase the photorefractive properties [95,119–124] or magnesium (Mg) and zinc (Zn) to optimize the optical laser-induced damage threshold [116,125,126]. Particularly, iron-doped lithium niobate (Fe:LN) is of utmost importance for this thesis and is considered in the following in more detail.

Iron is incorporated into the crystal as Fe^{2+} and Fe^{3+} on lithium sites. After the growing procedure, the Fe^{2+}/Fe^{3+}-ratio can be tuned in a wide range by reduction and oxidation, respectively. The incorporated Fe^{2+}-centers give rise to an additional broad absorption band in the visible spectral range peaking at around 2.6 eV [119, 127]. This iron D-band allows an electron transfer from the iron center into the conduction band ($Fe_{Li}^{2+} \rightarrow Nb_{Nb}^{5+}$), which highly increases the photoconductivity or photorefractive sensitivity [95, 119, 121, 124]. However, in case of Fe^{3+}, the electron can be optically transferred from the valence band into the iron center (iron C-band, $O^{2-} \rightarrow Fe_{Li}^{3+}$) for photon energies larger than approx. 3.1 eV [127]. Hence, Fe^{3+}-center serve as electron acceptor.

Apart from the above presented iron defect centers, lithium niobate is known to form transient states under light illumination, i.e., small polarons and (self-trapped) excitons which will be summarized in the next section.

2.6.2 Self-trapped quasiparticles

Small polarons

If an electron is excited from one lattice site to another one, the additional charge carrier (or the remaining hole) can alter the equilibrium position of the surrounding atoms by coulomb or short-range interactions [34–36] which is illustrated in Fig. 2.10 (left). The achieved distortion of the crystal lattice leads to a self-induced potential well where the particle is self-trapped. This charge carrier localization together with the crystal lattice distortion is then called polaron. Depending on the spatial range of the lattice distortion on a unit cell of beyond, a distinction between small and large polarons is made [36]. Further information on the general microscopic model of small polarons are given in references [34–36] and is out of the scope of this thesis.

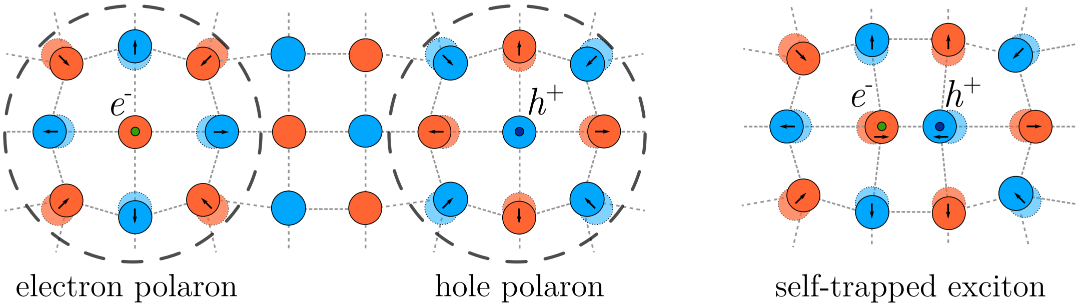

Figure 2.10 – Illustration of the lattice distortion induced by additional charge carriers according to reference [36] and taken with permission of S. Messerschmidt from reference [128] licensed under ©BY-NC-ND 3.0 DE [129]. **Left:** An additional negative or positive charge results in a lattice distortion which creates a potential well were it is self-trapped (electron or hole polaron). **Right:** An electron-hole pair within one lattice constant can alter the equilibrium position of the surrounding atoms in which the electron-hole pair is self-trapped.

In lithium niobate, four intrinsic small polarons are known whose characteristic absorption bands in the VIS to NIR-spectral range have recently been recalculated [128]:

- free polaron (FP): an additional electron located at a niobium-atom on a regular Nb-site ($\mathrm{Nb}_{\mathrm{Nb}}^{4+}$) gives rise to an additional absorption band peaking around 1.0 eV ($\widehat{=}$1240 nm) [130].
- bound polaron (GP): an additional electron located at a niobium-atom on a lithium site ($\mathrm{Nb}_{\mathrm{Li}}^{4+}$) gives rise to an additional absorption band peaking around 1.6 eV ($\widehat{=}$775 nm) [116].
- bipolaron (BP): the superposition of the individual potential wells of a free and bound polaron on adjacent lattice sites results in a combined distortion of the lattice ($\mathrm{Nb}_{\mathrm{Nb}}^{4+}$:$\mathrm{Nb}_{\mathrm{Li}}^{4+}$). Depending on the literature source, the resulting absorption band covers the complete visible range with a local maximum around 2.5 eV ($\approx$ 500 nm) [11, 131] and between $\approx 2.6 - 3.0$ eV ($\approx 480 - 410$ nm) [128], respectively.
- hole polaron (HP): a missing electron at an oxygen ion in close vicinity to a lithium vacancy ($\mathrm{O}^- - \mathrm{V}_{\mathrm{Li}}$) gives rise to an additional absorption band peaking around 2.5 eV ($\approx$ 500 nm) [11, 132] and $2.0 - 2.1$ eV ($\approx 620 - 590$ nm) [128], respectively.

Besides, an electron which is located at an extrinsic defect such as $\mathrm{Fe}_{\mathrm{Li}}^{2+}$ can be modeled by the small polaron approach as well [98, 133]. The respective absorption bands related to $\mathrm{Fe}_{\mathrm{Li}}^{2+}$/$\mathrm{Fe}_{\mathrm{Li}}^{3+}$-center and small polarons (excluding free polarons) are illustrated in Fig. 2.11 [128]. For the sake of completeness, the absorption cross-section of the $Fe^{2+}-O^{-}-V_{Li}$ excitonic state (cf. section 2.6.2) determined in appendix A.2 is depicted.

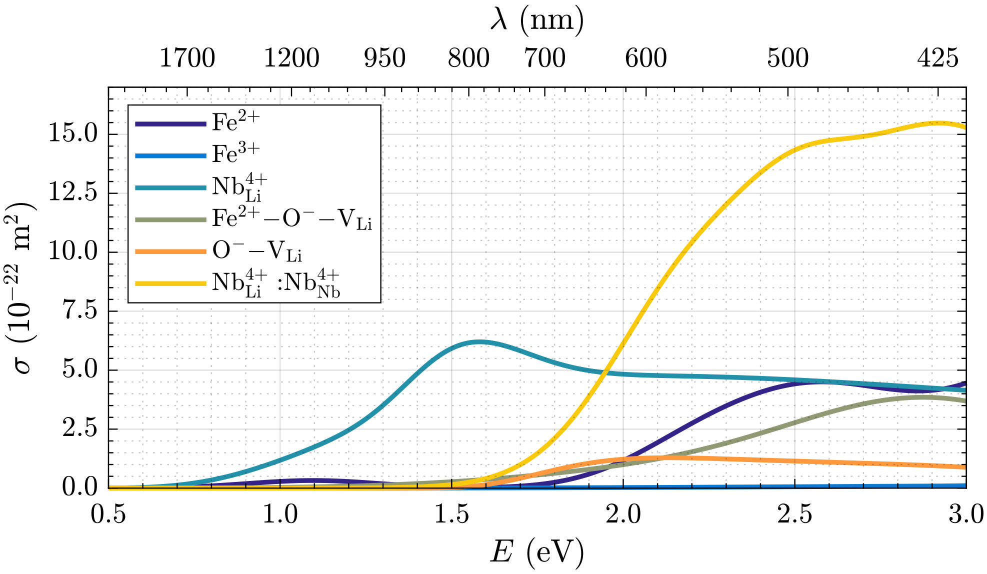

Figure 2.11 – Overview of the optical absorption cross-section of Fe_{Li}^{2+}-centers, Fe_{Li}^{3+}-centers, Nb_{Li}^{4+} bound polarons, $O^{-}-V_{Li}$ hole polarons, $Nb_{Nb}^{4+}:Nb_{Li}^{4+}$ bipolarons, and $Fe^{2+}-O^{-}-V_{Li}$ excitonic states (cf. section 2.6.2) in lithium niobate, taken with permission of S. Messerschmidt from reference [128] licensed under ©BY-NC-ND 3.0 DE [129]. The latter is deduced for the first time within this work in appendix A.2.

The optical generation and relaxation of small polarons result in a transient change of the absorption coefficient which consists of the steady state absorption coefficient $\alpha_0(E)$ and the polaronic light-induced absorption coefficient $\alpha_{\mathrm{li},i}(E,t)$ of different polaronic centers i:

$$\alpha(E,t) = \alpha_0(E) + \sum_i \alpha_{\mathrm{li},i}(E,t). \tag{2.94}$$

$$\alpha_{\mathrm{li},i}(E,t) = \sigma_i(E)\, N_{\mathrm{li},i}(t). \tag{2.95}$$

The individual contribution of a single polaronic state to the overall light-induced absorption is expressed by Eq. 2.95 and is given by the energy dependent absorption cross-section $\sigma_{\mathrm{i}}(E)$ and the time-dependent number density of generated quasiparticles $N_{\mathrm{li},i}(t)$. Detailed information about the optical generation, decay and recombination dynamics as well as absorption cross-sections and number densities are often deduced from transient light-induced absorption measurements [7, 8, 11–13]. All references reveal that the temporal decay of the quasiparticles can be best described by a sum of stretched-exponential functions, known as KWW-function (Kohlrausch-Williams-Watts-function) [134, 135]:

$$\alpha_{\mathrm{li}}(t) = \sum_i \alpha_{\mathrm{li},i}^{(0)} \exp\left[-\left(\frac{t}{\tau_i}\right)^{\beta_i}\right], \tag{2.96}$$

$$\langle\tau_i\rangle = \Gamma\left(1+\frac{1}{\beta_i}\right)\tau_i, \tag{2.97}$$

where $\alpha_{\mathrm{li},i}^{(0)}$ is the induced absorption for $t = 0$, τ_i represents the characteristic lifetime and $\beta_i \in [0;1]$ describes the stretching-factor related to a single KWW-function, i.e., to the absorption features of a single polaronic center. The characteristic lifetime τ_i is connected to the average decay time $\langle\tau_i\rangle$ via Eq. 2.97, where $\Gamma(x)$ is the Gamma-function [136]. A common explanation of the stretched decay of a polaron population is based on a broad distribution of recombination probabilities due to different covered distances after excitation [9] and, thus, a broad distribution of decay times. Hence, one interpretation of the stretching factor β in Eq 2.96 is related to the spreading of the individual decay times. The application of more than one KWW-function is an indication for either multiple recombination paths or the transformation of one quasiparticle into another one (see e.g. references [8, 12]).

Small polarons are known to be responsible for various effects in lithium niobate. This includes for example their contribution to the photovoltaic effect [98, 99] or the intensity dependence of the nonlinear refractive index determined by the z-scan technique [18, 137]. Moreover, the pronounced light-induced absorption features $\alpha_{\mathrm{li}}(E)$ of small polarons are related to light-induced refractive index change $n_{\mathrm{li}}(E)$ via the Kramers-Kronig relation (cf. section 2.1.2). For instance, this relationship is applied to elucidate the recording of efficient holographic gratings in thermally reduced, undoped lithium niobate [13, 73, 138].

Self-trapped excitons

The second type of quasiparticles in a crystal is an exciton which consists of a negatively charged electron and a positively charged hole [40, 41]. Although an exciton is neutral, it can lower its total energy by the attractive Coulomb-interaction of its constituents which is known as free exciton. Moreover, an electron-hole pair can couple to the crystal lattice by short-range forces, thus, altering the equilibrium position of the surrounding atoms (cf. right part of Fig. 2.10). Similar to the polaron theory, the lattice distortion results in a potential well where the exciton is trapped. In this case, the exciton is called self-trapped (abbr.: STE) [37, 39]. Williams *et al.* have shown that STEs reveal several broad absorption bands resembling the excitation of the constituents to higher states within the exciton or the ionization of the STE [38, 40].

In lithium niobate, self-trapped electron-hole pairs are assumed to be localized in Nb-O-octahedra, either on a regular $\mathrm{Nb}_{\mathrm{Nb}}$-site or a $\mathrm{Nb}_{\mathrm{Li}}$-antisite defect [139,140]. The recombination process of such generated excitons is accompanied by (photo)-luminescence phenomena which have been investigated in nominally pure and doped LN at temperatures below 100 K [139, 140] and at room temperature using fs-NIR-pulse trains in Mg-doped LN [141]. However, recently, Messerschmidt *et al.* have proposed a comprehensive model of charge-transport phenomena in Mg- and Fe-doped LN by additionally considering pinned excitonic states as intermediate steps [12]. In this regard, apart from the above mentioned recombination process, the excited electron-hole pair can be pinned to extrinsic defects, e.g., $\mathrm{Fe}_{\mathrm{Li}}^{3+}$ in close vicinity to a charge-compensating lithium vacancy ($\mathrm{Fe}_{\mathrm{Li}}^{3+}-\mathrm{V}_{\mathrm{Li}}$). Subsequently, the electron of the $\mathrm{Nb}_{\mathrm{Nb}}^{4+}$-constituent can jump to the $\mathrm{Fe}_{\mathrm{Li}}^{3+}$, thus, transforming the pinned-STE into an $\mathrm{Fe}_{\mathrm{Li}}^{2+} - \mathrm{O}^{-} - \mathrm{V}_{\mathrm{Li}}$ excitonic state (abbr.: Fe-STE) which causes a long-lived blue absorption [12].

3 Mechanisms of the light-matter/surface interaction

3.1 Mechanisms of the hologram formation in photoswitchable molecule-enriched polymer films

Detailed studies of the light-matter interaction reveal pronounced absorption changes in the visible spectral range, metastable state lifetimes of up to 10^5 s at room temperature and elevated temperatures, respectively, and switching times in the range of picoseconds of photoswitchable ruthenium sulfoxide compounds [29, 30, 33]. First attempts of spatially modulated illumination point out a high-contrast, high-contour sharpness and a high optical resolution when embedding the powdery OSO-compound into the silicon based, matrix-like polymer polydimethylsiloxane (abbr. PDMS) [33], thereby yielding a highly flexible, photoswitchable solid. Thus, the physical properties disclose a great potential with respect to (holographic) data storage and ultrafast switches.

The author contributed to the paper *Holographic performance of silicon polymer films based on photoswitchable molecules*. The abstract is printed here with friendly permission of the Optical Society of America (OSA). The complete article can be found in the appendix A.1.

B. Bourdon, S. Bock, C. Kijatkin, A. Shumelyuk, and M. Imlau
Holographic performance of silicon polymer films based on photoswitchable molecules
Opt. Mater. Express **8**, 1951-1967 (2018); doi: 10.1364/OME.8.001951.

Abstract: Holographic silicon polymer films based on photoswitchable molecules are studied with respect to their performance for hologram recording, with photoswitchable ruthenium sulfoxide complexes as an example. Our systematic study reveals that it is possible to record elementary holographic lossy gratings with outstanding quality with respect to their dynamics and in- and off-Bragg read-out features. Furthermore, the possibility for the recording of multiple holograms within the same volume element via angular multiplexing as well as the recording with continuous-wave

and a fs-laser pulse train is successfully demonstrated. At the same time, a strong limitation of the maximum diffraction efficiency in the order of $\sim 10^{-3}$ is found that cannot be counterbalanced by either the tuning of material (thickness, concentration, ...) or recording parameters (repetition rate, wavelength, ...). This limitation – being severe for any type of holographic applications – is discussed and compared with the performance of high-efficient single-crystalline reference holographic media. We conclude that the potential of sulfoxide compounds may be hidden in holography until it becomes possible to synthesize polymer films with appropriate three-dimensional structural arrangement of the photoswitchable compounds.

3.2 Pulse-induced transient blue absorption related with long-lived excitonic states in iron-doped lithium niobate

Recently, Messerschmidt *et al.* have shown that a long-lived blue absorption feature in iron-doped lithium niobate can be attributed to the generation of excitonic states bound to $\mathrm{Fe_{Li}}$ defect centers (Fe-STE) rather than to the formation of bound, hole and/or iron polarons [12]. Nanosecond-pump, supercontinuum probe transient absorption spectroscopy is applied to crystals of distinct compositions to further investigate and control the corresponding peculiarities.

The author contributed to the paper *Pulse-induced transient blue absorption related with long-lived excitonic states in iron-doped lithium niobate.* The abstract is printed here with friendly permission of the Optical Society of America (OSA). The complete article can be found in the appendix A.2.

S. Messerschmidt, B. Bourdon, D. Brinkmann, A. Krampf, L. Vittadello, and M. Imlau
Pulse-induced transient blue absorption related with long-lived excitonic states in iron-doped lithium niobate
Opt. Mater. Express **9**, 2748-2760 (2019); doi: 10.1364/OME.9.002748.

Abstract: Transient absorption is studied in Fe-doped lithium niobate single crystals with the goal to control and probe a blue absorption feature related with excitonic states bound to $\mathrm{Fe_{Li}}$ defect centers. The exciton absorption is deduced from the comparison of ns-pump, supercontinuum-probe spectra obtained in crystals with different Fe-concentration and $\mathrm{Fe_{Li}^{2+/3+}}$-ratio, at different pulse peak and photon energies as well as by signal separation taking well-known small polaron absorption bands into account. As a result, a broad-band absorption feature is deduced being characterized by an absorption cross-section of up to $\sigma^{\max}(2.85\,\mathrm{eV}) = (4 \pm 2) \cdot 10^{-22}\,\mathrm{m}^2$. The band peaks at about 2.85 eV and can be reconstructed by the sum of two Gaussians centered at 2.2 eV (width ≈ 0.5 eV) and 2.9 eV (width ≈ 0.4 eV), respectively. The appropriate build-up and decay properties strongly depend on the crystals' composition as well as the incident pulse parameters. All findings are comprehensively analyzed and discussed within the model of $\mathrm{Fe_{Li}^{2+} - O^{-} - V_{Li}}$ excitonic states.

Besides the determination of the absorption cross-section, the direct generation of Fe-STEs via the iron C-band is demonstrated for a pump wavelength of 355 nm. However, due to the temporal resolution, the performed supercontinuum probe spectroscopy measurements are not suitable to precisely determine temporal dynamics. Moreover, systematic studies of the ns-pump pulse intensity dependence are missing so far. For this purpose, the light-induced absorption changes are investigated in the following with a pump wavelength of $\lambda_\mathrm{p} = 355\,\mathrm{nm}$ and a fixed sample configuration to support the predicted one-photon absorption process.

3.2.1 Experimental methods

Sample

According to the results on the sample configuration dependence (appendix A.2), a congruent lithium niobate crystal doped with 0.1 mol% iron in the melt and grown by the University of Padova with the parameters summarized in Tab. 3.1 is used. To highly prefer the excitation via the iron C-band (see reference [119], appendix A.2) the sample was treated to minimize the absorption related to Fe^{2+}-center. Their concentration is determined by optical absorption measurements [7, 95] with a commercial two-beam spectrometer (*Shimadzu UV-3600*) illustrated in Fig. 3.1.

Table 3.1 – Properties of the iron-doped LN crystal used in the following studies from the University of Padova. The $\mathrm{Fe}_\mathrm{Li}^{2+}$-concentration was determined by optical absorption measurements [7, 95]. Here, d is denoting the thickness of the sample.

$c_{\mathrm{Fe_{Li}}}$ (mol %)	$c_{\mathrm{Fe}_\mathrm{Li}^{2+}}$ ($10^{17}\,\mathrm{cm}^{-3}$)	$c_{\mathrm{Fe}_\mathrm{Li}^{3+}}$ ($10^{19}\,\mathrm{cm}^{-3}$)	$c_{\mathrm{Fe}_\mathrm{Li}^{2+}}/c_{\mathrm{Fe}_\mathrm{Li}^{3+}}$	d (mm)
0.1	≈ 0.0	1.89	≈ 0.0	(1.00 ± 0.01)

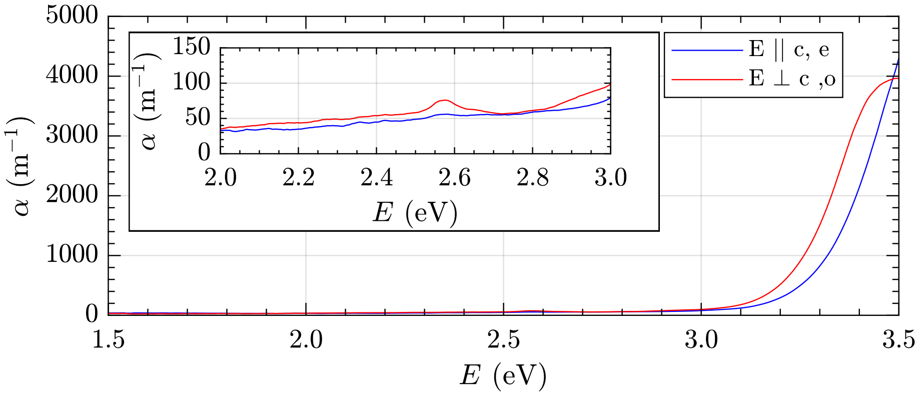

Figure 3.1 – Absorption spectrum of the 0.1 mol% oxidized iron doped lithium niobate crystal for an extraordinary (blue) and ordinary (red) probe polarization in the range of 1.5 – 3.5 eV. The inset shows a zoom of the spectra between 2.0 – 3.0 eV.

Both spectra show a vanishing absorption in the near infrared (NIR) to visible (VIS) spectral range. Thus, an electron excitation via the iron D-band ($\mathrm{Fe}_{\mathrm{Li}}^{2+} \rightarrow \mathrm{Nb}_{\mathrm{Nb}}^{5+}$) can be neglected, hence, nearly all iron centers are in the valence state 3+. Instead, the absorption coefficient α reveals a strong increase of up to $\approx 4000\,\mathrm{m}^{-1}$ for photon energies $E \gtrsim 3.1\,\mathrm{eV}$ which can be attributed to the iron C-band [119]. An additional weak absorption band is detectable around 2.6 eV (ordinary polarization) which belongs to the iron F-band [119]. It is worth mentioning that the high-energetic saturation of the absorption coefficient caused by Fe^{3+} in case of an ordinary polarization is owed to the detection limit of the two-beam spectrometer in combination with the sample thickness of $d = 1\,\mathrm{mm}$.

Setup

A frequency tripled Nd:YAG pulse laser (Innolas inc., type *Spitlight 600*) serves as pump source ($\lambda_{\mathrm{P}} = 355\,\mathrm{nm}$, $\tau_{\mathrm{FWHM}} = 8\,\mathrm{ns}$, extraordinary polarized) and impinges perpendicular onto the sample's surface. An electronic circuit enables the reduction of the repetition rate from 10 Hz down to single-shot experiments. The induced material changes are investigated by measuring the transmission change of two continuous wave lasers (*Coherent Sapphire* $\lambda = 488\,\mathrm{nm}$ and *Coherent Cube* $\lambda = 785\,\mathrm{nm}$) with extraordinary polarization. After focusing and passing appropriate laser line filters, the transmitted

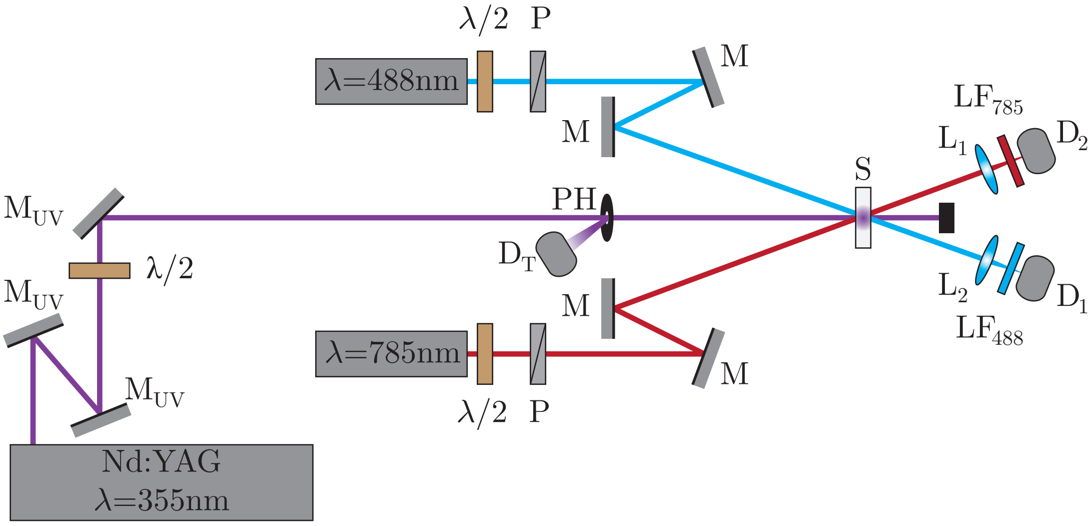

Figure 3.2 – Experimental setup for measuring the transient absorption induced by a frequency tripled Nd:YAG pulse laser at $\lambda_{\mathrm{p}} = 355\,\mathrm{nm}$. Two cw-laser at $\lambda = 488\,\mathrm{nm}$ and $\lambda = 785\,\mathrm{nm}$ are used for detecting the absorption changes, respectively. M_{UV}: UV protected mirror, $\lambda/2$: half wave-plate, PH: pinhole, S: lithium niobate sample, P: polarizer, M: mirror, $\mathrm{L}_{1,2}$: lens, $\mathrm{LF}_{488,785}$: laser line filter, $\mathrm{D}_{1,2,\mathrm{T}}$: Si-PIN diodes.

intensities are detected via Si-pin diodes which are connected to a digital oscilloscope (LeCroy, type *Waverunner LT584*) triggered by diode D_T. Recording is performed over three different time ranges to ensure sufficient sampling rates: (i) -100 μs to 900 μs, (ii) -50 ms to 450 ms, and (iii) -10 s to 90 s. At least five measurements are performed within each time resolution which are subsequently combined and averaged. The values for $t \leq 0$ s are used as unaffected transmitted signal for the calculation of the light-induced absorption

$$\alpha_{\mathrm{li}}(E,t) = -\frac{1}{d} \ln \left[\frac{I(E,t)}{I(E,t \leq 0)} \right]. \tag{3.1}$$

3.2.2 Temporal dynamics and intensity dependence

Temporal dynamics

The temporal dynamic of the light-induced absorption probed at $\lambda = 488$ nm with an intensity of $I_{488} = (15 \pm 1)\,\mathrm{mW/cm^2}$ is illustrated in the left part of Fig. 3.3. An absorption coefficient of $\approx 60\,\mathrm{m^{-1}}$ is detected immediately after the incident ns-pump pulse ($\lambda_\mathrm{p} = 355$ nm, $I_\mathrm{p} = (13.5 \pm 1.0)\,\mathrm{MW/cm^2}$) which increases by $\approx 15\,\mathrm{m^{-1}}$ within the first 10 μs. This dynamic is further called fast decay/process. Subsequently, a plateau in the time range of $10^{-5} - 10^{-2}$ s with a maximum absorption change of $(75 \pm 5)\,\mathrm{m^{-1}}$ is reached that decays on a time scale of a few seconds to zero (slow decay/process). The fitting parameters of the applied sum of two KWW-functions (cf. Eq. 2.96) are summarized in Tab. 3.2.

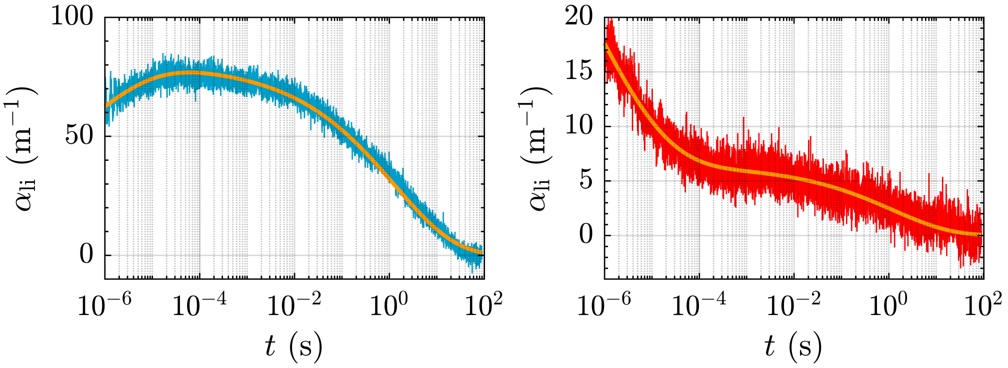

Figure 3.3 – Light-induced transient absorption coefficient α_{li} after an incident ns-pulse ($\lambda_\mathrm{p} = 355$ nm, $I_\mathrm{p} = (13.5 \pm 1.0)\,\mathrm{MW/cm^2}$) probed at 488 nm (**left**) and 785 nm (**right**). Orange lines represent a fit by two KWW-functions (cf. Eq. 2.96).

The development of α_{li} at a probe wavelength of 785 nm ($I_{785} = (20 \pm 2)\,\mathrm{mW/cm^2}$) is depicted in the right part of Fig. 3.3. In contrast to the previous measurement, there is a significant decrease of α_{li} immediately after the pump pulse that decays to a nearly constant absorption change of $(6 \pm 2)\,\mathrm{m}^{-1}$ in the time range of $10^{-4} - 10^{-2}\,\mathrm{s}$. The slow decay component features a characteristic decay time of nearly one second (cf. Tab. 3.2). However, the decay times and stretching coefficients of both long-lived decay components are in accordance with those determined at $\lambda = 488\,\mathrm{nm}$.

Table 3.2 – Parameters of the KWW-functions used to describe the temporal dynamic of the transient light-induced absorption probed at 488 nm and 785 nm and depicted in Fig. 3.3.

	488 nm	785 nm
$\alpha_{\mathrm{li,f}}$ (m^{-1})	-60 ± 5	40 ± 5
τ_{f} (μs)	0.5 ± 0.1	0.4 ± 0.1
β_{f}	0.33 ± 0.05	0.25 ± 0.05
$\alpha_{\mathrm{li,s}}$ (m^{-1})	80 ± 10	6 ± 2
τ_{s} (s)	1.3 ± 0.2	1.2 ± 0.2
β_{s}	0.34 ± 0.05	0.35 ± 0.05

Intensity dependence

Fig. 3.4 shows the pump-intensity dependence of the light-induced absorption coefficient α_{li} at 488 nm (left) and 785 nm (right). For $\lambda = 488\,\mathrm{nm}$, the overall maximum of the applied KWW-functions and the amplitude of the slow decay component are examined. Both reveal a linear increase of α_{li} for $I > 5\,\mathrm{MW/cm}^2$ within the margins of error. However, both lines do not pass the point of origin. The offset value is in the order of $\approx 25 - 30\,\%$ of the respective maximum absorption coefficient (cf Tab. 3.3).

In case of $\lambda = 785\,\mathrm{nm}$, the amplitude of both, the fast and slow decay component are analyzed. The first results in absorption changes of up to $\approx 200\,\mathrm{m}^{-1}$ and can be described by a quadratic fit within the measuring inaccuracy (orange line). In contrast, a linear dependence between the intensity and the amplitude of the slow decay component is applied which passes the point of origin. With increasing pump intensity, its relative contribution decreases, thus, the overall change of the absorption coefficient in the short time range is dominated by the fast decay component.

3.2.3 Discussion

The temporal dynamics after an incident ns-pump pulse ($\lambda_{\mathrm{p}} = 355\,\mathrm{nm}$) probed at 488 nm and 785 nm at room temperature are in accordance with the model proposed by Messerschmidt *et al.* [12] for a pump wavelength of 532 nm. In the blue spectral range, the dynamic is dominated by a long-lived decay component exhibiting a pronounced, constant absorption change over several decades and a decay time in the range of seconds

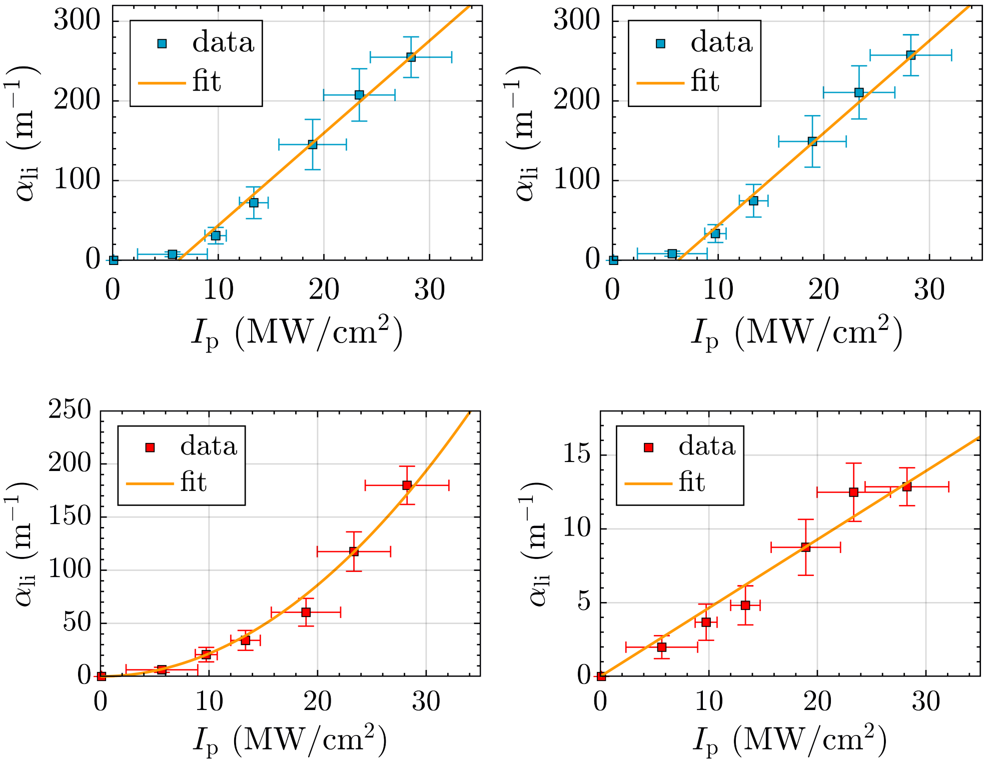

Figure 3.4 – Intensity dependence of the light-induced absorption coefficient α_{li} after an incident ns-pulse ($\lambda_{\mathrm{p}} = 355\,\mathrm{nm}$) probed at 488 nm (**top**) and 785 nm (**bottom**) with $I_{488} = (15 \pm 1)\,\mathrm{mW/cm^2}$ and $I_{785} = (20 \pm 2)\,\mathrm{mW/cm^2}$, respectively. **Top, left:** Maximum amplitude of the fit according to Fig. 3.3 (left). **Bottom, left:** Amplitude of the fast decay component. **Top/Bottom, right:** Amplitude of the partial KWW-function to adjust the slow decay. The orange line represents a fit to the data (see text for further information).

Table 3.3 – Fit parameter used to describe the pump intensity dependence shown in Fig. 3.4. For $\lambda = 488\,\mathrm{nm}$, the maximum amplitude and amplitude of the slow decay component is examined while both, the fast and slow decay component is analyzed for $\lambda = 785\,\mathrm{nm}$. In general, a quadratic equation of the form $\alpha_{\mathrm{li}} = aI_{\mathrm{p}}^2 + bI_{\mathrm{p}} + c$ is applied. The parameter is not used during the fitting procedure if its value is given by "$--$".

		a $(10^{-8}\,\frac{\mathrm{m}^3}{\mathrm{MW}^2})$	b $(10^{-4}\,\frac{\mathrm{m}}{\mathrm{MW}})$	c (m^{-1})
488 nm	max. amplitude	$--$	11.6 ± 1.6	-72.1 ± 29.5
	slow decay	$--$	11.6 ± 1.6	-72.1 ± 29.5
785 nm	fast decay	0.21 ± 0.02	$--$	$--$
	slow decay	$--$	0.46 ± 0.06	$--$

which is in line with the results presented in appendix A.2. The increase to this plateau within the first $10\,\mu$s can be related to the formation of pinned STEs that are subsequently transferred into $\mathrm{Fe}_{\mathrm{Li}}^{2+} - \mathrm{O}^{-} - \mathrm{V}_{\mathrm{Li}}$ excitonic states [12]. However, in contrast to references [8, 12], a pump wavelength of 355 nm, moderate pump intensities of maximal $30\,\mathrm{MW/cm}^2$ and a strongly oxidized iron-doped sample are used to highly favor the excitation via the iron C-Band, i.e., valence band to $\mathrm{Fe}_{\mathrm{Li}}^{3+}$ (cf. appendix A.2). Therefore, a direct generation of the $\mathrm{Fe}_{\mathrm{Li}}^{2+} - \mathrm{O}^{-} - \mathrm{V}_{\mathrm{Li}}$ excitonic state is more probable compared to the formation via a TPA accompanied by the subsequent transformation of the pinned STE. This is further supported by the linear intensity dependence of the maximal light-induced absorption change.

However, the temporal dynamics investigated at a probe wavelength of 785 nm exhibit a fast decay component which is in accordance with the model proposed by Messerschmidt *et al.* and attributed to the formation of bound polarons via a two-photon absorption process from the valence band to the conduction band [12]. An excitation from $\mathrm{Fe}_{\mathrm{Li}}^{2+}$-center to the conduction band can be excluded here due to the high oxidation degree of the sample ($c_{\mathrm{Fe}_{\mathrm{Li}}^{2+}}/c_{\mathrm{Fe}_{\mathrm{Li}}^{3+}} \approx 0$), although the pump photon energy is below the isosbestic point at about 3.6 eV, i.e., the absorption cross-section of the iron D-band is larger compared to the iron C-band [142]. This is supported by the corresponding intensity dependent measurement (cf. Fig. 3.4) indicating a quadratic relation between the light-induced absorption change and pump intensity. However, in contrast to the measurements performed in reference [12], a second long-lived decay is detected with a characteristic lifetime in the range of seconds. The coincidence with the decay time and stretching coefficient of the KWW-function to describe the decay in the blue spectral range (cf. Tab. 3.2) suggests that the $\mathrm{Fe}_{\mathrm{Li}}^{2+} - \mathrm{O}^{-} - \mathrm{V}_{\mathrm{Li}}$ excitonic state is at the origin of the second decay component. These Fe-STEs are mainly generated via the iron C-band and less via TPA as concluded from the linear intensity dependence (cf. Fig. 3.4). They further exhibit a remaining absorption cross-section in the red to NIR spectral range (cf. appendix A.2). Due to the significantly higher Fe^{3+}-concentration with respect to reference [12] and the wavelength shift towards the UV spectral range, the generation efficiency of the excitonic states is increased in particular with respect to the excitation via the iron C-band. Hence, the enhanced number density of Fe-STEs allows to detect the residual absorption even at a probe wavelength of 785 nm. Thus, the temporal dynamic of the light-induced absorption coefficient probed at 785 nm can be described comprehensively by the revised model of Messerschmidt *et al.* in combination with the determined absorption cross-section of the $\mathrm{Fe}_{\mathrm{Li}}^{2+} - \mathrm{O}^{-} - \mathrm{V}_{\mathrm{Li}}$ excitonic state.

In comparison to the intensity dependence performed by Herth *et al.* with a pump wavelength of $\lambda_{\mathrm{p}} = 532\,\mathrm{nm}$ [8], a considerable decrease of the pump intensity from $500\,\mathrm{MW/cm}^2$ to $\approx 15\,\mathrm{MW/cm}^2$ ($\lambda_{\mathrm{p}} = 355\,\mathrm{nm}$) is obtained in order to achieve an absorption change of $\approx 100\,\mathrm{m}^{-1}$ in the blue spectral range (cf. Fig. 3.4). Similar relations are deduced from the results presented in appendix A.2 (cf. Fig. 3) which are generated in a crystal of comparable configuration with respect to reference [8], in combination with the linear intensity dependence (cf. Fig. 3.4). These deviations can be clearly assigned to the different photophysical mechanism. While the optical generation of Fe-STEs is related to TPA within reference [8], a predominant one-photon absorption process is utilized within this thesis. As a consequence, a significant increase of the excitation efficiency is achieved by optical charge carrier excitation via the iron C-band.

The linear intensity dependencies presented in Fig. 3.4 (probe wavelength $\lambda = 488\,\mathrm{nm}$) clearly show that a description by a line through the point of origin is not possible. Due to the linear relation between absorption and pump intensity, effects scaling relatively with the pump intensity can be excluded. Additionally, the experimental system can be ruled out since previous intensity dependent measurements performed with the same or comparable setup included the point of origin [11, 73, 131, 138, 143]. Instead an offset value has to be considered. However, the measurements do not allow for concluding whether this offset has to be taken into account with respect to the determination of the intensity or the light-induced absorption coefficient. The latter will have the consequence that the positive absorption change due to the generation of the Fe-STEs is superimposed by a negative contribution. However, only a few scenarios are known in literature which describe a light-induced transparency in the blue spectral range, e.g., the disruption of bipolarons in thermally reduced lithium niobate [73, 74] or the excitation via the iron D-band, thus increasing the number density of non-absorbing $\mathrm{Fe}_{\mathrm{Li}}^{3+}$-centers. According to the previous discussion and absorption spectrum, both mechanisms can be excluded, thus switching the focus to further defect centers.

First of all, the Fe-STE itself must be listed here. In appendix A.2, the absorption band up to approximately 3.1 eV was determined. An extrapolation to higher photon energies suggests a non-negligible absorption cross-section at the pump wavelength of 355 nm. Thus, the excitonic state cannot only be formed by a one-photon absorption of the pump pulse, but additionally excited into higher states or even separated into its constituents [38, 40]. This is a fundamental difference to the conventional investigations of polaron dynamics. Even though the pump wavelength (typically 532 nm) is in the range of the respective polaron absorption bands, an excitation of the polaron will only lead to a jump to the nearest neighbor, therefore, maintaining the polaron properties. However, detailed information about the impact of an excitation to higher states or separation into the constituents on the temporal dynamics and, in particular, on the absorption bands are missing in literature so far. Thus, further investigations by double pump pulse experiments are required.

Moreover, impurities could have diffused into the crystal especially during the oxidation treatment. For example, atoms like manganese (Mn), copper (Cu) or cobalt (Co) are known to exhibit a steady state absorption in the UV (see section 2.6.1 for references). Excitation of these atoms which are most probably located near to the surface due to the oxidation treatment, could lead to an offset in the intensity dependence. Even though a direct evidence of these impurities is not possible due to the high concentration of $\mathrm{Fe}_{\mathrm{Li}}^{3+}$-ions in the investigated sample, a contribution to the overall absorption dynamics cannot be excluded.

3.2.4 Conclusion

Light-induced absorption changes after an incident ns-pump pulse at 355 nm are probed in the blue ($\lambda = 488\,\mathrm{nm}$) and NIR spectral range ($\lambda = 785\,\mathrm{nm}$). The temporal dynamics are in full agreement with the revised model of the formation, transport, recombination, relaxation processes in iron-doped lithium niobate according to reference [12]. This model is further supported by intensity dependent measurements that reveal a direct generation of the $\mathrm{Fe}_{\mathrm{Li}}^{2+} - \mathrm{O}^{-} - \mathrm{V}_{\mathrm{Li}}$ excitonic states via a one-photon absorption process. At low intensities, a hitherto unknown effect is detected resulting in an offset value of either the intensity or absorption coefficient. However, it is not possible to finally clarify its origin within the scope of this thesis. Again, systematic studies including variations of the sample configuration as well as double pulse- and fs-pump-probe-experiments are required.

3.3 Pulse-induced transient holography related with long-lived excitonic states in iron-doped lithium niobate

The direct generation of the $\mathrm{Fe}_{\mathrm{Li}}^{2+} - \mathrm{O}^{-} - \mathrm{V}_{\mathrm{Li}}$ excitonic state after an incident 355 nm-ns-pump pulse represents a new one-photon absorption mechanism to generate long-lived quasiparticles with a pronounced change of the absorption coefficient in the visible spectral range (see section 3.2.2 and appendix A.2). This excitation path is of particular importance for the UV-photorefraction. On the one hand, these excitons represent additional long-lived broad-band absorption states which could contribute to the optical damage or affect the calculation of, e.g., the diffraction efficiency (cf. Eq. 2.68) of holographic gratings. On the other hand, even though STEs will not result in an optical separation of charges which is mandatory for the photorefractive effect, their generation represents a competitive process to the formation of a space charge field and subsequently an elementary holographic grating. However, the pronounced change of the absorption coefficient of several hundred reciprocal meters suggests the potential to write a pulse-induced transient absorption grating related with long-lived excitonic states which is investigated within the next section. Intensity dependent measurements are again performed to determine the relation between the diffraction efficiency η and modulation of the absorption coefficient $\Delta\alpha$ via Eq. 2.68.

3.3.1 Experimental methods

Fig. 3.5 represents the setup used for transient holographic measurements. In comparison to the setup presented in section 3.2.2, a separation of the ns-pump pulses (extraordinary polarized) into reference and signal path is performed by installing a 50:50 beamsplitter positioned on an optical delay line for adjusting equal path lengths. The external angle of incidence θ_{UV} is set to $(5.1 \pm 0.3)^\circ$.

The 488 nm cw-laser with an intensity of $I_{488} = (17 \pm 1)\,\mathrm{mW/cm}^2$ and extraordinary polarization is again used for read-out. Because of the divergence, the beam diameter is reduced to $(700 \pm 50)\,\mu\mathrm{m}$ at the position of the sample by a telescope (L_3 and L_4). According to the Bragg-condition (Eq. 2.54), an external angle of $(7.0 \pm 0.2)^\circ$ is applied. The zeroth order diffraction is measured with a combination of lens, laser line filter and Si-pin diode while the first order diffraction is recorded with a photomultiplier tube (PMT, *Hamamatsu* H5783 series). Both detectors are connected to the digital oscilloscope triggered by D_{T}. Residual UV-light is suppressed by an additional laser line filter in front of the PMT. As described in section 3.2.2, the temporal dynamics of the light-induced transient holography under UV-excitation are measured over three different time ranges from $10^{-6} - 10^{2}$ seconds. The values for $t < 0\,\mathrm{s}$ are used as background signal for the determination of the diffraction efficiency $\eta(t)$ defined via

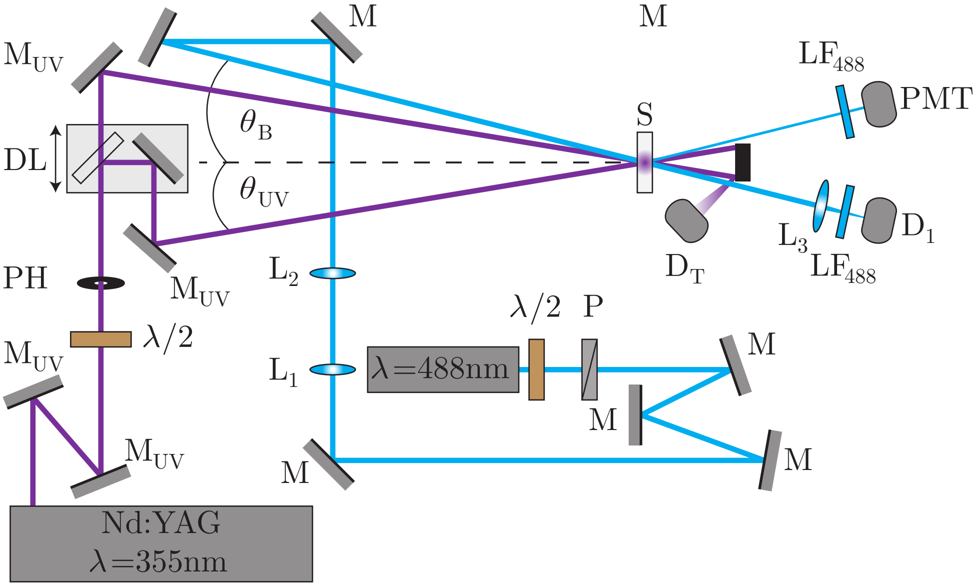

Figure 3.5 – Experimental setup for recording transient, holographic gratings with a frequency tripled Nd:YAG pulse laser at $\lambda_\mathrm{p} = 355\,\mathrm{nm}$. Read-out is performed by a cw-laser at $\lambda = 488\,\mathrm{nm}$. $\mathrm{M_{UV}}$: UV protected mirror, $\lambda/2$: half wave-plate, PH: pinhole, S: lithium niobate sample, DL: delay line, consisting of a 50:50 UV beamsplitter and $\mathrm{M_{UV}}$, P: polarizer, M: mirror, $\mathrm{L_{1\ldots3}}$: lens, $\mathrm{LF_{488}}$: laser line filter, $\mathrm{D_{1,T}}$: Si-pin diodes, PMT: photomultiplier tube.

Eq. 2.55. All measurements are performed on the 0.1 mol% oxidized iron-doped lithium niobate characterized in section 3.2.2. The c-axis is perpendicular to the K-vector of the holographic grating.

3.3.2 Diffraction efficiency

Temporal Dynamics

The measurement of the temporal dynamic of the diffraction efficiency is performed with a pump intensity of $I_\mathrm{p} = (25 \pm 2)\,\mathrm{MW/cm^2}$ ($I_\mathrm{p}^\mathrm{R} = 12.9\,\mathrm{MW/cm^2}$, $I_\mathrm{p}^\mathrm{S} = 12.1\,\mathrm{MW/cm^2}$, modulation depth $m \approx 1.00$) and is depicted in Fig. 3.6. It can be detected with a sufficient signal-to-noise-ratio and reveals a maximum diffraction efficiency $\eta = (2.0 \pm 0.3) \cdot 10^{-3}$. According to the temporal dynamics of the light-induced absorption measurements (section 3.2.2), the sum of two stretched exponential functions is applied to the transient signal yielding a decay time $\tau = (0.3 \pm 0.1)\,\mathrm{s}$ and stretching coefficient $\beta = 0.39 \pm 0.06$ for the slow decay. The fast decay component will be omitted in the following because the main information about the Fe-STE dynamic can be gained from analyzing the slow decay (cf. section 3.2.2). The simultaneously detected zeroth order diffraction signal can also be described by the sum of two stretched-exponential functions with a maximum absorption $\alpha_{\mathrm{li}}^{\max} = (160 \pm 20)\,\mathrm{m}^{-1}$, decay time $\tau = (1.1 \pm 0.2)\,\mathrm{s}$ and stretching coefficient $\beta = 0.37 \pm 0.06$ for the long-lived decay.

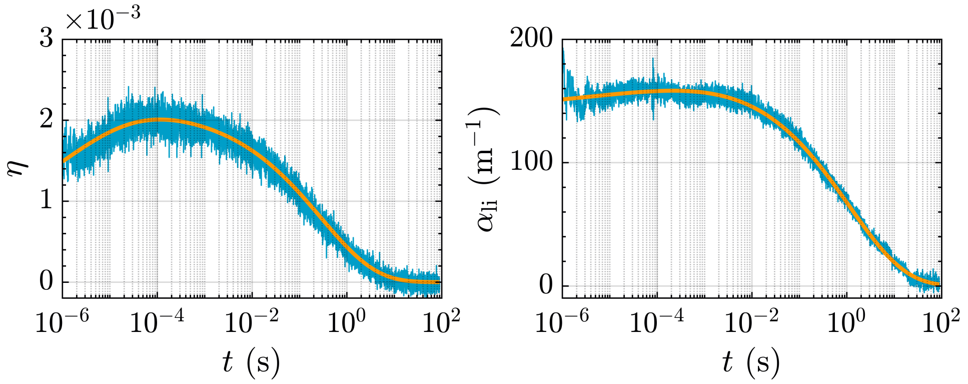

Figure 3.6 – **Left:** Temporal evolution of the diffraction efficiency η on a logarithmic time scale after an incident ns-pump pulse ($\lambda_{\mathrm{p}} = 355\,\mathrm{nm}$, $I_{\mathrm{p}} = (25 \pm 2)\,\mathrm{MW/cm^2}$). **Right:** Light-induced absorption coefficient α_{li} as a function of time t deduced from the transmitted signal.

Intensity dependence

In a next step, the influence of the pump intensity on the first order diffraction efficiency is investigated in the range of $I_{\mathrm{p}} < 30\,\mathrm{MW/cm^2}$ (cf. Fig. 3.7 (top)). The plot shows a monotonous, nonlinear increase of the diffraction efficiency $\eta(I)$ with a maximum value of $\eta_{\max} = (2.1 \pm 0.3) \cdot 10^{-3}$. All data points with included errorbars can be modeled by Kogelnik's coupled wave theory (Eq. 2.68) for a pure absorption grating ($\Delta n = 0$) with a fundamental absorption $\alpha_0 = (50 \pm 5)\,\mathrm{m}^{-1}$ and the intensity dependent light-induced absorption coefficient modulation $\Delta\alpha_{\mathrm{li}}(I) = \alpha_{\mathrm{li}}(I)/2$ [138] (orange line):

$$\eta(I) = \sinh^2\left(\frac{\Delta\alpha_{\mathrm{li}}(I) d_{\mathrm{h}}}{2\cos\theta_{\mathrm{B}}}\right) \exp\left(-\frac{2(\alpha_0 + \Delta\alpha_{\mathrm{li}}(I)) d_{\mathrm{h}}}{\cos\theta_{\mathrm{B}}}\right). \tag{3.2}$$

Here, a hologram thickness of $d_{\mathrm{h}} = d = 1.0\,\mathrm{mm}$ is assumed. According to the results of the previous section, a linear intensity dependence with offset value for $\alpha_{\mathrm{li}}(I)$ is invested which is in line with the simultaneously measured absorption change (bottom part of Fig. 3.7). A maximum value $\Delta\alpha_{\mathrm{li}} = (165 \pm 25)\,\mathrm{m}^{-1}$ is detected for the highest intensity.

The individual stretching coefficients β, decay times τ and thereby determined mean decay times $\langle\tau\rangle$ of the stretched-exponential functions describing the long-lived decay are summarized in Fig. 3.8. A nearly constant value of $\beta = 0.36 \pm 0.05$ results for the stretching coefficient over the complete intensity range, while the decay time τ shows statistic fluctuations between $0.1\,\mathrm{s}$ and $0.6\,\mathrm{s}$. As a consequence, the calculated mean decay time fluctuates in the range of $(1.1 \pm 0.5)\,\mathrm{s}$.

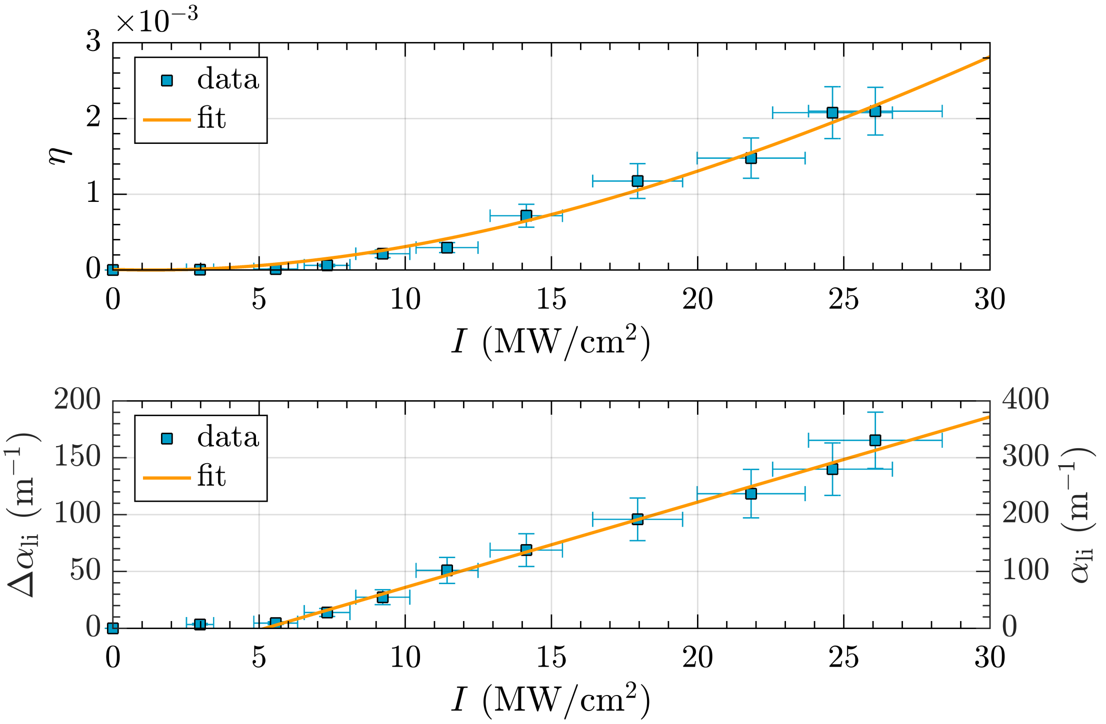

Figure 3.7 – **Top:** Diffraction efficiency as a function of pump intensity (blue). The orange line is a fit of Eq. 2.68 ($\Delta n = 0$) to the data. **Bottom:** Change of the light-induced absorption coefficient modulation $\Delta\alpha_{\mathrm{li}}$ and absorption coefficient α_{li} as a function of intensity calculated via Eq. 2.68.

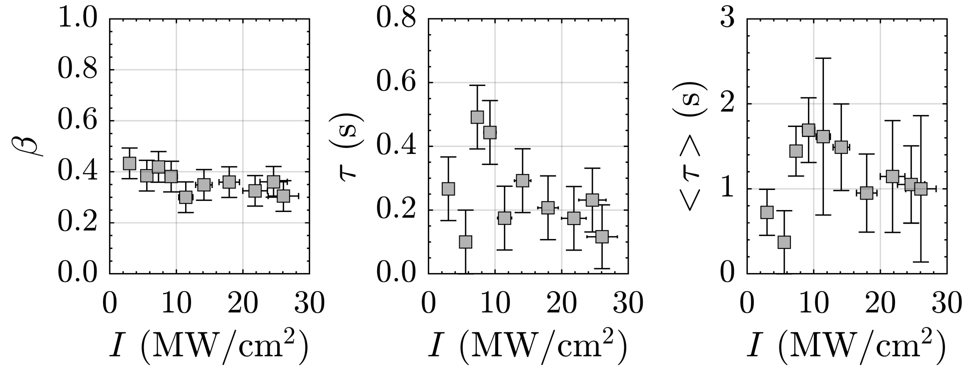

Figure 3.8 – Stretching coefficient (**left**), decay time (**middle**) and mean decay time (**right**) calculated via Eq. 2.97 as function of pump intensity.

Polarization dependence

Finally, the dependence of the recording configuration, i.e., c-axis, K-vector, pump e_{pu} and probe beam polarization e_{pr} on the maximum diffraction efficiency is analyzed to account for possible influences of the electro-optic or photovoltaic effect (cf. section 2.4.5 and 2.4.5). Fig. 3.9 illustrates the temporal evolution of the diffraction efficiency for three different combinations of the above mentioned parameters and a pump intensity of $I = (19 \pm 2)\,\mathrm{MW/cm^2}$. Here, only the time range from $10^{-4}\,\mathrm{s}$ to $10^{2}\,\mathrm{s}$ is shown since the focus is only on the maximum diffraction efficiency. The associated electro-optic and photovoltaic tensor elements as well as the maximum diffraction efficiency are summarized in Tab. 3.4. Note that r_{jk} and β_{jk} feature the reduced notation. Furthermore, r_{jk} is taken from reference [69] for a wavelength of 633 nm while the values for β_{jk} have been determined for Fe^{2+}-doped lithium niobate at a photon energy of 2.48 eV (500 nm) [98, 144]. Within the margins of error, the recording configurations reveal no significant impact on the temporal dynamic and maximum diffraction efficiency although strong deviations of the respective tensor elements are presented (cf Tab. 3.4).

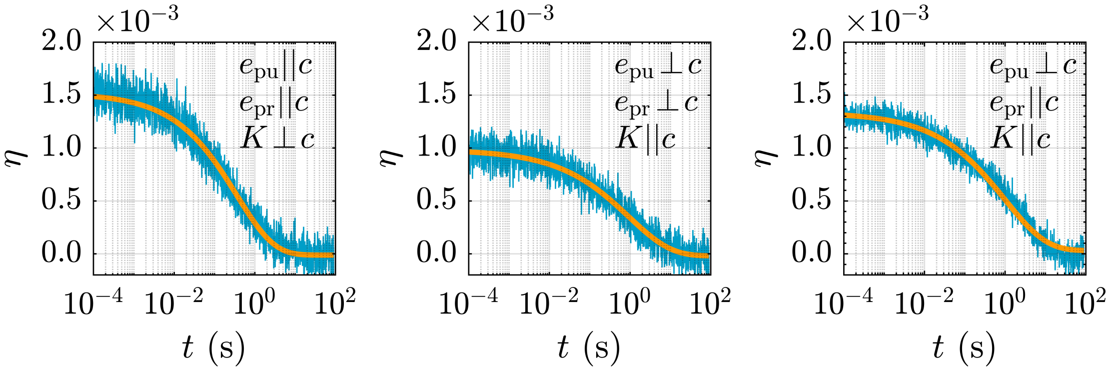

Figure 3.9 – Temporal evolution of the diffraction efficiency for different combinations of c-axis, K-vector, pump and probe beam polarization e_{pu} and e_{pr}, respectively.

Table 3.4 – Maximum diffraction efficiency for different combinations of c-axis, K-vector, pump and probe beam polarization e_{pu} and e_{pr}, respectively. Additionally, the respective elements of the electro-optic and photovoltaic tensor are given according to references [69, 98, 144].

	$e_{\mathrm{pu}}\|\|c$, $e_{\mathrm{pr}}\|\|c$, $K \perp c$	$e_{\mathrm{pu}} \perp c$, $e_{\mathrm{pr}} \perp c$, $K\|\|c$	$e_{\mathrm{pu}} \perp c$, $e_{\mathrm{pr}}\|\|c$, $K\|\|c$
η (10^{-3})	1.5 ± 0.2	1.0 ± 0.2	1.3 ± 0.2
r_{jk} (pm/V)	$r_{31} = 0$	$r_{13} = 9.6$	$r_{33} = 30.9$
β_{jk} (10^{-9}/V)	$\beta_{13} = 0$	$\beta_{31} = 40$	$\beta_{31} = 40$

Kramers-Kronig relation and theoretical calculation of the diffraction efficiency

The broad-band absorption feature related to Fe-STEs has been deduced in appendix A.2. By applying the Kramers-Kronig relation (see section 2.1.2), the spectral dependence of the light-induced refractive index $n_{\mathrm{li}}(E)$ and refractive index modulation Δn_{li}, respectively, can be calculated from the spectral dependence of the absorption coefficient $\alpha_{\mathrm{li}}(E)$. For this purpose, the spectral shape of the absorption cross-section $\sigma(E)$ is first transferred into the spectral shape of the absorption coefficient. A maximum absorption coefficient of $\alpha_{\mathrm{li}}^{\mathrm{max}}(E = 2.54\,\mathrm{eV}) = (330 \pm 50)\,\mathrm{m}^{-1}$ for $I_{\mathrm{pump}} < 30\,\mathrm{MW/cm}^2$ is taken from Fig. 3.7. The determined spectral dependence of α_{li} together with the calculated light-induced refractive index n_{li} is shown in the left part of Fig. 3.10. It is worth mentioning that the used absorption coefficient is not the saturation value of the light-induced absorption change due to the Fe-STE. Larger values have not been determined due to surface damages induced by higher pump intensities.

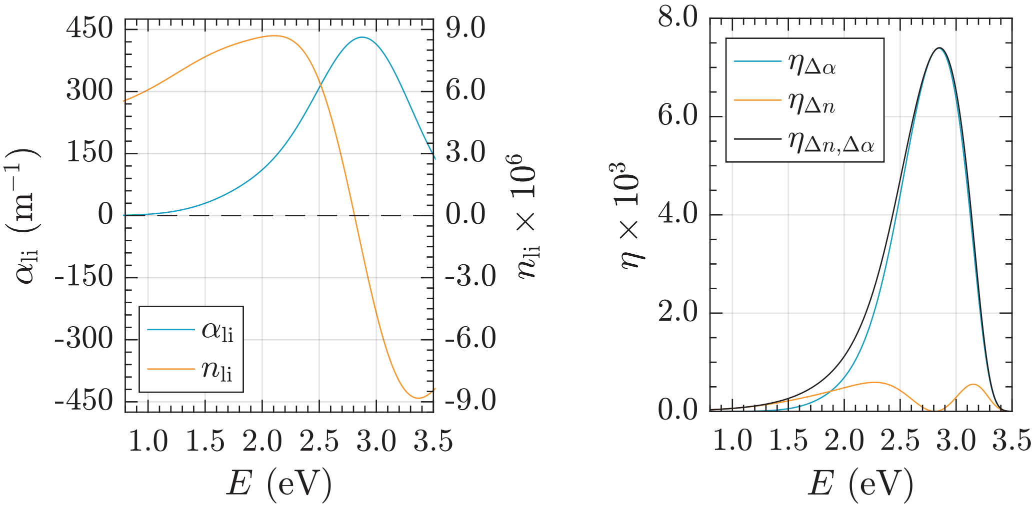

Figure 3.10 – **Left:** Spectral dependence of the experimentally determined light-induced absorption α_{li} (blue) and refractive index n_{li} (orange) calculated via the Kramers-Kronig relation (section 2.1.2). **Right:** Thereby estimated spectral dependence of the diffraction efficiency of a pure absorption grating $\eta_{\Delta\alpha}$ (blue), pure refractive grating $\eta_{\Delta n}$ (orange) and mixed grating $\eta_{\Delta n,\Delta\alpha}$ (black) via Eq. 2.68 with the hologram thickness $d_{\mathrm{h}} = d = 1.0\,\mathrm{mm}$.

The calculated change of the refractive index is in the order of 10^{-6}. From the infrared to green/blue spectral range, n_{li} has a positive sign while it is negative for $E > (2.85 \pm 0.05)\,\mathrm{eV}$. A value of $n_{\mathrm{li}} = (6.0 \pm 0.9) \cdot 10^{-6}$ is deduced for the probe wavelength of 488 nm ($E = 2.54\,\mathrm{eV}$).

The spectral dependence of the absorption coefficient as well as the index of refraction enable the calculation of the dispersion of the diffraction efficiency via Eq. 2.68 of all three, a pure absorption grating $\eta_{\Delta\alpha}$ ($\Delta n = 0$), a pure refractive grating $\eta_{\Delta n}$ ($\Delta\alpha = 0$)

and a mixed grating $\eta_{\Delta n,\Delta\alpha}$ ($\Delta\alpha \neq 0$, $\Delta n \neq 0$), illustrated in the right part of Fig. 3.10 with a fundamental absorption coefficient according to the steady state absorption spectrum (cf. Fig. 3.1). The spectral shape of a pure absorption grating reveals a maximum diffraction efficiency of $(7.4 \pm 1.6) \cdot 10^{-3}$ at $(2.85 \pm 0.05)\,\mathrm{eV}$ where the amplitude of a pure refractive grating obtains its minimum. For photon energies $E \in [1.9; 3.5]\,\mathrm{eV}$, the overall diffraction efficiency is dominated by the contribution of the absorption grating.

3.3.3 Discussion

Relation between the temporal dynamics

The temporal dynamic of the absorption change determined via the transmitted signal is in accordance with the temporal development deduced from light-induced absorption measurements in section 3.2.2. The decay time and stretching coefficient of both techniques agree within the scope of the measurement errors. However, the temporal dynamic of the first order diffracted signal reveals a significantly reduced decay time while the stretching coefficients coincide. This deviation might be explained by considering the relation between absorption change and diffraction efficiency, given by Eq. 3.2 where the intensity dependence $\alpha_{\mathrm{li}}(I)$ has to be substituted by the temporal development $\alpha_{\mathrm{li}}(t)$. Under the assumption of a negligible attenuation, the theoretical relationship

$$\tau_\eta = \tau_{\Delta\alpha} \cdot 2^{-\frac{1}{\beta}} \tag{3.3}$$

between the decay time of the diffracted (τ_η) and transmitted ($\tau_{\Delta\alpha}$) signal can be deduced. With $\tau_{\Delta\alpha} = (1.1 \pm 0.2)\,\mathrm{s}$, a value of $\tau_\eta = (0.2 \pm 0.1)\,\mathrm{s}$ is calculated which is in accordance with the experimentally determined decay time of $(0.3 \pm 0.1)\,\mathrm{s}$. Consequently, the comparison of the decay dynamics leads to the conclusion that the diffracted signal is solely based on the periodic formation of $\mathrm{Fe}_{\mathrm{Li}}^{2+} - \mathrm{O}^- - \mathrm{V}_{\mathrm{Li}}$ excitonic states, thus, confirming their potential to write holographic gratings.

Decay time and stretching coefficient

Intensity dependent measurements performed by Herth *et al.* and Berben *et al.* in reduced iron-doped lithium niobate crystals yield an increase of both, the stretching coefficient and decay time of the temporal development of the light-induced transient absorption [7,9]. In both publications, this is explained by the effective distance between the point of electron excitation and localization as polaron, e.g. on $\mathrm{Nb}_{\mathrm{Li}}^{5+}$- or $\mathrm{Fe}_{\mathrm{Li}}^{2+}$-center. Low light intensities result in the population of the nearest surrounding trapping centers. In contrast, high pump intensities lead to a homogenization of the polaron distribution over the crystal. Thus, the total decay time and stretching coefficient (describing the homogeneity of the individual decay processes) increases.

However, this intensity dependent distribution of τ and β changes in case of self-trapped excitons. Here, the recombination occurs directly between its constituents, thus, there is no distribution of the spatial separation of trapping site and the point of electron localization. As a result and according to the previous discussion, a constant decay time and a constant stretching coefficient is expected which is confirmed by Fig. 3.8. However, the theoretical considerations of the recombination dynamics presented above claims $\beta = 1$ which is not in line with the average value of $\beta = 0.36 \pm 0.05$. It can therefore be concluded that additional effects alter the local energy landscape and thereby the decay time of the Fe-STEs, e.g., anti-site defects in close vicinity to the excitonic states or temperature dependent phonons. Moreover, the impact of a possible STE excitation/separation on the recombination dynamic has not yet been clarified and demands further investigations (see section 3.2.3).

Recording configuration and limit of the maximum diffraction efficiency

Within most experiments, the geometric configuration of the crystallographic *c*-axis, light polarizations and holographic grating vector is chosen in such a manner, that the effective elements r_{31} and β_{13} of the electro-optic and photovoltaic tensor, respectively, are equal to zero. Correspondingly, any contribution from the electro-optic Pockels effect and bulk-photovoltaic effect can be excluded. The calculated change of the refractive index deduced from applying the Kramers-Kronig relation (cf. Fig. 3.10) is in the order of 10^{-6} which is in accordance with the values reported for small polarons [13, 73, 74]. However, polarization dependent measurements (cf. Fig. 3.9) disclose no significant influence of the recording configuration as reported for small polarons in thermally reduced lithium niobate [13, 73, 143]. Therefore, the appearance of holographic gratings can be related to the photochromic properties of the excited excitonic states. However, it is worth mentioning that the reported values for r_{jk} and β_{jk} have to be taken with caution since they are in principle deduced for a different wavelength and/or iron concentration.

Theoretical calculations from the Kramers-Kronig relation together with the definition of the diffraction efficiency according to the coupled wave theory of Kogelnik enable to ascertain the maximum diffraction efficiency for the particular probe photon energy of 2.54 eV (cf. Fig. 3.10). The respective contribution of a pure absorption and phase grating are determined to $\eta_{\Delta\alpha} = (4.9 \pm 1.3) \cdot 10^{-3}$ and $\eta_{\Delta n} = (0.4 \pm 0.2) \cdot 10^{-3}$. Correspondingly, the contribution of a phase grating for the particular probe wavelength can be neglected. Hence, the application of Eq. 3.2 and its modified version for the calculation of the temporal diffraction efficiency is justified. The maximum measured diffraction efficiency of $\eta = (2.1 \pm 0.3) \cdot 10^{-3}$, however, corresponds to only 40 % of $\eta_{\Delta\alpha}$. One possible origin for this deviation might be the effective hologram thickness d_{h} with respect to the sample thickness d. Holographic investigations in sodium nitroprusside by a cw-argon laser reveal an effective hologram thickness of 100 % [87], while a value of approx. 50 % is reported for iron-doped and thermally reduced lithium niobate under cw- or ns-pulse-exposure [74,138]. Moreover, appendix A.1 reveals a hologram thickness of about 60 % for a photochromic material excited with a 405 nm-cw-laser. Besides, a strong absorption coefficient at the excitation wavelength (cf. Fig. 3.1) suggests that pulse intensity and, subsequently, the modulation depth of the holographic grating diminishes with increasing propagation length. It is therefore to be expected that the effective hologram thickness does not necessarily correspond to the sample thickness. For instance, a reduced thickness of $d_\mathrm{h} = 0.65\,d$ will lead to a decrease by $\approx 50\,\%$ of the maximum diffraction efficiency (theoretical calculations) which would be in line with the experimentally determined values.

3.3.4 Conclusion

It has been successfully demonstrated that Fe-STEs can be utilized to write elementary holographic gratings in the UV spectral range in iron-doped lithium niobate. As a consequence of geometrical considerations and theoretical calculations via the Kramers-Kronig relation, the diffraction processes can be solely related to the photochromic properties of the excitonic states, thereby yielding a local response of the material. Furthermore, diffraction efficiencies in the range of 10^{-3} are reported that coincide with theoretical estimations for pure absorption gratings. Even if the diffraction efficiencies are in general very low, the results should be considered in case of UV-excitation/-photorefraction since the generation of STEs strongly prohibits the charge separation mandatory for the photorefractive effect.

3.4 Elucidating the mechanisms of fs-pulse amplification based on dynamic gratings

Odoulov *et al.* have demonstrated the interference and holography with femtosecond laser pulses of different colors [17]. Beside the recording and reconstruction of a permanent image hologram, self-diffraction on a recorded moving grating is observed where the diffracted light gets affected by the Doppler-effect [88]. Furthermore, two-beam coupling gain between both pulses is discovered in a conventional pump-probe experiment. Comprehensive studies performed within this thesis are carried out to investigate the strength and underlying, photo-physical wave mixing processes that ensure considerable energy transfer between the interacting beams.

The author contributed to the paper *Dynamic-grating-assisted energy transfer between ultrashort laser pulses in lithium niobate.* The abstract is printed here with friendly permission of the Optical Society of America (OSA). The complete article can be found in the appendix A.3.

S. Nolte, B. Bourdon, F. Freytag, M. Imlau, A. Shumelyuk, and S. Odoulov
Dynamic-grating-assisted energy transfer between ultrashort laser pulses in lithium niobate
Opt. Express **26**, 21558–21573, (2018), doi: 10.1364/OE.26.021558.

Abstract: Energy redistribution between two subpicosecond laser pulses of 2.5 eV photon energy is observed and studied in congruent, nominally undoped $\mathrm{LiNbO_3}$, aiming to reveal the underlying coupling mechanisms. The dependences of pulse amplification on intensity, frequency detuning and pulse duration point to two different contributions of coupling, both based on selfdiffraction from a recorded dynamic grating. The first one is caused by a difference in pulse intensities (transient energy transfer) while the second one originates from a difference in pulse frequencies. The latter appears when chirped pulses are mutually delayed in time. A quite high coupling efficiency has been observed in a 280 μm thin crystal: one order of magnitude energy amplification of a weak pulse and nearly 10 % net energy enhancement of one pulse for the case of equal input intensities.

As a main result, two coupling mechanisms are deduced that both are based on selfdiffraction from a self-induced dynamic grating. Hence, a phase shift between the refractive index modulation and the incident intensity pattern is required. However, pulse durations in the range of 100 fs limit the optically induced displacement, i.e., the transport length of charge carriers to a few angstrom [98, 99] which entails $\phi_\mathrm{n} \approx 0$. Cumulative effects by repetitive excitation ($f_\mathrm{rep} = 12.5\,\mathrm{Hz}$) as utilized in iron-doped LN to realize a phase shift of $\pi/2$ [75, 145] have not been detected. Moreover, instantaneous

$\chi^{(3)}$-nonlinearities like the electro-optic Kerr-effect or two-photon absorption [146, 147] can be excluded as well since they expose a local response.

Though, in materials featuring a local response, the mandatory phase shift is commonly caused by a non-instantaneous/time-delayed response of the nonlinear recording medium according to the theory of dynamic gratings (c.f. section 2.4.3). In lithium niobate, photogenerated quasiparticles, such as excitons, small polarons or free carriers are known for their optical nonlinearities [18, 146, 148]. Their responses are i.a. refractive and inertial, thus, suggesting their involvement in the underlying coupling mechanism. In particular, small polarons expose a non-negligible contribution to the nonlinear index of refraction [18, 137]. On the other hand, as proposed in reference [68], a frequency detuning in the THz-range might indicate a relation to phonons which are known to exhibit frequencies in the THz-regime in $LiNbO_3$ as well [149]: The frequency detuning could lead to the instantaneous parametric $\chi^{(2)}$-process of difference frequency generation where it is trivial to show that the generated photons will have the same frequency as the detuning. These photons can then either excite phonons or couple to phonons with equal frequency which is commonly described as phonon-polaritons [150, 151]. The frequency peaks deduced within this thesis seem to coincide with the resonance frequencies deduced in reference [151]. However, further measurements are required to develop a consisting model and to determine the origin of the involved, non-instantaneous nonlinearities.

3.5 Light-surface interaction of fs-pulses on a relief grating

In 2015/2016, Imlau *et al.* have presented a sensor concept which enables cw-laser based non-contact investigations of structured surface-relief degradation [152–154]. On the example of drag-reducing riblets, reflection, scattering, and diffraction phenomena arise from the light-surface interaction on the periodic surface grating. The latter contain valuable information about the periodicity of the microstructure. At the same time the interference phenomenon can cause fluctuations of the measurement signal if the fringe pattern and detector periodicity coincide (Moiré pattern) which subsequently lowers the signal-to-noise ratio. However, ultrafast spectroscopic/holographic studies (c.f. appendix A.3) reveal a strong correlation of the arising diffraction phenomena and the applied pulse parameters such as pulse duration, chirp, mutual detuning etc. Consequently and since the appearance of the interference pattern is a coherence phenomenon, the interaction of fs- and ps-pulses with the periodic surface grating is investigated.

The author contributed to the paper *Chirp control of femtosecond-pulse scattering from drag-reducing surface-relief gratings.* The abstract is printed here with friendly permission of the Optical Society of America (OSA). The complete article can be found in the appendix A.4.

J. Eggert, B. Bourdon, S. Nolte, J. Rischmueller, and M. Imlau
Chirp control of femtosecond-pulse scattering from drag-reducing surface-relief gratings
Photon. Res. **6**, 542–548, (2018); doi: 10.1364/PRJ.6.000542

Abstract: The role of chirp on the light–matter interaction of femto- and pico-second laser pulses with functional structured surfaces is studied using drag-reducing riblets as an example. The three-dimensional, periodic microstructure naturally gives rise to a mutual interplay of (i) reflection, (ii) scattering, and (iii) diffraction phenomena of incident coherent light. Furthermore, for femtosecond pulses, the structure induces (iv) an optical delay equivalent to a consecutive temporal delay of 230 fs in places of the pulse. These features enable studying experimentally and numerically the effect of tuning both pulse duration τ and spectral bandwidth $\Delta\omega$ on the features of the wideangle scattering pattern from the riblet structure. As a result, we discovered a significant breakdown of fringes in the scattering pattern with decreasing pulse duration and/or increasing spectral bandwidth. This unique type of chirp control is straightforwardly explained and verified by numerical modeling considering the spectral and temporal interaction between different segments within the scattered, linearly chirped pulse and the

particular geometric features of the riblet structure. The visibility of the fringe pattern can be precisely adjusted, and the offstate is achieved using $\tau < 230\,\mathrm{fs}$ or $\Delta\omega > 2.85 \times 10^{13}\,\mathrm{rad/s}$.

Accordingly, a precise control of the arising diffraction pattern can be achieved by appropriate adjustment of the pulse parameters, i.e., pulse duration, chirp and spectral width. Hence, a considerable improvement of the signal-to-noise ratio might be achieved by using fs-laser pulses as light source in the modular sensor.

In a next step, the impact of these results on the diffraction of ultrashort laser pulses on self-induced, holographic gratings is evaluated. Within this thesis, holographic gratings are recorded by the interference of two parallel polarized electromagnetic waves within the holographic medium. Small angles of incident of $2\theta \lesssim 10\,^\circ$ and recording wavelength in the UV to visible spectral range lead to grating constants of a few micrometers. The mutual temporal delay from adjacent grating lines is then in the range below approx. 50 fs for lithium niobate and approx. 30 fs for the photopolymer. Hence, if read-out is performed with fs-laser pulses featuring pulse durations well below these threshold values, an interference quenching might appear. However, even though the minimum used pulse duration of $\tau \approx 80\,\mathrm{fs}$ is close to the threshold value in LN, a considerable energy redistribution related to the coupling on a self-induced grating is observed (cf. appendix A.3). Moreover, within this thesis, holographic gratings are mainly analyzed by the diffraction of cw-lasers. In this case, the spatial/temporal delay induced by the structure has no significant influence on the arising diffraction phenomena (cf. appendix A.4 and the corresponding references therein). Thus, the discovered effect of interference quenching has not to be considered in any of the holographic experiments.

4 The elusive role of structural order

Light-matter interaction in tailored and photofunctional materials that strongly differ in their optical and structural properties is studied by appropriate adjustment of the experimental conditions. In the following, the individual photophysical and photochemical processes of the hologram formation are outlined and correlated with each other in order to draw further conclusions and provide new insight into the light-matter interaction. Particular emphasize is devoted to the impact of internal structure and the relative arrangement of the induced dipoles. The deviation of both processes, i.e., photophysical and -chemical, is made on the basis of reference [26] where photochemical reactions lead to a change of the chemical structure, e.g., linkage isomerism after light exposure, whereas photophysical processes maintain the chemical structure.

4.1 Photo-induced mechanisms of the hologram formation - generation of metastable and transient states

The distinction between metastable and transient states is in general not precisely defined. In the following, excited states with lifetimes of a few minutes to hours are termed metastable while decay times in the range of microseconds to a few seconds are related to transient states.

The underlying mechanism of holographic grating recording in the event of the investigated transition metal compound can be described briefly as follows: applying an electric field E results in a structural isomerization of the molecule from the S-bonded ground state to the O-bonded metastable state. The hereby induced dipole moment is linked to a light-induced change of the absorption coefficient and refractive index, respectively, via the Clausius-Mossotti-relation (c.f. section 2.1.1). Theoretical calculations via the Kramers-Kronig relation disclose refractive index changes in the order of 10^{-6} while absorption changes of a few 100 /m are determined by spectroscopic investigations. According to the holographic measurements, a modulated intensity pattern provokes a local, structural isomerization of the photoswitchable molecules which subsequently yields a spatially modulated absorption coefficient via the population of metastable states [31] while contributions from a phase grating can be neglected. Therefore, the material exhibits a local, photochromic response after optical excitation.

Similar results are obtained from spectroscopic and holographic measurements based on long-lived excitonic states in iron-doped LN by applying ns-pulses as light source. Here, a charge carrier is excited from the valence band to an $\mathrm{Fe}_{\mathrm{Li}}^{3+}$-center via a one-photon absorption process. Due to the attractive coulomb-force, the excited electron and remaining hole form an $\mathrm{Fe}_{\mathrm{Li}}^{2+} - \mathrm{O}^{-} - \mathrm{V}_{\mathrm{Li}}$ excitonic state. The local bonding and lattice distortion of the electron-hole pair prevent from far-reaching charge separations driven via diffusion or the photovoltaic effect. Thus, the separation is limited to one unit cell. Correspondingly, macroscopic refractive index modulations via the Pockels effect cannot arise which is in any case suppressed by the chosen configuration of light polarization, grating vector and crystallographic *c*-axis resulting in an electro-optic tensor element of $r_{31} = 0$. Instead, pronounced absorption changes primarily in the blue spectral range are detected (c.f. appendix A.2). Theoretical calculations via the Kramers-Kronig relation again reveal refractive index alterations in the range of 10^{-6}. Consequently, the holographic grating also features a local response which is, similarly to the OSO-complex, solely based on the photochromic properties. Thus, a contribution of the well known nonlinear effects in lithium niobate can be disregarded.

These results can also be compared with holographic investigations on thermally reduced lithium niobate. Here, holographic grating recording is based on a local change of the absorption coefficient which is related to the separation of bipolarons and the associated generation of bound polarons and hole polarons [13, 73, 143]. Comparable results were obtained under the same experimental configuration of *c*-axis, grating vector, and polarization states, i.e., $e_{\mathrm{pu}}||c$, $e_{\mathrm{pr}}||c$, $K \perp c$. However, significantly larger diffraction efficiencies of nearly a factor 1,000 were achieved if the pump and probe polarization as well as the grating vector are aligned parallel to the *c*-axis. Since possible iron impurities have been determined to be well below the spectroscopic limit, this observation was assigned to a bulk photovoltaic effect based on small polarons [13, 98]. However, varying the geometric arrangement of the holographic measurements based on excitonic states does not lead to any noteworthy impact on the maximum diffraction efficiency. As expected, a photovoltaic effect based on excitons can therefore be excluded. Hence, the polaron- and in particular the exciton-based holographic performance of lithium niobate is in principle comparable to molecular photoswitchable polymers and vice versa, provided contributions of the bulk photovoltaic effect and photorefractive effect can be ruled out.

In conclusion, although the photophysical and photochemical processes of holographic grating recording and especially the structure/composition of the investigated samples are fundamentally different, all systems exhibit a local material response in terms of an absorption coefficient alteration. This modulation as well as the refractive index change calculated via the Kramers-Kronig relation are both in the same order of magnitude within the individual samples. This result is of particular importance since the internal structure of lithium niobate and photofunctionalized polymers significantly differ.

What is the origin of the limitation of the diffraction efficiency and refractive index change, respectively?

Within appendix A.1, the detailed comparison to sodium nitroprusside (SNP) single crystals highly suggests that the origin of this limitation is most likely at the random arrangement of the photoswitchable molecules within the solid-state polymer. In comparison, the SNP single crystals feature a well ordered molecular structure which is preserved even in case of the metastable states. Therefore, the molecular order of the photoswitchable compounds seems to have a significant impact on the light-matter interaction in particular with respect to macroscopic refractive index changes. This together with the transfer from photoswitchable molecules to generated quasiparticles in lithium niobate will be discussed in more detail within the next section using the liquid crystal model.

4.2 The liquid crystal model and its application to macroscopic refractive index changes

4.2.1 Liquid crystals

The following description of liquid crystals will be given along references [93, 155, 156]. Liquid crystals are a type of matter that feature properties of crystalline solids as well as

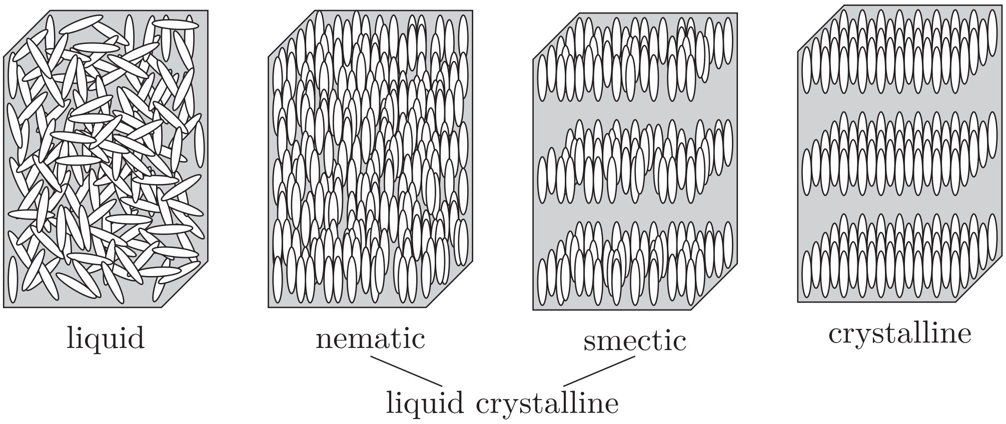

Figure 4.1 – Model structure of different material phases according to references [93,155] where dipoles are illustrated as rods. Liquid: all molecules are randomly distributed. Nematic: the molecules exhibit orientational (here perfectly aligned) but no positional order. Smectic: the molecules are arranged in layers because of additional positional order in one dimension. Within the layer, the molecule positions can be randomly distributed. Crystalline: orientational and positional order in all spatial coordinates.

isotropic liquids depending on the spatial arrangement of molecules. These molecules or more precisely, the orientation of dipoles, are typically described as rods. Their spatial arrangement can be divided into orientational and positional order. These two terms can be understood as follows: starting from the system of highest disorder, i.e. a liquid, the molecules and, thus, their orientation and position are isotropically distributed which is depicted in fig. 4.1. In the next higher order state, the molecules are mainly oriented along a specific direction (orientational order) which is described by the dimensionless unit vector n, the so-called director. This liquid crystal phase is called nematic phase and exhibits orientational order but no positional order. Additionally, an order parameter S is defined which characterizes the degree of orientation

$$S = \frac{1}{2}\left(3\langle\cos^2\theta\rangle - 1\right), \tag{4.1}$$

where θ is the angle between director vector and molecule axes (rod) and $\langle\cos^2\theta\rangle$ indicates the averaging over all orientations. Note that $S = 1$ for perfect alignment ($\theta = 0,\pi$) and $S = 0$ for randomly distributed molecules which is corresponds to the liquid phase.

The next higher symmetry state additionally accounts for positional order in one spatial coordinate (smectic phase), so that the molecules are arranged in layers. Several smectic subclasses exist in which the order of molecules within the layers or the orientation of the director vector with respect to the layer normal differ. However, a detailed description of these subclasses is out of the scope of thesis. The highest degree of symmetry is achieved in case of the crystalline phase in which the molecules reveal orientational and positional order for all three spatial coordinates.

4.2.2 Application to the investigated materials

The concept of the liquid crystal phase model will now be transferred to the investigated samples and to sodium nitroprusside single crystals in order to further expand the comparison to the ruthenium sulfoxides.

SNP single crystals reveal contrawise oriented photoswitchable compounds within each a-b-mirror plane of the orthorhombic unit cell and with $\pm 37.6\,^\circ$ with respect to the a-axis alternating along the c-axis [106,157,158]. Hence, the photoswitchable compounds are arranged in layers where the director vector is tilted with respect to the a- and b-axis and perpendicular to the c-axis. The structure within each layer can be compared to a crystalline phase with a perfect positional and orientational order $S = 1$ (but alternating along c). Illumination with light causes a structural isomerization from the ground state into a metastable state thereby altering the nitrosyl-ligand from the N-bonded to the O-bonded configuration. Hence, the dipole moment is only related to the nitrosyl-ligand which maintains the relative orientation even in the metastable state [106, 158]. This intrinsic order of the photoswitchable units and, correspondingly, of the induced dipole moments (atomic polarization) adds up to a macroscopic polarization (orientation polarization) and refractive index change. Polarization dependent measurements highly support the correlation between the induced refractive index changes and the orientation of the photoswitchable molecules within the a-b-mirror plane while the induced refractive index alterations along c are negligible [87, 106].

Contrary, the OSO-compound is homogeneously dissolved within dichlormethane and subsequently embedded into the high-viscous polymer PDMS. Thermal treatment causes the polymer to harden resulting in a solid with randomly arranged photoswitches. Therefore, the molecules feature neither a positional nor an orientational order which is comparable to the arrangement within a liquid phase. Even though polarization dependent measurements exhibit an anistropy of the population kinetics for high-concentrated solutions $c = 0.8\,\mathrm{mM}$, the absorption change in saturation (and also the kinetics for low-concentrated solutions $c = 0.2\,\mathrm{mM}$) is identical for the investigated polarization states [32] which supports the isotropic molecule distribution. Hence, only those dipoles are addressed whose projection on the oscillation direction of the pump wave is unequal to zero. Correspondingly, an atomic polarization is present while the orientational polarization adds up to zero (random distribution). As a consequence, the induced polarization and thereby the induced refractive index changes are significantly lower than in SNP. However, even though the molecules are initially homogeneously distributed and randomly orientated, the linearly polarized pump wave selects only those molecules with appropriate orientation. Hence, the metastable states or in more detail the associated dipoles might feature an orientational order which could be compared with a nematic phase. Consequently, a slightly structured sample might be present in case of read-out. This type of structuring might be labeled as polarization structuring.

The third investigated system is iron-doped, oxidized lithium niobate. Iron is incorporated within the regular, non-centrosymmetric lattice on a Li-site within an oxygen-octahedron. Hence, a positional order is present. A detailed treatment of the position and absolute distances to the surrounding, next-neighboring atoms is performed by Schirmer *et al.* [98] for the incorporation of $\mathrm{Fe}_{\mathrm{Li}}^{2+}$-centers. There it is assumed that the atom positions are unchanged with respect to the defect-free crystal structure. For a first approximation, the same will be presumed in case of $\mathrm{Fe}_{\mathrm{Li}}^{3+}$-centers. As previously described, transient states are generated by the excitation of an electron from an oxygen atom in direct vicinity of a Li-vacancy to an $\mathrm{Fe}_{\mathrm{Li}}^{3+}$-center. Perpendicular to the c-axis, three oxygen atoms each (arranged in a layer) are above and below the central $\mathrm{Fe}_{\mathrm{Li}}^{3+}$-atom where the distance to the oxygen layer below ($-c$ direction) is smaller. However, within a layer, all three oxygen atoms reveal the same distance, hence, the induced dipoles are of equal size. Due to the $C_{3\mathrm{v}}$-symmetry in Schoenflies-notation, no net orientational order is present in the x-y-layer. As a result of the different distances between the oxygen layer above and below the iron center, respectively, the induced dipole moment in $+c$ direction will be larger compared to $-c$. Therefore, even though the $C_{3\mathrm{v}}$-symmetry again prevents from orientational order in terms of the liquid crystal phases, a net orientational order of the dipoles could be assumed due to the different dipole moment strength in $+c$ and $-c$direction (analogous to the explanation of the bulk photovoltaic effect in Fe^{2+}-doped lithium niobate [98]). However, as a consequence of polarization dependent measurements, no significantly different diffraction efficiencies along and perpendicular to the c-axis are detected. Therefore, it might be assumed that the excited dipoles feature no orientational order and order is only induced by polarization structuring similar to the considerations for the OSO-compound. Thus, the intrinsic crystalline order of the lithium niobate host is not necessarily a prerequisite for macroscopic refractive index modulations.

4.3 Conclusion

The detailed studies of the holographic performance of photoswitchable polymer films and iron-doped, oxidized lithium niobate exhibits striking similarities of the diffraction efficiency as well as light-induced absorption and refractive index changes although both samples differ significantly with respect to their optical and structural properties. A local, photochromic response is derived which can be attributed to the isomerization of photoswitchable ruthenium sulfoxide molecules and the generation of excitonic states, respectively. By comparing these results to the holographic performance of photorefractive sodium nitroprusside single crystals, a considerable impact of the molecular structure and relative arrangement of the appropriate excited states can be concluded. The realization of order/structure can be roughly divided into three categories. In the event of the investigated riblets, a well-structured surface is produced artificially. The second type can be attributed to intrinsic order as particularly present in case of solid state crystals, for example lithium niobate or SNP single crystals which are manufactured by expensive and long-lasting crystal growth processes. This procedure is to be regarded as disadvantageous in terms of scalability, flexibility and cost reduction which all can be remedied by embedding the photoswitchable molecules into an amorphous solid polymer. However, as a drawback, the OSO-complexes are homogeneously distributed in the polymer and feature no preferred orientation which prevents from the formation of macroscopic refractive index changes. Similar results are obtained from a detailed study of the structure/orientation of transient excitonic states in iron-doped, oxidized lithium niobate. Even though the crystal itself features a well structured intrinsic order, there is neither an intrinsic nor an artificially generated order of the excited states. Hence, the intrinsic crystalline order is not necessarily a prerequisite for macroscopic refractive index modulations. Rather, an orientational order of the excited states is mandatory. Molecular order might, however, be achieved by optical structuring (third type), i.e., by the polarization of the incident light waves. Either way, it is obvious that an appropriate three-dimensional structural arrangement of the photoactive molecules within the amorphous polymer is essential for achieving significant refractive index changes.

5 Summary

Within this thesis, photo-induced mechanisms of the light-matter interaction are investigated in tailored and photofunctional materials that differ significantly in their optical and structural properties. The individual coupling mechanisms in congruently melted, nominally undoped or iron doped lithium niobate crystals as well as in structurally disordered photoswitchable molecules embedded into a solid state polymer are examined in particular by the principle of holographic grating recording and transient absorption spectroscopy which provide new insight into a variety of material response properties.

In case of photoswitchable ruthenium sulfoxide compounds, the underlying mechanism can be unambiguously assigned to a photochromic material response evoked by a photochemical reaction, i.e., a non-instantaneous, local ligand isomerisation. Comparable results are obtained for iron-doped, oxidized lithium niobate where holographic grating recording is related to the photophysical generation of transient excitonic states whose photochromic properties are characterized by targeted ns-pump, supercontinuum probe spectroscopy. In the event of nominally undoped lithium niobate, the holographic amplification of two sub-picosecond pulses is attached to the phenomenon of two-beam coupling on a self-induced dynamic grating. By correlating the individually obtained mechanisms of the light-matter interaction and the light-induced material response, generally accepted conclusions on a microscopic level can be achieved. A major influence of the internal structure and orientation of the excited states, i.e., an appropriate three-dimensional structural arrangement, is deduced as a prerequisite for the formation of light-induced, macroscopic refractive index changes while absorption and microscopic refractive index alterations linked via the Kramers-Kronig relation are unaffected. In systems featuring a random distribution of excited states, an orientational order might be achieved as a consequence of linear polarized light, i.e., by polarization structuring. Moreover, if the photorefractive effect can be ruled out, the material response in lithium niobate can be solely assigned to a local alteration of the transient electronic states, i.e., to the photochromic properties of polarons and/or excitonic states, which is in particular comparable to the linkage isomerism of molecular photoswitchable molecules.

In addition, the influence of structural parameters on the light-matter/surface interaction is studied on the μm-scale by analyzing the diffraction phenomenon arising from a relief grating. A considerable impact on the surface grating assisted coupling is determined by the transition from cw-lasers to ultrashort laser pulses which enables interference quenching. However, this phenomenon is of no consequence in case of self-induced holographic gratings.

Bibliography

[1] J. C. Maxwell. *VIII. A dynamical theory of the electromagnetic field.* Philosophical Transactions of the Royal Society of London **155**, 459–512 (1865).

[2] F. Zernike, J. E. Midwinter. *Applied Nonlinear Optics.* Wiley-Interscience (1973).

[3] D. Meschede. *Optik, Licht und Laser.* Teubner B.G. GmbH (2008).

[4] P. Van Rysselberghe. *Remarks concerning the Clausius-Mossotti Law.* The Journal of Physical Chemistry **36**, 1152–1155 (1932).

[5] D. C. Hutchings, M. Sheik-Bahae, D. J. Hagan, E. W. Van Stryland. *Kramers-Krönig relations in nonlinear optics.* Optical and Quantum Electronics **24**, 1–30 (1992).

[6] K.-E. Peiponen, J. J. Saarinen. *Generalized Kramers–Kronig relations in nonlinear optical- and THz-spectroscopy.* Reports on Progress in Physics **72**, 056401 (2009).

[7] D. Berben, K. Buse, S. Wevering, P. Herth, M. Imlau, Th. Woike. *Lifetime of small polarons in iron-doped lithium–niobate crystals.* Journal of Applied Physics **87**, 1034–1041 (2000).

[8] P. Herth, T. Granzow, D. Schaniel, Th. Woike, M. Imlau, E. Krätzig. *Evidence for Light-Induced Hole Polarons in* $LiNbO_3$. Physical Review Letters **95** (2005).

[9] P. Herth, D. Schaniel, Th. Woike, T. Granzow, M. Imlau, E. Krätzig. *Polarons generated by laser pulses in doped* $LiNbO_3$. Physical Review B **71** (2005).

[10] D. Conradi, C. Merschjann, B. Schoke, M. Imlau, G. Corradi, K. Polgár. *Influence of Mg doping on the behaviour of polaronic light-induced absorption in* $LiNbO_3$. phys. stat. sol. (RRL) **2**, 284–286 (2008).

[11] C. Merschjann, B. Schoke, D. Conradi, M. Imlau, G. Corradi, K. Polgár. *Absorption cross sections and number densities of electron and hole polarons in congruently melting* $LiNbO_3$. Journal of Physics: Condensed Matter **21**, 015906 (2008).

[12] S. Messerschmidt, A. Krampf, F. Freytag, M. Imlau, L. Vittadello, M. Bazzan, G. Corradi. *The role of self-trapped excitons in polaronic recombination processes in lithium niobate.* Journal of Physics: Condensed Matter **31**, 065701 (2018).

[13] M. Imlau, H. Badorreck, C. Merschjann. *Optical nonlinearities of small polarons in lithium niobate.* Applied Physics Reviews **2**, 040606 (2015).

[14] O. Beyer, D. Maxein, K. Buse, B. Sturman, H. T. Hsieh, D. Psaltis. *Femtosecond time-resolved absorption processes in lithium niobate crystals.* Optics Letters **30**,

1366 (2005).

[15] O. Beyer, D. Maxein, K. Buse, B. Sturman, H. T. Hsieh, D. Psaltis. *Investigation of nonlinear absorption processes with femtosecond light pulses in lithium niobate crystals.* Physical Review E **71** (2005).

[16] O. Beyer, D. Maxein, Th. Woike, K. Buse. *Generation of small bound polarons in lithium niobate crystals on the subpicosecond time scale.* Applied Physics B **83**, 527–530 (2006).

[17] S. Odoulov, A. Shumelyuk, H. Badorreck, S. Nolte, K.-M. Voit, M. Imlau. *Interference and holography with femtosecond laser pulses of different colours.* Nature Communications **6** (2015).

[18] H. Badorreck, S. Nolte, F. Freytag, P. Bäune, V. Dieckmann, M. Imlau. *Scanning nonlinear absorption in lithium niobate over the time regime of small polaron formation.* Optical Materials Express **5**, 2729 (2015).

[19] M. Hase, M. Kitajima, A. M. Constantinescu, H. Petek. *The birth of a quasiparticle in silicon observed in time–frequency space.* Nature **426**, 51–54 (2003).

[20] A. Leitenstorfer. *Femtophysics: Birth of a quasiparticle.* Nature **426**, 23–24 (2003).

[21] J. Manz, L. Wöste. *Femtosecond Chemistry, Vol 1 + 2.* VDH Verlagsgesellschaft (1995).

[22] M. Dantus, R. M. Bowman, A. H. Zewail. *Femtosecond laser observations of molecular vibration and rotation.* Nature **343**, 737–739 (1990).

[23] Professor Bengt Nordén. *The Nobel Prize in Chemistry 1999 - The work of Professor Ahmed H. Zewail*, (1999).

[24] D. Gabor. *A New Microscopic Principle.* Nature **161**, 777–778 (1948).

[25] H. Kogelnik. *Coupled Wave Theory for Thick Hologram Gratings.* Bell System Technical Journal **48**, 2909–2947 (1969).

[26] S. E. Braslavsky. *Glossary of terms used in photochemistry, 3rd edition (IUPAC Recommendations 2006).* Pure and Applied Chemistry **79**, 293–465 (2007).

[27] C. Pop. *Herstellung von monodispersen Polydimethylsiloxan-Netzwerken und Charakterisierung der Mikrostruktur und der Permeationseigenschaften..* Dissertation, University of Wuerzburg, 2006.

[28] D. P. Butcher, A. A. Rachford, J. L. Petersen, J. J. Rack. *Phototriggered S $\rightarrow$ O Isomerization of a Ruthenium-Bound Chelating Sulfoxide.* Inorganic Chemistry **45**, 9178–9180 (2006).

[29] B. A. McClure, J. J. Rack. *Ultrafast Spectroscopy of a Photochromic Ruthenium Sulfoxide Complex.* Inorganic Chemistry **50**, 7586–7590 (2011).

[30] V. Dieckmann, S. Eicke, J. J. Rack, Th. Woike, M. Imlau. *Pronounced photosensitivity of molecular [Ru(bpy)_2(OSO)]$^{\wedge +}$ solutions based on two photoinduced linkage isomers.* Optics Express **17**, 15052 (2009).

[31] V. Dieckmann, S. Eicke, K. Springfeld, M. Imlau. *Transition Metal Compounds Towards Holography.* Materials **5**, 1155–1175 (2012).

[32] S. Eicke. *Populations- und Relaxationskinetiken laserangeregter photofunktionaler Ruthenium-Sulfoxid-Komplexe in hochkonztrierten Lösungen.* Dissertation, Osnabrueck Universtiy, 2012.

[33] K. Springfeld, V. Dieckmann, M. Imlau. *High-contrast, high-resolution photochromic silicone polymer based on photoswitchable* $[Ru(bpy)_2OSO]PF_6$ *buiding blocks.* Photonics Research **1**, 197 (2013).

[34] T. Holstein. *Studies of polaron motion: Part I. The molecular-crystal model.* Annals of Physics **8**, 325–342 (1959).

[35] T. Holstein. *Studies of polaron motion: Part II. The "small" polaron.* Annals of Physics **8**, 343–389 (1959).

[36] D. Emin. *Polarons.* Cambridge University Press (2012).

[37] Y. Toyozawa. *Phonon structures in the spectra of solids.* Journal of Luminescence **1-2**, 732–746 (1970).

[38] R. T. Williams, M. N. Kabler. *Excited-state absorption spectroscopy of self-trapped excitons in alkali halides.* Physical Review B **9**, 1897–1907 (1974).

[39] Y. Toyozawa. *Dynamics of excitons in deformable lattice.* Journal of Luminescence **24-25**, 23–30 (1981).

[40] K. S. Song, R. T. Williams. *Self-trapped Excitons.* Springer Series in Solid-State Sciences Springer Berlin Heidelberg (1993).

[41] Y. Toyozawa. *Optical Processes in Solids.* Cambridge University Press (2013).

[42] H. Ibach, H. Lüth. *Festkörperphysik.* Springer Berlin Heidelberg (2008).

[43] W. von Sellmeier. *Zur Erklärung der abnormen Farbenfolge im Spectrum einiger Substanzen.* Annalen der Physik und Chemie **219**, 272–282 (1871).

[44] J.-C. Diels, W. Rudolph. *Ultrashort Laser Pulse Phenomena.* Elsevier LTD, Oxford (2006).

[45] R. Menzel. *Photonics.* Springer (2007).

[46] R. W. Boyd. *Nonlinear Optics.* Elsevier LTD, Oxford (2008).

[47] F. Träger. *Springer Handbook of Lasers and Optics.* Springer-Verlag (2012).

[48] R. S. Weis, T. K. Gaylord. *Lithium niobate: Summary of physical properties and crystal structure.* Appl. Phys. A **37**, 191–203 (1985).

[49] Y.-R. Shen. *Principles of Nonlinear Optics.* John Wiley & Sons, Inc. (2002).

[50] J. E. Moffatt, G. Tsiminis, E. Klantsataya, T. J. de Prinse, D. Ottaway, N. A. Spooner. *A practical review of shorter than excitation wavelength light emission processes.* Applied Spectroscopy Reviews 1–23 (2019).

[51] P. N. Butcher, D. Cotter. *The Elements of Nonlinear Optics.* Cambridge University

press (1990).

[52] R. L. Sutherland. *Handbook of Nonlinear Optics.* Marcel Dekker, Inc. (2003).

[53] R. H. Stolen, A. Ashkin. *Optical Kerr effect in glass waveguide.* Applied Physics Letters **22**, 294–296 (1973).

[54] P. Yeh. *Two-wave mixing in nonlinear media.* IEEE Journal of Quantum Electronics **25**, 484–519 (1989).

[55] R. del Coso, J. Solis. *Relation between nonlinear refractive index and third-order susceptibility in absorbing media.* Journal of the Optical Society of America B **21**, 640 (2004).

[56] G. P. Agrawal, N. A. Olsson. *Self-phase modulation and spectral broadening of optical pulses in semiconductor laser amplifiers.* IEEE Journal of Quantum Electronics **25**, 2297–2306 (1989).

[57] A. Brodeur, S. L. Chin. *Ultrafast white-light continuum generation and self-focusing in transparent condensed media.* Journal of the Optical Society of America B **16**, 637 (1999).

[58] D. E. Spence, P. N. Kean, W. Sibbett. *60-fsec pulse generation from a self-mode-locked Ti:sapphire laser.* Optics Letters **16**, 42 (1991).

[59] F. Salin, M. Piché, J. Squier. *Mode locking of Ti:*Al_2O_3 *lasers and self-focusing: a Gaussian approximation.* Optics Letters **16**, 1674 (1991).

[60] T. Brabec, Ch. Spielmann, P. F. Curley, F. Krausz. *Kerr lens mode locking.* Optics Letters **17**, 1292 (1992).

[61] I. Kang, T. Krauss, F. Wise. *Sensitive measurement of nonlinear refraction and two-photon absorption by spectrally resolved two-beam coupling.* Optics Letters **22**, 1077 (1997).

[62] M. Göppert-Mayer. *Über Elementarakte mit zwei Quantensprüngen.* Ann. Phys. **401**, 273–294 (1931).

[63] W. Kaiser, C. G. B. Garrett. *Two-Photon Excitation in* CaF_2*:*Eu^{2+}. Phys. Rev. Lett. **7**, 229–231 (1961).

[64] S. Sasamoto, J. Hirohashi, S. Ashihara. *Polaron dynamics in lithium niobate upon femtosecond pulse irradiation: Influence of magnesium doping and stoichiometry control.* Journal of Applied Physics **105**, 083102 (2009).

[65] F. Auzel. *Upconversion and Anti-Stokes Processes with f and d Ions in Solids.* Chemical Reviews **104**, 139–174 (2004).

[66] F. Wang, X. Liu. *Recent advances in the chemistry of lanthanide-doped upconversion nanocrystals.* Chemical Society Reviews **38**, 976 (2009).

[67] M. Haase, H. Schäfer. *Upconverting Nanoparticles.* Angewandte Chemie International Edition **50**, 5808–5829 (2011).

[68] S. Nolte. *Mutual interactions of femtosecond pulses and transient gratings in nonlinear optical spectroscopy.* Dissertation, Osnabrueck University, 2018.

[69] P. Yeh. *Introduction to Photorefractive Nonlinear Optics.* JOHN WILEY & SONS INC (1993).

[70] H. J. Eichler, P. Günter, D. W. Pohl. *Laser-Induced Dynamic Gratings.* Springer Berlin Heidelberg (2013).

[71] K. Buse. *Light-induced charge transport processes in photorefractive crystals I: Models and experimental methods.* Applied Physics B: Lasers and Optics **64**, 273–291 (1997).

[72] K. Buse. *Light-induced charge transport processes in photorefractive crystals II: Materials.* Applied Physics B: Lasers and Optics **64**, 391–407 (1997).

[73] H. Brüning, V. Dieckmann, B. Schoke, K.-M. Voit, M. Imlau, G. Corradi, C. Merschjann. *Small-polaron based holograms in $LiNbO_3$ in the visible spectrum.* Optics Express **20**, 13326 (2012).

[74] M. Imlau, H. Brüning, B. Schoke, R.-S. Hardt, D. Conradi, C. Merschjann. *Hologram recording via spatial density modulation of $Nb_{\mathrm{Li}}^{4+/5+}$ antisites in lithium niobate.* Optics Express **19**, 15322 (2011).

[75] D. Maxein, J. Bückers, D. Haertle, K. Buse. *Photorefraction in $LiNbO_3$:Fe crystals with femtosecond pulses at 532 nm.* Applied Physics B **95**, 399–405 (2009).

[76] J. Frejlich. *Photorefractive Materials - Fundamental Concepts, Holographic Recording and Materials Characterization.* John Wiley & Sons, Inc. (2007).

[77] T. Kubota. *The diffraction efficiency of hologram grating recorded in an absorptive medium.* Optics Communications **16**, 347–349 (1976).

[78] V. L. Vinetskiĭ, N. V. Kukhtarev, S. G. Odoulov, M. S. Soskin. *Dynamic self-diffraction of coherent light beams.* Soviet Physics Ispekhi **22**, 742–756 (1979).

[79] D. Udo. *Der lichtinduzierte Ladungstransport und der Relaxor-Phasenübergang in Strontium-Barium-Niobat ($Sr_{\mathrm{x}}\,Ba_{1-\mathrm{x}}Nb_2O_6$) dotiert mit Ce, Cr, Rh, Tm oder Co.* Cuvillier Verlag (2002).

[80] P. Günter, J.-P. Huignard. *Topics in Applied Physics: Photorefractive Materials and Their Applications II.* Springer Verlag (1989).

[81] V. L. Vinetskiĭ, N. V. Kukhtarev, M. S. Soskin. *Transformation of intensities and phases of light beams by a transient "undisplaced" holographic grating.* Sov. J. Quantum Electron. **7**, 230–233 (1977).

[82] N. Kukhtarev, V. Markov, S. Odulov. *Transient energy transfer during hologram formation in $LiNbO_3$ in external electric field.* Optics Communications **23**, 338–343 (1977).

[83] V. Markov, S. Odulov, M. Soskin. *Dynamic holography and optical image processing.* Optics & Laser Technology **11**, 95–99 (1979).

[84] J. M. Heaton, L. Solymar. *Transient Energy Transfer during Hologram Formation in Photorefractive Crystals.* Optica Acta: International Journal of Optics **32**, 397–408 (1985).

[85] N. S.-K. Kwong, Y. Tamita, A. Yariv. *Optical tracking filter using transient energy coupling.* Journal of the Optical Society of America B **5**, 1788 (1988).

[86] V. L. Vinetskiĭ, N. V. Kukhtarev. *Transient energy transfer between coherent light beams in a resonant medium.* Sov. J. Quantum Electron. **8**, 491–493 (1978).

[87] M. Imlau, S. Haussühl, T. Woike, R. Schieder, V. Angelov, R.A. Rupp, K. Schwarz. *Holographic recording by excitation of metastable electronic states in* Na_2 *[Fe(CN)*$_5$*NO]·2*H_2O*: a new photorefractive effect.* Applied Physics B: Lasers and Optics **68**, 877–885 (1999).

[88] H. Badorreck, A. Shumelyuk, S. Nolte, M. Imlau, S. Odoulov. *Doppler-shifted Raman-Nath diffraction from gratings recorded in* $LiNbO_3$ *with ultra-short laser pulses of different color.* Optical Materials Express **6**, 517 (2016).

[89] A. Ashkin, G. D. Boyd, J. M. Dziedzic, R. G. Smith, A. A. Ballman, J. J. Levinstein, K. Nassau. *OPTICALLY-INDUCED REFRACTIVE INDEX INHOMOGENEITIES IN* $LiNbO_3$ *AND* $LiTaO_3$. Applied Physics Letters **9**, 72–74 (1966).

[90] F. S. Chen, J. T. LaMacchia, D. B. Fraser. *HOLOGRAPHIC STORAGE IN LITHIUM NIOBATE.* Applied Physics Letters **13**, 223–225 (1968).

[91] F. S. Chen. *Optically Induced Change of Refractive Indices in* $LiNbO_3$ *and* $LiTaO_3$. Journal of Applied Physics **40**, 3389–3396 (1969).

[92] N. V. Kukhtarev, V. B. Markov, S. G. Odulov, M. S. Soskin, V. L. Vinetskii. *Holographic storage in electrooptic crystals. i. steady state.* Ferroelectrics **22**, 949–960 (1978).

[93] R. Waser. *Nanoelectronics and Information Technology: Advanced Materials and Novel Devices.* Wiley-VCH Verlag (2003).

[94] A. M. Glass, D. von der Linde, T. J. Negran. *High-voltage bulk photovoltaic effect and the photorefractive process in* $LiNbO_3$. Applied Physics Letters **25**, 233–235 (1974).

[95] H. Kurz, E. Krätzig, W. Keune, H. Engelmann, U. Gonser, B. Dischler, A. Räuber. *Photorefractive centers in* $LiNbO_3$*, studied by optical-, Mössbauer- and EPR-methods.* Applied physics **12**, 355–368 (1977).

[96] F. Jermann, J. Otten. *Light-induced charge transport in* $LiNbO_3$*:Fe at high light intensities.* Journal of the Optical Society of America B **10**, 2085 (1993).

[97] V. M. Fridkin. *Bulk photovoltaic effect in noncentrosymmetric crystals.* Crystallography Reports **46**, 654–658 (2001).

[98] O. F. Schirmer, M. Imlau, C. Merschjann. *Bulk photovoltaic effect of* $LiNbO_3$*:Fe and its small-polaron-based microscopic interpretation.* Physical Review B **83**

(2011).

[99] L. Vittadello, M. Bazzan, A. Danielyan, E. Kokanyan, L. Guilbert, M. Aillerie. *A polaron approach to photorefractivity in Fe:LiNbO*$_3$. Journal of Physics Communications **2**, 125003 (2018).

[100] L. Young, M. G. Moharam, F. El. Guibaly, E. Lun. *Hologram writing in lithium niobate: Beam coupling and the transport length in the bulk photovoltaic effect.* Journal of Applied Physics **50**, 4201–4207 (1979).

[101] P. P. Birnbaum, J. H. Linford, D. W. G. Style. *The absorption spectra of azobenzene and some derivatives.* Transactions of the Faraday Society **49**, 735 (1953).

[102] G. Zimmerman, L.-Y. Chow, U.-J. Paik. *The Photochemical Isomerization of Azobenzene*[1]. Journal of the American Chemical Society **80**, 3528–3531 (1958).

[103] C. R. Crecca, A. E. Roitberg. *Theoretical Study of the Isomerization Mechanism of Azobenzene and Disubstituted Azobenzene Derivatives.* The Journal of Physical Chemistry A **110**, 8188–8203 (2006).

[104] H. M. D. Bandara, S. C. Burdette. *Photoisomerization in different classes of azobenzene.* Chem. Soc. Rev. **41**, 1809–1825 (2012).

[105] M. D. Carducci, M. R. Pressprich, P. Coppens. *Diffraction Studies of Photoexcited Crystals: Metastable Nitrosyl-Linkage Isomers of Sodium Nitroprusside.* Journal of the American Chemical Society **119**, 2669–2678 (1997).

[106] M. Imlau. *Der photorefraktive Effekt, holographische Informationsspeicherung und die Entdeckung holographischer Streuung in zentrosymmetrischen Kristallen.* Cuvillier Verlag (1999).

[107] J. J. Rack. *Photoinduced molecular switches.* U.S. Patent 6433270 (2002).

[108] B. A. McClure, N. V. Mockus, D. P. Butcher, D. A. Lutterman, C. Turro, J. L. Petersen, J. J. Rack. *Photochromic Ruthenium Sulfoxide Complexes: Evidence for Isomerization Through a Conical Intersection.* Inorganic Chemistry **48**, 8084–8091 (2009).

[109] A. Juris, V. Balzani, F. Barigelletti, S. Campagna, P. Belser, A. von Zelewsky. *Ru(II) polypyridine complexes: photophysics, photochemistry, eletrochemistry, and chemiluminescence.* Coordination Chemistry Reviews **84**, 85–277 (1988).

[110] G. J. Kavarnos, N. J. Turro. *Photosensitization by reversible electron transfer: theories, experimental evidence, and examples.* Chemical Reviews **86**, 401–449 (1986).

[111] D. Schaniel, M. Nicoul, Th. Woike. *Ultrafast reversible ligand isomerisation in* $Na_2[Fe(CN)_5NO]\cdot 2H_2O$ *single crystals.* Physical Chemistry Chemical Physics **12**, 9029 (2010).

[112] D. Schaniel, Th. Woike. *Necessary conditions for the photogeneration of nitrosyl linkage isomers.* Physical Chemistry Chemical Physics **11**, 4391 (2009).

[113] Th. Woike, W. Kirchner, G. Schetter, Th. Barthel, K. Hyung-sang, S. Haussühl. *New information storage elements on the basis of metastable electronic states.* Optics Communications **106**, 6–10 (1994).

[114] P. Günter. *Holography, coherent light amplification and optical phase conjugation with photorefractive materials.* Physics Reports **93**, 199–299 (1982).

[115] T. Volk, M. Wöhlecke. *Lithium Niobate.* Springer-Verlag GmbH (2008).

[116] O. F. Schirmer, O. Thiemann, M. Wöhlecke. *Defects in $LiNbO_3$—I. experimental aspects.* Journal of Physics and Chemistry of Solids **52**, 185–200 (1991).

[117] D. N. Nikogosyan. *Nonlinear Optical Crystals: A Complete Survey.* Springer New York (2006).

[118] L. Kovács, G. Ruschhaupt, K. Polgár, G. Corradi, M. Wöhlecke. *Composition dependence of the ultraviolet absorption edge in lithium niobate.* Applied Physics Letters **70**, 2801–2803 (1997).

[119] B. Dischler, J.R. Herrington, A. Räuber, H. Kurz. *Correlation of the photorefractive sensitivity in doped $LiNbO_3$ with chemically induced changes in the optical absorption spectra.* Solid State Communications **14**, 1233–1236 (1974).

[120] E. Krätzig, H. Kurz. *Photorefractive and Photovoltaic Effects in Doped $LiNbO_3$.* Optica Acta: International Journal of Optics **24**, 475–482 (1977).

[121] E. Krätzig. *Photorefractive effects and photoconductivity in $LiNbO_3$:Fe.* Ferroelectrics **21**, 635–636 (1978).

[122] L. Hesselink. *Photorefractive Materials for Nonvolatile Volume Holographic Data Storage.* Science **282**, 1089–1094 (1998).

[123] K. Buse, A. Adibi, D. Psaltis. *Non-volatile holographic storage in doubly doped lithium niobate crystals.* Nature **393**, 665–668 (1998).

[124] K. Peithmann, A. Wiebrock, K. Buse. *Photorefractive properties of highly-doped lithium niobate crystals in the visible and near-infrared.* Applied Physics B **68**, 777–784 (1999).

[125] G.-G. Zhong, J. Jian, Z.-K. Wu. *Measurements of optically induced refractive-index damage of lithium niobate doped with different concentrations of MgO (A).* Journal of the Optical Society of America (1917-1983) **70**, 631 (1980).

[126] T. R. Volk, V. I. Pryalkin, N. M. Rubinina. *Optical-damage-resistant $LiNbO_3$:Zn crystal.* Optics Letters **15**, 996 (1990).

[127] M. G. Clark, F. J. DiSalvo, A. M. Glass, G. E. Peterson. *Electronic structure and optical index damage of iron-doped lithium niobate.* The Journal of Chemical Physics **59**, 6209–6219 (1973).

[128] S. Messerschmidt. *Recombination dynamics of optically generated small polarons and self-trapped excitons in lithium niobate.* Dissertation, Osnabrueck University, 2019.

[129] License Url. *https://creativecommons.org/licenses/by-nc-nd/3.0/de/*, (call state: 31.12.2019).

[130] B. Faust, H. Muller, O. F. Schirmer. *Free small polarons in* $LiNbO_3$. Ferroelectrics **153**, 297–302 (1994).

[131] C. Merschjann, B. Schoke, M. Imlau. *Influence of chemical reduction on the particular number densities of light-induced small electron and hole polarons in nominally pure* $LiNbO_3$. Physical Review B **76** (2007).

[132] O F Schirmer. O^- *bound small polarons in oxide materials.* Journal of Physics: Condensed Matter **18**, R667–R704 (2006).

[133] A. Sanson, A. Zaltron, N. Argiolas, C. Sada, M. Bazzan, W. G. Schmidt, S. Sanna. *Polaronic deformation at the* $Fe^{2+/3+}$ *impurity site in Fe:*$LiNbO_3$ *crystals.* Physical Review B **91** (2015).

[134] R. Kohlrausch. *Ueber das Dellmann'sche Elektrometer.* Annalen der Physik und Chemie **148**, 353–405 (1847).

[135] G. Williams, D. C. Watts. *Non-symmetrical dielectric relaxation behaviour arising from a simple empirical decay function.* Transactions of the Faraday Society **66**, 80 (1970).

[136] F. Alvarez, A. Alegra, J. Colmenero. *Relationship between the time-domain Kohlrausch-Williams-Watts and frequency-domain Havriliak-Negami relaxation functions.* Physical Review B **44**, 7306–7312 (1991).

[137] H. Badorreck. *Nichtlineare Optik mit ultrakurzen Laserpulsen: Suszeptibilität dritter Ordnung und kleine Polaronen sowie Interferenz und Holographie verschiedenfarbiger Laserpulse.* Dissertation, Osnabrueck University, 2016.

[138] H. Brüning. *Transiente Gitter auf der Basis kleiner Polaronen in thermisch reduziertem* $LiNbO_3$. Dissertation, Osnabrueck University, 2012.

[139] D. M. Krol, G. Blasse, R. C. Powell. *The influence of the Li/Nb ratio on the luminescence properties of* $LiNbO_3$. The Journal of Chemical Physics **73**, 163–166 (1980).

[140] M. Wiegel, M. H. J. Emond, E. R. Stobbe, G. Blasse. *Luminescence of alkali tantalates and niobates.* Journal of Physics and Chemistry of Solids **55**, 773–778 (1994).

[141] P. Reichenbach, T. Kämpfe, A. Haußmann, A. Thiessen, Th. Woike, R. Steudtner, L. Kocsor, Z. Szaller, L. Kovács, L. Eng. *Polaron-mediated luminescence in lithium niobate and lithium tantalate and its domain ontrast.* Crystals **8**, 214 (2018).

[142] M. V. Ciampolillo, A. Zaltron, M. Bazzan, N. Argiolas, C. Sada. *Quantification of Iron (Fe) in Lithium Niobate by Optical Absorption.* Applied Spectroscopy **65**, 216–220 (2011).

[143] B. Schoke. *Optisch erzeugte kleine Polaronen in Lithiumniobat: Einfluss homo-*

gener und räumlich periodisch modulierter Konzentrationen von intrinsischen und extrinsischen Defekten auf die transiente polaronische Absorption. Dissertation, Osnabrueck University, 2010.

[144] H. G. Festl, P. Hertel, E. Krätzig, R. von Baltz. *Investigations of the Photovoltaic Tensor in Doped $LiNbO_3$.* physica status solidi (b) **113**, 157–164 (1982).

[145] O. Beyer, I. Breunig, F. Kalkum, K. Buse. *Photorefractive effect in iron-doped lithium niobate crystals induced by femtosecond pulses of* $1.5\,\mu m$ *wavelength.* Applied Physics Letters **88**, 051120 (2006).

[146] H.-T. Hsieh, D. Psaltis, O. Beyer, D. Maxein, C. von Korff Schmising, K. Buse, B. Sturman. *Femtosecond holography in lithium niobate crystals.* Optics Letters **30**, 2233 (2005).

[147] B. Sturman, O. Beyer, D. Maxein, K. Buse. *Femtosecond recording and time-resolved readout of spatial gratings in lithium niobate crystals.* Journal of the Optical Society of America B **24**, 419 (2007).

[148] P. Reckenthaeler, D. Maxein, Th. Woike, K. Buse, B. Sturman. *Separation of optical Kerr and free-carrier nonlinear responses with femtosecond light pulses in $LiNbO_3$ crystals.* Physical Review B **76** (2007).

[149] K. Parlinski, Z. Q. Li, Y. Kawazoe. *Ab initio calculations of phonons in $LiNbO_3$.* Physical Review B **61**, 272–278 (2000).

[150] D.P. Kien, J.C. Loulergue, J. Etchepare. *Nonlinear response to polariton waves driven in perovskites by femtosecond pulses.* Optics Communications **101**, 53–59 (1993).

[151] H. J. Bakker, S. Hunsche, H. Kurz. *Investigation of anharmonic lattice vibrations with coherent phonon polaritons.* Physical Review B **50**, 914–920 (1994).

[152] M. Imlau, H. Brüning, K.-M. Voit, J.Tschentscher, S. Dieckhoff, U. Meyer, K. Brune, J. Derksen, C. Tornow. *A method for quality control of a micro-structuring and apparatus therefor.* DE102013220006A1 (April 2, 2015).

[153] M. Imlau, H. Brüning, K.-M. Voit, J. Tschentscher, V. Dieckmann. *Riblet sensor — light scattering on micro structured surface coatings.* arXiv: 1601.04694 (2016).

[154] J. Tschentscher, S. Hochheim, H. Brüning, K. Brune, K.-M. Voit, M. Imlau. *Optical Riblet Sensor: Beam Parameter Requirements for the Probing Laser Source.* Sensors **16**, 458 (2016).

[155] I. Dierking. *Texture of Liquid Crystals.* WILEY-VCH Verlag (2003).

[156] W. González-Viñas. *An Introduction to Materials Science.* Princeton University Press (2004).

[157] P. T. Manoharan, W. C. Hamilton. *The Crystal Structure of Sodium Nitroprusside.* Inorganic Chemistry **2**, 1043–1047 (1963).

[158] Th. Woike, W. Krasser, H. Zöllner, W. Kirchner, S. Haussühl. *Population dy-*

namics of the two light induced metastable states in $Na_2[Fe(CN)_5NO]\cdot 2H_2O$ *single crystals.* Zeitschrift für Physik D Atoms, Molecules and Clusters **25**, 351–356 (1993).

A Publications

A.1 Holographic performance of silicon polymer films based on photoswitchable molecules

- Bjoern Bourdon, Sergej Bock, Christian Kijatkin, Alexandr Shumelyuk, and Mirco Imlau
  Holographic performance of silicon polymer films based on photoswitchable molecules
  Opt. Mater. Express **8**, 1951-1967 (2018); doi: 10.1364/OME.8.001951.

Research Article
Vol. 8, No. 7 | 1 Jul 2018 | OPTICAL MATERIALS EXPRESS 1951
Optical Materials EXPRESS

Holographic performance of silicon polymer films based on photoswitchable molecules

BJOERN BOURDON,[1,2] **SERGEJ BOCK,**[1,3] **CHRISTIAN KIJATKIN,**[1,2] **ALEXANDR SHUMELYUK,**[4] **AND MIRCO IMLAU**[1,2,*]

[1] *Department of Physics, Barbarastrasse 7, Osnabrueck University, D-49076 Osnabrueck, Germany*
[2] *Center for Cellular Nanoanalytics, Barbarastrasse 11, Osnabrueck University, D-49076 Osnabrueck, Germany*
[3] *Faculty of Electrical Engineering and Information Technology, South Westphalia University of Applied Sciences, Haldener Strasse 182, D-58095 Hagen, Germany*
[4] *Institute of Physics, National Academy of Sciences, 03650 Kyiv, Ukraine*
[*] *mirco.imlau@uni-osnabrueck.de*

Abstract: Holographic silicon polymer films based on photoswitchable molecules are studied with respect to their performance for hologram recording, with photoswitchable ruthenium sulfoxide complexes as an example. Our systematic study reveals that it is possible to record elementary holographic lossy gratings with outstanding quality with respect to their dynamics and in- and off-Bragg read-out features. Furthermore, the possibility for the recording of multiple holograms within the same volume element via angular multiplexing as well as the recording with continuous-wave and a fs-laser pulse train is successfully demonstrated. At the same time, a strong limitation of the maximum diffraction efficiency in the order of $\sim 10^{-3}$ is found that cannot be counterbalanced by either the tuning of material (thickness, concentration, ...) or recording parameters (repetition rate, wavelength, ...). This limitation – being severe for any type of holographic applications – is discussed and compared with the performance of high-efficient single-crystalline reference holographic media. We conclude that the potential of sulfoxide compounds may be hidden in holography until it becomes possible to synthesize polymer films with appropriate three-dimensional structural arrangement of the photoswitchable compounds.

OCIS codes: (090.2900) Optical storage materials; (090.7330) Volume gratings; (160.4330) Nonlinear optical materials; (160.5335) Photosensitive materials; (190.4380) Nonlinear optics, four-wave mixing (190.7110) Ultrafast nonlinear optics.

References and links

1. Th. Woike, W. Krasser, P. S. Bechthold, and S. Haussühl, "Extremely Long-Living Metastable State of $Na_2[Fe(CN)_5NO]\cdot 2H_2O$ Single Crystals: Optical Properties," Phys. Rev. Lett. **53**(18), 1767–1770 (1984).
2. Th. Woike, W. Krasser, and S. Haussühl, "Optical switch, especially for information storage and retrieval," U. S. Patent 4713795 (1987).
3. Th. Woike, W. Kirchner, G. Schetter, T. Barthel, K. Hyung-sang, and S. Haussühl, "New information storage elements on the basis of metastable electronic states," Opt. Commun. **106**(1–3), 6–10 (1994).
4. V. Dieckmann, S. Eicke, K. Springfeld, and M. Imlau, "Transition Metal Compounds Towards Holography," Materials. **5**(6), 1155–1175 (2012).
5. L. Cao, Z. Wang, S. Zong, S. Zhang, F. Zhang, and G. Jin, "Volume holographic polymer of photochromic diarylethene for updatable three-dimensional display," J. Polym. Sci. Pol. Phys. **54**(20), 2050–2058 (2016).
6. R. Häussler, Y. Gritsai, E. Zschau, R. Missbach, H. Sahm, M. Stock, and H. Stolle, "Large real-time holographic 3D displays: enabling components and results," Appl. Opt. **56**(13), F45–F52 (2017).
7. J. J. Rack, "Photoinduced molecular switches," U.S. Patent 6433270 (2002).
8. B. A. McClure and J. J. Rack, "Isomerization in Photochromic Ruthenium Sulfoxide Complexes," Eur. J. Inorg. Chem. **2010**(25), 3895–3904 (2010).
9. V. Dieckmann, S. Eicke, J. J. Rack, Th. Woike, and M. Imlau, "Pronounced photosensitivity of molecular $[Ru(bpy)_2(OSO)]^+$ solutions based on two photoinduced linkage isomers," Opt. Express **17**(17), 15052–15060 (2009).
10. V. Dieckmann, K. Springfeld, S. Eicke, M. Imlau, and J. J. Rack, "Thermal stability, photochromic sensitivity and optical properties of $[Ru(bpy)_2(OSOR)]^+$ compounds with R = Bn, BnCl, BnMe," Opt. Express **18**(22), 23495–23503

#330430 https://doi.org/10.1364/OME.8.001951
Journal © 2018 Received 26 Apr 2018; revised 30 May 2018; accepted 31 May 2018; published 26 Jun 2018

(2010).

11. K. Springfeld, V. Dieckmann, and M. Imlau, “High-contrast, high-resolution photochromic silicone polymer based on photoswitchable $[Ru(bpy)_2OSO]PF_6$ building blocks,” Photonics Res. **1**(4), 197–201 (2013).
12. V. Dieckmann, “Lichtinduzierte Isomerisierung in Sulfoxid- und Nitrosyl-Komplexen: Photosensitivität und Modifikation,” Ph.D. thesis, Osnabrueck University, Osnabrueck, Germany (2010).
13. K. Springfeld, “Photoschaltbare Koordinationskomplexe: Festkörpereinbettung und Schwingungsspektroskopie mit MIR-Femtosekundenpulsen,” Ph.D. thesis, Osnabrueck University, Osnabrueck, Germany (2013).
14. M. Y. Livshits and J. J. Rack, “Photorefraction from a Photochromic Soft Material,” J. Phys. Chem. C **120**(46), 26459–26464 (2016).
15. M. Imlau, S. Haussühl, Th. Woike, R. Schieder, V. Angelov, R. A. Rupp, and K. Schwarz, “Holographic recording by excitation of metastable electronic states in $Na_2[Fe(CN)_5NO]{\cdot}2H_2O$: a new photorefractive effect,” Appl. Phys. B **68**(5), 877–885 (1999).
16. E. N. Leith, A. Kozma, J. Upatnieks, J. Marks, and N. Massey, “Holographic Data Storage in Three-Dimensional Media,” Appl. Opt. **5**(8), 1303–1311 (1966).
17. D. L. Staebler, W. J. Burke, W. Phillips, and J. J. Amodei, “Multiple storage and erasure of fixed holograms in Fe-doped $LiNbO_3$,” Appl. Phys. Lett. **26**(4), 182–184 (1975).
18. M. Imlau, Th. Woike, R. Schieder, and R. A. Rupp, “Holographic recording with orthogonally polarized waves in centrosymmetric $Na_2[Fe(CN)_5NO]{\cdot}2H_2O$,” EPL **53**(4), 471–477 (2001).
19. K.-M. Voit and M. Imlau, “Holographic Spectroscopy: Wavelength-Dependent Analysis of Photosensitive Materials by Means of Holographic Techniques,” Materials. **6**(1), 334–358 (2013).
20. B. A. McClure, N. V. Mockus, D. P. Butcher, D. A. Lutterman, C. Turro, J. L. Petersen, and J. J. Rack, “Photochromic Ruthenium Sulfoxide Complexes: Evidence for Isomerization Through a Conical Intersection,” Inorg. Chem. **48**(17), 8084–8091 (2009).
21. D. P. Butcher, A. A. Rachford, J. L. Petersen, and J. J. Rack, “Phototriggered S → O Isomerization of a Ruthenium-Bound Chelating Sulfoxide,” Inorg. Chem. **45**(23), 9178–9180 (2006).
22. N. V. Mockus, D. Rabinovich, J. L. Petersen, and J. J. Rack, “Femtosecond Isomerization in a Photochromic Molecular Switch,” Angew. Chem. Int. Ed. **47**(8), 1458–1461 (2008).
23. B. A. McClure and J. J. Rack, “Ultrafast Spectroscopy of a Photochromic Ruthenium Sulfoxide Complex,” Inorg. Chem. **50**(16), 7586–7590 (2011).
24. T. A. Grusenmeyer, B. A. McClure, C. J. Ziegler, and J. J. Rack, “Solvent Effects on Isomerization in a Ruthenium Sulfoxide Complex,” Inorg. Chem. **49**(10), 4466–4470 (2010).
25. H. Kogelnik, “Coupled wave theory for thick hologram gratings,” Bell Syst. Tech. J. **48**(9), 2909–2947 (1969).
26. M. Fally, M. Imlau, R. A. Rupp, M. A. Ellabban, and Th. Woike, “Specific Recording Kinetics as a General Property of Unconventional Photorefractive Media,” Phys. Rev. Lett. **93**(24), 243903 (2004).
27. G. Borrmann, “Die Absorption von Röntgenstrahlen im Fall der Interferenz,” Z. Phys. **127**(4), 297–323 (1950).
28. S. Eicke, “Populations- und Relaxationskinetiken laserangeregter photofunktionaler Ruthenium-Sulfoxid-Komnplexe in hochkonzentrierten Lösungen,” Ph.D. thesis, Osnabrueck University, Osnabrueck, Germany (2012).
29. S. Eicke, V. Dieckmann, A. Kruse, K.-M. Voit, M. Imlau, and L. Walder, “Dynamics of the light-induced absorption in photochromic $[Ru(bpy)_2(OSO)]^+$,” J. Spectrosc. Dyn. **4**, 6 (2014).
30. P.-A. Blanche, A. Bablumian, R. Voorakaranam, C. Christenson, W. Lin, T. Gu, D. Flores, P. Wang, W.-Y. Hsieh, M. Kathaperumal, B. Rachwal, O. Siddiqui, J. Thomas, R. A. Norwood, M. Yamamoto, and N. Peyghambarian, “Holographic three-dimensional telepresence using large-area photorefractive polymer,” Nature. **468**(7320), 80–83 (2010).
31. N. Ishii, T. Kato, and J. Abe, “A real-time dynamic holographic material using a fast photochromic molecule,” Sci. Rep. **2**, 819 (2012).
32. H. J. Coufal, D. Psaltis, and G. T. Sincerbox, eds., *Holographic Data Storage*, Springer Series in Optical Sciences (Springer-Verlag, Berlin Heidelberg, 2000).
33. M. Imlau, T. Bieringer, S.G. Odoulov, and Th. Woike, “Holographic Data Storage,” in *Nanoelectronics and Information Technology: Advanced Electronic Materials and Novel Devices*, R. Waser, ed. (Wiley-VCH, Weinheim, 2012), 3rd ed., pp. 725–750
34. M. Imlau, R. Schieder, R. A. Rupp, and Th. Woike, “Anisotropic holographic scattering in centrosymmetric sodium nitroprusside,” Appl. Phys. Lett. **75**(1), 16–18 (1999).
35. M. A. Ellabban, M. Fally, M. Imlau, Th. Woike, R. A. Rupp, and T. Granzow, “Angular and wavelength selectivity of parasitic holograms in cerium doped strontium barium niobate,” J. Appl. Phys. **96**(12), 6987–6993 (2004).
36. H. Brüning, V. Dieckmann, B. Schoke, K.-M. Voit, M. Imlau, G. Corradi, and C. Merschjann, “Small-polaron based holograms in $LiNbO_3$ in the visible spectrum,” Opt. Express **20**(12), 13326–13336 (2012).
37. M. Goulkov, D. Schaniel, and Th. Woike, “Pulse recording of thermal and linkage isomer gratings in nitrosyl compounds,” J. Opt. Soc. Am. B **27**(5), 927–932 (2010).
38. P. T. Manoharan and W. C. Hamilton, “The Crystal Structure of Sodium Nitroprusside,” Inorg. Chem. **2**(5), 1043–1047 (1963).
39. Th. Woike, S. Haussühl, B. Sugg, R. A. Rupp, J. Beckers, M. Imlau, and R. Schieder, “Phase gratings in the visible and near-infrared spectral range realized by metastable electronic states in $Na_2[Fe(CN)_5NO]{\cdot}2H_2O$,” Appl. Phys. B **63**(3), 243–248 (1996).

1. Introduction

The approach to use photoswitchable molecular compounds as photofunctional building blocks in holographic materials goes back to the original proposal of Woike et al. [1–3]. The molecular level potentially enables a number of important features within the same material: (i) a high tuning ability of the spectral sensitivity due to targeted substitution of ligands and/or central atoms, (ii) the possibility for enabling a reversible write-read-erase cycle, (iii) a ultra-high (holographic) spatial resolution down to the molecular level, (iv) a cheap and quick synthesis on (v) a large scale, (vi) a good mechanical flexibility, (vii) the possibility for tailored dimensioning, (viii) the possibility for adapting the optical density via concentration optimization, and (ix) the possibility to record with either continuous wave (cw) or fs-laser light pulses [4].

Current potential applications include three-dimensional real-time displays [5, 6] either with large scale or as integrated head-on display. Still, however, holographic media based on photoswitchable compounds are not available commercially. The reasons are manifold and include large costs for laborious molecular crystal growth, large optical damping by fundamental absorption, toxicity, and/or the requirement for liquid-nitrogen temperatures [4].

The photoswitchable compounds of the sulfoxide family here are very promising candidates to overcome the majority of these limitations [7,8]. Our previous reports have already addressed the unique features of photofunctionality at room temperature [9, 10]. Furthermore, we were able to demonstrate the possibility for embedding ruthenium sulfoxides compounds in a polymer matrix with conserved photochromic response [4]. Based on these pre-investigations, the ability to record elementary gratings with promising features for consumer-market holographic applications was proposed [11]. First inspection of the underlying mechanisms are interpreted as index gratings as a result of a causal connection between absorption and index change via Kramers-Kronig relation [4, 12–14]. The question about a dominating role of refractive index changes based on pronounced changes of the molecular polarization by means of light-induced structural alterations, as it has been verified for the photoswitchable sodium nitroprusside $Na_2[Fe(CN)_5NO]\cdot 2H_2O$ (abbr. SNP) [15], has never been addressed so far.

In this contribution, we focus on the investigation of two sulfoxide representatives embedded into the matrix-like polymer polydimethylsiloxane (abbr. PDMS) [4, 11, 13] by means of established holographic analyzing methods [15]: $[Ru(bpy)_2(OSO)]^+$ (abbr. OSO), where bpy is 2,2'-bipyridine, and the $[Ru(bpy)(biq)(OSO)]^+$ complex (abbr. BIQ), where biq is 2,2'-biquinoline and OSO is 2-methylsulfinylbenzoate. By recording up to four elementary gratings within the sample at room temperature, the isomerization of ruthenium sulfoxides from an applied point of view is analyzed. Special attention is given to the measurement of the kinetics of the diffraction efficiency under in- as well as off-Bragg conditions. For the first time, the multiplexed recording of holograms within the same PDMS volume element by means of in-plane angular multiplexing [16, 17] is demonstrated. Furthermore, pioneering results acquired via exposure to a femtosecond-laser pulse train are shown. While these features point to an outstanding performance of OSO-PDMS and BIQ-PDMS polymer films, a severe limitation of the diffraction efficiency of not more than $\sim 10^{-3}$ is found independent on the experimental conditions.

We discuss these findings in direct comparison with SNP as a single-crystalline reference system, that reveals a similar photofunctionality: Two metastable states $MS_{1,2}$ can be (i) populated in the blue-green spectral range and are (ii) reversibly switched to the ground state with red and near-infrared light. Grating recording has been successfully demonstrated in SNP under illumination with laser light in the blue-green spectral range and at temperatures below 200 K. It is attributed to light-induced structural alterations of the photoadressable N-O-bond which results in large absorption and refraction index changes in the order of $\Delta\alpha \sim 10^3\ m^{-1}$ and $\delta n \sim 10^{-2}$, respectively, and diffraction efficiencies of up to unity [15, 18]. Due to the spectral sensitivity which enables write-read-erase cycles and the possibility to write multiple holograms within the same volume (multiplexing) [15], SNP was analyzed in the context of holographic data storage

Research Article Vol. 8, No. 7 | 1 Jul 2018 | OPTICAL MATERIALS EXPRESS 1954

Optical Materials EXPRESS

already proposed by Woike et al. in 1984 [1–3]. From the direct comparison of the holographic performance of ruthenium sulfoxide compounds with SNP, it can be concluded that the missing crystallographic order of OSO- and BIQ-compounds within the PDMS matrix is decisive for the lack of a pronounced change of the refractive index, i.e. for a diffraction efficiency that is sufficient for holographic applications.

2. Experimental methods

2.1. Film samples

Photochromic, non-toxic OSO-PDMS and BIQ-PDMS silicon polymers were synthesized according to the procedure introduced by Springfeld et al. [11]. The procedure is adopted for medium-scale film synthesis ($> 15\,\mathrm{cm}^2$) with sulfoxide concentrations in a broad range between $c = (0.01 - 0.97)\,\mathrm{mM}$ (OSO-PDMS) and up to $c = (1.86 \pm 0.03)\,\mathrm{mM}$ for BIQ-PDMS. We succeeded in the preparation of films of high optical quality even for large thicknesses between 1 and 3 mm. For the purpose of our systematic investigation, the films were cut into stripes of dimensions 80 mm × 20 mm. Figure 1 shows a photograph of a typical OSO-PDMS sample with a concentration $c = (0.97 \pm 0.03)\,\mathrm{mM}$ and thickness $d = (2.2 \pm 0.1)\,\mathrm{mm}$ as an example. All films exhibit an orange/yellow, translucent color and show a moderate number of surface inclusions (cf. also Ref. [4, 11]).

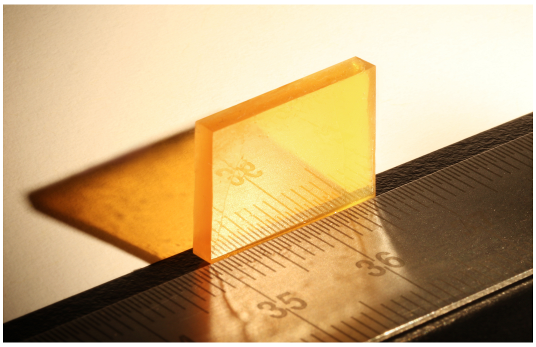

Fig. 1. Photograph of a typical as-prepared OSO-PDMS film sample ($c = (0.97 \pm 0.03)\,\mathrm{mM}$ and thickness $d = (2.2 \pm 0.1)\,\mathrm{mm}$). The bulky stripe of dimension 17 mm ×13 mm exhibits an orange/yellow, translucent color and shows a moderate number of surface inclusions.

Figure 2 shows the ground state absorption spectra (black lines) of the a) OSO-PDMS and b) BIQ-PDMS samples as used in the experiments of our study. The measurements were performed in relation to a nominally pure PDMS sample of same thickness in the reference path of a two-beam photospectrometer (Shimadzu Scientific Instruments, *UV-3600*).

2.2. Setup for cw-investigations

A self-made two-beam interferometer, schematically depicted in Fig. 3, is applied for the investigation of the as-prepared OSO-silicon polymer films (cf. our technical paper of Ref. [19] for a detailed description). The interferometer is designed for the recording of unslanted elementary holographic gratings with an external Bragg angle of $\Theta_B^{\mathrm{ext}} = (4.9 \pm 0.2)\,^\circ$. Collimated, linearly polarized beams at a measured center wavelength of $\lambda_{\mathrm{record}} = (406.6 \pm 0.8)\,\mathrm{nm}$ of a nitride-based semiconductor laser diode (s-polarization; type: *iPulse-405-S* from TOPTICA Photonics AG) were used according to the absorption spectrum of the OSO-complex in the ground state (Fig. 2a), and [9, 11, 20]). Careful adjustment of the optical beam paths ensured

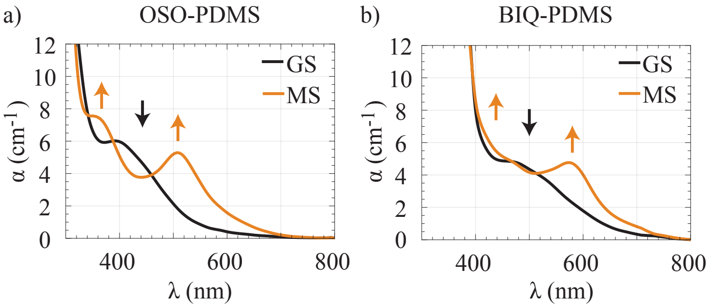

Fig. 2. a) Absorption spectrum of the ground state (GS, black) and metastable state (MS, orange) for OSO embedded in PDMS, concentration $c = (0.36 \pm 0.03)$ mM and thickness $d = (2.1 \pm 0.1)$ mm. b) Absorption spectrum of the ground state (GS, black) and metastable states (MS, orange) for BIQ embedded in PDMS, concentration $c = (1.86 \pm 0.03)$ mM and thickness $d = (1.3 \pm 0.1)$ mm. Orange and black arrows indicate an increase and decrease of the absorption coefficient with respect to the ground state absorption, respectively.

a high-contrast fringe pattern (modulation depth $m = 2\sqrt{I^R \times I^S}/(I^R + I^S) \approx 0.88$ at a total intensity of $I^R + I^S = (19.6 \pm 0.2)\,\mathrm{mW/cm^2}$, where I^R and I^S are the intensities of the reference and signal beams, respectively).

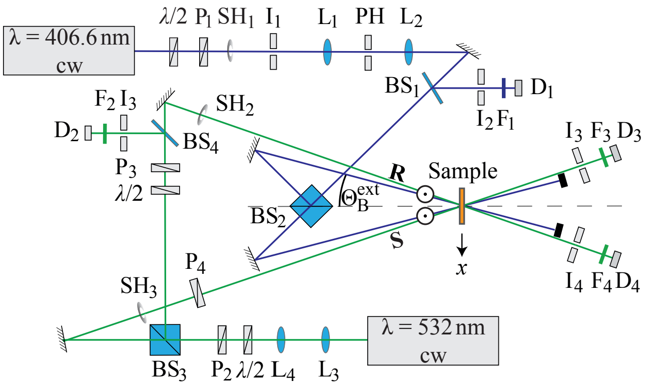

Fig. 3. Experimental setup of our self-made two-beam interferometer. $\mathrm{SH}_{1\ldots3}$: shutters, PH: pinhole, $\mathrm{I}_{1\ldots4}$: iris diaphragm, $\mathrm{BS}_{1\ldots4}$: beam splitters, $\mathrm{D}_{1\ldots4}$: diodes, $\mathrm{L}_{1\ldots4}$: lenses, $\mathrm{P}_{1\ldots4}$: polarizers, $\lambda/2$: half-wave plate, $\mathrm{F}_{1\ldots4}$: single line filters, R,S: reference and signal beams. The half angle between the two recording beams at $\lambda_{\mathrm{record}} = (406.6 \pm 0.8)$ nm is adjusted to $\Theta_B^{\mathrm{ext}} = (4.9 \pm 0.2)^\circ$ that accords with a read-out angle $\Theta^{\mathrm{ext}} \approx 6.4^\circ$ at $\lambda_{\mathrm{read}} = 532$ nm.

In bright regions, the ultraviolet exposure triggers a Ru d$\pi \longrightarrow$ bpy π^* metal-to-ligand-charge-transfer (MLCT) into an S-bonded excited state of the Ru-S-O bond [20–23]. This excited state may relax vibrationally to one of the two O-bonded (Ru-O-S bond) metastable states (MS_1 or MS_2) as schematically depicted in Fig. 4a) (yellow-shaded box). In total, the rise time for the formation of MS_1 or MS_2 upon an incident pump pulse is found below 200 ps [20, 23].

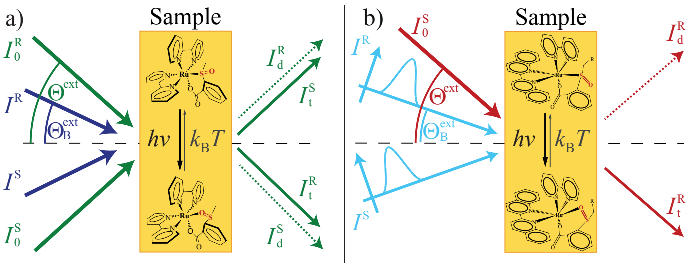

Fig. 4. a) Principal sketch of the incident recording and read-out beam paths with cw-laser light. All intensities were measured with Si-PIN diodes. Furthermore, the light-induced structural changes inside the OSO-complex upon UV/blue light exposure, i.e. the change from a Ru-S-O to a Ru-O-S bond according to Ref. [23], is schematically shown. b) Equivalent principal sketch for fs-pulse recording in BIQ-PDMS polymer films [24].

This photochemical process together with the spatially inhomogeneous exposure results in the appearance of a spatial modulation of the concentration densities $c_{MS_1}(x)$, $c_{MS_2}(x)$. We use in- and off-Bragg-matched read-out in two principle directions both symmetrical with respect to the sample's normal. A continuous-wave laser (frequency-doubled Nd:YAG laser at $\lambda_{read} = 532$ nm, *s*-polarization, type: *Compass 215M-75* from Coherent, Inc.) is applied to probe the temporal evolution $c_{MS_1,MS_2}(x,t)$ via diffraction ($\Theta^{ext} \approx 6.4°$ at 532 nm). According to the models introduced by Imlau et al. [15] and Dieckmann et al. [4], the diffraction process may be attributed to the interaction of the probe beam with either a spatial modulation of density and/or a transmission loss. We note that $MS_{1,2}$ feature a localized alteration of both the atomic and electronic structure. The related broad-band absorption in the visible spectral range [20] (see also absorption spectra of the metastable states in Fig. 2) may be applied for the recording of a spatial modulation of the absorption coefficient, that will appear in-phase with the incident light intensity pattern [4].

The diffraction efficiency $\eta^{R,S} = I_d^{R,S}/I_0^{R,S}$ is applied as key measure in our experimental study [25]. Here, $I_{0,d}^{R,S}$ describe the intensities of incident (0) and first-order diffracted (d) beams, respectively, as depicted in Fig. 4(a)). An influence of the read-out process on the hologram dynamics is suppressed due to small read-out intensities ($I_0^{R,S} = (0.11 \pm 0.01)\,\mathrm{mW/cm^2} \ll I^{R,S}$). Angular-dependent read-out of the diffraction efficiency $\eta(\Delta\Theta^{ext}) = \eta(\Theta^{ext} - \Theta_B^{ext})$ is realized by a high-precision, motorized rotation stage (Newport, type *URM80CC*) at a constant rotation velocity of 0.005°/s. If used for angular multiplexing, the velocity is increased to ≈ 0.01°/s in order to reduce the impact of thermal self-decay of the recorded grating and any influence of the read-out laser.

A similar two-beam interferometer is applied for the study of the film performance under repetitive fs-pulse exposure ($\tau_p \approx 100$ fs, $f_{rep} = 100$ Hz) as schematically depicted in Fig. 5.

Fs-pulses were generated with a standard optical parametric amplifier being pumped by a regeneratively amplified, mode locked Ti:Sapphire laser (*Libra-F HE* and *OPerA Solo*, Coherent, Inc.). It enables adjusting the OPA center wavelength ($\lambda_{record} = 488$ nm) close to the maximum MLCT absorption feature of polymer films with embedded BIQ-molecules (Fig. 2(b)), and [24]) that were used with this setup. The respective photochemical reaction is sketched in Fig. 4(b) (cf. yellow-shaded box). Figure 4(b) also shows a principal sketch of the paths of incident recording pulses and cw-read-out beam with *s*−polarization, a modulation depth close to unity ($m \approx 1$), an average intensity $\overline{I} = (20.6 \pm 2.2)\,\mathrm{W/cm^2}$ ($\equiv$ peak intensity $I_0 = (3.9 \pm 0.6)\,\mathrm{TW/cm^2}$), and an intersection angle of $\Theta_B^{ext} = (6.8 \pm 0.2)°$. A continuous-wave He-Ne-laser served for

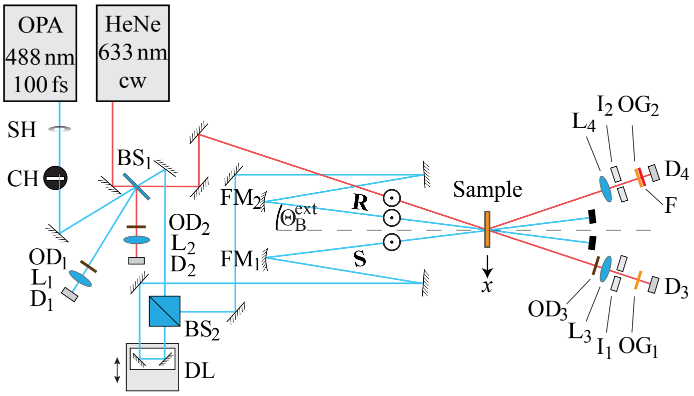

Fig. 5. Experimental setup for repetitive fs-pulse recording in BIQ-PDMS film samples. SH: shutter, CH: chopper (f_{rep} = 100 Hz), $\mathrm{FM}_{1,2}$: focusing mirrors (f_{focus} = 500 mm), $\mathrm{BS}_{1,2}$: beam splitters, $\mathrm{I}_{1,2}$: iris diaphragm, $\mathrm{D}_{1...4}$: diodes, $\mathrm{OD}_{1...3}$: optical density filters, $\mathrm{OG}_{1,2}$: orange glasses, F_1: single line filter, $\mathrm{L}_{1...4}$: lenses, DL: delay line, R,S: reference and signal beams. The half angle between the two recording beams at $\lambda_{\mathrm{record}}$ = 488 nm is adjusted to $\Theta_{\mathrm{B}}^{\mathrm{ext}} = (6.8 \pm 0.2)^\circ$ that accords with a read-out angle $\Theta^{\mathrm{ext}} \approx 8.8^\circ$ at λ_{read} = 632.8 nm.

Bragg-matched hologram read-out (λ_{read} = 632.8 nm, $\Theta^{\mathrm{ext}} \approx 8.8^\circ$). Here, an average probe intensity of $I_0 = (350 \pm 30)\,\mathrm{mW/cm^2}$ is used to minimize the probe-beam influence on the recording process.

3. Experimental results

3.1. In-Bragg read-out: cw-recording

Figure 6(a) shows the diffraction efficiency as a function of exposure $Q = (I_{\mathrm{R}} + I_{\mathrm{S}}) \times t$, i.e. the product of total recording intensity $I_{\mathrm{R}} + I_{\mathrm{S}}$ and time t, for the case of hologram recording with cw-laser light at 405 nm in OSO-PDMS films (c = (0.36 ± 0.03) mM) as an example.

The first-order diffraction efficiency shows a quadratic increase in the beginning of exposure ($Q < 0.2\,\mathrm{J/cm^2}$). It passes a maximum value of $\eta^{\mathrm{R}}_{\mathrm{max}} = (2.75 \pm 0.64) \times 10^{-4}$ at an exposure of $Q^{\mathrm{R}}_{\mathrm{max}} = (0.91 \pm 0.06)\,\mathrm{J/cm^2}$. Further exposure results in a monotonous decrease of the diffraction efficiency. The diffraction process disappears completely at exposures $> 10\,\mathrm{J/cm^2}$. This behavior is comparable with the earlier findings in photoswitchable SNP crystals [15]. SNP also features a light-induced linkage isomerism related with the Fe-N-O-bond and two metastable states $\mathrm{MS_1}$, $\mathrm{MS_2}$ (Fe-O-N bond for $\mathrm{MS_1}$ and a side-on-configuration of O-N with respect to Fe for $\mathrm{MS_2}$) and the possibility for hologram recording. The dynamics in SNP (and further materials featuring reversible ground/metastable state optical systems) were explained considering the temporal evolution of the spatial concentration density [26]. We thus have applied the according generalized function

$$\eta(Q) = A \times I_1\,[m(Q - \delta Q)/Q_0]^2 \times \exp\,[-2(Q - \delta Q)/Q_0] \tag{1}$$

as fitting function for our experimental data. Here, $I_1(x)$ represents the modified Bessel function of the first kind and order as a function of x and δQ is an offset in exposure. The result of the fitting procedure is shown as solid line in Fig. 6a). A very large agreement between data and fit

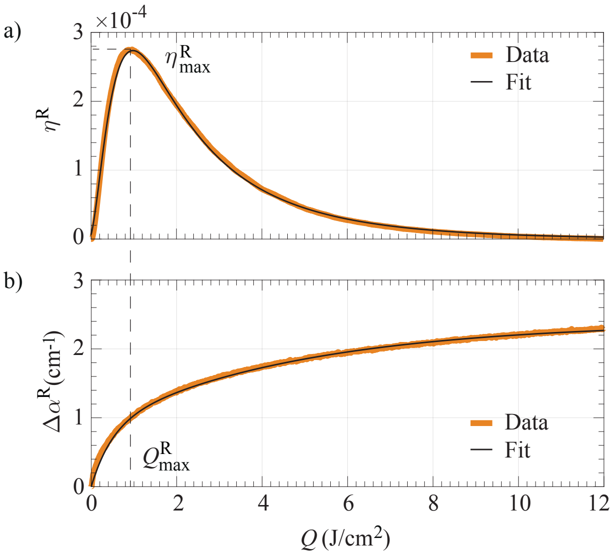

Fig. 6. **a)** Diffraction efficiency η^{R} (orange) as a function of exposure Q measured with a (0.36 ± 0.03) mM OSO-PDMS polymer film with a film thickness $d = (2.1 \pm 0.1)$ mm, and a fit (black) according to Eq. (1). A maximum value of $\eta^{R}_{max} = (2.75 \pm 0.64) \times 10^{-4}$ is reached at an exposure of $Q^{R}_{max} = (0.91 \pm 0.06)$ J/cm^2. **b)** Light-induced change of the absorption coefficient $\Delta\alpha^{R}$ (orange) as a function of exposure Q, and a fit (black) according to the two-fold exponential function of Eq. (2) with characteristic exposures $Q_1 = (4.74 \pm 0.29)$ J/cm^2 and $Q_2 = (0.49 \pm 0.11)$ J/cm^2, respectively.

could be obtained with the amplitude A set to $(7.94 \pm 0.79) \times 10^{-3}$, $Q_0 = (0.77 \pm 0.08)$ J/cm^2, $\delta Q = (0.05 \pm 0.01)$ J/cm^2, and $m = (0.89 \pm 0.03)$. We note that $\eta^{R,S}(Q)$ were both detected during the hologram recording process. The analysis of the temporal dynamics $\eta^{S}(Q)$ yields similar values for Q_0, δQ, and m within the error margin of 10 %. Indications for the presence of the Borrmann effect were not found [27].

The sum of the intensities of zero and first order diffracted beams $I_{\sum} = I_t + I_d$ is used to simultaneously inspect the temporal evolution of the absorption change $\Delta\alpha(Q)$ by means of the Beer-Lambert law: $\Delta\alpha(Q) = -1/d \ln\left(I_{\sum}(Q)/I_{\sum}(Q = 0)\right)$, as it is shown in Fig. 6(b). Our data set resembles the exponential growth reported for OSO-compound solvents in the work of Springfeld et al. [11] and Eicke et al. [28, 29]. A saturation value of $\Delta\alpha \approx 2.4\,\mathrm{cm}^{-1}$ is reached at the end of exposure. The dynamics are best described by the sum of two exponential functions:

$$\alpha_{fit} = \alpha_0 + A_1 \exp(-Q/Q_1) + A_2 \exp(-Q/Q_2) \tag{2}$$

with $\alpha_0 = |A_1 + A_2|$ being the maximum change in absorption expected for $Q \to \infty$, and characteristic absorption and exposure $A_{1,2}$ and $Q_{1,2}$, respectively. This two-fold exponential function was originally introduced by Eicke et al. in order to take into account the significantly different lifetimes of the two O-bonded isomers MS$_1$, MS$_2$ at room temperatures [28, 29]: $\tau_1 \approx 1.6 \times 10^3$ s and $\tau_2 \approx 3.5 \times 10^4$ s [9]. Here, the outcome of the fitting procedure yields characteristic exposures of $Q_1 = (4.74 \pm 0.29)$ J/cm^2 and $Q_2 = (0.49 \pm 0.11)$ J/cm^2, i.e. a ratio $Q_1/Q_2 \approx 10$ ($A_1/A_2 \approx 1.8$, $A_1 = (-1.54 \pm 0.04)\,\mathrm{cm}^{-1}$, $A_2 = (-0.85 \pm 0.02)\,\mathrm{cm}^{-1}$).

We have repeated this type of measurements for OSO-PDMS samples with different OSO concentrations, while all other experimental parameters were kept largely identical (thickness $\bar{d} = (1.9 \pm 0.4)\,\mathrm{mm}$). Figure 7 shows the maximum obtained diffraction efficiency $\eta^{\mathrm{R}}_{\mathrm{max}}$ as a function of concentration c in the range up to about 1 mM. Throughout the investigated span, a monotonous growth of $\eta^{\mathrm{R}}_{\mathrm{max}}$ as a function of concentration becomes obvious. In particular, it turns out that it becomes possible to tune the maximum efficiency up to a factor of about three by concentration management.

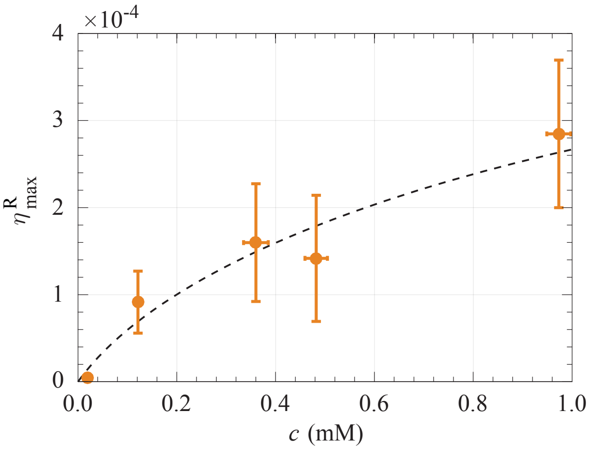

Fig. 7. Dependence of the maximum value of the diffraction efficiency $\eta^{\mathrm{R}}_{\mathrm{max}}$ as a function of OSO-concentration c in OSO-PDMS polymer films ($\bar{d} = (1.9 \pm 0.4)\,\mathrm{mm}$). An increase of $\eta^{\mathrm{R}}_{\mathrm{max}}(c)$ up to its threefold value is obvious. The dashed black line serves as a guide to the eye.

3.2. Off-Bragg read-out

Figure 8 shows the diffraction efficiency as a function of angular detuning $\Delta\Theta^{\mathrm{ext}}$ with respect to Bragg-incidence. The holographic grating under inspection has been recorded up to an efficiency of $\eta^{\mathrm{S}} = (1.21 \pm 0.23) \times 10^{-4}$ ($Q = (0.85 \pm 0.11)\,\mathrm{J/cm^2}$). The data set, often referred to as *rocking curve*, resembles the expected shape of a $\mathrm{sinc}^2(\Delta\Theta^{\mathrm{ext}})$ function. It shows a clear break-down of the diffraction efficiency for slight angular mismatches already in the order of 1/10 degree (Full width at half maximum, FWHM = $(0.18 \pm 0.01)^\circ$). Remarkably, secondary and tertiary maxima can be resolved as well. The determined maximum value $\eta^{\mathrm{S}}_{\mathrm{max}}(\Delta\Theta^{\mathrm{ext}})$ slightly exceeds the value that was determined at the end of the grating recording process (η^{S}) by $\sim$ 15%. This may be attributed to the limitations in the experimental adjustment of the Bragg angle for read-out of about 0.1° that are in the order of magnitude of the FWHM of the grating's angular sharpness.

Nevertheless, the high quality of the experimental data set enables a fitting procedure using the original function $\eta(z, \Theta)$ as derived in Ref. [19] for lossy absorption gratings in accordance with Kogelnik's coupled wave theory [25]:

$$\eta(z,\Theta) = A_{\mathrm{LB}}(\Theta)\epsilon_1''(\lambda)^2 \frac{\left|\sinh\left(\frac{\left\{\epsilon_1''(\lambda)^2 - \left[2\beta(|\Theta|)\cos(\Theta)\epsilon_0'(\lambda)\right]^2\right\}^{1/2} k_0 z}{4\left[\epsilon_0'(\lambda)\right]^{1/2}\cos(\Theta)}\right)\right|^2}{\left|\left[2\beta(|\Theta|)\cos(\Theta)\epsilon_0'(\lambda)\right]^2 - \left[\epsilon_1''(\lambda)\right]^2\right|} \qquad (3)$$

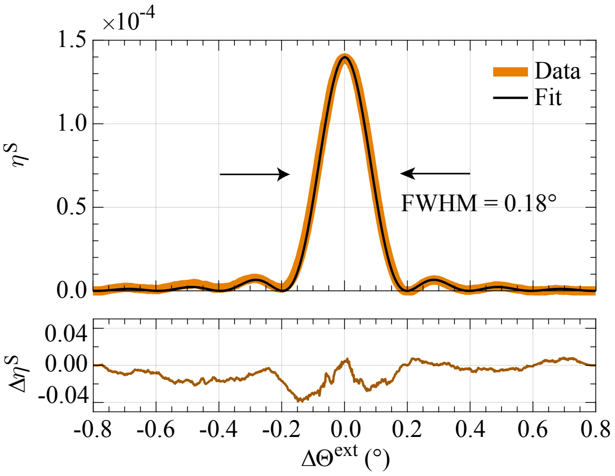

Fig. 8. Rocking curve as a function of deviation from the external Bragg angle $\Theta_B^{\text{ext}} = (6.4 \pm 0.2)°$ for a (1.1 ± 0.1) mm thick (0.36 ± 0.03) mM OSO-PDMS sample after an exposure $Q = (0.85 \pm 0.11)\,\mathrm{J/cm^2}$ at $\lambda = (406.6 \pm 0.8)$ nm. The black line corresponds to the result of fitting Eq. (3) to the data set. Absolute deviations $\Delta\eta^S$ between data set and fitting result are shown below (identical decimal power).

with the abbreviations $A_{\mathrm{LB}}(\Theta) = \exp\left[-\bar{\alpha} z/\cos(\Theta)\right]$ and $\beta(\Theta) = 2\sin(\Theta_B)^2/\cos(\Theta) - 2\sin(\Theta_B)\tan(\Theta)$. Here, z denotes the hologram thickness, Θ is the internally measured read-out angle with respect to the internal Bragg angle Θ_B, and $\bar{\alpha} = (\alpha_{\mathrm{GS}} + \alpha_{\mathrm{MS}})/2$ is the average absorption coefficient calculated from ground (GS) and metastable state (MS) absorption. The amplitude of the real permittivity grating is defined through $\epsilon_1''(\lambda) = \alpha_1 n_0/k_0$, where $\alpha_1 = (\alpha_{\mathrm{MS}} - \alpha_{\mathrm{GS}})/2$ is the modulation amplitude of the absorption coefficient, $\epsilon_0'(\lambda) = n_0^2$ is the average real permittivity or squared refractive index as a function of the wavelength, $k_0 = 2\pi/\lambda$ with λ the read-out wavelength. We note that the presence of a lossy absorption grating is well justified by the experimentally determined pronounced change of the absorption coefficient as a function of light exposure, as depicted in Fig. 6.

The result of the fitting procedure is depicted in Fig. 8 by the solid black line. A very good agreement between fit and data set is obtained for a hologram thickness $z = (690 \pm 10)\,\mu$m and the fitting parameters summarized in Table 1.

Table 1. Parameters obtained from fitting the theoretical function of a rocking curve for the case of a lossy grating (Eq. (3)) to the experimental data set (cf. black line in Fig. 8).

fitting parameters	
fixed	open
$\lambda = 532$ nm	$n_0 = (1.35 \pm 0.05)$
$\alpha_{\mathrm{GS}} = (1.17 \pm 0.05)\,\mathrm{cm^{-1}}$	$\Theta_B = (4.73 \pm 0.35)\,°$
$\alpha_{\mathrm{MS}} = (2.63 \pm 0.05)\,\mathrm{cm^{-1}}$	$z = (690 \pm 10)\,\mu$m

3.3. Angular multiplexing

The previous section reveals the angular dependence of the diffraction efficiency for one hologram written into the OSO-PDMS-sample. In a next step, taking into account the FWHM, several holograms can be written within the same volume without any crosstalk between the gratings. This technique is called angular multiplexing and is crucial for evaluating the suitability of materials towards high information storage densities and therefore mass data storage applications.

Figure 9 shows the result of angular read-out after the recording of four individual volume holograms within (nearly) the same volume element of an OSO-PDMS film (concentration $c = (0.36 \pm 0.03)$ mM, thickness $d = (2.1 \pm 0.1)$ mm) by means of in-plane angular multiplexing [16, 17]. Recording of each holographic grating within the sequence #1...#4 was performed analogously to the scheme presented in the previous section. Here, an exposure of up to $Q = (1.2 \pm 0.2)$ J/cm^2 was used for a single hologram. At the end of each recording process, the film was rotated in the dark by predefined angular steps of 1.0°, i.e. by an angle far exceeding the FWHM of a single grating (cf. Fig. 8). Diffraction of the recording beams at previously recorded gratings therefore was suppressed. After the recording of all four holograms within the same volume element, the data set of Fig. 9 was obtained by read-out with the probe beam I_0^R ($\lambda = 532$ nm) during film rotation at constant velocity (0.01°/s) over the angular range from -1° to +4°. The diffracted signals appear with clear angular separation of about 1° and without the appearance of mutual interaction or of ghost images. The first hologram features a maximum diffraction efficiency of $\eta^R_{\max} = (1.97 \pm 0.38) \times 10^{-5}$ that is reduced by about 25% with increasing hologram number.

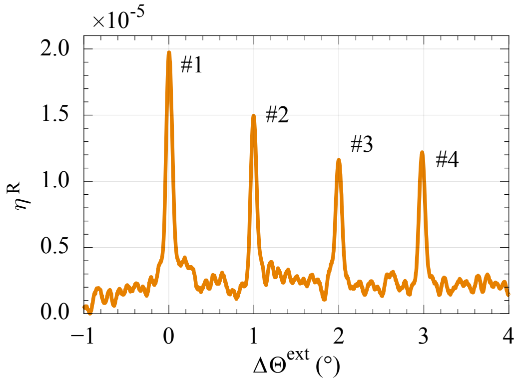

Fig. 9. Four holographic gratings have been written into a (0.36 ± 0.03) mM OSO-PDMS sample with a thickness $d = (2.1 \pm 0.1)$ mm and with a mutual angular mismatch of 1° in the sequence #1...#4. Recording for each hologram was stopped at an exposure of $Q = (1.2 \pm 0.2)$ J/cm^2. At the end of the entire recording scheme, read-out was performed with the probe beam I_0^R ($\lambda = 532$ nm) during film rotation at constant velocity (0.01°/s) over the angular range from -1° to +4°.

3.4. In-Bragg read-out: fs-pulse recording

Figure 10 shows the result for hologram recording in BIQ-PDMS polymer films using repetitive fs-pulse exposure ($f_{\mathrm{rep}} = 100$ Hz). The diffraction efficiency is shown as a function of average exposure $\overline{Q}$ that here is determined by the product of average intensity $\overline{I}$ and time t. The data set was obtained with a BIQ-PDMS film at a recording wavelength $\lambda_{\mathrm{record}} = 488$ nm. A Bragg

Research Article Vol. 8, No. 7 | 1 Jul 2018 | OPTICAL MATERIALS EXPRESS 1962

Optical Materials EXPRESS

angle $\Theta_B^{ext} = (6.8 \pm 0.2)°$, s-polarization and average intensity of $\overline{I} = (20.6 \pm 2.2)\,\mathrm{W/cm^2}$ were chosen. Bragg-matched read-out was performed with a HeNe laser beam at $\lambda_{read} = 632.8\,\mathrm{nm}$ ($\Theta^{ext} \approx 8.8°$).

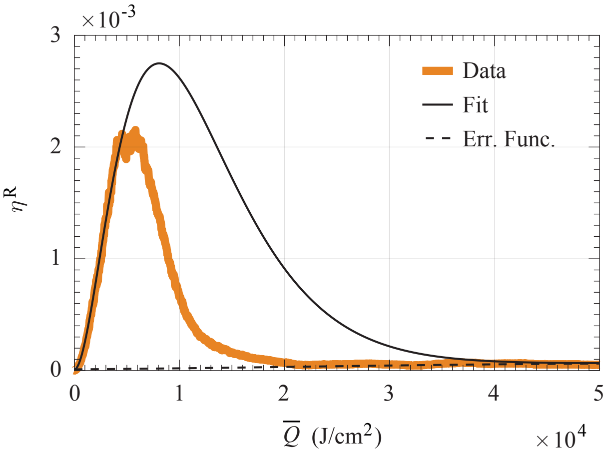

Fig. 10. Diffraction efficiency (orange) as a function of average exposure using a (1.86 ± 0.03) mM BIQ-PDMS sample with a thickness $d = (1.3 \pm 0.1)\,\mathrm{mm}$ for the particular case of repetitive fs-pulse exposure ($f_{rep} = 100\,\mathrm{Hz}$). The fit (black solid line) according to Eq. (1) for $0 < \overline{Q} < 0.4 \times 10^4\,\mathrm{J/cm^2}$ requires an additional term modeled by a Gauss error function (black dashed line). A maximum value of $\eta^R_{max} = (2.0 \pm 0.1) \times 10^{-3}$ is reached at an average exposure of $\overline{Q}^R_{max} = (5.3 \pm 1.3) \times 10^3\,\mathrm{J/cm^2}$.

The data set shows a temporal evolution of $\eta^R(\overline{Q})$ that is qualitatively comparable with the cw-recording case for OSO-PDMS films. The initial increase follows a quadratic dependence. A striking maximum of $\eta^R_{max} = (2.0 \pm 0.1) \times 10^{-3}$ is reached for $\overline{Q}^R_{max} = (5.3 \pm 1.3) \times 10^3\,\mathrm{J/cm^2}$. Thereafter, $\eta^R(\overline{Q})$ decreases significantly as a function of average exposure. There are three obvious differences with respect to cw-recording: (i) the maximum value $\eta^R_{max}(\overline{Q}^R_{max})$ exceeds the respective value for the case of cw-recording by nearly a factor of ten compared to OSO, (ii) the diffraction efficiency remains constant as a function of average exposure between $4.0 \times 10^3\,\mathrm{J/cm^2}$ and $6.6 \times 10^3\,\mathrm{J/cm^2}$, i.e. upon reaching the maximum, and (iii) a saturation value of $\eta(\overline{Q} \to \infty) \approx 6.9 \times 10^{-5}$ remains even for very large average exposure ($\overline{Q} \gg 10^4\,\mathrm{J/cm^2}$), i.e. light in direction of the reconstructed beam cannot be erased completely. As a result, the fitting function as defined via Eq. (1) requires an additional term modeled by a Gauss error function (black dashed line). Furthermore, successful fitting of the data set becomes only possible for low average exposure ($\overline{Q} \ll 1 \times 10^4\,\mathrm{J/cm^2}$). The solid black line in Fig. 10 represents the outcome of the fitting procedure within the limits of $0 < \overline{Q} < 0.4 \times 10^4\,\mathrm{J/cm^2}$ (fit parameters: $A = (2.8 \pm 0.5)$, $Q_0 = (0.80 \pm 0.04) \times 10^4\,\mathrm{J/cm^2}$, and $m = 0.17 \pm 0.04$). An overestimation of $\eta(\overline{Q})$ for $\overline{Q} \gg 0.5 \times 10^4\,\mathrm{J/cm^2}$ is self-evident.

The data set is further used to estimate the rise in the diffraction efficiency during a single fs-pulse event. A value of $\eta_{pulse} = (1.26 \pm 0.16) \times 10^{-7}$ is obtained by considering a pulse duration of 100 fs, a total average recording intensity of $\overline{I} = (20.6 \pm 2.2)\,\mathrm{W/cm^2}$, i.e. a single fs-laser-pulse exposure of $\overline{Q}_{100\,\mathrm{fs}} = (0.21 \pm 0.02)\,\mathrm{J/cm^2}$, and the value of the gradient $\delta\eta/\delta\overline{Q}$. The latter was determined from the experimental data set in the regime of monotonous growth at

$\overline{Q} \approx 3,000\,\mathrm{J/cm^2}$.

4. Discussion

4.1. Holographic performance of ruthenium sulfoxide complexes

Our results allow for a reliable evaluation of the performance of OSO-PDMS and BIQ-PDMS polymer films as holographic recording media. The holographic studies and the material synthesis approach aim at a discussion of predominantly consumer-market holographic applications such as (real-time) 3D holographic imaging [30, 31] or holographic mass data storage [32, 33]. In what follows, we will first discuss the individual results of our holographic analysis. Then, we will focus on a comparison of our data with SNP, that we regard as reference material system with embedded molecular switches. Finally, based on the discussed issues, we will tackle the question about the origin of the poor diffraction efficiency, i.e. on how to improve it for modern holographic applications.

4.1.1. Dynamics of the hologram diffraction efficiency

Let us first focus on the main features of the holographic polymer films: Unambiguously, our results verify the possibility of hologram recording in as-prepared OSO-PDMS and BIQ-PDMS polymer films by using either cw- and femtosecond pulse-train exposure at wavelengths in the blue-green spectral range. Independent on the light source, the recording process follows the well-known temporal evolution of the diffraction efficiency as a function of exposure for an optical system with two addressable states and exposure with a sinusoidal intensity pattern [26]. The rise and subsequent decay of the diffraction efficiency represents the temporal evolution of the modulation depth of the recorded hologram. The transient feature is a result of the fact that the population of the states $\mathrm{MS}_{1,2}$ is exclusively dependent on the exposure, and not on the intensity. Therefore, saturation population can be reached even in the regions of the fringe pattern with very low light intensity. The quality of reconstruction of $\eta(Q)$ for the cw-case using the fitting function Eq. (1) as derived in the original work of Fally et al. [26] is very remarkable. Furthermore, the determined rise of the absorption change as a function of exposure is in full agreement with literature data. It represents the clear dependence of the population, being proportional to the absorption change via the absorption cross-section, on the exposure under cw-laser light illumination. It can be successfully fitted using a two-exponential function which has been investigated systematically by Eicke et al. [28, 29] in the framework of two individually addressable metastable states $\mathrm{MS}_{1,2}$ as well as the nearly collinear geometry of the pump-probe beams.

A similar statement on the dynamics of $\eta(Q)$ is possible for the recording with a fs-laser pulse train in BIQ-PDMS polymer films. However, the temporal evolution can be reconstructed with sufficient quality within the limits of a low average exposure, i.e. prior to reaching the maximum of η. We here note that the average exposure required for sufficient hologram recording is by three orders of magnitude larger in direct comparison with the cw-recording case. This can be attributed to: i) the photosensitivity of BIQ-sulfoxides is by nearly a factor of 10 smaller than for OSO [28] and ii) the fs-pulse train exposure used for the study of BIQ-PDMS polymer films cannot be compared straightforwardly with the cw-recording case applied for the OSO-PDMS polymer film. In particular, we here use femtosecond laser pulses with pulse durations that are below the typical rise time of linkage isomerism in sulfoxide compounds (usually in the order of 200 ps [23]). Thus, this pulse duration is sufficient to trigger an instantaneous metal-to-ligand-charge-transfer (MLCT) via Franck-Condon's principle, but it is much shorter than the lifetime of the molecule in the excited (transient) state. As a result, relaxation of the excited molecule is solely driven by the principle of energy minimizing. Repetitive excitation, as it may occur in the case of pulse durations much larger than 200 ps or cw-exposure, must be excluded and may be a reason for the decelerated population of metastable states as a function of average exposure. The observation of a plateau value of η in its maximum may be attributed to stability limits of our setup. Furthermore, this may explain the decrease of η to a non-zero saturation value. The very low value of the diffraction efficiency most probably points to the presence of light-scattering, e.g. due to parasitically recorded holograms [34, 35], and/or the generation of laser-induced damage at the sample's surface.

4.1.2. Hologram thickness

From the optics viewpoint, OSO-PDMS and BIQ-PDMS polymer films feature a very high quality of the recorded holograms as represented by the experimental results of the rocking curve in Fig. 8. The fit function for off-Bragg read-out as derived from Kogelnik's formula for an unslanted lossy grating [19, 25] shows excellent agreement with the experimental data. This high quality of the data set allows for a straight-forward analysis of the recorded absorption hologram. We obtain a hologram thickness of $z \approx 690\,\mu$m that is by about 40% lower than the film thickness of 1.1 mm. The hologram therefore has not been recorded within the entire volume of the polymer film. It is very likely to attribute this finding to geometrical factors taking into account the widths of the recording beams and the internal intersection angle. Larger hologram thicknesses thus may be obtained by larger beam diameters that, however, require a recording laser with increased power.

4.1.3. Hologram multiplexing

The appearance of the higher-order side-maxima needs to be considered in the framework of recording multiple holograms. We here successfully demonstrate the recording of four individual holograms using angular multiplexing. The appearance of ghost images could be suppressed using intermediate angular steps of about 1°. Both, the FWHM of the rocking curve of $\approx 0.2°$ and the intermediate step width strongly limit the number of multiplexed holograms in the film under investigation. This limit may also be overcome by choosing larger hologram thicknesses that considerably reduce the FWHM of the rocking curve, i.e. it then becomes possible to reduce the intermediate angular step width.

4.1.4. Hologram recording with fs-pulse trains

The possibility of hologram recording with fs-pulse trains is of major importance considering the market growth of low-cost, high-power sub-picosecond laser systems. Furthermore, the possibility of an efficient hologram within a single laser pulse event is of interest for rapid changes of hologram images. In crystalline systems, single-pulse recording was demonstrated in lithium niobate, $LiNbO_3$, where a diffraction efficiency of more than 10 % was reached within an 8 ns laser pulse [36]. Moreover, fs-pulse recording was also successful in SNP single crystals. The possibility of fs-pulse recording therefore is another striking feature of OSO-PDMS and BIQ-PDMS polymer films that could be demonstrated with our study. This feature reflects the ultrafast response of the molecular switching process. However, in order to reach a maximum efficiency, a large concentration of OSO- and BIQ-molecules in the metastable states is desired that requires a fs-pulse train over an extended time range.

4.1.5. Limitations of the hologram diffraction efficiency

All these features so far point to an outstanding performance of OSO-PDMS and BIQ-PDMS polymer films. A severe disadvantage of these materials, however, is related to the maximum reached diffraction efficiency. Already, in the first proof-of-principle reports of elementary holograms in similar OSO-PDMS samples, η-values of up to $\approx 8 \times 10^{-6}$ were reported [14]. Our study here shows very remarkably that it is possible to improve this value by adjusting the OSO concentration, etc., and the use of a professional two-beam interferometer by a factor

Research Article Vol. 8, No. 7 | 1 Jul 2018 | OPTICAL MATERIALS EXPRESS 1965

Optical Materials EXPRESS

of about 100. Nevertheless, we were not able to exceed values of $\sim 10^{-3}$ for η in any of our samples and experimental conditions. A further possibility to enhance η would be by increasing the hologram thickness z. Considering Eq. (3) and the given experimental conditions, a rise by a factor of 10 may be reasonable for this particular case by adjusting $z \approx 11$ mm and for the OSO concentration under study. However, all these efforts will not be satisfying from the viewpoint of any application.

4.2. Comparison with crystalline holographic materials based on photoswitchable compounds

4.2.1. Holographic performance and material properties

Several advantages of OSO-PDMS and BIQ-PDMS polymer films reflected by the further studies become obvious when compared to crystalline photoswitchable compounds used for hologram recording in recent years. The most prominent candidate is sodium nitroprusside, $Na_2[Fe(CN)_5NO]\cdot 2H_2O$, (SNP). The single crystals will now serve as reference material for our further discussion due to their outstanding properties including the possibility for reaching diffraction efficiencies of up to 100% ($\eta = I_d/(I_t + I_d)$) due to large light-induced index changes of up to $\delta n \sim 10^{-2}$. SNP is also very similar to OSO-PDMS and BIQ-PDMS films with respect to its spectral sensitivity of the population process of both metastable states $MS_{1,2}$ using blue-green laser light.

The general holographic features can be well compared: The diffraction efficiency of SNP shows a transient evolution in full accordance with the results presented in this contribution for OSO-PDMS and BIQ-PDMS and were analyzed in detail in Ref. [26]. Off-Bragg read-out revealed similar rocking curves as for ruthenium sulfoxide polymers, though higher-order side maxima of the rocking curve (Fig. 8) were experimentally not observed. A reason is the comparably large fundamental absorption of SNP at the read-out wavelengths. Recording of up to eight holograms was verified within the same volume in 200μm thin plates of SNP [34].

Despite these holographic similarities, the materials themselves and their photofunctional properties are rather different: The synthesis of SNP requires a time-consuming crystal growth procedure from aqueous solution and polishing to optical quality. For recording of long-lived holograms ($\gg 100$)s, SNP samples need to be cooled below 200 K [15,34]. For comparison, the relaxation dynamics of the metastable states $MS_{1,2}$ in ruthenium sulfoxide complexes possess lifetimes in the order of hours at room temperature [9], thus imposing holographic grating lifetimes at a similar temporal scale. Moreover, the dimensions of SNP crystals remain limited to sizes of a few square centimeters. The large density of NP compounds within the crystalline matrix limits the crystal thickness to a few 100 μm for optical experiments due to pronounced absorption in the visible spectrum. On the contrary, the synthesis of OSO-PDMS polymer films and BIQ-PDMS polymer films can be realized on a large scale with sufficient optical quality. It is possible to carefully adjust the transmission loss by concentration tuning. A further striking advantage is the mechanical flexibility of the films [4]. This particularly widens the range of possible applications, e.g. for integrated head-up displays in curved windshields.

4.2.2. Diffraction efficiency

The striking similarities of the underlying photophysics in OSO-PDMS polymer films and SNP single crystals require a more fundamental discussion on the exceedingly different values of the diffraction efficiency in these two systems (about 10^{-4} in OSO-PDMS and 10^{-3} in BIQ-PDMS compared with up to 1 in SNP). One attempt to explain the measured small efficiency may be related to a small concentration of molecules in our film samples. We limit the concentration to $c \leq 1.0$ mM (OSO-PDMS) and $c \approx 1.9$ mM (BIQ-PDMS) in order to counterbalance diffraction efficiency against fundamental absorption. In SNP, the density of photoswitchable compounds is comparably large (4 molecules per unit cell) due to their role as building blocks in the crystallographic system and up to 50% of the ground state molecules may be switched to MS_1. Our results show that in OSO, η can be increased with growing concentration in our polymer films and it becomes possible to obtain a rise of η by a factor of three. However, concentration-dependent tuning by a factor of more than 1,000 seems not very likely.

The fs-pulse train investigation allows for a more detailed comparison between the diffraction efficiencies of OSO- and BIQ-PDMS polymer films and SNP single crystals, in particular if we consider the rise of the diffraction efficiency upon a single pulse event. For SNP it was already shown that single-pulse exposure with pulse durations of 4 ns reveal strongly limited values of $\eta \approx 10^{-4}$ [37]. We here demonstrate that BIQ-PDMS polymer films allow for hologram recording with $\eta \approx 1.3 \times 10^{-7}$ within a single sub-ps laser pulse event. For comparison with an average exposure of about 1 ns a diffraction efficiency of $\eta \approx 10^{-4}$ may be reached after about 10,000 consecutive 100 fs laser pulses. This shows that the efficiency in a single-pulse recording step is quite comparable between SNP single crystals and BIQ-PDMS polymer films. While consecutive single-pulse recording is capable to increase the diffraction efficiency by a factor of ten in comparison to the *cw*-recording case (cf. Fig. 8), we were not able to determine η values of more than $\approx 10^{-3}$ for any experimental condition.

4.3. Holographic performance: the role of symmetry and order of photoswitchable compounds

It is very likely to assume that OSO-PDMS and BIQ-PDMS polymer films generally reveal diffraction efficiencies that are far below any relevance for holographic applications. By comparison with the SNP reference system the main reason most probably may be attributed to the structural disorder of the OSO- and BIQ-molecules. In single crystalline SNP two photoswitchable compounds are oriented contrariwise within each a-b-mirror plane of the orthorhombic unit cell and with about ±45° to the a-axis alternating along the c-axis [38]. This symmetry is conserved even in the metastable state, i.e. there are no hints for a light-induced structural phase transition. On the contrary, it is solely a result of the N-O-inversion, i.e. a rotation of the N-O-bond by about 180° with respect to the Fe-N-O axis (MS_1). The symmetry may be responsible for a major contribution of light-induced index changes with the photo-induced structural changes of the nitrosyl compound. This already was experimentally verified and discussed in Ref. [39] from the viewpoint of related changes of the molecular polarization. The pronounced and periodic alteration of the local structure of the molecular crystal adds up to major changes of the index of refraction of up to 10^{-2}. The use of thin crystalline plates of $\approx 200\mu$m is sufficient for elementary grating recording with efficiencies of up to 100%. The crystallographic feature particularly is reflected in the dependence of recording and read-out polarizations with respect to the crystallographic axis, but furthermore in the possibility for grating recording with mutually orthogonal polarized laser beams in SNP [15, 18, 39].

The high symmetry and order of the photoswitchable compounds is clearly missing in OSO-PDMS and BIQ-PDMS (and any other PDMS-based polymer film based on photoswitchable compounds). Thus, the major contribution to the grating recording process is the optically induced change of the molecular absorption which is directly determined by the population of molecules in the ground and/or excited state (depending on the probe wavelength). Kramers-Kronig relation demands for the causal consideration of an additional contribution of the index of refraction as discussed in Ref. [13] with $\eta \approx 10^{-6}$. In other words, a contribution from a pure index grating is negligible and thus supports the applicability of Eq. (3). Taking into account the limits of the diffraction efficiency of lossy gratings ($\approx$ 3.7% following Kogelnik's definition for η [25]), it does not reveal any potential for breathtaking results.

On the contrary, it may be very promising to foster further material scientific efforts with the goal to synthesize OSO- or BIQ-PDMS polymer films with an intrinsic structural order. The latter may be inspired by the SNP model system, i.e. the director of structural change of the individual molecule may be oriented anti-parallel to each other within a single layer and all molecules may be aligned layer by layer. This may be reached by promising approaches of synthetic crystallography also including organic chemistry. Though potentially promising, the aspect of keeping synthesis at low cost must be considered carefully in the framework of consumer applications. Also, any structural approach may be connected with losing the material's softness of the polymer film.

5. Conclusion

An outstanding performance of OSO-PDMS and BIQ-PDMS polymer films is reflected by the dynamics of the efficiency, the quality of the off-Bragg read-out of the recorded holographic elementary lossy gratings, the possibility for angular multiplexing as well as the recording with continuous-wave and even a fs-laser pulse train at room temperature. These features already indicate some of the most important aspects for achieving high holographic storage densities. Together with its mechanical and tuning flexibility, e.g. concentration, as well as the scalability at a low-cost and short-time synthesis process provides a competitive advantage over established materials for holographic information storage. These advantages, however, remain limited by maximum values of the diffraction efficiencies of up to $\sim 10^{-3}$. Further tuning by means of adjustment of molecular concentration, holographic grating thickness, recording parameters, etc. fail to overcome this threshold value. In comparison to single crystalline reference media, it can be concluded that the structural disorder of the photoswitchable molecules is at the origin of this limitation. It may be overcome by targeted synthesis of polymer films with oriented and structurally ordered sulfoxide compounds. Then, however, the question about synthesis costs and lack of mechanical flexibility will represent well-known challenges of holographic media based on photoswitchable compounds.

Funding

Deutsche Forschungsgemeinschaft (DFG) (INST 190/165-1 FUGG); Open Access Publishing Fund of Osnabrueck University.

Acknowledgments

We particularly express our thanks to Jeffrey J. Rack and his research group, including Maksim Livshits, from the university of Albuquerque (New Mexico, United States of America) for providing the OSO- and BIQ-sulfoxide compounds for our study. We thank Sebastian Eicke, Kristin Springfeld, Volker Dieckmann and Holger Badorreck for discussion.

A.2 Pulse-induced transient blue absorption related with long-lived excitonic states in iron-doped lithium niobate

- Simon Messerschmidt, Bjoern Bourdon, David Brinkmann, Andreas Krampf, Laura Vittadello, and Mirco Imlau
  Pulse-induced transient blue absorption related with long-lived excitonic states in iron-doped lithium niobate
  Opt. Mater. Express **9**, 2748-2760 (2019); doi: 10.1364/OME.9.002748.

Research Article Vol. 9, No. 7 / 1 July 2019 / *Optical Materials Express* 2748

Optical Materials EXPRESS

Pulse-induced transient blue absorption related with long-lived excitonic states in iron-doped lithium niobate

SIMON MESSERSCHMIDT, BJOERN BOURDON, DAVID BRINKMANN, ANDREAS KRAMPF, LAURA VITTADELLO, AND MIRCO IMLAU*[*]

School of Physics, Osnabrueck University, Barbarastraße 7, 49076 Osnabrueck, Germany
[*]*mirco.imlau@uni-osnabrueck.de*

Abstract: Transient absorption is studied in Fe-doped lithium niobate single crystals with the goal to control and probe a blue absorption feature related with excitonic states bound to $\mathrm{Fe_{Li}}$ defect centers. The exciton absorption is deduced from the comparison of ns-pump, supercontinuum-probe spectra obtained in crystals with different Fe-concentration and $\mathrm{Fe_{Li}^{2+/3+}}$-ratio, at different pulse peak and photon energies as well as by signal separation taking well-known small polaron absorption bands into account. As a result, a broad-band absorption feature is deduced being characterized by an absorption cross-section of up to $\sigma^{\max}(2.85\,\mathrm{eV}) = (4 \pm 2) \cdot 10^{-22}\,\mathrm{m^2}$. The band peaks at about 2.85 eV and can be reconstructed by the sum of two Gaussians centered at 2.2 eV (width ≈ 0.5 eV) and 2.9 eV (width ≈ 0.4 eV), respectively. The appropriate build-up and decay properties strongly depend on the crystals' composition as well as the incident pulse parameters. All findings are comprehensively analyzed and discussed within the model of $\mathrm{Fe_{Li}^{2+}} - \mathrm{O^-} - \mathrm{V_{Li}}$ excitonic states.

1. Introduction

The microscopic understanding of pulse-induced transient absorption phenomena, such as green-induced infrared absorption (GRIIRA) [1] or blue-induced infrared absorption (BLIIRA) [2], is mandatory for the control of laser-induced damage mechanisms in lithium niobate ($\mathrm{LiNbO_3}$, LN) and, thus, for applications of LN in nonlinear photonics [3]. From the beginning, the appearance of transient infrared absorption was successfully explained by the coupling of optically generated electrons with phonons, i.e., by the formation of $\mathrm{Nb_{Nb/Li}^{4+}}$ small, strong-coupling electron polarons [4]. In contrast, the microscopic origin of transient blue-absorption remains fairly unexplained since advanced information about its respective features is still unsettled. In detail, neither the involved localized carrier states, nor their exact peak position, the shape, the band-width, and the absorption cross-section are known for the most of them. Furthermore, important knowledge to control the appearance of blue absorption by adjustment of, e.g., Fe-concentration, of the $\mathrm{Fe_{Li}^{2+/3+}}$-ratio, and/or by means of pulse peak energy and/or photon energies is missing in literature completely, so far.

The presence of transient absorption in the blue-green spectral range in LN was discovered in 2005 by Herth *et al.* in Fe-doped LN using single probe-laser lines [5] and – as a first attempt – has been attributed to the coupling of optically generated holes with the lattice in direct vicinity of $\mathrm{V_{Li}}$ lithium vacancies. The formation of $\mathrm{O^-}$-hole polarons with strong coupling is in full accordance with the original expectations formulated by Schirmer *et al.* for nearly all polar oxide crystals [6]. Later on, investigations with continuous wave [7] and pulsed laser light [8,9], however, revealed several discrepancies to the hole polaron model. The results of Waasem *et al.* [7] demanded for the existence of further electronic states within the band-gap, being handled

#363158 https://doi.org/10.1364/OME.9.002748
Journal © 2019 Received 22 Mar 2019; revised 8 May 2019; accepted 10 May 2019; published 3 Jun 2019

as X-center of unknown microscopic nature. Quite recently, Messerschmidt *et al.* discussed excitonic states at the origin of long-lived transient blue absorption [9].

Self-trapped electron-hole-pairs at Nb-O-octahedra, commonly called *self-trapped excitons* (STEs) were widely investigated by Blasse *et al.* in nominally pure and doped LN by means of photoluminescence at temperatures below 100 K [10–12]. Similar luminescence phenomena were observed at room temperature using fs-NIR-pulse trains in Mg-doped LN [13] and have been assigned to the recombination of electron and hole polarons [14]. The goal of the work of Messerschmidt *et al.* [9] was to re-address charge-transport phenomena in LN by considering excitonic states as intermediate steps in addition. The authors succeeded to show, that the temperature dependence of transient absorption in LN crystals with Fe (and Mg) doping can be explained comprehensively by considering the presence of further (pinned) excitonic states, e.g., $\mathrm{Fe}_{\mathrm{Li}}^{2+} - \mathrm{O}^{-} - \mathrm{V}_{\mathrm{Li}}$. It is noteworthy, that a main conclusion of this model approach is, that (pinned) STEs cause a pronounced long-lived blue absorption in Fe-doped LN (Fe:LN). We use the expression "pinned" in the context of this paper, if lattice defects or doping atoms hamper the movement and recombination of an STE in the regular lattice. In some cases, the pinned STE can be transformed into a self-trapped excitonic state in which at least one constituent is bound to the defect, e.g., the $\mathrm{Fe}_{\mathrm{Li}}^{2+} - \mathrm{O}^{-} - \mathrm{V}_{\mathrm{Li}}$ STE.

In this paper, we address the open question about peak position, shape, bandwidth and absorption cross-section of the long-lived transient blue absorption under the assumption of self-trapped excitonic states as microscopic origin, i.e., following the general model approach of Ref. [9]. The study is performed using Fe-doped LN crystals according to previously reported pronounced transient blue absorption observed in these crystals. For the first time, ns-pump, supercontinuum-probe spectroscopy is applied in order to get a direct experimental access to the spectral shape of the optically induced excitonic blue absorption bands. At the same time, the determination of the temporal evolution of the absorption over a broad spectral range is mandatory for our analysis since it enables the spectral separation from further bound electronic states, such as, e.g., $\mathrm{Nb}_{\mathrm{Li}}^{4+/5+}$ or $\mathrm{Fe}_{\mathrm{Li}}^{2+/3+}$. These centers additionally show individual broad-band (≈ 1.0 eV) transient absorption [15] and, therefore, strongly overlap with the expected excitonic optical fingerprints. Quite recently, Schirmer *et al.* [16] and Sanson *et al.* [17] showed that the $\mathrm{Fe}_{\mathrm{Li}}^{2+/3+}$ center can be described in the small polaron model as well.

The experimental study is performed with LN crystals of various doping concentrations and $\mathrm{Fe}_{\mathrm{Li}}^{2+/3+}$-ratio in order to account for three of the most common optical excitation paths in Fe:LN [18–20]:

- Iron D-band excitation, $E_{\mathrm{abs}}^{\mathrm{max}} = 2.6$ eV: A charge transfer from iron to the conduction band: $\mathrm{Fe}_{\mathrm{Li}}^{2+} \longrightarrow \mathrm{Nb}_{\mathrm{Nb}}^{5+}$
- Iron C-band excitation, $E_{\mathrm{abs}} > 3.1$ eV: A charge transfer from the valence band to iron: $\mathrm{O}^{2-} \longrightarrow \mathrm{Fe}_{\mathrm{Li}}^{3+}$
- Interband excitation, $E_{\mathrm{abs}} > (3.8 - 4.1)$ eV: A charge transfer from the valence to the conduction band: $\mathrm{O}^{2-} \longrightarrow \mathrm{Nb}_{\mathrm{Nb}}^{5+}$

Accordingly, photon energies at 2.33 eV (532 nm) and 3.49 eV (355 nm) are used to pump the transients.

The individual spectra reveal that any spectral and temporal feature of the $(E - t)$-plots can be modeled straightforwardly considering the additional presence of (pinned) excitonic states at iron. This knowledge is the anchor for the assignment of the excitonic absorption fingerprint from spectra obtained under rather different conditions. Finally, it is possible to analyze the main features (peak position, width) of the absorption band and, particularly to determine the respective absorption cross-section. For this purpose, the saturation of the $\mathrm{Fe}_{\mathrm{Li}}^{2+} - \mathrm{O}^{-} - \mathrm{V}_{\mathrm{Li}}$ STE population is estimated by a pump intensity dependent measurement series. An instruction for the control of the transient blue absorption can be clearly deduced for Fe-doped LN. At the same time, the reconstruction of the excitonic absorption feature with probably two individual absorption bands demands for further investigations, in particular of the electronic transition mechanisms of excitonic states in LN.

2. Experimental methods

Our experimental series is performed by means of ns-pump, supercontinuum-probe absorption spectroscopy. Electronic detection at room temperature using continuous-wave, single line probe lasers at 2.54 eV (488 nm) and 1.58 eV (785 nm) are additionally applied as described in previous studies (cf. e.g. [9]). The combined setup is schematically depicted in Fig. 1. The supercontinuum setup obtains an accessible time range of 100 ns up to 100 s and is capable to detect carrier-lattice phenomena with strong coupling, whereas formation dynamics and intermediate trapping states, such as the intermediate trapping of small, free $\mathrm{Nb}_{\mathrm{Nb}}^{4+}$ electron polarons, remain hidden.

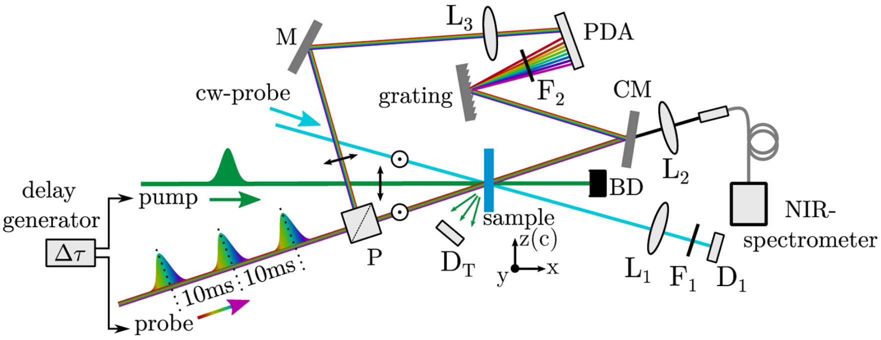

Fig. 1. Sketch of the ns-pump, supercontinuum-probe spectrometer applied in this study. The sample is pumped by a single pulse of a ns-pump pulse laser. Detection of the transient absorption is performed (i) using a diode (D_1) for the detection of the dynamic transmission change of a continuous wave probe laser transmitted through the sample (for a better visibility, only one cw-probe beam is shown) or (ii) by means of a supercontinuum. Here, the ns-pump pulse can be delayed for a certain time by a delay generator with respect to the supercontinuum probe pulse. The transmission change per wavelength is detected with two different spectrometers, one for the near-infrared part and one for the visible part of the supercontinuum pulse. $L_{1,2,3}$: lenses, $F_{1,2}$: optical filters, M: mirror, CM: cold mirror, P: polarizing beamsplitter cube, D_T: trigger diode for setup (i), BD: beam dump, PDA: photodiode array. The reader is referred to the text for further details.

A frequency-doubled and -tripled Nd:YAG pulse laser (Innolas Inc., *Spitlight*) and a broad-bandwidth light of a supercontinuum ns-pulse laser (LEUKOS, *STM-1-UV*) serve as pump (τ_{FWHM} = 8 ns, extraordinarily polarized, λ = 532 nm (2.33 eV) or λ = 355 nm (3.49 eV), respectively) and probe sources ($\tau_{\mathrm{FWHM}} < 1$ ns, unpolarized, $\lambda = (350 - 1800)\,\mathrm{nm} \equiv E = (3.54 - 0.69)\,\mathrm{eV}$, total average pulse energy of 35µJ). The probe pulse is split by a broadband polarizing beamsplitter cube into two parts with perpendicular polarization states, i.e., ordinary (transmitted) and extraordinary (reflected) with respect to the crystal's c-axis. The latter is used as a reference signal whereas the ordinary polarized part is adjusted to an optimum overlap with the pump within the sample's volume. After the sample, the probe light is split in a near-infrared (NIR) and visible (VIS) spectral region by a longpass dichroic mirror (λ_{cut} = 950 nm). A fiber-spectrometer (OceanOptics *NIRQuest 512*) and a discrete photodiode array (PDA, *Hamamatsu-S3902-512Q, TEC5*) are used simultaneously for the detection of the NIR and VIS signal fractions. A time resolution of up to 100 ns is achieved using an electronic delay of the pump. The time delay $\Delta\tau$ between pump and probe pulse is exponentially increased for $t = 100\,\text{ns}-10\,\text{ms}$ so that the data points are equidistant on a logarithmic time axis. Data points for $t > 10\,\text{ms}$ are obtained by measuring the subsequent pulses of the supercontinuum laser taking advantage of its repetition rate of 100 Hz. The signal-to-noise ratio is increased by signal averaging over 20 individual measurements. The transient absorption is calculated from the transmitted intensities via $\alpha_{\text{li}}(E,t) = -(1/d)\cdot\ln[I(E,t)/I(E,t\leq 0)]$, where $I(E,t)$ and $I(E,t\leq 0)$ are the transmitted probe light intensities after and before the pump pulse, respectively.

Our setup obeys minor limitations with respect to the spectral detection window, most of them being irrelevant for the purpose of our study: A lack of detection at 1.17 eV (1064 nm) and 2.33 eV (532 nm) due to a residual pump signal within the supercontinuum light and the SHG of the Nd:YAG pulse laser; one between 1.3 eV and 1.4 eV due to a low intensity of the supercontinuum laser and a weak sensitivity of the detectors; one above ≈ 3 eV due to a low intensity of the supercontinuum laser and a high intrinsic $\text{Fe}_{\text{Li}}^{2+}$ steady-state absorption of Fe-doped LN (particularly visible in the data of section 3.1).

Four LN crystals of the congruently melting composition [21,22] with different Fe dopant concentrations in the melt were used as depicted in Table 1. All samples were cut in a manner that the crystallographic c-axis is parallel to the polished surface and the y-axis along one edge. The $\text{Fe}_{\text{Li}}^{2+}$-concentration ($c_{\text{Fe}_{\text{Li}}^{2+}}$) in the samples, obtained from MolTech GmbH (Fe:LN_1) and the University of Padova (Fe:LN_2, Fe:LN_3, and Fe:LN_4), was estimated by optical absorption measurements [23,24].

Table 1. Fe-doped LN crystals used in this study as obtained from MolTech GmbH (Fe:LN_1) and the University of Padova (Fe:LN_2, Fe:LN_3, and Fe:LN_4). The $\text{Fe}_{\text{Li}}^{2+}$-concentrations were determined by optical absorption measurements [23,24]. *d* is denoting the thickness of the sample and α(2.6 eV) the steady-state absorption at 2.6 eV.

Sample	d (mm)	α (2.6 eV) (m^{-1})	$c_{\text{Fe}_{\text{Li}}}$ (mol %)	$c_{\text{Fe}_{\text{Li}}^{2+}}$ (10^{17}cm^{-3})	$c_{\text{Fe}_{\text{Li}}^{2+}}/c_{\text{Fe}_{\text{Li}}^{3+}}$
Fe:LN_1	2.0	468	0.185	10.4	0.029
Fe:LN_2	0.8	230	0.100	5.1	0.028
Fe:LN_3	2.0	45	0.020	1.0	0.027
Fe:LN_4	1.0	14	0.005	0.3	0.033

3. Experimental results

3.1. Excitation via the iron D-band

Figure 2 (left) shows the experimentally determined transient absorption for the case of optical excitation via the iron D-band, i.e., by means of a one-photon absorption process from $\text{Fe}_{\text{Li}}^{2+}$ to $\text{Nb}_{\text{Nb}}^{5+}$ (schematically sketched in Fig. 2 (right)).

The study is performed with sample Fe:LN_1 that obeys a high $\text{Fe}_{\text{Li}}^{2+}$-concentration. Furthermore, we have chosen a photon energy of 2.33 eV for the pump pulse that is close to resonant excitation ($\text{Fe}_{\text{Li}}^{2+}$ peaks at 2.6 eV). The transients can be detected with sufficient signal-to-noise ratio in the spectral range of 0.7 eV to ≈ 3 eV and are exemplarily shown for a weak pulse peak intensity of $I_{\text{P}} \approx 30\,\text{MW/cm}^2$. The $(E-t)$-color plots are composed of two data sets that have been determined simultaneously with the VIS and NIR detector systems. The change of the light-induced absorption α_{li} is visualized by blue-yellow color coding as shown by the legend. Here, blue areas denote spectral regions with no change of the absorption upon the pump event, i.e., $\alpha_{\text{li}} \approx 0\,\text{m}^{-1}$ and yellow regions mark noticeable changes with amplitudes up to $\alpha_{\text{li}} = 75\,\text{m}^{-1}$. Black lines indicate a contour plot in steps of $\Delta\alpha_{\text{li}} = 15\,\text{m}^{-1}$. Boxed white areas refer to the regions where spectral detection is not possible due to the above mentioned experimental limitations.

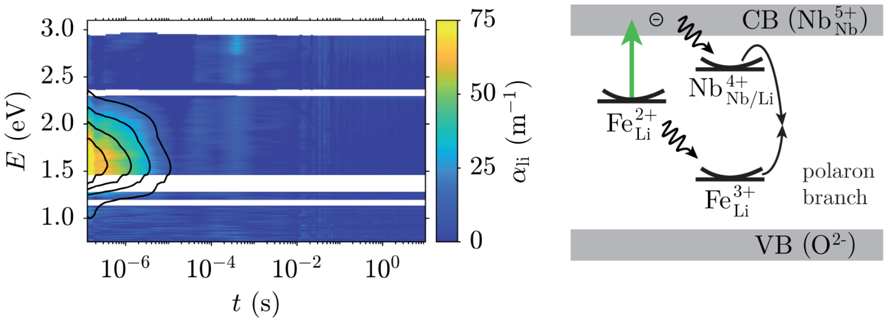

Fig. 2. **Left:** Transient absorption after an incident ns-pulse (E = 2.33 eV, $I_\mathrm{P} \approx$ 30 MW/cm^2) in the sample Fe:LN_1. The color coding of the light-induced absorption change is given in the legend on the right. Black lines indicate contour lines for steps of $\Delta\alpha_\mathrm{li}$ = 15 m^{-1}. Boxed white areas refer to the regions where spectral detection is not possible. **Right:** Excitation and recombination scheme for the case of optical excitation via the iron D-band. For details see text.

This plot shows that a single, broad-band light-induced absorption feature is induced in the near-infrared immediately after the incident pump pulse. In more detail, it appears in the spectral window of E = (0.7 – 2.5) eV with a peak at about 1.6 eV and shows a noticeable signal on the timescale up to 10μs. Within the experimental errors no change of the absorption shape during the decay can be observed. Further analysis of the spectra measured at t = 100 ns reveals a maximum value of $\alpha_\mathrm{li}^\mathrm{max} \approx$ 75 m^{-1} with a full width at half maximum of ≈ 0.9 eV. In addition, the dynamic trace measured with a cw-laser at 1.58 eV can be reconstructed by means of a single stretched-exponential function [24] with a lifetime τ_KWW(1.58 eV) = 10 μs and stretching factor β(1.58 eV) = 0.4.

3.2. Excitation via the iron D-band + C-band

Figure 3 (left) shows the experimentally obtained spectrum using conditions that additionally account for optical excitation via the C-band, i.e., via one-photon absorption from the O^{2-} valence band to $\mathrm{Fe}^{3+}_{\mathrm{Li}}$ (cf. Fig. 3 (right)).

For this purpose, the sample Fe:LN_2 is used that was grown with a lower concentration of Fe in the melt. In addition, a photon energy of 3.49 eV of the pump pulse is used. Again, a moderate pump pulse intensity of $I_\mathrm{P} \approx$ 27 MW/cm^2 is chosen. The plot shows a considerable change of the transient absorption in comparison with the data of Fig. 2: a broad-band absorption feature appears immediately upon the incident pulse; it covers the total spectral range from the near-infrared to the blue, i.e., from 1.0 eV to 3.1 eV. A maximum of the light-induced absorption with values up to $\alpha_\mathrm{li}^\mathrm{max} \approx$ 350 m^{-1} is determined. Along the time axis, a disappearance of the NIR signal within a few microseconds is obvious (τ_KWW(1.58 eV) = 2 μs and stretching factor β(1.58 eV) = 0.3). In contrast, the long-lived blue absorption is nearly constant over tenth of milliseconds and develops a significant peak around 2.85 eV. It follows as well a single stretched-exponential function with τ_KWW(2.54 eV) = 2 s and β(2.54 eV) = 0.7.

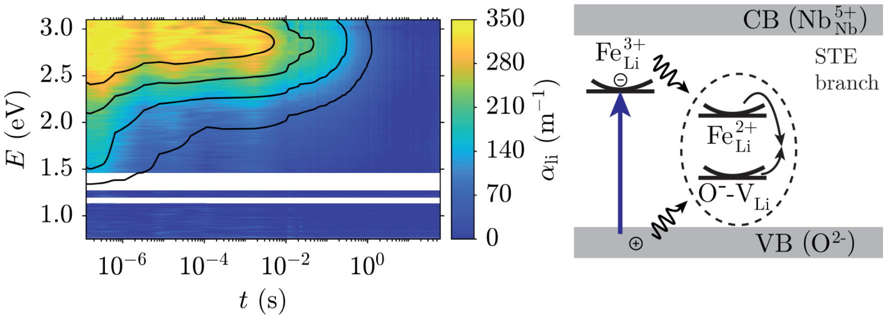

Fig. 3. **Left:** Transient absorption after an incident ns-pump pulse ($E = 3.49$ eV, $I_{\mathrm{P}} \approx 27$ MW/cm^2) in the sample Fe:LN_2. Color coding according to the legend on the right. The contour plot marks steps of $\Delta\alpha_{\mathrm{li}} = 70\,\mathrm{m}^{-1}$. Boxed white areas refer to the regions where spectral detection is not possible. **Right:** Excitation and recombination scheme for optical excitation via the iron C-band. For details see text.

3.3. Excitation via the iron D-band + C-band + TPA

Figure 4 (left) shows the results of our study using the sample Fe:LN_3, that features again a lower iron concentration in order to foster optical interband excitation, i.e., from the O^{2-} valence band to the $\mathrm{Nb}^{5+}_{\mathrm{Nb}}$ conduction band (cf. Fig. 4 (right)).

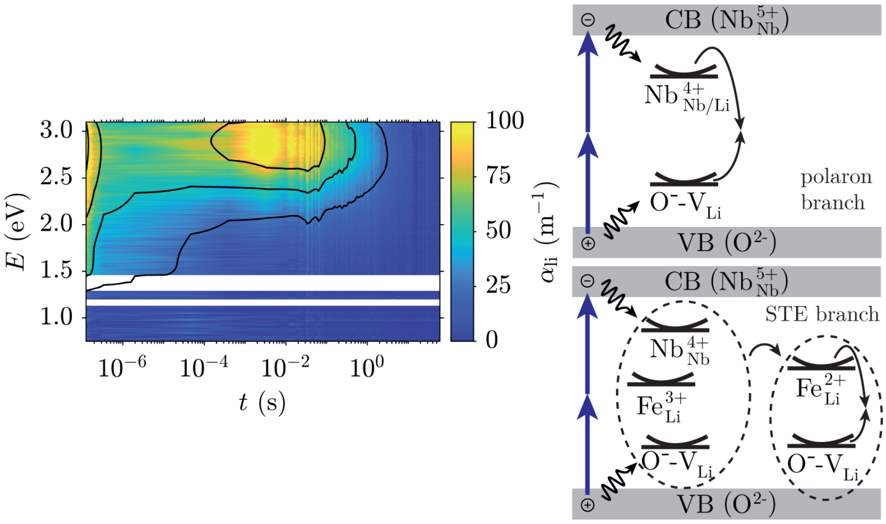

Fig. 4. **Left:** Supercontinuum transient absorption after 3.49 eV pulse exposure ($I_{\mathrm{P}} \approx 12$ MW/cm^2) in the sample Fe:LN_3 for the case of optical excitation via the D-band, C-Band and two-photon absorption. See legend on the right for color coding. The contour lines indicate steps of $\Delta\alpha_{\mathrm{li}} = 25\,\mathrm{m}^{-1}$. Boxed white areas refer to the regions where spectral detection is not possible. **Right:** Excitation and recombination scheme after excitation via a two-photon-absorption. For details see text.

Again, a photon energy of 3.49 eV is chosen for the pump pulse with a comparably weak pulse peak intensity of $I_P \approx 12\,\mathrm{MW/cm^2}$. These experimental conditions result in the most complex dynamics of the transient absorption in Fe-doped LN: immediately upon the pump pulse, a broad-band absorption feature is detected with characteristics very similar to the situation in section 3.2, but with reduced maximum amplitude of the light-induced absorption with values up to $\alpha_{\mathrm{li}}^{\max} \approx 100\,\mathrm{m^{-1}}$. It is very remarkable that this initial absorption shows a fast decay all over the blue and NIR spectral range with nearly the same temporal behavior. It results in a complete decay of the signal in the NIR with $\tau_{\mathrm{KWW}}(1.58\,\mathrm{eV}) = 10\,\mu\mathrm{s}$ and $\beta(1.58\,\mathrm{eV}) = 0.3$. In contrast, a temporally constant transient absorption value ($\alpha_{\mathrm{li}} > 0\,\mathrm{m^{-1}}$) can be detected in the blue that remains over a duration of hundreds of microseconds. Subsequently, in the time range of milliseconds, the appearance of a delayed maximum with values up to $\alpha_{\mathrm{li}}^{\max} \approx 100\,\mathrm{m^{-1}}$ is detected. Similar to the findings in section 3.2, it peaks around 2.85 eV and the long decay can be described with the parameters $\tau_{\mathrm{KWW}}(2.54\,\mathrm{eV}) = 2\,\mathrm{s}$ and $\beta(2.54\,\mathrm{eV}) = 0.6$.

3.4. *Absorption spectra and saturation of the long-lived blue absorption*

Figure 5 shows the direct comparison of the long-lived transient blue absorption features as obtained from a more detailed analysis of the spectra depicted in Figs. 3 and 4.

The spectra were deduced by normalizing the data points at every delay position to the respective spectral maximum of the light-induced absorption and subsequently averaging the data set over the time interval from $t > 1 \cdot 10^{-3}$ s to 10 s. Obviously, both spectra reveal a comparable shape with respect to the peak position of $E_{\mathrm{peak}} = (2.85 \pm 0.05)$ eV and full width at half maximum of FWHM= (1.00 ± 0.25) eV.

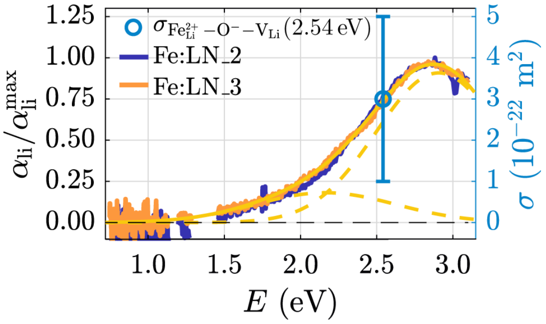

Fig. 5. Spectra of the long-lived blue absorption as deduced from the data in Fig. 3 and Fig. 4 by normalizing the data points at every delay position to the spectral maximum of the light-induced absorption and averaging the data set over the time interval from $t > 1 \cdot 10^{-3}$ s to 10 s. The yellow line represents a converging result of fitting Eq. (1) to the data. The dashed yellow lines refer to the individual Gaussians as given in Table 2. The blue data point is an experimentally determined value of the absorption cross-section at 2.54 eV and serves as scaling factor for the y-axis on the right.

Table 2. Parameters obtained from fitting the sum of two Gaussian functions (Eq. (1)) to the experimental data set for the case of two distinct absorption bands as sketched in Fig. 5. The fitting procedure reveals two solutions with a root mean square error of RMSE = 0.0387.

fit	a_1	a_2	b_1 (eV)	b_2 (eV)	c_1 (eV)	c_2 (eV)
1	0.91 ± 0.18	0.18 ± 0.17	2.91 ± 0.07	2.16 ± 0.50	0.41 ± 0.06	0.46 ± 0.17
2	0.37 ± 0.08	0.60 ± 0.40	2.88 ± 0.15	2.88 ± 0.34	0.31 ± 0.04	0.64 ± 0.03

It is possible to reconstruct the absorption shape by the sum of two Gaussians via:

$$\frac{\alpha_{\mathrm{li}}(E)}{\alpha_{\mathrm{li}}^{\mathrm{max}}} = a_1 \cdot \exp\left[-\frac{(E-b_1)^2}{2c_1^2}\right] + a_2 \cdot \exp\left[-\frac{(E-b_2)^2}{2c_2^2}\right], \tag{1}$$

where $a_{1,2}$, $b_{1,2}$ and $c_{1,2}$ represent the amplitude, peak position and standard deviation of the individual Gaussian functions. As a result of the fitting procedure, two converging solutions are found. One, with two distinct absorption bands, is shown in Fig. 5. The associated fitting parameters are given in Table 2. A second converging solution of the fitting procedure results in two absorption bands peaking at the same photon energy of $E_{\mathrm{peak}} \approx 2.88\,\mathrm{eV}$, but with rather different amplitudes and FWHM values.

In order to check whether the long-lived blue absorption shows a saturation value at high intensities, we have performed appropriate measurements using our standard pump-probe experiment due to the higher signal-to-noise ratio and signal stability along with the use of a 2.54 eV continuous-wave laser system. Figure 6 shows the maximum amplitude $\alpha_{\mathrm{li}}^{\mathrm{max}}(2.54\,\mathrm{eV})$ measured for various pump intensities at $E_{\mathrm{P}} = 3.49\,\mathrm{eV}$ in the sample Fe:LN_4 which contains the lowest iron concentration in this study. The maximum amplitude follows at low pump intensities a quadratic behavior with increasing intensities. However, above $I_{\mathrm{P}} \approx 50\,\mathrm{MW/cm^2}$ the amplitudes start to saturate. The data can be described with the following function:

$$\alpha_{\mathrm{li}}^{\mathrm{max}}(E, I) = \alpha_{\mathrm{li}}^{\mathrm{max}}(E, I \to \infty) \cdot \left[1 - \exp\left(-\frac{I^2}{I_\alpha^2}\right)\right], \tag{2}$$

where $\alpha_{\mathrm{li}}^{\mathrm{max}}(E, I \to \infty)$ is the saturation value and I_α is the characteristic intensity. A fit of Eq. (2) to the data reveals $\alpha_{\mathrm{li}}^{\mathrm{max}}(2.54\,\mathrm{eV}, I \to \infty) = (276 \pm 25)\,\mathrm{m^{-1}}$ and $I_\alpha = (50 \pm 5)\,\mathrm{MW/cm^2}$.

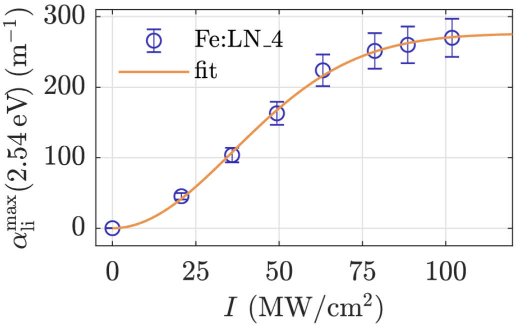

Fig. 6. Maximum amplitude of the long-lived blue absorption probed at 2.54 eV after pulse exposure at 3.49 eV for various intensities in the sample Fe:LN_4. The orange line is a fit of Eq. (2) to the data.

4. Discussion

Our experimental study reveals that ns-pump, supercontinuum-probe spectroscopy is successfully applied for the detection of transient absorption in Fe-doped lithium niobate. New insight to the temporal and, particularly, spectral evolution of pulse-induced absorption phenomena is obtained in the time interval from nanoseconds up to a few seconds and (nearly) without a gap from the blue to the near infrared spectral range. At a glance, the obtained $(E-t)$-plots demonstrate (i) the variety of transient absorption phenomena that appear in Fe-doped LN upon a single laser pulse, (ii) their complexity with respect to the spectral overlap of different absorption features as well as to a time-delayed build-up and (iii) their dependence on the experimental boundary conditions. The signal-to-noise-ratio is sufficient to resolve intensity changes in the order of $\delta I/I_0 \approx 0.5\,\%$. In this respect, the experimental detection by means of single-line continuous-wave laser beams remains as a mandatory tool for the detection of very weak signals and/or for the detailed inspection of the temporal shapes of the absorption features. The presented experimental combination brings together the advantage of both techniques and enables the comprehensive analysis of transient absorption in LN without any constraint.

In what follows, we will first discuss the individual data sets in more detail according to the state-of-the-art knowledge of small polarons with strong coupling and considering the model of (pinned) excitonic states, i.e., according to the previously reported model approach by Messerschmidt *et al.* [9]. Then, we focus on the absorption features of the $\mathrm{Fe}_{\mathrm{Li}}^{2+}-\mathrm{O}^{-}-\mathrm{V}_{\mathrm{Li}}$ excitonic state and will deduce the respective absorption cross-section, peak position and bandwidth. It should be noted that we neglect the inclusion of the intrinsic luminescent $\mathrm{Nb}_{\mathrm{Nb}}^{4+}-\mathrm{O}^{-}$ STE in all excitation/recombination schemes. It is because such centers are expected to appear predominantly in stoichiometric or Mg-doped LN in a time range much shorter than the used pulse duration, i.e., not accessible with our experimental setup (at room temperature) [9,25].

4.1. Excitation via the iron D-band

The experimental conditions resulting in the data presented in Fig. 2 (left) were prepared in a manner that a one-photon excitation via the iron D-band is highly preferred (high $\mathrm{Fe}_{\mathrm{Li}}^{2+}$-concentration, pump wavelength near the maximum of the $\mathrm{Fe}_{\mathrm{Li}}^{2+}$ absorption band). We therefore analyze the transients by considering optical excitation/subsequent relaxation from/back to $\mathrm{Fe}_{\mathrm{Li}}^{2+/3+}$ and the interim formation of small $\mathrm{Nb}_{\mathrm{Li/Nb}}^{4+}$ polarons (c.f. Fig. 2 (right)). In particular, we expect that the pulse-induced absorption over the entire spectral range results from the interplay of a light-induced transparency due to less $\mathrm{Fe}_{\mathrm{Li}}^{2+}$ (ground-state bleach) and an increased absorption due to the formation of small bound polarons, i.e., $\alpha_{\mathrm{li}}(E) = \Delta N_{\mathrm{Nb}_{\mathrm{Li}}^{4+}} \cdot \sigma_{\mathrm{Nb}_{\mathrm{Li}}^{4+}}(E) + \Delta N_{\mathrm{Fe}_{\mathrm{Li}}^{2+}} \cdot \sigma_{\mathrm{Fe}_{\mathrm{Li}}^{2+}}(E)$. Here, $\Delta N_{\mathrm{Nb}_{\mathrm{Li}}^{4+}} = -\Delta N_{\mathrm{Fe}_{\mathrm{Li}}^{2+}}$ where ΔN is the change of concentration induced by the pump pulse. Considering the dispersion features of the two absorption species with well separated peak positions (1.6 eV and 2.6 eV) [15], a pronounced NIR absorption change shall remain that is mainly attributed to $\mathrm{Nb}_{\mathrm{Li}}^{4+}$. At the same time, no changes are expected for the blue-green spectral range since the absorption cross sections of $\mathrm{Nb}_{\mathrm{Li}}^{4+}$ and $\mathrm{Fe}_{\mathrm{Li}}^{2+}$ strongly overlap in this region and are nearly identical: $\sigma_{\mathrm{Fe}_{\mathrm{Li}}^{2+}}(\mathrm{blue}) \approx \sigma_{\mathrm{Nb}_{\mathrm{Li}}^{4+}}(\mathrm{blue})$ [15]. Our experimental findings in Fig. 2 are in full agreement with both expectations: a broad-band NIR absorption is clearly visible with nearly no absorption change in the blue-green spectral range (within the noise of our experiment). Moreover, three significant polaron fingerprints can be verified, particularly considering $\mathrm{Nb}_{\mathrm{Li}}^{4+}$: a lifetime in the sub-ms-time range, a NIR absorption feature with a peak at about 1.6 eV and a stretched-exponential decay behavior with a β-value below 1/2. We need to note, that in this discussion, we neglect the interim formation of $\mathrm{Nb}_{\mathrm{Nb}}^{4+}$ free polarons due to experimental constraints: the free polaron lifetime is much shorter than the temporal resolution of our experiment [8]. A transient signal at the the peak maximum of small free polarons of about 1.0 eV [15] was therefore not observed. All these findings and interpretations are in full agreement with the state-of-the-art knowledge of the interaction of continuous-wave and pulsed laser light with Fe-doped LN at moderate average power [24,26].

4.2. Excitation via the iron D-band + C-band

The second measurement was performed with an iron-doped LN sample containing a lower Fe-concentration and with a pump wavelength in the UV. This fosters the optical excitation via the iron C-band, though an excitation via the D-band cannot be excluded. We additionally need to consider that the cross-sections of these two excitation paths are very similar at 355 nm [27], i.e, a contribution of both paths to the transient spectrum is to be expected. In this sense, and in direct comparison with the discussion of the previous section, it is likely to assume that the observed NIR absorption feature with fast decay in the spectra of Fig. 3 originates from the mechanisms associated with the D-band excitation (see section 4.1). All deduced experimental features (peak position, lifetime, stretching factor) support this assumption. Accordingly, the UV-induced long-lived blue absorption in Fig. 3 is assigned to the second excitation path via the iron C-band. To the best of our knowledge, the latter has not been investigated in the context of either small polarons or STEs in lithium niobate, so far. At a first glance, a relation to the formation of small $O^- - V_{Li}$ hole and Fe_{Li}^{2+} polarons may be assumed considering the charge-transfer from O^{2-} to Fe_{Li}^{3+} [18] (c.f. Fig. 3 (right)). However, in this case, the blue absorption must feature a broad-band absorption centered in the range of 2.5 – 2.6 eV [6,15], that does not correspond with the experimentally determined peak position of about 2.85 eV in our spectra (see Fig. 5 and discussion below). An alternative microscopic approach is to consider $Fe_{Li}^{2+} - O^- - V_{Li}$ STEs as proposed by Messerschmidt *et al.* [9]. Such states are reported to form after pinning and subsequent transformation of an intrinsic STE at an iron center within a few hundred microseconds. They show absorption in the blue-green spectral range and their decay dynamics feature a stretching factor $\beta > 2/3$. According to the characteristics of the induced blue absorption deduced from the data in Fig. 2 (absorption feature with a peak at about 2.85 eV, an increased stretching factor of $\beta \approx 0.7$), it is reasonable to assume the presence of such states in our case, as well. A remarkable consequence of this approach is that the direct STE formation via the C-band is discovered for the first time. This finding is of particular importance of applications with doped LN and ultraviolet laser pulses, e.g., UV photorefraction.

4.3. Excitation via the iron D-band + C-band + TPA

The third measurement in this study was performed with a sample containing a lower Fe_{Li}^{2+}- and Fe_{Li}^{3+}-concentration and, thus, also obeys the one-photon excitation and the subsequent recombination paths via the iron C- and D-band as discussed in the two previous sections 4.1 and 4.2. In addition, the low Fe-concentration increases the probability for excitation via two-photon absorption (TPA). It is because the negligible fundamental absorption conserves the peak intensity of the incident laser pulse. The influence of the electron-hole-pairs generated via TPA on the decay dynamics can be deduced by comparing the results in the two previous sections 4.1 and 4.2 with the data in section 3.3 (c.f. Fig. 4). The main differences are (i) an additional fast decay and (ii) a delayed increase in the blue spectral range. Both phenomena can be explained as follows: the generation of electron-hole pairs in the LN-host lattice results in the formation of $O^- - V_{Li}$ hole and Nb_{Li}^{4+} bound polarons as well as STEs which can be pinned next to Fe_{Li}^{3+} (c.f. Fig. 4 (right)). The formed polarons/STEs contribute to the transient spectra with absorption features in the blue and near-infrared spectral range. The decay of the initial transient signals in the blue and NIR spectral range is a characteristic fingerprint for the recombination of hole polarons with bound polarons known from undoped lithium niobate samples [3,15]. However, in contrast to an undoped sample, the initial temporal decay in the blue spectral range is superimposed by the transformation of pinned STEs at Fe_{Li}^{3+} into $Fe_{Li}^{2+} - O^- - V_{Li}$ inducing a strong blue absorption in the time range of milliseconds [9]. The observed complex behavior in the blue spectral range then is due to the different decay dynamics of the hole/bound polaron recombination on the one hand and the transformation of pinned STEs on the other hand.

4.4. Determination of the shape and absorption cross-section of the long-lived blue absorption

The discussion of the previous sections points to a dominant role of $Fe_{Li}^{2+} - O^- - V_{Li}$ STEs at the origin of the long-lived blue absorption in Fe-doped LN which is in accordance with Ref. [9]. Following this microscopic approach, the spectra of Fig. 3 and Fig. 4 will both be related with this excitonic state. Figure 5 compares the spectral shapes of the long-lived blue absorption as obtained from a further analysis of these data sets. Obviously, both spectra are characterized by a comparable shape, peak position and bandwidth and are nearly indistinguishable from each other. This result is very remarkable since the data sets were obtained in two completely different Fe-doped LN crystals and by using different pulse intensities for excitation. Moreover, it supports the finding that $\mathrm{Fe}_{\mathrm{Li}}^{2+} - \mathrm{O}^{-} - \mathrm{V}_{\mathrm{Li}}$ STEs can be formed directly after the pump pulse via the iron C-band.

Let us now further analyze the absorption spectrum depicted in Fig. 5 in the microscopic model of $\mathrm{Fe}_{\mathrm{Li}}^{2+} - \mathrm{O}^{-} - \mathrm{V}_{\mathrm{Li}}$ STEs. First, we discuss the shape of the STE absorption feature. Figure 5 shows that the pulse-induced absorption appears with a large amplitude over the entire VIS-NIR spectral region that is experimentally accessible with our setup. It can be expected that the band extends even far into the ultraviolet region and, that it overlaps with the interband absorption (starting at about 3.8 eV). Fitting the spectrum in the accessible region reveals that at least the sum of two Gaussian functions (c.f. Eq. (1)) with six free fitting parameters is required for its description. Exemplarily, one of the converging solutions is depicted in Fig. 5 with different peak positions (2.2 eV and 2.8 eV, respectively) but comparable FWHMs of the constituents (c.f. Table 2). We note that it is alternatively possible to perform the fitting procedure with two Gaussians at the same peak position (of about 2.9 eV), but with different FWHM values.

Taking these findings into account, we refer to the state-of-the-art knowledge of STE absorption bands and find that they typically resemble the interplay of at least two spectrally separated single bands in a first approximation [28–30]: a straightforward explanation is that the two bands originate from an optical excitation of both the electron and the hole to higher states, respectively. Or, the two bands refer to the photo-ionization process of STEs. Against this background, it is reasonable to expect two absorption bands for STEs in LN as well, one associated with the electron excitation from $\mathrm{Fe}_{\mathrm{Li}}^{2+}$ and the other one from the $\mathrm{O}^{-} - \mathrm{V}_{\mathrm{Li}}$-center. Peak position, bandwidth and the relative fraction of the total absorption amplitude (c.f. Table 2) then reflect the individual absorption features and absorption cross-sections of the two constituents involved. In particular, the effective absorption coefficient of the STE then is given by $\alpha_{\mathrm{eff}}(E) = \alpha_1(E) + \alpha_2(E)$ in this case.

Second, we intend to estimate the effective absorption cross-section of the $\mathrm{Fe}_{\mathrm{Li}}^{2+} - \mathrm{O}^{-} - \mathrm{V}_{\mathrm{Li}}$ STE. For this purpose, following the discussion of the previous paragraph, it is assumed that the absorption feature originates from a single absorption center of number density N, i.e., $\alpha_{\mathrm{eff}}(E) = \sigma_{\mathrm{eff}}(E) \cdot N$. In our case, the number density N can be determined experimentally by intensity dependent measurements of $\alpha_{\mathrm{li}}(I)$ as depicted in Fig. 6. It is because $N(I)$ saturates due to a limited $\mathrm{Fe}_{\mathrm{Li}}^{3+}$-concentration such that $\alpha_{\mathrm{li}}(I)$ saturates, too. The experimentally determined saturation value $\alpha_{\mathrm{li}}^{\mathrm{max}}(E, I \to \infty)$ then enables the calculation of the effective cross-section via $\sigma_{\mathrm{eff}}(E) = \alpha_{\mathrm{li}}^{\mathrm{max}}(E, I \to \infty)/\mathrm{c}_{\mathrm{Fe}_{\mathrm{Li}}^{3+}}$. This study has been performed at a minimum total iron concentration to (i) ensure that a saturation value can be achieved with our experimental conditions and (ii) enable the utilization of low pump intensities to avoid laser induced damages. With the data deduced from Fig. 6 we obtain $\sigma_{\mathrm{eff}}(2.54\,\mathrm{eV}) = (3 \pm 2) \cdot 10^{-22}\,\mathrm{m}^2$. This value serves for scaling the right y-axis in Fig. 5 which leads to a maximum effective cross-section of $\sigma_{\mathrm{eff}}^{\mathrm{max}}(2.85\,\mathrm{eV}) = (4 \pm 2) \cdot 10^{-22}\,\mathrm{m}^2$. The large error of these values is a combination of both, the precision of our measurement and the determination of the iron concentration. We would also like to mention that the estimated values are only a lower bound because the calculation is based on the assumption that all $\mathrm{Fe}_{\mathrm{Li}}^{3+}$-centers are occupied in the saturation state. If this assumption is inapplicable, the number density of STEs is reduced which will result in a larger value of the absorption cross-section. In comparison to small polarons in lithium niobate [15], the absorption cross-section of the STE is in the same order of magnitude. Assuming that (pinned) STEs formed under similar conditions, e.g., in Mg-doped LN, exhibit similar absorption bands and cross-sections, they have to play an important role in the blue absorption and might be responsible for a damping of frequency conversion and laser induced damages in this spectral range.

5. Conclusion

This study reveals the striking impact of ns-pump, supercontinuum-probe spectroscopy for the microscopic understanding of strongly localized electronic states in oxide crystals with lithium niobate as an example. The spectra allow to distinguish the temporal and spectral action of individual optically generated species under rather different experimental conditions and their formation/transport/recombination/relaxation description within a quite complex band model scheme. As a result it is possible to discover new properties of the interaction of light pulses with a strong polar crystal, e.g., the possibility to optically generate $\mathrm{Fe}_{\mathrm{Li}}^{2+} - \mathrm{O}^{-} - \mathrm{V}_{\mathrm{Li}}$ STEs directly by a charge transfer via the iron C-band. Furthermore, the STE absorption cross-section obeys similar values as reported for small polarons. Another impressive result of this study is that the combination of transient spectroscopy and the polaron/exciton model in LN enables the precise prediction of the complex dynamics of transient absorption over a large spectral and temporal range. At the same time, it supports the validity of the model of (pinned) STEs for lithium niobate, which have been disregarded in the mechanisms of light-induced transport, so far. Our findings are of particular importance for the field of photorefraction since the formation of STEs will not result in the optically induced separation of charges that is mandatory for the photorefractive effect. The possibility to solely generate excitonic states by means of optical adjustment of pulse parameters (photon energy, pulse peak energy) and/or material adjustment ($\mathrm{Fe}^{2+/3+}$-ratio) enables, e.g., the efficient suppression of optical damage in LN-based frequency converters. In the same manner, it is possible to determine temporal regimes that allow for photorefractive recording at elevated efficiencies, such as, e.g., the sub-millisecond time range for recording with a single, intense laser pulse.

Funding

Deutscher Akademischer Austauschdienst (DAAD) (57390412); Deutsche Forschungsgemeinschaft (DFG) (IM37/11-1, INST 190/165-1 FUGG); Osnabrueck University (Open Access Fund).

Acknowledgements

The authors are indebted to thank Marco Bazzan and coworkers for crystals and crystal preparation as well as Christoph Merschjann for fruitful discussion.

References

1. R. Batchko, G. Miller, A. Alexandrovski, M. Fejer, and R. Byer, “Limitations of high-power visible wavelength periodically poled lithium niobate devices due to green-induced infrared absorption and thermal lensing,” Tech. Dig. Summ. Pap. Present. at Conf. on Lasers Electro-Optics. Conf. Ed. 1998 Tech. Dig. Series, Vol. 6 (IEEE Cat. No.98CH36178) (1998).
2. H. M. Yochum, K. B. Üçer, R. T. Williams, L. Grigorjeva, D. Millers, and G. Corradi, “Subpicosecond Laser Spectroscopy of Blue-Light-Induced Absorption in $\mathrm{KNbO_3}$ and $\mathrm{LiNbO_3}$,” Defects Surface-Induced Eff. Adv. Perovskites pp. 125–138 (2000).
3. M. Imlau, H. Badorreck, and C. Merschjann, “Optical nonlinearities of small polarons in lithium niobate,” Appl. Phys. Rev. **2**(4), 040606 (2015).
4. Y. Furukawa, K. Kitamura, A. Alexandrovski, R. K. Route, M. M. Fejer, and G. Foulon, “Green-induced infrared absorption in MgO doped $\mathrm{LiNbO_3}$,” Appl. Phys. Lett. **78**(14), 1970–1972 (2001).
5. P. Herth, T. Granzow, D. Schaniel, T. Woike, M. Imlau, and E. Krätzig, “Evidence for Light-Induced Hole Polarons in $\mathrm{LiNbO_3}$,” Phys. Rev. Lett. **95**(6), 067404 (2005).
6. O. F. Schirmer, “$\mathrm{O^-}$ bound small polarons in oxide materials,” J. Phys.: Condens. Matter **18**(43), R667–R704 (2006).
7. N. Waasem, A. Markosyan, M. M. Fejer, and K. Buse, “Green-induced blue absorption in MgO-doped lithium niobate crystals,” Opt. Lett. **38**(16), 2953 (2013).

8. D. Conradi, C. Merschjann, B. Schoke, M. Imlau, G. Corradi, and K. Polgár, “Influence of Mg doping on the behaviour of polaronic light-induced absorption in $LiNbO_3$,” Phys. Status Solidi RRL **2**(6), 284–286 (2008).
9. S. Messerschmidt, A. Krampf, F. Freytag, M. Imlau, L. Vittadello, M. Bazzan, and G. Corradi, “The role of self-trapped excitons in polaronic recombination processes in lithium niobate,” J. Phys.: Condens. Matter **31**(6), 065701 (2019).
10. D. M. Krol, G. Blasse, and R. C. Powell, “The influence of the Li/Nb ratio on the luminescence properties of $LiNbO_3$,” J. Chem. Phys. **73**(1), 163–166 (1980).
11. M. Wiegel, M. Emond, E. Stobbe, and G. Blasse, “Luminescence of alkali tantalates and niobates,” J. Phys. Chem. Solids **55**(8), 773–778 (1994).
12. M. Wiegel, G. Blasse, A. Navrotsky, A. Mehta, N. Kumada, and N. Kinomura, “Luminescence of the Ilmenite Phase of $LiNbO_3$,” J. Solid State Chem. **109**(2), 413–415 (1994).
13. P. Reichenbach, T. Kämpfe, A. Haußmann, A. Thiessen, T. Woike, R. Steudtner, L. Kocsor, Z. Szaller, L. Kovács, and L. Eng, “Polaron-Mediated Luminescence in Lithium Niobate and Lithium Tantalate and Its Domain Contrast,” Crystals **8**(5), 214 (2018).
14. T. Kämpfe, A. Haußmann, L. M. Eng, P. Reichenbach, A. Thiessen, T. Woike, and R. Steudtner, “Time-resolved photoluminescence spectroscopy of Nb_{Nb}^{4+} and O^- polarons in $LiNbO_3$ single crystals,” Phys. Rev. B **93**(17), 174116 (2016).
15. C. Merschjann, B. Schoke, D. Conradi, M. Imlau, G. Corradi, and K. Polgár, “Absorption cross sections and number densities of electron and hole polarons in congruently melting $LiNbO_3$,” J. Phys.: Condens. Matter **21**(1), 015906 (2009).
16. O. F. Schirmer, M. Imlau, and C. Merschjann, “Bulk photovoltaic effect of $LiNbO_3$:Fe and its small-polaron-based microscopic interpretation,” Phys. Rev. B **83**(16), 165106 (2011).
17. A. Sanson, A. Zaltron, N. Argiolas, C. Sada, M. Bazzan, W. G. Schmidt, and S. Sanna, “Polaronic deformation at the $Fe^{2+/3+}$ impurity site in Fe:$LiNbO_3$ crystals,” Phys. Rev. B **91**(9), 094109 (2015).
18. M. G. Clark, F. J. DiSalvo, A. M. Glass, and G. E. Peterson, “Electronic structure and optical index damage of iron-doped lithium niobate,” J. Chem. Phys. **59**(12), 6209–6219 (1973).
19. B. Dischler, J. Herrington, A. Räuber, and H. Kurz, “Correlation of the photorefractive sensitivity in doped $LiNbO_3$ with chemically induced changes in the optical absorption spectra,” Solid State Commun. **14**(11), 1233–1236 (1974).
20. L. Kovács, G. Ruschhaupt, K. Polgár, G. Corradi, and M. Wöhlecke, “Composition dependence of the ultraviolet absorption edge in lithium niobate,” Appl. Phys. Lett. **70**(21), 2801–2803 (1997).
21. J. R. Carruthers, G. E. Peterson, M. Grasso, and P. M. Bridenbaugh, “Nonstoichiometry and Crystal Growth of Lithium Niobate,” J. Appl. Phys. **42**(5), 1846–1851 (1971).
22. T. Volk and M. Wöhlecke, *Lithium Niobate: Defects, Photorefraction and Ferroelectric Switching*, Springer Series in Materials Science (Springer Berlin Heidelberg, 2008).
23. H. Kurz, E. Krätzig, W. Keune, H. Engelmann, U. Gonser, B. Dischler, and A. Räuber, “Photorefractive centers in $LiNbO_3$, studied by optical-, Mössbauer- and EPR-methods,” Appl. Phys. **12**(4), 355–368 (1977).
24. D. Berben, K. Buse, S. Wevering, P. Herth, M. Imlau, and T. Woike, “Lifetime of small polarons in iron-doped lithium–niobate crystals,” J. Appl. Phys. **87**(3), 1034–1041 (2000).
25. F. Klose, M. Wöhlecke, and S. Kapphan, “UV-excited luminescence of $LiNbO_3$ and $LiNbO_3$:Mg,” Ferroelectrics **92**(1), 181–187 (1989).
26. P. Herth, D. Schaniel, T. Woike, T. Granzow, M. Imlau, and E. Krätzig, “Polarons generated by laser pulses in doped $LiNbO_3$,” Phys. Rev. B **71**(12), 125128 (2005).
27. M. V. Ciampolillo, A. Zaltron, M. Bazzan, N. Argiolas, and C. Sada, “Quantification of Iron (Fe) in Lithium Niobate by Optical Absorption,” Appl. Spectrosc. **65**(2), 216–220 (2011).
28. R. T. Williams and M. N. Kabler, “Excited-state absorption spectroscopy of self-trapped excitons in alkali halides,” Phys. Rev. B **9**(4), 1897–1907 (1974).
29. R. Williams and K. Song, “The self-trapped exciton,” J. Phys. Chem. Solids **51**(7), 679–716 (1990).
30. P. Li, S. Gridin, K. B. Ucer, R. T. Williams, and P. R. Menge, “Picosecond absorption spectroscopy of self-trapped excitons and transient Ce states in $LaBr_3$ and $LaBr_3$:Ce,” Phys. Rev. B **97**(14), 144303 (2018).

A.3 Dynamic-grating-assisted energy transfer between ultrashort laser pulses in lithium niobate

- Stefan Nolte, Bjoern Bourdon, Felix Freytag, Mirco Imlau, Alexandr Shumelyuk, and Serguey Odoulov
  Dynamic-grating-assisted energy transfer between ultrashort laser pulses in lithium niobate
  Opt. Express **26**, 21558-21573 (2018); doi: 10.1364/OE.26.021558.

Research Article Vol. 26, No. 17 | 20 Aug 2018 | OPTICS EXPRESS 21558

Optics EXPRESS

Dynamic-grating-assisted energy transfer between ultrashort laser pulses in lithium niobate

STEFAN NOLTE,[1] BJOERN BOURDON,[1] FELIX FREYTAG,[1] MIRCO IMLAU,[1,*] ALEXANDR SHUMELYUK,[2] AND SERGUEY ODOULOV[2]

[1] *Department of Physics, Osnabrueck University, Barbarastrasse 7, D-49076 Osnabrueck, Germany*
[2] *Institute of Physics, National Academy of Sciences, 03650 Kyiv, Ukraine*
[*] *mimlau@uni-osnabrueck.de*

Abstract: Energy redistribution between two subpicosecond laser pulses of 2.5 eV photon energy is observed and studied in congruent, nominally undoped $LiNbO_3$, aiming to reveal the underlying coupling mechanisms. The dependences of pulse amplification on intensity, frequency detuning and pulse duration point to two different contributions of coupling, both based on self-diffraction from a recorded dynamic grating. The first one is caused by a difference in pulse intensities (transient energy transfer) while the second one originates from a difference in pulse frequencies. The latter appears when chirped pulses are mutually delayed in time. A quite high coupling efficiency has been observed in a 280 µm thin crystal: one order of magnitude energy amplification of a weak pulse and nearly 10% net energy enhancement of one pulse for the case of equal input intensities.

1. Introduction

The intensity coupling of two light waves that propagate in a nonlinear medium (two-beam coupling) is one of the basic phenomena of dynamic holography [1]. This type of coupling has attracted the interest of researchers since the discovery in 1980's of unidirectional intensity transfer between two waves that are recording a shifted phase grating in a nonlinear optical crystal (see, e.g., [2, 3]). A new type of coherent light wave amplification became possible, various dynamic-grating-based coherent optical oscillators were designed and used as self-starting phase conjugate mirrors [4].

In the early stage of the dynamic holography, emphasis was put on the intensity coupling of continuous waves (cw), both in theory and in experiment. Quite quickly the developed approaches were extended for the description of the interaction of light pulses. The term "two-beam coupling" was still used to define the interaction of pulses (see, e.g., [5–7]), but it became often replaced by "pulse energy transfer" [8–12] or "energy exchange" [13]. The researchers dealing with pump-probe techniques were facing the problem of so called "coherent peaks" [14, 15], which is a consequence of pump and probe pulse coupling via a dynamic grating, too [16]. It should be mentioned that the fundamental phenomenon of gain in stimulated Rayleigh-wing scattering had been treated well before the appearance of femtosecond lasers [17–21], but never in terms of diffraction from a grating. A comprehensive analysis of pulse coupling is given in the review article [22] and textbooks [23, 24]. More than a hundred original publications that consider different aspects of grating-assisted interaction of pulses have been published.

The self-diffraction of the recording pulses themselves, or diffraction of an auxiliary probe pulse from the developing instantaneous or inertial grating, are still studied nowadays [25]. It has been used for the characterization of the pulses themselves [26, 27], plasma filament control in air [6] and nonlinear liquids [11], nonlinear spectroscopy of the materials themselves [7, 13], frequency conversion [28, 29], etc. The subpicosecond pulses even allowed, quite counter-intuitively, for grating recording with light being strongly nondegenerate in frequency [30]. Both, dynamic

#330440 https://doi.org/10.1364/OE.26.021558
Journal © 2018 Received 26 Apr 2018; revised 9 Jul 2018; accepted 9 Jul 2018; published 7 Aug 2018

and permanent gratings were recorded. The recording of static holograms with image bearing pulses proved to be possible with subpicosecond pulses of different color, with further image reconstruction by a cw laser beam [30].

Commonly, the description of grating-assisted pulse interaction is based on the solution of coupled wave equations for a spatial variation of slowly varying complex amplitudes (see, e.g., [2, 3, 22–24]). While these equations are nearly always the same, the material equations, which are necessary to calculate the temporal dynamics of interaction, depend on the particular nonlinear medium and the particular type of nonlinearity involved. The present work is an experimental study in which the measured dependences are compared with predictions of already existing theories that describe particular coupling processes. We conduct this study to estimate the strength of the coupling of subpicosecond pulses in $LiNbO_3$ and to reveal the types of underlying wave mixing process(es) that is (are) responsible for an energy redistribution between the interacting pulses. Lithium niobate was the first crystal in which a photorefractive nonlinearity and grating-assisted intensity redistribution of the recording waves have been discovered [4, 31]. Apart from the instantaneous high-frequency Kerr nonlinearity [32] and two-photon absorption (TPA) nonlinearity [33], several inertial nonlinear responses have been revealed, too. They include photoexcitation of free carriers [34, 35], and the formation of various kinds of polarons [36]. The identification of the physical process of nonlinearity that is responsible for the investigated pulse coupling will be, however, the topic of a separate study.

The structure of the present paper is as follows. After this *Introduction*, the section *Experimental technique* presents the description of chirped femtosecond laser pulses, the nonlinear optical crystal itself, and the experimental setup. The third section, the *Experimental results*, consists of four parts, devoted to particular sets of measurements. In subsection 3.1 a small signal amplification is studied, with a weak probe pulse which interacts with a stronger pump pulse, both pulses being perfectly matched in time. Subsection 3.2, on the opposite, focuses on the interaction of pulses of equal energies that become detuned in frequencies being temporally mismatched. In subsection 3.3 the effect of the pulse duration is analyzed for the interaction of identical pulses. Finally, in the last subsection 3.4, a possible influence of extended temporal spectra of ultrashort pulses on their energy coupling is analyzed. In the *Discussion* section it is shown that the major contribution to energy transfer between subpicosecond pulses in congruent, nominally undoped $LiNbO_3$ is due to two different coupling processes: (*i*) quasi steady-state coupling of waves of equal intensity with mutually shifted frequencies and (*ii*) transient, non-steady-state coupling of waves of different intensities but with identical spectra. The first process was already proven to be responsible for the interaction of frequency-chirped pulses in gases, plasma and liquids (see, e.g., [6, 7, 11, 13]). Our study shows that it results in a quite strong pulse interaction in a solid-state material as well. The second process has never been considered, to the best of our knowledge, for the interaction of short pulses in spite of the fact that it was revealed long ago for interactions in photorefractive crystals [37] and media with a thermal nonlinearity [38, 39].

2. Experimental technique

All experiments in this paper are performed with a classical interaction geometry of two-beam coupling of co-propagating light beams which is also standard for pump-probe techniques. Figure 1 shows schematically the experimental setup used for our studies. Two ultrashort light pulses with equal central wavelengths of $\lambda = 488\,\mathrm{nm}$ (or $\lambda = 590\,\mathrm{nm}$) impinge upon a $LiNbO_3$ sample with a full crossing angle in air of $2\theta < 5^\circ$. A relatively small angle can be set by the use of a single focusing lens (L) for both pulses to ensure a good spatial overlap of the femtosecond pulses. An optical delay line (DL) is installed in one of the two beams to adjust a temporal mismatch Δt between both pulses of up to several picoseconds.

The main measured characteristic in this paper is the normalized transmission $T_i = W_i/W_i^0$ for each of the two interacting pulses (subscripts pu and pr for pump and probe pulses, respectively).

Here, W_i denotes the transmitted pulse energy of one pulse in presence of the other pulse, while W_i^0 is the energy of the unaffected transmitted pulse, with no other pulse in the sample. The transmission T_i is measured as a function of different experimental parameters: total intensity of the two pulses I, pulse intensity ratio $R = I_{\mathrm{pu}}/I_{\mathrm{pr}}$, temporal delay between the two pulses Δt, and FWHM pulse duration τ_{c}. These data make it possible to evaluate a weak-probe gain G_{wp} (when the probe pulse propagates in presence of a stronger pump pulse) and a strong-probe gain G_{sp} (in case of energy transfer between pulses with equal energies), as it is explained in the next sections. The energies of the incident and transmitted pulses are measured with a laser power meter (*Coherent LabMax*) as well as biased silicon detectors (*Thorlabs DET10A*).

The y-cut sample of congruent, nominally undoped lithium niobate with plane parallel input/output faces has a thickness of $d \approx 280\,\mu\mathrm{m}$. At the particular wavelength of $\lambda = 488\,\mathrm{nm}$ the pronounced two-photon absorption and small polaron absorption have been reported [36, 40]; the coefficients of two-photon absorption, $\beta_{\mathrm{TPA}} \simeq 5.6\,\mathrm{mm/GW}$, and optical Kerr effect, $n_2 \simeq 5 \cdot 10^{-20}\,\mathrm{m^2/W}$, are known from z-scan experiments [40].

The femtosecond pulses are generated by a mode-locked Ti:Sapphire laser (*Coherent, Libra*) that feeds two independently tunable Optical Parametric Amplifiers (OPA, *Coherent, OPerA-Solo*) [29, 30]. Pulses with central wavelengths of $\lambda = 488\,\mathrm{nm}$ and spectral bandwidths of $\Delta\lambda = 4.7\,\mathrm{nm}$ from only one OPA are used for frequency non-degenerated experiments, unless otherwise stated. The central wavelength and spectral bandwidth of the interacting pulses are monitored with a fiber spectrometer (*Ocean Optics, USB4000*).

To evaluate the peak intensity $I_{\mathrm{pu,pr}}$ of a pulse with an energy W, its spatial and temporal profiles need to be known. Measurements of the transverse intensity distribution at the sample input face revealed a Gaussian-like shape of both beams with nearly identical radii of $r \approx 55\,\mu\mathrm{m}$ at the e^{-2} level of the peak intensity. The durations τ_{c} of the incident pulses are estimated with a commercial autocorrelator (*APE, pulseCheck PD15*) assuming a Gaussian temporal intensity profile with peak value:

$$I = \sqrt{\frac{16\ln(2)}{\pi^3}}\,\frac{W}{r^2\tau_{\mathrm{c}}}\,. \tag{1}$$

The pulse energies W (and therefore the peak intensities I) of the two pulses were controlled by using variable neutral density filters (VFs) so that different ratios $R = I_{\mathrm{pu}}/I_{\mathrm{pr}}$ could be adjusted. The pulse duration could be changed within a range of $\tau_{\mathrm{c}} = (80 - 830)\,\mathrm{fs}$ using a pulse

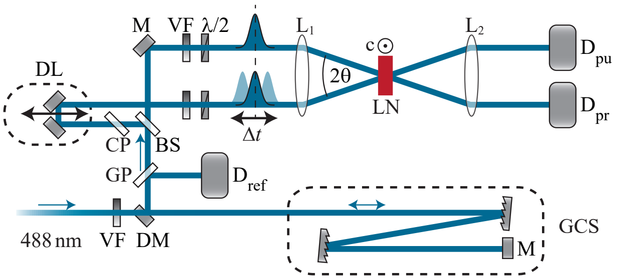

Fig. 1. Schematic of the experimental setup: variable neutral density filter (VF), double grating compressor/stretcher (GCS), glass plate (GP), 50/50 beamsplitter (BS), compensator plate (CP), optical delay line (DL), mirror (M), D-shaped mirror (DM), $\lambda/2$-waveplate, lenses $f = 500\,\mathrm{mm}$ ($\mathrm{L}_{1,2}$), full crossing angle in air 2θ, lithium niobate sample (LN) with the polar **c**-axis normal to the plane of drawing, and silicon detectors ($\mathrm{D_{ref}}$, $\mathrm{D_{pu}}$ and $\mathrm{D_{pr}}$).

Research Article
Vol. 26, No. 17 | 20 Aug 2018 | OPTICS EXPRESS 21561
Optics EXPRESS

compressor/stretcher (GCS). A folded double-grating setup allows for introducing a negative pulse chirp in our experiment. Otherwise, a double prism setup could be used to impose a positive pulse chirp, profiting from the material dispersion (N-SF11 glass, for example).

The spectral bandwidth $\Delta\omega = 3.7 \cdot 10^{13}$ rad/s of the Gaussian shaped pulses defines the theoretically smallest, Fourier-transform-limited pulse duration of $\tau_0 = 75$ fs. For deliberately stretched pulses the frequency chirp coefficient $\dot{\omega}$ depends on the pulse duration τ_c (cf. [41]):

$$\dot{\omega} = (\Delta\omega/\tau_c)\sqrt{1-(\tau_0/\tau_c)^2}. \tag{2}$$

The total peak intensity $I = I_{pu} + I_{pr}$ never exceeded 640 GW/cm^2 to avoid laser-induced damage of the sample. The kHz repetition rate of the pulse train was reduced by an optical chopper to 12.5 Hz. All coupling processes under investigation emerge in a single pulse shot and no cumulative effects have been observed for repetitive-rate operation. This enabled us to average data of 200 consecutive pulses to reduce the impact of pulse-to-pulse fluctuations and to improve accuracy.

Both interacting pulses enter the sample in a plane perpendicular to the axis of spontaneous polarization **c**. The light polarization could be adjusted to each beam independently by two $\lambda/2$ phase retarders, with care taken to avoid possible changes in the temporal delay Δt between the pulses. Usually, the polarization unit vectors are set parallel to the polar axis, $\mathbf{e}_1 \parallel \mathbf{e}_2 \parallel \mathbf{c}$, unless stated otherwise. This particular configuration excludes a possible contribution to pulse coupling from the space charge field grating because the relevant Pockels tensor components of LiNbO$_3$ are vanishing (see, e.g., [42]).

3. Experimental results

3.1. Coupling of pulses with different energies

We start from the description of experiments with pulses of significantly different energies that allow to characterize a weak-probe gain G_{wp}. Figure 2 gives a typical example of the probe pulse transmission in presence of a pump pulse with the same polarization $T_\parallel$ as a function of the temporal delay Δt between both pulses (black data points). The pulse duration of each pulse $\tau_c \approx 80$ fs is close to the Fourier limit τ_0. The transmission $T_\parallel(\Delta t)$ features a considerable increase in the vicinity of $\Delta t = 0$ with a maximum value of $T \approx 2.3$. An asymmetry of the signal

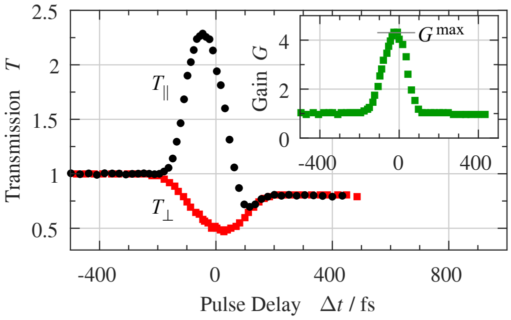

Fig. 2. Pulse delay dependence of the normalized probe pulse transmission with parallel ($T_\parallel$, black dots) and orthogonal polarization ($T_\perp$, red squares). The inset shows the gain G (green squares) evaluated from Eq. (3). The total peak intensity of the two pulses is $I \approx 635$ GW/cm^2 with a peak intensity ratio of $R \approx 100$, pulses duration of $\tau_c = (80 \pm 5)$ fs and beam radii of $r = (55 \pm 5)$ µm.

Research Article Vol. 26, No. 17 | 20 Aug 2018 | OPTICS EXPRESS 21562
Optics EXPRESS

$T_{\|}(\Delta t)$ is obvious, with the transmission saturated at $T_{\|}^{\mathrm{sat}} \approx 0.8$ for large positive Δt. This value of $T_{\|}^{\mathrm{sat}}$ below unity can be attributed to the light-induced absorption caused by optically generated small, strong-coupling polarons [33, 36].

It is noteworthy that the appearance of additional oblique beams behind the sample has been detected within the Δt interval where probe amplification occurs ($T \geq 1$) . Their angular position suggests that these are higher orders of diffraction from a grating recorded with the two incident pulses. The largest overall energy of these higher diffraction orders could approach 10% of the total transmitted energy.

The transmission of the probe pulse changes dramatically if the polarization of the pump pulse is turned to 90°, as depicted by the red data points. Here, the transmission $T_{\perp}$ shows a dip in the vicinity of $\Delta t = 0$ that can be attributed to the effect of two-photon absorption [33]. In agreement with this assumption, we found that the temporal width of this dip depends on the duration τ_{c} of the incident pulses, while possible broadening of the dip caused by the group velocity mismatch can be neglected for the used thin birefringent crystal. The saturation is again reached at $T_{\perp}^{\mathrm{sat}} \approx 0.8$.

From the comparison of both curves in Fig. 2 one can deduce that in presence of the pump pulse with the same polarization the probe pulse experiences simultaneously attenuation and gain. The attenuation is caused by two-photon absorption, polaron absorption, and the appearance of higher diffraction orders. It is the diffraction of the strong pump pulse into the weak probe which is responsible for amplification.

A simplified approach can be used to account for all these processes. It represents the normalized transmission of the probe pulse $T(\Delta t)$ as a product of two factors $A(\Delta t)$ and $G(\Delta t)$ that describe the fractional changes of transmission which are due to losses and gain, respectively. As all losses can only decrease the transmission, A should be smaller than unity but should remain always positive, $0 \leq A \leq 1$. The gain factor G is always larger than unity but it is limited by the intensity ratio R of the interacting pulses $1 \leq G \leq R + 1$, as energy can be transferred to the probe only from the pump pulse.

For further analysis, the energy gain is introduced as an experimentally measurable quantity

$$G(\Delta t) = \frac{T_{\|}(\Delta t)}{T_{\perp}(\Delta t)} = \frac{A(\Delta t) G(\Delta t)}{A(\Delta t)}, \tag{3}$$

i.e., the ratio of the transmission with identically polarized $T_{\|}$ (gain and losses) and cross-polarized $T_{\perp}$ (losses only) pump and probe pulses. According to Eq. (3), the ratio $T_{\|}(\Delta t)\,/\,T_{\perp}(\Delta t)$ is not affected by nonlinear absorption $A(\Delta t)$. Such a treatment is justified under the assumption that both, the instantaneous losses for TPA as well as losses for residual polaron absorption, exhibit a negligible polarization dependence [36, 43]. A small difference in $A(\Delta t)$ for ordinary and extraordinary pump waves can therefore be neglected. The pulse delay dependence of the gain $G(\Delta t)$ extracted in such a way is shown in the inset to Fig. 2; the value of $G^{\max} = (4.4 \pm 0.2)$ is reached in the vicinity of $\Delta t = 0$.

The gain intensity dependence as well as its intensity ratio dependence are important characteristics for the identification of a particular coupling process. Figure 3 shows the gain $G^{\max}$ as a function of peak intensity for the shortest pulses used ($\tau_{\mathrm{c}} \simeq 80\,\mathrm{fs}$) and two different ratios of the peak intensities R. A nonlinear increase of the gain is observed for intensities I below 300 GW/cm^2 for both values of R. Within the quite large error bars the data can be fitted by a $I^{2.5}$ dependence.

The gray area in Fig. 3 represents the possible range of gain variation only for the black squares ($R \approx 1000$). Both dependences, for $R \approx 1000$ and $R \approx 100$, show an obvious tendency to saturation of the gain at high intensities, with saturation level decreasing for $R \longrightarrow 1$.

Figure 4 shows the gain $G(\Delta t = 0)$ as a function of the input pump/probe peak intensity ratio R while keeping the total peak intensity I constant. The logarithmic plot used here underlines

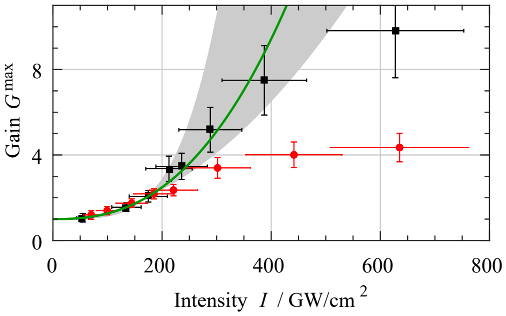

Fig. 3. Gain $G^{\max}$ versus total pulse peak intensity I. Black and red symbols show the data for the intensity ratios $R \approx 1000$ and $R \approx 100$, respectively, for pulses with durations $\tau_c = (80 \pm 5)$ fs and beam radii $r = (55 \pm 5)$ µm. For intensities below 300 GW/cm^2 the measured data can be fitted with $G^{\max}$-1 $\propto I^{\mathrm{m}}$. For R = 1000 such a fit gives m = 2.5 (green line); the gray shaded area is limited by functions with the exponents 2 < m < 4.

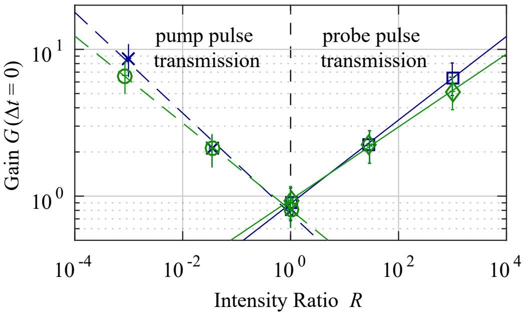

Fig. 4. Gain $G(\Delta t = 0)$ versus peak intensity ratio R in a log-log plot. Right and left branches show the experimentally measured gain for weak probe and weak pump pulses, respectively. The total peak intensity of two pulses is $I \approx 630$ GW/cm^2 (blue) and $I \approx 380$ GW/cm^2 (green) with pulses duration $\tau_c = (80 \pm 5)$ fs and beam radii $r = (55 \pm 5)$ µm. Solid and dashed lines are plotted as a guide to the eye.

that the energy flows always from the strong to the weak pulse. For $R \leq 1$ the peak intensity of the probe pulse becomes larger than that of the pump, and the measured gain G is related here to the normalized pump pulse transmission. It is obvious that the gain $G(\Delta t = 0)$ increases with growing R and vanishes for equal peak intensities $R = 1$ for a weak probe pulse. Similarly, for $R \leq 1$ the gain of a weak pump pulse increases with R^{-1}. The branches for $R \leq 1$ and $R \geq 1$ are basically symmetric, with approximately the same absolute exponent for the intensity ratio dependence $G \propto R^{\pm 0.3}$. The fact that the measured values of gain $G(\Delta t = 0)$ at $R = 1$ are roughly 10% smaller than unity indicates that additional losses exist besides those already accounted for TPA and polaron absorption. These losses are due to the light going into higher orders of diffraction. They become the most significant for a 1 : 1 intensity ratio of the recording pulses.

The measured dependences of gain [Figs. 3 and 4] are typical for transient beam coupling [37–39] what will be explained in details in section 4, Discussion.

3.2. Coupling of pulses with equal energies

As it was demonstrated in the previous subsection no energy redistribution occurs between two perfectly synchronized pulses ($\Delta t = 0$) with equal energies [see Fig. 4]. In what follows we show that even with $R = 1$ an energy redistribution becomes possible when a temporal mismatch between two frequency-chirped pulses is introduced. Two pulses with equal energies are chosen in these experiments to avoid any possible energy flow from a strong to a weak pulse.

It is known that the removal of frequency degeneracy of two recording waves may result in a strong intensity coupling, both for interactions of continuous waves [2] and sub-picosecond pulses [13,21,44]. The pulse delay of two otherwise identical pulses with a linear frequency chirp $\dot{\omega}$ [see Eq. (2)] is used in our further experiments to adjust a controllable frequency detuning Ω. Both pulses, still called pump and probe in a formal way, have time-dependent frequencies $\omega_{\mathrm{pr,pu}}(t) = \omega_0 + \dot{\omega}t$. Thus, for any non-zero Δt an instantaneous frequency detuning $\Omega(\Delta t)$ appears that does not depend on time:

$$\Omega(\Delta t) = \omega_{\mathrm{pr,pu}}(t - \Delta t) - \omega_{\mathrm{pu,pr}}(t) = -\dot{\omega} \cdot \Delta t\,. \tag{4}$$

Figure 5(a) gives a representative example of the pulse delay dependence of the normalized transmission $T_{\mathrm{pr,pu}}(\Delta t)$ for two identical pulses, i.e., with the same peak intensity ($R = 1$), chirp coefficient, polarization, pulse duration, beam radius, central wavelength, spectral width and symmetrical angles of incidence [as shown in Fig. 1]. The labeling of pulses as pump and probe is a matter of convention here because both pulses are indistinguishable. However, the sign of the temporal delay is chosen in such a way that for positive values of Δt, the pump pulse passes the sample prior to the probe pulse.

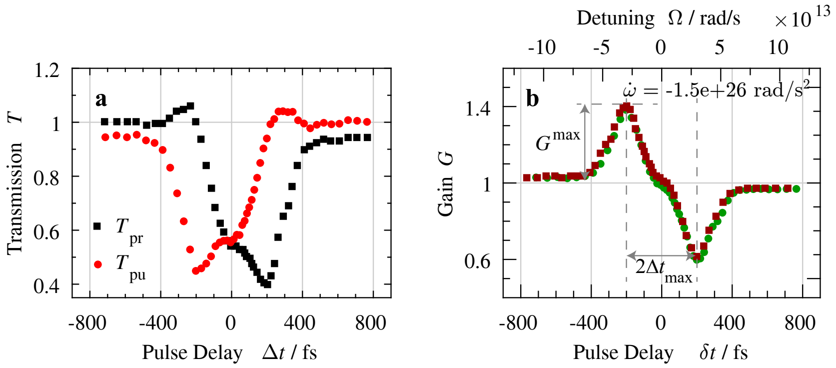

Fig. 5. Pulse delay dependences of (a) normalized transmission $T(\Delta t)$ for pump and probe pulses and (b) gain $G(\delta t)$ evaluated according Eq. (5) (with flipped curve $\delta t = -\Delta t$ for the data T_{pu}). Each pulse has an energy of $W = (5.1 \pm 0.1)\,\mu\mathrm{J}$, a pulse duration of $\tau_c \approx 235$ fs and a bandwidth of $\Delta\omega = 3.7 \times 10^{13}$ rad/s. The beam radii are $r \approx 160\,\mu\mathrm{m}$ and the sum of the peak intensities of both pulses is $I \approx 100\,\mathrm{GW/cm^2}$.

First of all, in Fig. 5(a) a mirror symmetry is obvious for the two curves that define pump and probe transmission. This symmetry could be expected because the advanced pulse becomes the delayed pulse (and vice versa) when the pulse temporal mismatch Δt changes its sign. For this reason the axis of symmetry can be used to find the position of perfect temporal overlap of the pulses $\Delta t = 0$. At this particular position the transmission values are nearly the same for both pulses, thus indicating no energy redistribution. This is in agreement with the data of Fig. 4 for $G(\Delta t = 0)$ at $R = 1$, where only additional losses and no energy redistribution have been detected.

As distinct from the data of Fig. 2, the maximum of the pulse transmission T is reached now at a much longer pulse delay; it approaches 1.1 roughly at $\Delta t \simeq \pm 260$ fs. The transmission of the second pulse shows a pronounced dip at the same time, thus indicating that the energy gain of one pulse is caused by a depletion of the other one.

In this new set of measurements with $R = 1$ the transmission is measured for both interacting pulses simultaneously. This allows for estimating the gain G without an additional measurement of the transmission for orthogonally polarized pulses. New expressions for G are derived instead of Eq. (3), still maintaining the same definition of the normalized transmission as a product of loss and gain factors $T(\Delta t) = A(\Delta t)G(\Delta t)$. It is assumed, however, that the pulse delay dependent loss factors are the same for both pulses $A_{\mathrm{pr}}(\Delta t) = A_{\mathrm{pu}}(\Delta t)$. As a consequence, the transmission ratio of both pulses appears to be equal to the ratio of the pulse energy gain $T_{\mathrm{pr}}(\Delta t)/T_{\mathrm{pu}}(\Delta t) = G_{\mathrm{pr}}(\Delta t)/G_{\mathrm{pu}}(\Delta t) = P(\Delta t)$ and it becomes possible to quantify the gain factors as follows:

$$G_{\mathrm{pr}}(\Delta t) = \frac{2P(\Delta t)}{1 + P(\Delta t)} \quad , \quad G_{\mathrm{pu}}(\Delta t) = \frac{2}{1 + P(\Delta t)} \quad . \tag{5}$$

The G values defined by Eq. (5) cannot exceed $G = 2$ for both interacting pulses, what corresponds to a total energy transfer from one pulse to the other. Therefore, the "gain" of the depleted pulse cannot become smaller than $G = 0$; $G = 1$ still indicates no pulse amplification. Because of energy conservation the sum of these two gain parameters should always be constant $G_{\mathrm{pr}}(\Delta t) + G_{\mathrm{pu}}(\Delta t) = 2$.

Figure 5(b) represents the time delay dependence of the gain G replotted from the data of Fig. 5(a) according to Eq. (5). A new variable δt is introduced to pin the gain measured for the delayed pulse always to positive values of δt. Thus, δt coincides with Δt for the black curve of Fig. 5(a) and is inverted in its sign for the red data points $\delta t = -\Delta t$. This change of the pulse delay variable in Fig. 5 does not only underline the similarity of the shown curves, it further allows for adding a second axis for the frequency detuning Ω as estimated from Eq. (4). The data of Fig. 5(b) indicate an energy flow from the delayed to the advanced pulse, i.e., from the pulse with higher frequencies to the pulse with lower frequencies. It should be noted that the coupling direction is insensitive to the LiNbO$_3$ sample rotation to 180° along the z-axis as well as along the x-axis. The gain extrema are separated by $2\Delta t_{\mathrm{max}} \approx 400$ fs and the maximum gain reaches $G^{\mathrm{max}} \approx 1.4$. This pulse delay, that ensures the strongest coupling, corresponds to a certain fixed frequency detuning of $\Omega_{\mathrm{max}} = 3.0 \times 10^{13}$ rad/s.

The assumption $A_{\mathrm{pr}}(\Delta t) = A_{\mathrm{pu}}(\Delta t)$ that has been formulated when deriving Eq. (5) can be justified as follows: within the area of strong temporal overlap of two pulses, $|\Delta t| \leq 2\tau_c$, the dominant losses are due to two-photon absorption and diffraction into higher orders, whereas the contribution of residual absorption from small polarons is much smaller. The latter can only be seen for large values of $|\Delta t|$ with transmission values slightly below unity. Because of the small magnitude of the polaron absorption in comparison to instantaneous losses, its impact on the gain evaluation should be minor. This estimate is supported by the data of Fig. 5(b), where the deviation of the gain from unity is hardly detectable for large pulse delays $|\delta t|$, and is much smaller than the maximum gain.

In the measurements presented above, the sign of the chirp coefficient is imposed to be negative $\dot{\omega} < 0$, resulting from the negative dispersion introduced by the grating compressor. To verify the sensitivity of the energy transfer direction to the sign of the frequency chirp, the latter was reversed to become positive $\dot{\omega} > 0$ by profiting from the material dispersion of a double prism compressor (N-SF11 dense flint glass).

In Fig. 6 the left and right graphs show the time delay dependences of G for pulses with negative and positive chirp coefficients $\dot{\omega}$, respectively. It is obvious that the flip of the chirp sign results in a change of the energy flow direction, whereas their extrema still occur roughly at same detunings Ω. The difference in gain magnitudes in Fig. 6(a) and Fig. 6(b) might be caused

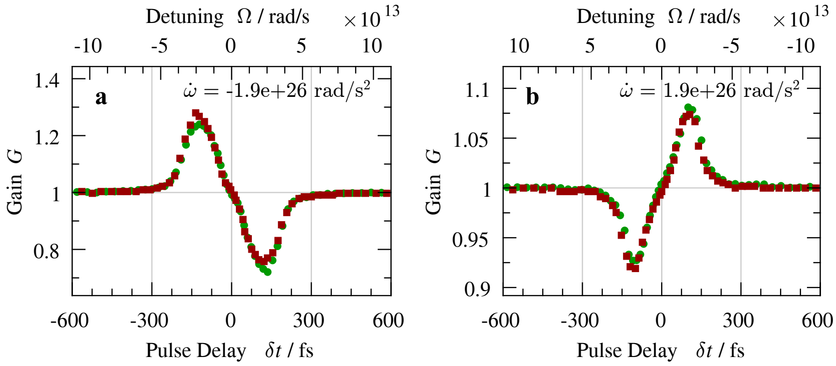

Fig. 6. Pulse delay dependence of gain $G(\delta t)$ for (a) pulses with a negative frequency chirp and energies $W = (2.6 \pm 0.1)\,\mu$J and (b) pulses with a positive frequency chirp and energies $W < 2\,\mu$J. Identical pulses are used, with central wavelengths $\lambda = 590$ nm, bandwidths of $\Delta\omega = 4.0 \times 10^{13}$ rad/s and durations $\tau_c \approx 200$ fs. The pulse frequency detuning Ω estimated according to Eq. (4) is shown as the upper x-axis. Red and green colors mark two interacting pulses.

by different pulse energies. It should be mentioned that these measurements are performed at a higher wavelength ($\lambda = 590$ nm) than previous measurements. The two-photon absorption coefficient is smaller for higher wavelength and the residual absorption of photogenerated small polarons is reduced, too. As a consequence, the deviation of the gain from unity in a range of large pulse delays becomes basically undetectable.

The position of gain extrema can be used to determine the optimum frequency detuning for the pulses to ensure the highest energy transfer: $\Omega_{\text{max}} = 2.4 \times 10^{13}$ rad/s for Fig. 6(a) and $\Omega_{\text{max}} = 2.0 \times 10^{13}$ rad/s for Fig. 6(b). The measured dependences of gain are obviously antisymmetric (odd) functions, i.e., the change of the detuning sign results in the inversion of the energy transfer direction. This leads to the conclusion that in this set of measurements the reason of the pulse energy coupling is the frequency difference of the two pulses.

3.3. Pulse duration dependence

The pulse-delay dependences of gain, similar to that shown in Fig. 5(b), are collected in the next set of experiments for negatively chirped pulses of different durations τ_c. A double grating pulse stretcher is used to control τ_c, sketched in Fig. 1. The measured data are used to plot in Fig. 7(a) the dependence of the largest values of the gain $G^{\text{max}}(\tau_c)$ versus pulse duration (red dots). In the same Fig. 7(a) one can see how the temporal mismatch of the interacting pulses $\Delta t_{\text{max}}(\tau_c)$, which is necessary to ensure G^{max}, varies with the pulse duration (black squares).

The maximum gain increases with the pulse duration up to $\tau_c \approx 300$ fs; for longer pulses it saturates at $G^{\text{max}} \approx 1.45$. At the same time, the pulse duration dependence of the largest gain position is linear: $\Delta t_{\text{max}} = \epsilon\tau_c$, and can be fitted with a slope of $\epsilon \simeq 0.9$.

According to Eq. (2), the chirp coefficient $\dot{\omega}$ depends on the chirped pulse duration τ_c, as it is shown by the gray shaded curve in Fig.7(b). For long pulses $\dot{\omega}$ is inversely proportional to the pulse duration τ_c (see hyperbolic asymptote shown with black dots); it decreases, however, in the vicinity of the Fourier-limited pulse duration $\tau_0 \approx 75$ fs. The measured temporal mismatch, which is necessary for reaching the maximum gain Δt_{max}, can be used for the evaluation of a corresponding frequency detuning $\Omega_{\text{max}} = -\dot{\omega}\Delta t_{\text{max}}$. The result is plotted with blue squares in Fig. 7(b) for different pulse durations τ_c. For long pulses with $\tau_c > 300$ fs the largest gain is

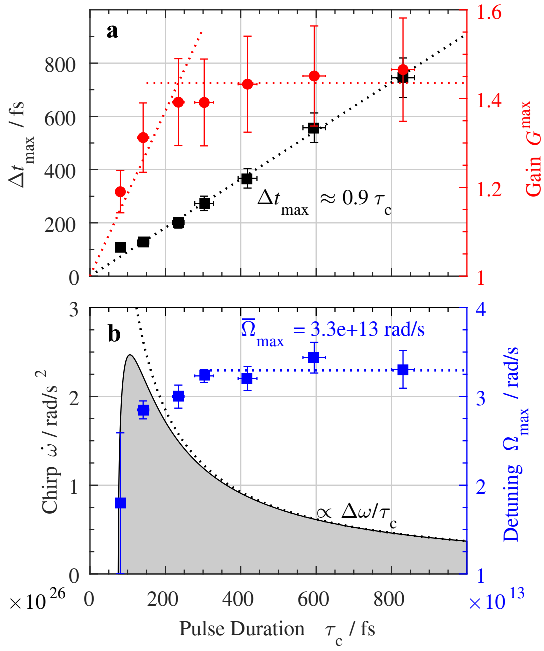

Fig. 7. (a) Pulse duration dependences of largest gain $G^{\max}$ (red dots) and pulse temporal mismatch that ensures this largest gain $\Delta t_{\max}$ (black squares). The red dotted lines are guiding the eye, while the black dotted line is a linear fit. (b) Pulse duration dependences of the chirp coefficient $\dot{\omega}$ (gray shaded curve) and pulse frequency difference that provides the maximum gain $\Omega_{\max}$ (blue squares), extracted from the data plotted in (a). The blue dotted line represents $\bar{\Omega}_{\max}$, the mean value of data above $\tau_c = 300$ fs. A hyperbolic dependence $\propto 1/\tau_c$ (black dots) shows the asymptotic behavior of the chirp coefficient $\dot{\omega}$ for long pulses. Both pulses have the same central wavelengths $\lambda = 488$ nm and bandwidths of $\Delta\omega = 3.7 \times 10^{13}$ rad/s.

always reached roughly at the same frequency detuning $\bar{\Omega}_{\max} = 3.3 \times 10^{13}$ rad/s (dotted blue line); this optimum detuning value decreases for shorter pulses. The same constant value of $\Omega_{\max}$ can be extracted by combining Eq. (2) and Eq. (4):

$$\Omega_{\max} = \frac{\Delta\omega}{\tau_c}\epsilon\tau_c = \Delta\omega\epsilon \quad . \tag{6}$$

Furthermore, the ϵ value close to unity indicates that for a maximum gain the pulses are temporally separated by almost their FWHM.

Thus, the presented data confirm the conclusion of subsection 3.2 that the reason of the energy redistribution between two identical pulses nests in their frequency difference. It is shown in addition that the most efficient coupling occurs always at the same optimum detuning $\bar{\Omega}_{\max}$ within a rather wide range of pulse durations.

3.4. Coupling of frequency-shifted pulses with different energies

The results of the previous subsections allow for the conclusion that the energy transfer can appear either because of a difference in incident pulse energies (subsection 3.1) or a difference in frequencies of the two pulses (subsections 3.2 and 3.3). Whereas the origin of energy exchange for the interaction of delayed chirped pulses of equal energies can be unambiguously attributed to self-diffraction from the moving grating, caused by the frequency difference of the pulses, the non-zero gain of temporally matched, nearly Fourier-transform-limited pulses with different energies requires a more careful analysis.

At first glance, the chirp coefficient is close to zero for Fourier-transform-limited pulses and one cannot expect the removal of frequency degeneracy within the range of pulse temporal mismatch of Fig. 2. At the same time we are dealing with pulses that are not monochromatic. They possess spectra with FWHM $(3.7-4.0)\cdot 10^{13}$ rad/s, that exceed the optimum detuning $\Omega_{\max} = (2.0-3.3)\cdot 10^{13}$ rad/s [see Fig. 6(b)]. Therefore, it is not excluded that a "blue" spectral slice (with a higher frequency) in one pulse may interact with a "red" slice of lower frequency in the other pulse, and vice versa. This will not result in energy redistribution for identical pulses with the same energies because the contradirectional energy flows will fully compensate for each other. Such compensation becomes, however, only partial if two pulses have different energies; the direction of the resulting energy flow being always from the strong pulse to the weak one [cf. Fig. 4].

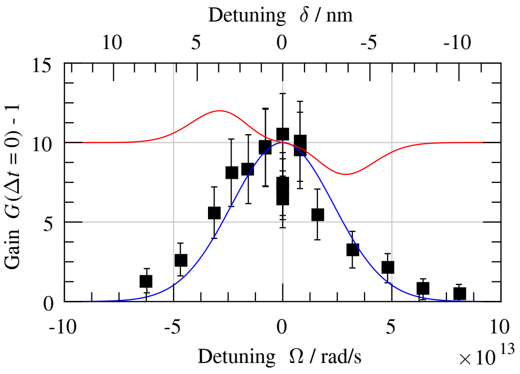

Fig. 8. Gain of a weak probe pulse G-1 versus probe-pump pulse frequency detuning $\Omega = \omega_{\mathrm{pr}} - \omega_{\mathrm{pu}}$ (black squares). Blue and red solid lines show qualitatively the expected contributions to the overall gain from transient beam-coupling and coupling from a moving grating (see text).

To clarify a possible influence of the pulse bandwidth and to identify an interaction process which is responsible for the coupling between the weak and strong pulses we have performed an additional experiment with pulses from two independently tunable OPAs. The gain of the weak probe is studied with pump and probe pulses that are matched in time but have deliberately detuned central frequencies $\Omega = \omega_{\mathrm{pr}} - \omega_{\mathrm{pu}}$.

As it was mentioned above, the enhancement of the "red" component of the weak pulse spectrum might be larger than the depletion of its "blue" component thus bringing overall amplification of the weak pulse. Assuming this explanation is valid, one can expect an increase of the measured gain for probe pulses which are gradually tuned to smaller frequencies until $\Omega_{\max}$ is reached. For increasing probe frequency, on the contrary, the gain is expected to drop down, becoming even smaller than unity at a certain positive Ω. Thus, one should see a strongly asymmetric detuning dependence of the gain, that is qualitatively similar to the slightly deformed dependence shown in Fig. 5(b).

The measured detuning spectrum of $G-1$ (filled squares) is depicted in Fig. 8. The wavelength of the pump pulse $\lambda_{\mathrm{pu}} = 488$ nm is fixed, while the probe pulse wavelength λ_{pr} is varied. The wavelength detuning $\delta = \lambda_{\text{pr}} - \lambda_{\text{pu}}$ is added as the second x-axis on the top.

The detuning dependence of Fig. 8 is only slightly asymmetric, with the maximum shifted to longer wavelength of the probe pulse (negative frequency detuning). It looks like a superposition of a dominating bell-shaped (even) and an odd function with a smaller amplitude. These two functions are shown by blue and red solid lines for guiding the eye, red line being up-shifted to the maximum of the blue one.

Thus, we can conclude that self-diffraction from a moving grating that is recorded by the "red" spectral component of the weak pulse and the "blue" spectral component of the strong pulse does exist and manifests itself in a slight asymmetry of the spectrum shown in Fig. 8. At the same time, the dominating process responsible for coupling of weak and strong pulses in this experiment and all experiments described in subsection 3.1 is the transient energy transfer [37, 38].

4. Discussion

All presented results clearly show a net gain of a probe pulse when it is interacting with a pump pulse within congruent, nominally undoped lithium niobate. This gain cannot be a consequence of sample bleaching because of a very small linear absorption of the used sample in the blue-green spectral domain ($\alpha_{488} \leq 1\,\text{cm}^{-1}$). Moreover, to become clearly visible ($T > 1$) the gain should overcome two-photon absorption, which is quite pronounced within the intensity range of the pulses used in these experiments.

As we mentioned already, we attribute the pulse coupling effects and appearance of higher diffraction orders to self-diffraction from one and the same dynamic grating. Thus, the measured efficiency of diffraction into the first non-Bragg order $\eta \approx 0.01$ allows for estimating roughly the refractive-index modulation $\Delta n \geq (\sqrt{\eta}\lambda/\pi\ell)$. With a sample thickness of $\ell = 280\,\mu\text{m}$ and a light wavelength of $\lambda \simeq 0.5\,\mu\text{m}$ we get Δn on the order of 10^{-4}. Taking into account Gaussian transverse intensity distribution, a nonuniform distribution within the sample thickness because of TPA and its nearly Gaussian temporal variation, the peak value of Δn should be much larger than 10^{-4} and quite strong coupling can be expected. At the same time, to ensure an efficient beam-coupling, the recorded grating should have a component which is $\pi/2$ shifted in phase with respect to the recording fringes [1–3]. The use of various inertial refractive $\chi^{(3)}$ nonlinearities can ensure the necessary phase shift between the grating and the fringes if two interacting waves differ in temporal frequencies and thus form a moving fringe pattern. The response of the inertial nonlinear medium is time-delayed. Therefore, the moving fringes produce a grating which propagates in space with the same speed as the fringes but with the extrema that do not coincide with the maxima of the intensity.

In lithium niobate, phase and/or amplitude gratings can be recorded by several known processes when using femtosecond excitation. The two-photon absorption and optical Kerr effect nonlinearities which have been considered previously as origin of dynamic grating recording [32, 33] are essentially instantaneous. Therefore, self-diffraction from relevant dynamic gratings cannot result in the intensity coupling of the recording waves. The TPA grating can only decrease the intensity of the probe beam while an instantaneous refractive index grating from the optical Kerr effect by definition can never be shifted in space with respect to the light fringes. Other known nonlinearities of LiNbO_3 are caused by photogeneration of excitons, free carrier and small polarons [29, 32, 35] as also by excitation of optical phonons. All mentioned nonlinearities are refractive and inertial and therefore can be involved in pulse coupling. Additional studies will be necessary to identify the origin of the nonlinearity which is responsible for pulse coupling in our experiments.

The intensity redistribution between two waves which are recording a moving index grating [2, 3, 6, 11, 13] is a well known phenomenon. It was reported for laser filaments in gases [6, 13] and in liquids [11] for subpicosecond pulses. Being not qualitatively new, this type of coupling is revealed now for the first time in a solid-state nonlinear material and shown to be very efficient.

The quantitative data for pulse coupling in a LiNbO$_3$ sample with an interaction length of only 280 μm are quite impressive: one order of magnitude amplification of the weak probe pulse energy [Fig. 3] and nearly 10% net enhancement of one of two pulses with same input energies [Fig. 6] are demonstrated. The energy is transferred from the high frequency pulse to the low frequency one with an optimum detuning of $\Omega \approx 3 \times 10^{13}$ rad/s. The frequency detuning dependences of gain G given in Fig. 6 are obviously odd functions, qualitatively similar to

$$g \propto g_0 \frac{\Omega \tau_c}{1 + \Omega^2 \tau_c^2} \ , \tag{7}$$

predicted by simple models for lossless media [see, e.g., Eq. (129) of [22]]. The gain factor g defines here the steady-state exponential gain of a weak probe beam, $I_{\text{pr}} \simeq I_{\text{pr}}^{(0)} \exp(g\ell)$. It can be expressed via G used in this article, $g \approx (G - 1)/\ell$, ℓ standing for the interaction length. The deviation of experimental dependences of Fig. 6 from the simple form expressed by Eq. (7) might be helpful for the identification of the physical origin of nonlinearity, most probably related to certain crystal lattice resonances.

Let us compare now the manifestations of weak-to-strong pulse coupling in our experiment with the results of the transient beam-coupling model [37]. Being developed for continuous wave interaction, this model predicts no intensity coupling in the steady-state and an appearance of probe wave amplification during a time interval comparable to the grating build-up or decay time τ_r. The intensity is always transferred from a strong wave into a weak one. For the initial stage of recording, $t \ll \tau_r$, the gain increases nonlinearly with intensity I, sample thickness ℓ and time t. The relationship between the relative changes of the probe intensity I_{pr} and parameters mentioned above is as follows [37] :

$$\frac{I_{\text{pr}} - I_{\text{pr}}^{(0)}}{I_{\text{pr}}^{(0)}} = 4\Phi^2 \left[\frac{I_{\text{pu}}^{(0)} - I_{\text{pr}}^{(0)}}{I_{\text{pu}}^{(0)} + I_{\text{pr}}^{(0)}} \right] \exp\left(-\frac{t}{\tau_r}\right) \left[1 - \left(\frac{t}{\tau_r}\right) - \exp\left(-\frac{t}{\tau_r}\right) \right]. \tag{8}$$

Here, $\Phi = k_0 \Delta n \ell / 2 \cos\theta$ stands for the light-induced phase modulation in a sample with a thickness ℓ, $k_0 = 2\pi/\lambda_0$ is a wavenumber, θ is a half-angle between the interacting beams and all superscripts (0) indicate the transmitted intensity with no second wave present. In fact, Eq. (8) gives the expression for the temporal variation of the instantaneous transmission $[T(t) - 1]$ or instantaneous gain $[G(t) - 1]$.

Several assumptions in the above summarized theories prevent from a more quantitative description of the nonlinear interactions of ultrashort pulses: (*i*) the pulses have a particular temporal envelope which is quite different from a step-like onset in time of the pump intensity, considered in these theories, (*ii*) pulses with a Gaussian transverse intensity profile can hardly be treated in the plane-wave approximation, and (*iii*) the propagation effects are not considered in the existing theories. The analysis of the experimental data presented below allows, however, for confirming their qualitative agreement with the predictions of this simplified model.

First, it should be noted that the relationship of Eq. (8) was derived for photorefractive media in which Δn is independent of the light intensity, i.e., the gain is independent of the cw-laser beams intensity in an appropriate experiment. Taking into account that in the subpicosecond time domain the most probable processes of nonlinear index variation $\Delta n(I)$ in lithium niobate are caused by free-carriers or polarons generated via two-photon absorption [36] one can expect, even from Eq. (8), an experimental intensity dependence I^{m} with an exponent larger than 2. The measured gain of a probe pulse increases, as could be expected, superlinearly with the total peak intensity with $2 < \text{m} < 4$ [Fig. 3], showing an impact of the peak intensity ratio. For pulses with different peak intensities it is always the weak pulse that gains intensity [Fig. 4]. The intensity coupling disappears completely for equal peak intensities of both pulses $I_{\text{pr}} = I_{\text{pu}}$ or $R = 1$ [Fig. 4], if the pulses are perfectly matched in time. All these features permit to attribute the coupling of the weak and strong pulses to a transient-type nonlinear interaction with an inertial phase grating involved [37, 38].

We claim, therefore, that two qualitatively different coupling processes are revealed in the experiments with grating-assisted pulse coupling in $LiNbO_3$, one with a steady-state gain from a moving grating recorded by pulses with different frequencies and the other with a transient gain of a weak pulse in presence of a strong pump pulse with the same frequency. The experimental conditions were selected in a way to inhibit one of these two processes and to study the other one in more detail. The coupling of pulses with equal energies is, in the first instance, feasible because of the frequency difference of two temporally mismatched pulses while the transient beam-coupling can manifest itself in a small-signal amplification of pulses that are perfectly matched in time.

The physical processes that are responsible for the optical nonlinearities at the origin of grating recording itself are not yet established. Some qualitative considerations allow for formulating the requirements for their parameters. In order to observe a transient energy transfer, as it is known, the decay time of the nonlinearity should be longer compared to the pulse duration. For efficient coupling of pulses that are non-degenerated in frequency this time should be, on the other hand, comparable or shorter than the pulse duration. Thus, a good candidate for dominating inertial nonlinearity is the photoexcitation of electron-hole pairs which are further responsible for the appearance of (self-trapped) excitons and/or small, strong-coupling polarons. The nonlinearity which is contributing for coupling from moving gratings might be related to the inherent optical resonances of the $LiNbO_3$ lattice.

5. Conclusion

The experimental study of the dynamic grating assisted energy transfer between two sub-picosecond pulses reveals that this process can be quite efficient in $LiNbO_3$. The weak probe pulse can be amplified more than 10 times and the redistribution of energy between two pulses of equal intensities might approach 50% of each pulse energy. This efficient coupling is accompanied, however, by a considerable attenuation of both pulses because of two-photon absorption.

The analysis of the whole scope of experimental data leads to the conclusion that at least two different coupling processes are strongly involved, both related to self-diffraction from the recorded dynamic phase grating. The first coupling process results from the appearance of a moving grating which is shifted with respect to the moving fringe pattern, induced by two pulses with different frequencies. The frequency shift may either be introduced deliberately by using pulses from two different OPAs with adjustable wavelengths, or it may appear if the grating is recorded by two frequency chirped and temporally mismatched pulses from a single OPA. The second process manifests all characteristic features of the transient energy transfer which was first reported for cw and is closely related to stimulated Rayleigh-wing scattering. While the first process ensures an efficient unidirectional coupling between two pulses regardless of their intensity ratios, the second one always provides an efficient energy flow from the stronger to the weaker pulse.

Funding

Deutsche Forschungsgemeinschaft (DFG) (IM 37/11-1, INST 190/165-1 FUGG); Open Access Publishing Fund of Osnabrück University.

Acknowledgment

The authors gratefully acknowledge crystal preparation by K. Polgár and coworkers at the Wigner Research Centre for Physics, Budapest.

References

1. V. L. Vinetskii, N. V. Kukhtarev, S. G. Odulov, and M. S. Soskin, "Dynamic self-diffraction of coherent light beams," Sov. Phys. Usp. **22**, 742–756 (1979).
2. L. Solymar, D. J. Webb, and A. Grunnet-Jepsen, *The Physics and Applications of Photorefractive Materials* (Clarendon, 1996).
3. P. Yeh, *Introduction to Photorefractive Nonlinear Optics*, Wiley series in pure and applied optics (Wiley, 1993).
4. P. Günter and J.-P. Huignard, eds., *Photorefractive Materials and Their Applications*, Vol. 1–3, Springer series in Optical Science, (Springer, 2007).
5. S. Smolorz and F. Wise, "Femtosecond two-beam coupling energy transfer from Raman and electronic nonlinearities," J. Opt. Soc. Am. B **17**, 1636–1644 (2000).
6. A. C. Bernstein, M. McCormick, G. M. Dyer, J. C. Sanders, and T. Ditmire, "Two-beam coupling between filament-forming beams in air," Phys. Rev. Lett. **22**, 13–16 (2009).
7. J. K. Wahlstrand, J. H. Odhner, E. T. McCole, Y.-H. Cheng, J. P. Palastro, R. J. Levis, and H. M. Milchberg, "Effect of two-beam coupling in strong-field optical pump-probe experimets," Phys. Rev. A **87**, 053801 (2013).
8. R. L. Sutherland, "Energy transfer between incident laser and elastically backscattered waves in nonlinear absorption media," Opt. Express **13**, 9788–9795 (2005).
9. Y. Zhao, T. E. Witt, and R. J. Gordon, "Efficient energy transfer between laser beams by stimulated Raman scattering," Phys. Rev. Lett. **103**, 173903 (2009).
10. X. Yang, J. Wu, Y. Tong, L. Ding, Z. Xu, and H. Zheng, "Femtosecond laser pulse energy transfer induced by plasma grating due to filament interaction in air," Appl. Phys. Lett. **97**, 071108 (2010).
11. B. D. Stryker, M. Springer, C. Trendafilova, X. Hus, M. Zhi, A. A. Klolomenskii, H. Shroeder, J. Strohbaber, G. W. Kattawar, and A. V. Sokolov, "Energy transfer between laser filamentrs in liquid methanol," Opt. Lett. **37**, 16–18 (2012).
12. C. Gong, Y. Zheng, Z. Zheng, C. Li, X. Ge, R. Li, and Z. Xu, "Energy trsnsfer between few-cycle laser filamentrs in air," Appl. Phys. Lett. **101**, 251111 (2012).
13. Y. Liu, M. Durand, S. Chen, A. Houdard, B. Prade, B. Forrestier, amd A. Mysyrowicz, "Energy exchange between femtosecond laser filaments in air," Phys. Rev. Lett. **105**, 055003 (2010).
14. H. J. Eichler, D. Langhans, and F. Massmann, "Coherence peaks in picosecond sampling experiments," Opt. Commun. **50**, 117–122 (1984).
15. C. W. Luo, Y. T. Wang, F. W. Chen, H. C. Shin, and T. Kobayashi, "Eliminate coherence spike in reflection-type pump-probe measurements," Opt. Express **17**, 11321-11327 (2009).
16. N. Tang and R. L. Sutherland, "Time-domain theory for pump-probe experiments with chirped pulses," J. Opt. Soc. Am. B **14**, 3412–3423 (1997).
17. F. Gires, "Résultats expérimentaux sur la reflexion thermique stimulée," C. R. Acad. Sci. Ser. B **t. 266** 596–600 (1968).
18. M. E. Mack, "Stimulated thermal light scattering in the picosecond regime," Phys. Rev. Lett. **22**, 13–16 (1969).
19. G. Rivoire and D. Wang, "Dynamics of CS_2 in a large spectral bandwidth stimulated Rayleigh-wing scattering," J. Chem. Phys. **99**, 9460–9464 (1993).
20. K. D. Dorkenoo, D. Wang, N. P. Xuan, J. P. Lecoq, R. Chevalier, and G. Rivoire, "Stimulated Rayleigh-wing scattering with two-beam coupling in CS_2," J. Opt. Soc. Am. B **12**, 37–42 (1995).
21. A. Dogariu, T. Xia, D. J. Hagan, A. A. Said, E. W. Van Stryland, and N. Bloembergen, "Purely refractive transient energy transfer by stimulated Rayleigh-wing scattering," J. Opt. Soc. Am. B **14**, 769–803 (1997).
22. P. Yeh, "Two-wave mixing in nonlinear media," IEEE J. Quantum Electron. **25**, 484–517 (1989).
23. R. L. Sutherland, D. G.McLean, and S. Kirkpatrick, *Handbook of Nonlinear Optics*, 2nd ed. (CRC, 2003).
24. R. W. Boyd, *Nonlinear Optics*, 3rd ed. (Academic, 2008).
25. Y. Sivan, S. Rozenberg, A. Halstuch, and A.A. Ishaaya, "Nonlinear wave interactions between short pulses of different spatio-temporal extents," Sci. Rep. **6**, 29010 (2016).
26. R. Trebino, *Frequency-Resolved Optical Gating: The Measurement of Ultrashort Laser Pulses* (Springer Science & Business Media, 2012).
27. R. M. Brubaker, Q. N. Wang, D. D. Nolte, E. S. Harmon, and M. R. Melloch, "Steady-state four-wave mixing in photorefractive quantum wells with femtosecond pulses," J. Opt. Soc. Am. B **11**, 1038–1044 (1994).
28. H. Crespo, J. T. Mendonca, and A. Dos Santos, "Cascaded highly nondegenerate four-wave-mixing phenomenon in transparent isotropic condensed media," Opt. Lett. **25**, 829–831 (2000).
29. H. Badorreck, A. Shumelyuk, S. Nolte, M. Imlau, and S. Odoulov, "Doppler-shifted Raman-Nath diffraction from gratings recorded in $LiNbO_3$ with ultra-short laser pulses of different color," Opt. Mater. Express **6**, 517–522 (2015).
30. S. Odoulov, A. Shumelyuk, H. Badorreck, S. Nolte, K. M. Voit, and M. Imlau, "Interference and holography with femtosecong laser pulses of different colours," Nat. Commun. **6**, 5866 (2015).
31. D. Staebler and J. Amodei, "Coupled wave analysis of holographic storage in $LiNbO_3$," J. Appl. Pnys. **43**, 1042–1049 (1972).
32. H. T. Hsieh, D. Psaltis, O. Beyer, D. Maxien, C. von Korff Schmising, K. Buse, and B. Sturman, "Femtosecond holographgy in lithium niobate crystals," Opt. Lett. **30**, 2233–2235 (2005).
33. O. Beyer, D. Maxien, K. Buse, B. Sturman, H. T. Hsieh, and D. Psaltis,"Femtosecond time-resolved absorption processes in Lithium niobate crystals," Opt. Lett. **30**, 1366–1368 (2005).

34. J. P. Woerdman, “Some optical and electrical properties of a laser-generated free-carrier plasma in Si (Thesis),” Philips Res. Repts Suppl. #7 (1971).
35. P. Reckenthaeler, D. Maxien, Th. Woike, and K. Buse, “Separation of optical Kerr and free-carrier nonlinear responses with femtosecond light pulses in $LiNbO_3$ crystals,” Phys. Rev. B **76**, 195117 (2007).
36. M. Imlau, H. Badorreck, and C. Merschjann, “Optical nonlinearities of small polarons in lithium niobate,” Appl. Phys. Rev. **2**, 040606 (2015).
37. N. Kukhtarev, V. Markov, and S. Odoulov, “Transient energy transfer during hologram formation in $LiNbO_3$ in external electric field,” Opt. Commun. **23**, 338–343 (1977).
38. V. Bryksin, A. Groznyj, V. Sidorovich, and D. Stasel’ko, “Efficient amplification of weak light beams by 3D dynamic holograms in media with thermal nonlinearity,” Soviet Physics: Technical Physics Letters, **2**, 561 (1976).
39. B. Ya. Zel’dovich, N. F. Pilipetsky, and V. V. Shkunov, *Principles of Phase Conjugation* (Springer, 1985).
40. H. Badorreck, S. Nolte, F. Freytag, P. Bäune, V. Dieckmann, and M. Imlau, “Scanning nonlinear absorption in lithium niobate over the time regime of small polaron formation,” Opt. Mater. Express **5**, 2729–2741 (2015).
41. F. Träger, *Springer Handbook of Lasers and Optics* 2nd ed. (Springer Science & Business Media, 2012), Chap. 12.
42. P. Yeh and A. Yariv, *Optical Waves in Crystals,* Wiley Series in Pure and Applied Optics (Wiley, 1984).
43. S. Sasamoto, J. Hirohashi and S. Ashihara, “Polaron dynamics in lithium niobate upon femtosecond pulse irradiation: Influence of magnesium doping and stoichiometry control,” J. Appl. Phys. **105**, 083102 (2009).
44. A. Dogariu, and D. J. Hagan, “Low frequency Raman gain measurements using chirped pulses,” Opt. Express **1**, 73–76 (1997).

A.4 Chirp control of femtosecond-pulse scattering from drag-reducing surface-relief gratings

- Juliane Eggert, Bjoern Bourdon, Stefan Nolte, Joerg Rischmueller, and Mirco Imlau
  Chirp control of femtosecond-pulse scattering from drag-reducing surface-relief gratings
  Photon. Res. **6**, 542-548 (2018); doi: 10.1364/PRJ.6.000542..

542 Vol. 6, No. 6 / June 2018 / *Photonics Research* **Research Article**

PHOTONICS Research

Chirp control of femtosecond-pulse scattering from drag-reducing surface-relief gratings

Juliane Eggert, Bjoern Bourdon, Stefan Nolte, Joerg Rischmueller, and Mirco Imlau*

School of Physics, Osnabrück University, Barbarastr. 7, 49076 Osnabrück, Germany
**Corresponding author: mimlau@uos.de*

Received 22 January 2018; revised 12 March 2018; accepted 13 March 2018; posted 14 March 2018 (Doc. ID 320238); published 2 May 2018

The role of chirp on the light–matter interaction of femto- and pico-second laser pulses with functional structured surfaces is studied using drag-reducing riblets as an example. The three-dimensional, periodic microstructure naturally gives rise to a mutual interplay of (i) reflection, (ii) scattering, and (iii) diffraction phenomena of incident coherent light. Furthermore, for femtosecond pulses, the structure induces (iv) an optical delay equivalent to a consecutive temporal delay of 230 fs in places of the pulse. These features enable studying experimentally and numerically the effect of tuning both pulse duration τ and spectral bandwidth $\Delta\omega$ on the features of the wide-angle scattering pattern from the riblet structure. As a result, we discovered a significant breakdown of fringes in the scattering pattern with decreasing pulse duration and/or increasing spectral bandwidth. This unique type of chirp control is straightforwardly explained and verified by numerical modeling considering the spectral and temporal interaction between different segments within the scattered, linearly chirped pulse and the particular geometric features of the riblet structure. The visibility of the fringe pattern can be precisely adjusted, and the off-state is achieved using $\tau < 230$ fs or $\Delta\omega > 2.85 \times 10^{13}$ rad/s.

OCIS codes: (120.4630) Optical inspection; (120.6650) Surface measurements, figure; (240.3695) Linear and nonlinear light scattering from surfaces; (280.4788) Optical sensing and sensors; (320.1590) Chirping; (320.2250) Femtosecond phenomena.

https://doi.org/10.1364/PRJ.6.000542

1. INTRODUCTION

Non-contact, laser-based optical sensors are crucial for the quality inspection of micro- and nano-structured surfaces in a variety of technological branches including the semiconductor industry (e.g., integrated circuit control), photonics industry (e.g., optics control), medical technology (e.g., hip joints), and automotive and aerospace fields (e.g., anti-fog and anti-icing surfaces) [1–5]. The approach to use femtosecond (fs) laser pulses as the probing light source in optical sensor technology is driven by the increasing economical availability of stable and high-power ultrashort pulse laser systems. At the same time, sub-picosecond-laser pulses represent a state-of-the-art working tool within a variety of production processes and enable fast and precise marking, cutting, soldering, and welding [6]. We here pursue the question of whether and how the use of ultrashort laser pulses in optical sensor technology may affect the measurement signal with the goal to improve the key measures that are used for quality inspection. A particular focus is given to the impact of the geometry of a relief structure on the wide-angle scattering of an incident, linearly chirped fs-laser pulse. We will therefore neglect the possible effect of a nonlinear optical response of the surface itself, as it may be expected due to high pulse peak intensities.

The drag-reducing riblet surface [cf. scanning electron microscope (SEM) image in Fig. 1(a)] serves as an example for our study. The interaction of continuous-wave, coherent light with riblet surfaces [cf. Fig. 1(a)] has been intensively studied for the purpose of quality inspection before [7–10]. Riblets obey their relevance in the engineering of drag reduction as they affect skin friction considerably [11–15]. The riblet functionality depends essentially on the integrity of the geometrical shape and therefore on the possibility to detect geometric alterations during production and maintenance with high precision in the submicrometer range at high sensing speed. The optical sensor described in Ref. [8] ensures these demands at high reliability due to a simple optical design [Fig. 1(b)]: a laser beam is incident normal to the riblet sample's surface, such that a wide-angle scattering pattern appears. The pattern consists of three main features in the ±45° and 0° directions with respect to the sample's surface and in plane with the incoming beam in accordance with the triangular riblet structure and planes in between. Degradation of the riblets is measured as a decrease in the

2327-9125/18/060542-07 Journal © 2018 Chinese Laser Press

Research Article Vol. 6, No. 6 / June 2018 / Photonics Research 543

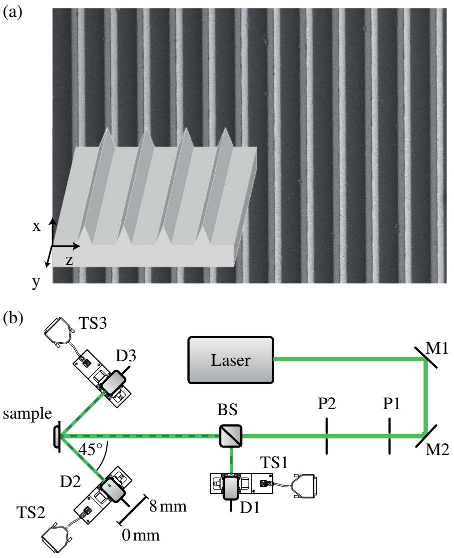

Fig. 1. (a) Scanning electron microscope (SEM) image and schematic, three-dimensional representation of the riblet structure under study. (b) Scheme of the optical setup of the riblet sensor described in Refs. [8,9]: the laser beam is incident normal to the riblet sample's surface, and the intensity distribution of the scattered light is detected in the 0° and ±45° directions. Degradation of the riblet structure is measured as a decrease in intensity around 45°. D1–D3, Si-PIN-diodes; BS, beam-splitter; M1, M2, mirrors; TS1–TS3, motorized translation stages.

intensity in the directions around 45°. Another characteristic of the scattered signal is the interference substructure [8] as a result from light diffraction at the periodic microstructure. It may be used for quality inspection as well [10] and contains information about riblet periodicity and duty cycle. However, we intend to disregard this signal due to signal fluctuations caused by the Moiré effect if fringe and detector array periodicities coincide [16].

One way to suppress the interference structure is to choose a detector diaphragm much larger than the fringe spacing. This strategy can be either realized by an appropriate Iris and/or distance between sample and photodiode. As a disadvantage, however, the dimensions of the optical setup are considerably extended, and the information about the riblet periodicity is lost.

In this work we introduce another strategy for the elimination of interference effects that is based on linearly chirped ultrashort laser pulses as the probing light source. The underlying idea is schematically sketched in Figs. 2(a) and 2(b): from ray-tracing considerations of an incident laser pulse onto a riblet structure, a difference of the optical path length in the ±45°-direction for waves reflected at neighboring flanks becomes obvious. This spatial delay can be estimated to about 70 μm for the given riblet structure under study ($\Lambda = 100$ μm, $h = 50$ μm). It corresponds with a temporal delay of about $\Delta t = 230$ fs. The latter is of importance if ultrashort laser pulses are used, in particular, if the pulse duration is in the order of magnitude of the temporal delay: when the pulse duration is adjusted below the temporal delay, $\tau < \Delta t$, the pulses do not overlap, and the interference should vanish.

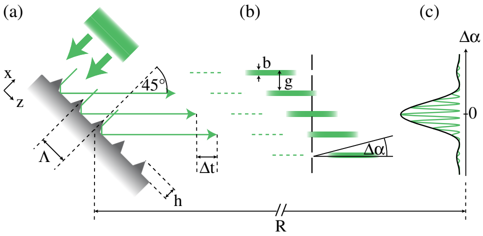

Fig. 2. (a) Scheme of the pulse front reflected in the 45° direction and distinct pulse path lengths from next-neighboring riblet flanks. Period Λ of the riblet structure is 100 μm, and riblet height h is 50 μm. The spatial delay induced by the riblet structure is 70 μm, and the correlated temporal delay is about $\Delta t = 230$ fs. (b) and (c) are discussed in the simulation section.

In what follows, and based on these preconsiderations, we will examine differences between the following three probing approaches:

- probing with pulse durations $\tau < \Delta t$;
- probing with pulse durations $\tau > \Delta t$ and a broad frequency spectrum;
- probing with pulse durations $\tau > \Delta t$ and both decreasing pulse duration and frequency spectrum.

Both experimental and simulation methods are applied. Our comprehensive study shows that a complete disappearance of the interference at ±45° can be obtained. At the same time, it is possible to keep the interference in the scattering pattern in the direction around 0°. Thus, full access to analyze all important features of the riblet structure (periodicity, deviations of periodicity) is maintained. Furthermore, in analyzing the effect of pulse duration and bandwidth in more detail, we are able to precisely deduce the pulse characteristics for an all-optical control of the appearing wide-angle, scattering pattern. Thus, it becomes possible to choose between on and off states of the interference pattern by proper adjustment of the pulse parameters. Our results enable the redesign of the optical setup with much smaller dimensions while maintaining its reliability and precision. All our findings can be transferred to fs-pulse sensing of surface relief structures with different geometric shapes and dimensions, if the optical delay induced by the structure falls in the time region of the applied pulse duration.

2. EXPERIMENTS

A. Femtosecond Pulses and Simplified Pulse Shaping

We will use the following textbook knowledge about femtosecond pulses as fundament for our study: the time-bandwidth product $\Delta\omega \cdot \tau \geq 4 \ln 2$ for Gaussian-shaped pulses defines a minimum duration τ_0 for a given bandwidth based on the uncertainty principle. As an example, fs pulses in the visible spectral range with durations of $\tau = 50$ fs cover a bandwidth of more than 10 nm. A pulse that is close to the time-bandwidth product is called Fourier-limited, but it does not preserve its shape when propagating through glass or several meters in air. Dispersion of the refractive index leads to different velocities of the spectral groups within the pulse, causing an extension of the pulse duration (group velocity dispersion) [17]. In the simplest case, a linear chirp results: $\omega(t) = \omega_0 + at$, with central frequency ω_0 and chirp parameter a. For what follows, it is important to note that the chirp parameter a, obtained via frequency gradient $a = \partial\omega/\partial t$, decreases as a function of increasing pulse duration of an incident pulse under the condition of a fixed bandwidth.

If the time-dependent frequency $\omega(t)$ is known, the spectral pulse shape can be transferred to a temporal pulse shape via Fourier transform and vice versa. In the following approach, the simplification

$$\frac{\partial\omega}{\partial t} = \frac{\Delta\omega}{\tau}\sqrt{1 - \left(\frac{\tau_0}{\tau}\right)^2} \approx \frac{\Delta\omega}{\tau} \qquad \textbf{(1)}$$

is used to extract the frequency gradient from bandwidth and duration of a strongly chirped pulse $\tau_0/\tau \ll 1$.

Let us transfer this knowledge to design an optical setup for a proper experimental control. On the one hand, the magnitude of pulse chirp from dispersion can be varied by the thickness of the medium. On the other hand, the angular dispersion from prism and grating pairs is used so that the chirp is determined by the distance between them. This procedure is used in every pulse compressor/stretcher to achieve the desired pulse duration [18].

According to Eq. (1), for a fixed bandwidth, the pulse duration depends on the frequency gradient. But for strongly chirped pulses it is also possible to keep the frequency gradient fixed, so that the pulse duration depends on the bandwidth. Both processes are utilized in the following investigations to adapt the abovementioned dependencies.

The first applied method uses group velocity dispersion of borosilicate crown glass to extend the temporal profile by altering the pulse chirp while keeping the spectrum unchanged [cf. Eq. (1)]. A sketch of the experimental realization is shown in Fig. 3(a).

The second technique for fs-pulse shaping manipulates the spectral and temporal features of the pulse concurrently at constant pulse chirp inside a grating stretcher as shown in Fig. 3(b). The first grating BG1 decomposes the spectrum, and the second grating BG2 recollimates the beam while maintaining the spatial wavelength sort. A variable slit in the spatially dispersed spectrum cuts off the high- and low-frequency components [19,20]. Under the condition that the laser pulse is not bandwidth-limited, both the spectral bandwidth and the pulse duration are reduced as the slit width decreases. The advantage of this simplified setup is that an additional pulse duration stretch due to lenses and difficulties of chromatic aberration are eliminated [21].

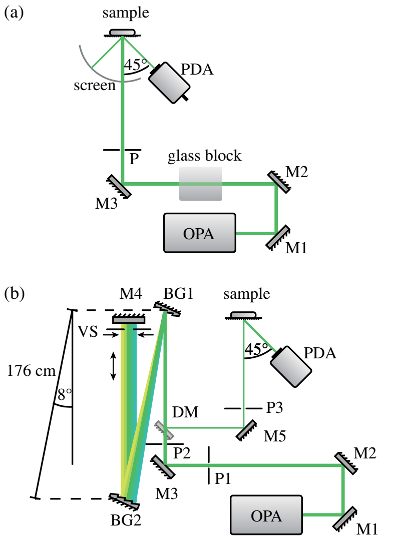

Fig. 3. (a) First setup: the laser beam is incident via mirrors M1–M3 normal to the riblet sample's surface and the scattered intensity pattern is observed on a screen or detected via a photodiode array in the 45° direction. The initial pulse duration is $\tau = 109$ fs. In order to expand the pulse duration, blocks of borosilicate crown glass are placed into the beam path. (b) Second setup: the laser beam is adjusted into a grating stretcher built of BG1, BG2, and M4. Distance between the two blazed gratings of 176(1) cm results in $\tau_2 = 2.4$ ps. The variable slit VS allows for a limitation of the effective bandwidth $\Delta\omega$ of the laser pulse. Its aperture a is varied from 1 to 7 mm. The D-shaped mirror DM separates incoming and stretched pulses. P1–P3 are pinholes to eliminate scattering.

B. Experimental Setups

An optical parametric amplifier (OPerA solo, Coherent Inc., USA) pumped by a regeneratively amplified Ti^{3+}:sapphire laser (Libra-F HE, Coherent Inc., USA) serves as the source for ultrashort laser pulses. The central wavelength is adjusted to $\lambda = 515$ nm, and the spectral bandwidth is $\Delta\omega = 3.56 \times 10^{13}$ rad/s, estimated via a fiber spectrometer (USB4000, Ocean Optics Inc., USA). In the first experimental setup, shown in Fig. 3(a), the laser beam is incident via mirrors M1–M3 normal to the riblet sample's surface, and the scattered intensity pattern is observed on a screen or detected via a photodiode array (S3902-512Q, Hamamatsu Photonics K.K., Japan) in the 45° direction at a distance between sample and detector of 36.0(5) cm. A pinhole limits the incident beam diameter to $d = (1.0 \pm 0.1)$ mm. The initial pulse duration is estimated via an autocorrelator (pulseCheck 15, APE, Germany) to be $\tau = 109(5)$ fs.

In order to expand the pulse duration, blocks of borosilicate crown glass with edge lengths of 56, 131, 171, and 211 mm are placed into the beam path, resulting in pulse durations of 234(5), 370(5), 680(5), and 900(5) fs, respectively.

In Fig. 3(b), a scheme of the second experimental setup is shown. The same laser beam as used above is adjusted into a double grating setup built of BG1, BG2, and M4 that stretches the pulse duration as a function of the distance between the two blazed diffraction gratings BG1 and BG2, blaze wavelength $\lambda_b = 500$ nm, and line spacing $1/d = 300\ \mathrm{mm}^{-1}$ (GR25-0305, Thorlabs, Inc., USA) [18]. The distance between the two blazed gratings is adjusted to 176(1) cm, resulting in a measured stretch of pulse duration of $\tau = 2.4(1)$ ps. In our

Table 1. Slit Apertures *a*, Pulse Duration τ, and Spectral Bandwidth $\Delta\omega$[a]

Slit Aperture *a* (mm)	Pulse Duration τ (ps)	Spectral Bandwidth $\Delta\omega$ (rad/s)	$\Omega\tau$
7.0(1)	2.40(10)	3.56×10^{13}	8.18
6.0(1)	2.30(10)	3.56×10^{13}	8.18
5.0(1)	2.25(10)	2.85×10^{13}	6.55
4.0(1)	2.00(10)	2.35×10^{13}	5.40
3.0(1)	1.70(10)	2.42×10^{13}	5.56
2.0(1)	1.25(20)	2.06×10^{13}	4.75
1.0(1)	0.90(20)	1.92×10^{13}	4.42

[a] The product $\Omega\tau$ is depicted in the discussion.

experiment, the product $\Delta\omega \cdot \tau \geq 17$ and is therefore well above the bandwidth limit. The variable slit VS allows for a limitation of the effective bandwidth $\Delta\omega$ of the laser pulse. Its aperture *a* is varied from 1 to 7 mm. The D-shaped mirror DM separates the incoming and stretched pulses. The hereby resulting pulse durations and spectral bandwidths are measured via autocorrelator and spectrometer, respectively; an overview is presented in Table 1. The D-shaped mirror DM separates the incoming and stretched pulses. The scattered intensity is measured around 45° by a photodiode array device (S3902-512Q, Hamamatsu Photonics K.K.) with a spatial resolution of approximately 202 pixels/cm, and the distance between sample and detector is 36.0(5) cm. The spectral bandwidth decreases with the slit aperture. It is understandable that the pulse duration, which is initially determined by the stretching induced by the two gratings, is decreased when the maximal and minimal wavelengths are cut off, provided the pulse is not Fourier-transform-limited.

3. RESULTS

A. Experimental Results

Figure 4(a) shows the intensity pattern of the 45° signal obtained with the first setup for pulse durations of (1) 109 fs, (2) 234 fs, (3) 370 fs, (4) 680 fs, and (5) 900 fs, respectively. At all pulse lengths, the intensity distribution is consistent and shows no substructure. The visual appearance of this intensity pattern is shown in the screen photograph in Fig. 4(b) at $\tau = 900$ fs and accordingly shows a smooth appearance. This finding is in contrast to the observable substructure of the 45° signal in Fig. 4(d), obtained with a continuous-wave laser (Compass 215M-75, $\lambda = 532$ nm, Coherent Inc., USA) and well-known from previous experiments [7–9]. In the 0° direction, both intensity patterns in Figs. 4(c) and 4(e) show distinct interference features with three prominent center peaks.

In the setup of Fig. 3(b), the fringe pattern is studied as a function of slit aperture *a* as depicted in Fig. 5. For a slit aperture of $a = 7$ mm, a smooth intensity distribution is visible as found in Figs. 4(a) and 4(b). As the slit aperture decreases, the interference fades in towards a well-defined substructure at $a = 1$ mm.

The results of the detected intensity patterns for $a = 1$ mm and $a = 7$ mm are shown and fitted to the sum of two Gaussian functions. As suggested in Ref. [8], the area integral of the Gaussian graph is used for degradation. The data set furthermore reveals that the position of the fringe maxima is slightly displaced as a function of slit aperture. This effect can be attributed unambiguously to the spatial displacement of the laser beam induced by the mechanical changes in the slit aperture. As a result, the laser spot position is slightly displaced on the riblet sample, that in turn displaces the position of the fringe maxima on our detector array.

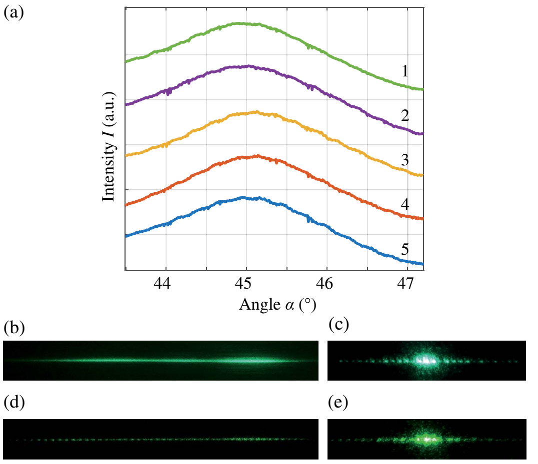

Fig. 4. (a) Intensity patterns of the 45° signal obtained with the first setup for pulse durations of (1) 109 fs, (2) 234 fs, (3) 370 fs, (4) 680 fs, and (5) 900 fs, respectively. (b)–(e) Photographs of the intensity patterns (b), (c) at 900 fs and (d), (e) with a continuous-wave laser ($\lambda = 532$ nm). (b) The 45° signal appears smoothly. This finding is in contrast to the observable substructure of the 45° signal well-known from continuous wave-experiments shown in (d). (c), (e) In 0° direction, both intensity patterns show distinct interference features with three prominent center peaks.

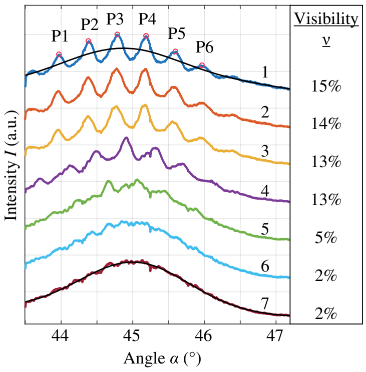

Fig. 5. Intensity pattern as a function of slit aperture *a* and accordingly labeled from 1 to 7. Smooth intensity distribution for $a = 7$ mm as found in Fig. 4(a). With decreasing slit aperture and consequently decreasing pulse duration and bandwidth, the interference pattern appears. The results of the detected intensity patterns for $a = 1$ mm and $a = 7$ mm are fitted to the sum of two Gaussian functions. On the right, the respective visibilities ν are specified.

Since the focus of this work is not on the evaluation of the degradation, but on the analysis of the interaction between chirped ultrashort pulses and the riblet structure, the fit parameters will not be discussed further. Rather, we turn to the appearance of interference. Related to the fringe pattern, we can define the interference by the contrast, namely given by the visibility ν

$$\nu = \frac{I_{\max} - I_{\min}}{I_{\max} + I_{\min}}. \tag{2}$$

It is determined by averaging the specific visibilities of the six main peaks of the pattern as marked in Fig. 5. The results for ν are listed in Fig. 5 and cover resulting visibility values between 2% and 15%.

B. Simulation

In what follows, we attempt to analyze in more detail the correlation of pulse duration, bandwidth, and fringe pattern in the 45° direction. For this purpose, we refer to Fig. 2(b) and introduce the periodicity g of light emission parallel to 45°, which is determined by the riblet period Λ: $g = \Lambda \cdot \sin 45°$, and width b of a single reflection, which is equal to the width of one riblet flank.

Under these conditions, the generated scattering pattern at distance R can be interpreted as a diffraction signal from a multiple slit as geometrically sketched in Figs. 2(a) and 2(b).

In order to simulate this intensity pattern we describe the time- and angle-dependent electrical field by a sum of a series of normalized plane waves as follows:

$$E(\Delta\alpha, t) = \sum_{n=1}^{N}\sum_{m=1}^{M} A_n(t_n)\exp[i(k_n R - (\omega_0 + \tfrac{1}{2}\dot{\omega} t_n)t_n + \phi_n + \phi_m)], \tag{3}$$

with

$$A_n(t_n) = \exp\left\{-\frac{2\{[n - \frac{1}{2}(N+1)]\Lambda\}^2}{w_r^2}\right\} \cdot \exp\left[-2(\ln 2)\frac{t_n^2}{\tau^2}\right], \tag{4}$$

$$t_n(t) = t - (n-1)\cdot\Delta t, \tag{5}$$

$$\omega_n(t_n) = \omega_0 + \dot{\omega}\cdot t_n, \tag{6}$$

$$\phi_n(\omega_n) = \frac{\omega_n}{c}\cdot\sin(45° + \Delta\alpha)\Lambda\cdot\sin 45°\cdot(n-1), \tag{7}$$

$$\phi_m(\omega_n) = \frac{\omega_n}{c}\cdot\sin(45° + \Delta\alpha)\frac{b}{M-1}\cdot(m-1). \tag{8}$$

The natural numbers N and M thereby describe the number of slits and the number of reflected waves at each slit, respectively. The term A_n determines the Gaussian-shaped envelope amplitude based on the transversal beam waist w_r [at exp(−2) intensity] and the pulse duration τ (full width at half-maximum, FWHM). The time t_n is a function of the slit number n because of the consecutive delay Δt. The frequency ω_n is a function of time, respecting the frequency gradient $\partial\omega/\partial t$, that results in a time dependence of the wave vector $k_n = \omega_n/c$ as well (c is the speed of light). The phase differences $\phi_{n,m}$ are determined by wave vectors k_n as a function of time due to pulse chirp, besides the geometrical conditions, namely Λ, b, R, and angle of observation $\Delta\alpha$.

Integration of Eq. (3) over time then yields the energy density pattern $W(\Delta\alpha)$

$$W(\Delta\alpha) = \int |E(\Delta\alpha, t)|^2 \mathrm{d}t. \tag{9}$$

With this model, it is possible to simulate both of the experimental setups. We like to note that based on Eq. (1), the frequency gradient, bandwidth, and pulse duration are coupled in a way that it is not possible to separately change one of them. Therefore the pulse duration τ can only be altered in expense of the frequency gradient $\partial\omega/\partial t$ [Fig. 6(a)] or the bandwidth $\Delta\omega$ [Fig. 6(b)].

Figure 6 shows the results of the simulations based on Eq. (9) for the bandwidth and frequency gradient according to the experiment. No interference effects are visible when changing the pulse duration, and thus the frequency gradient, at a constant bandwidth [Fig. 6(a)]. However, changing the bandwidth, and thus the pulse duration, at a constant frequency gradient reveals a different picture [Fig. 6(b)]: a diffraction pattern appears in a certain window of bandwidths between $\Delta\omega \approx (0.3\text{–}2.2) \times 10^{13}$ rad/s and pulse durations between $\tau \approx 200\text{–}1500$ fs.

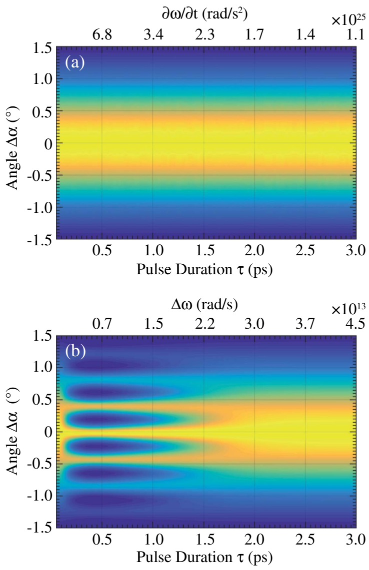

Fig. 6. Numeric energy pattern $W(\Delta\alpha)$ for 45° (a) for a constant bandwidth of $\Delta\omega = 3.41 \times 10^{13}$ rad/s ($\Delta\lambda = 4.8$ nm) and variable pulse duration τ and frequency gradient $\partial\omega/\partial t$, and (b) for a constant frequency gradient $\partial\omega/\partial t = 1.49 \times 10^{25}$ rad/s^2 and variable pulse duration τ and bandwidth $\Delta\omega$ ($N = 13$, $M = 5$, $b = 15$ μm, $\Lambda = 100$ μm, $R = 0.36$ m).

The calculations were also applied to the direct reflection signal in the 0° direction. In this case, a stationary interference pattern is formed regardless of the chosen parameters for pulse duration τ and bandwidth $\Delta\omega$ (not shown).

4. DISCUSSION

The results of the experiments and the simulation are consistent with each other, and the observed phenomena can be explained on the basis of temporal pulse sequences and interference.

In the 0° direction, the interference pattern is distinctly visible and can be directly attributed to the model of a multiple slit only. This signal originates from perpendicular reflection at the riblet plains, so that no optical path difference is induced in this direction ($\Delta t = 0$, cf. Ref. [9]). In the case of a linearly chirped pulse, the same frequencies simultaneously reach the detector while the chirp is maintained. This case is comparable to probing with continuous-wave light of bandwidth $\Delta\omega$.

In the 45° direction, we can distinguish between three cases. In the simplest case, the pulse duration τ is below the temporal delay Δt, and therefore there is no overlap of next-neighbouring pulse sections, i.e., no interference. The other two cases are depicted in Figs. 7(a) and 7(b) and represent the first [cf. Fig. 3(a)] and second experimental setup [cf. Fig. 3(b)] at $\tau = 900$ fs, respectively.

Shown is a plot of frequency ω and power P versus time for two next-neighbouring pulses with a mutual temporal delay of 230 fs. The slope of frequency is $\partial\omega/\partial t = \Delta\omega/\tau$.

The pulse durations in Figs. 7(a) and 7(b) are similar, whereas the bandwidths are different: $\Delta\omega_a > \Delta\omega_b$, and thus the frequency gradient $\partial\omega/\partial t$ in Fig. 7(a) is larger. Therefore, the difference Ω_a of superposing frequencies is high, and no stationary interference pattern is formed [21]. With decreasing bandwidth of the pulse $\Delta\omega_b < \Delta\omega_a$ [cf. Fig. 7(b)], the interference pattern appears (cf. Fig. 5) as the frequency difference Ω_b is reduced: $\Omega_b < \Omega_a$. The latter is determined by pulse duration τ and bandwidth $\Delta\omega$ or frequency gradient of the pulses $\partial\omega/\partial t$

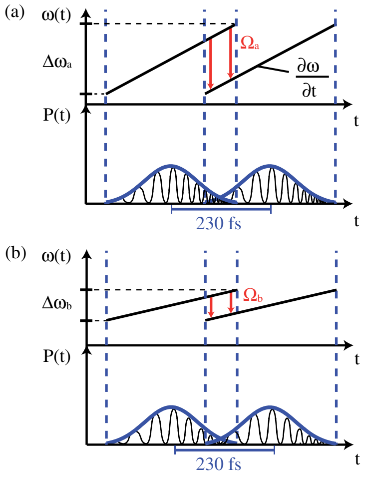

Fig. 7. Plot of frequency ω and power P versus time for two next-neighboring pulses with a mutual temporal delay of 230 fs. Slope of frequency is $\partial\omega/\partial t = \Delta\omega/\tau$. (a) Frequency detuning Ω_a for overlapping pulses. (b) Same pulse duration as in (a), while bandwidth is decreased, which results in the appearance of a stationary interference pattern.

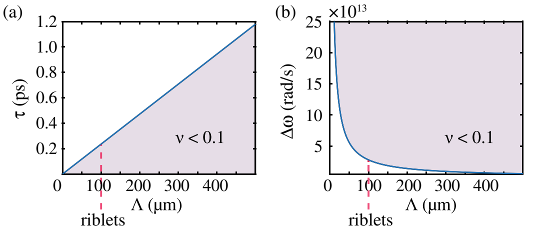

Fig. 8. Influence of structure period Λ on threshold values of (a) pulse duration τ and (b) bandwidth $\Delta\omega$ for a vanishing interference pattern ($\nu < 0.1$). Characteristic period $\Lambda = 100$ μm of the investigated riblet structure is marked, respectively.

$$\Omega = \frac{\Delta\omega}{\tau} \cdot \Delta t = \frac{\partial\omega}{\partial t} \cdot \Delta t. \quad \textbf{(10)}$$

For interference, however, Ω alone is not decisive but rather the product $\Omega\tau$. This is illustrated by the second experiment where the frequency gradient $\partial\omega/\partial t$ is constant and thus also $\Omega(t)$, but the visibility of the interference pattern differs essentially. As a condition for interference, an upper boundary value for the product $\Omega\tau$ can be estimated [22]. The values for $\Omega\tau$ of our experiments are depicted in Table 1. Concluding these considerations, the appearance of the interference can be adjusted via the pulse parameters. We note that further parameters may be deduced from the dependence of the scattering features on pulse duration and bandwidth, e.g., the determination of the pulse chirp from the fringe visibility. For this purpose and a sufficient precision, however, it will be necessary to make a point of improving the fringe contrast by appropriate laser (intensity, coherence length, etc.) and/or riblet (periodicity, riblet height, etc.) parameters.

For the particular case of a fixed temporal delay Δt, the product $\Omega\tau$ reads

$$\Omega\tau \leq C \Leftrightarrow \Delta\omega \leq \frac{C}{\Delta t}. \quad \textbf{(11)}$$

Constant C can be drawn from the measurement data. For a vanishing interference contrast of less than 10%, $\Delta\omega > 2.85 \times 10^{13}$ rad/s is valid, which corresponds to $C = 6.56$.

In Fig. 8 the influence of structure period Λ on the threshold values of pulse duration τ and bandwidth $\Delta\omega$ for a vanishing interference pattern ($\nu < 0.1$) is depicted for $C = 6.56$.

The investigations show clearly that the impact on measurements signals needs to be considered when using a chirped ultrashort laser pulse. In general, one can expect an influence on interference when a temporal delay Δt is induced to fractions of the chirped pulses by a microstructure. Besides the simple case with $\tau < \Delta t$, the choice of bandwidth and chirp affect the appearance of interference effects as well. According to the goal of our study, we were able to suppress the fringe pattern that overlays with the scattering pattern.

5. CONCLUSIONS

We have introduced the chirp as a novel parameter for the all-optical control of a wide-angle scattering pattern with a drag-reducing riblet structure as an example. In our particular example, we are able to deduce precise requirements for a smooth measurement signal in the 45° direction with a visibility of the interference $\nu < 0.1$ (pulse duration $\tau < 230$ fs or bandwidth $\Delta\omega > 2.85 \times 10^{13}$ rad/s for linearly chirped pulses). The vanishing of the interference substructure as main objective of our study enables the use of a photodiode array within the riblet sensor. This results in an effective improvement of the measurement speed and the possibility to redesign the optical sensor setup with much smaller dimensions. Reliability and precision of the sensor are maintained. It is noteworthy that a standard fs-pulse laser implemented into the riblet sensor fulfills the requirements for a smooth intensity signal in the 45° direction. All our considerations can be easily transferred to similar structured surfaces and specific limit values can be obtained if the optical delay induced by the geometric structure coincides with the pulse duration.

Funding. Seventh Framework Programme (FP7) (CSJU-GAM-SFWA-2008- 001); Deutsche Forschungsgemeinschaft (DFG); European Union's Seventh Framework Program (FP7/2007-2013); Clean Sky Joint Technology Initiative (CSJU-GAM-SFWA-2008-001).

Acknowledgment. The authors acknowledge financial support by the European Union's Seventh Framework Program for the Clean Sky Joint Technology Initiative. We acknowledge support by Deutsche Forschungsgemeinschaft (DFG) and Open Access Publishing Fund of Osnabrück University.

REFERENCES

1. M. M. Moslehi, "Sensor for semiconductor device manufacturing process control," U.S. patent 5,293,216 (March 8, 1994).
2. M. M. Moslehi, "Apparatus for semiconductor device fabrication diagnosis and prognosis," U.S. patent 5,719,495 (February 17, 1998).
3. J.-H. Lee, J. P. Singer, and E. L. Thomas, "Micro-/nanostructured mechanical metamaterials," Adv. Mater. **24**, 4782–4810 (2012).
4. B. Kasemo, "Biological surface science," Surf. Sci. **500**, 656–677 (2002).
5. V. A. Ganesh, H. K. Raut, A. S. Nair, and S. Ramakrishna, "A review on self-cleaning coatings," J. Mater. Chem. **21**, 16304–16322 (2011).
6. J. Ion, *Laser Processing of Engineering Materials: Principles, Procedure and Industrial Application* (Butterworth-Heinemann, 2005).
7. M. Imlau, H. Brüning, K.-M. Voit, J. Tschentscher, S. Dieckhoff, U. Meyer, K. Brune, J. Derksen, and C. Tornow, "A method for quality control of a micro-structuring and apparatus therefor," DE102013220006A1 (April 2, 2015).
8. M. Imlau, H. Bruening, K.-M. Voit, J. Tschentscher, and V. Dieckmann, "Riblet sensor—light scattering on micro structured surface coatings," arXiv: 1601.04694 (2016).
9. J. Tschentscher, S. Hochheim, H. Bruening, K. Brune, K.-M. Voit, and M. Imlau, "Optical riblet sensor: beam parameter requirements for the probing laser source," Sensors **16**, 458 (2016).
10. U. Meyer, S. Markus, and S. Dieckhoff, "Device for testing the quality of microstructurization," U.S. patent 8,842,271 (September 23, 2014).
11. D. W. Bechert, M. Bruse, W. Hage, J. G. T. van der Hoeven, and G. Hoppe, "Experiments on drag-reducing surfaces and their optimization with an adjustable geometry," J. Fluid Mech. **338**, 59–87 (1997).
12. M. Bruse, D. Bechert, J. T. van der Hoeven, W. Hage, and G. Hoppe, "Experiments with conventional and with novel adjustable drag-reducing surfaces," in *Proceedings of the International Conference on Near-Wall Turbulent Flows*, Tempe, Arizona (March 15–17, 1993), pp. 719–738.
13. M. J. Walsh, "Effect of detailed surface geometry on riblet drag reduction performance," J. Aircr. **27**, 572–573 (1990).
14. D. W. Bechert, M. Bruse, W. Hage, and R. Meyer, "Fluid mechanics of biological surfaces and their technological application," Naturwissenschaften **87**, 157–171 (2000).
15. B. Dean and B. Bhushan, "Shark-skin surfaces for fluid-drag reduction in turbulent flow: a review," Philos. Trans. R. Soc. London A **368**, 4775–4806 (2010).
16. G. C. Holst, *CCD Arrays, Cameras, and Displays* (JCD, 1998).
17. L. Brillouin, *Wave Propagation and Group Velocity* (Academic, 2013), Vol. **8**.
18. E. Treacy, "Optical pulse compression with diffraction gratings," IEEE J. Quantum Electron. **5**, 454–458 (1969).
19. J. P. Heritage, R. N. Thurston, W. J. Tomlinson, A. M. Weiner, and R. H. Stolen, "Spectral windowing of frequency-modulated optical pulses in a grating compressor," Appl. Phys. Lett. **47**, 87–89 (1985).
20. J. P. Heritage, A. M. Weiner, and R. N. Thurston, "Picosecond pulse shaping by spectral phase and amplitude manipulation," Opt. Lett. **10**, 609–611 (1985).
21. A. M. Weiner, "Ultrafast optical pulse shaping: a tutorial review," Opt. Commun. **284**, 3669–3692 (2011).
22. S. Odoulov, A. Shumelyuk, H. Badorreck, S. Nolte, K.-M. Voit, and M. Imlau, "Interference and holography with femtosecond laser pulses of different colours," Nat. Commun. **6**, 5866 (2015).

B Further Publications

B.1 Conference contributions

S. Nolte, B. Bourdon, F. Freytag, M. Imlau, and S. Odoulov, *Ultrafast holographic spectroscopy for the study of small polarons in lithium niobate*, DPG Spring Meeting 2016, Regensburg, Germany

S. Nolte, B. Bourdon, F. Freytag, M. Imlau, A. Shumelyuk, and S. Odoulov, *Transient energy transfer on the femtosecond timescale in lithium niobate*, Conference on Lasers and Electro-Optics Europe 2017, München, Germany

B. Bourdon, F. Freytag, M. Imlau, A. Shumelyuk, and S. Odoulov, *Mid-Infrared photorefractivity with non-degenerate two-photon absorption*, Photorefractive Photonics 2017, Qingdao, China

S. Nolte, B. Bourdon, F. Freytag, M. Imlau, A. Shumelyuk, and S. Odoulov, *Dynamic grating mediated energy transfer between two sub-picosecond pulses in* $LiNbO_3$, Photorefractive Photonics 2017, Qingdao, China

J. Klenen, C. Kijatkin, B. Bourdon, and M. Imlau, *Time-resolved multicolor emission of harmonic nanoparticles via nonlinear frequency mixing*, DPG Spring Meeting 2018, Regensburg, Germany

L. Vittadello, C. Kijatkin, B. Bourdon, D. Dzikonski, M. Imlau, K. Koempe, M. Haase, K. Lammers, and A. Paululat, *Niobate (nano-)crystals beyond photorefraction: towards understanding heart valve morphogenesis*, Photorefractive Photonics and beyond 2019, Gérardmer, France

B. Bourdon, F. Freytag, M. Imlau, A. Shumelyuk, and S. Odoulov, *Recording of space-charge gratings in* $Fe{:}LiNbO_3$ *with trains of sub-picosecond infrared pulses*, Photorefractive Photonics and beyond 2019, Gérardmer, France

S. Messerschmidt, B. Bourdon, D. Brinkmann, A. Krampf, L. Vittadello, and M. Imlau, *Light-induced absorption in Fe:LN by means of ns-pump supercontinuum probe spectroscopy*, Photorefractive Photonics and beyond 2019, Gérardmer, France

B.2 Books

S. Klompmaker, F. Lager, B. Bourdon, and M. Imlau, *Interferometer zum Selberbauen (1000 Laser-Hacks für Maker)*, Bombini Verlags GmbH (2019), ISBN: 978-3946496090

F. Lager, S. Klompmaker, B. Bourdon, and M. Imlau, *Hologramme zum Selbermachen (1000 Laser-Hacks für Maker)*, Bombini Verlags GmbH (2019), ISBN: 978-3946496137

Acknowledgment

An dieser Stelle möchte ich den nachstehenden Personen meinen besonderen Dank ausdrücken, ohne deren Mithilfe und Unterstützung die Anfertigung dieser Dissertation nicht zustande gekommen wäre.

An erster Stelle möchte ich mich hiermit insbesondere bei Herrn Prof. Dr. rer. nat. Mirco Imlau für die Aufnahme in die Forschungsgruppe Ultrakurzzeitphysik, die damit verbundene Möglichkeit, meine Bachelor- und Masterarbeit sowie nun auch meine Promotion unter seiner Leitung durchzuführen, die hervorragende Betreuung, große Diskussionsbereitschaft und Unterstützung zu jeder Phase meiner Promotion bedanken.

Herzlich bedanken möchte ich mich darüber hinaus für die Begutachtung dieser Arbeit bei Herrn Prof. Dr. rer. nat. Joachim Wollschläger, sowie den weiteren Mitgliedern der Prüfungskommission Herrn Prof. Dr. rer. nat. Jochen Gemmer und Frau Dr. Monika Wesner.

Des Weiteren bedanke ich mich bei der gesamten Forschungsgruppe für die ständige Hilfs- und Diskussionsbereitschaft. Besonders hervorheben möchte ich dabei Herrn Dr. rer. nat. Simon Messerschmidt und Herrn Dr. rer. nat. Stefan Klompmaker für die interessanten Diskussionen und Anregungen während diverser Tagungen und Auslandsaufenthalte, sowie Herrn Dr. rer. nat Christian Kijatkin für seine ständige Diskussionsbereitschaft. Außerdem geht ein besonderer Dank an Frau Dr. rer. nat. Laura Vittadello sowie Herrn Dr. rer. nat. Simon Messerschmidt für die großartige Unterstützung in den letzten Zügen. Zusätzlich möchte ich mich bei Herrn Sergej Bock, Herrn Dr. rer. nat. Stefan Nolte, Herrn Dr. rer. nat Felix Freytag, Frau Dr. rer. nat. Juliane Eggert, Herrn Jörg Rischmüller, Herrn Andreas Krampf, Herrn David Brinkmann, Herrn Jan Klenen, Frau Janina Ringel, Frau Gerda Cornelsen sowie den weiteren Mitgliedern der Forschungsgruppe für die gute Zusammenarbeit bedanken.

Special thanks are devoted to Prof. Dr. rer. nat. Serguey Odoulov and Dr. Alexandr Shumelyuk from the National Academy of Sciences in Kiev, Ukraine for fruitful discussions and support during their stays in our research group.

Für die Förderung des Projekts "myphotonics" und die damit verbundene Finanzierung meiner Promotionsstelle möchte ich mich beim Bundesministerium für Bildung und Forschung bedanken.

Außerdem möchte ich mich besonders bei der Elektronikwerkstatt, der Feinmechanikwerkstatt sowie der Tischlerei der Universität für die schnellen Reparaturen, Umbauten und Erstellungen einiger Bauteile bedanken.

Bei meinen Eltern, Geschwistern und meiner Frau Jessi möchte ich mich ganz besonders für die uneingeschränkte, liebevolle und vielseitige Unterstützung während meiner Promotion bedanken, ohne die diese Arbeit so nicht möglich gewesen wäre.

Vielen Dank, thank you very much, mille grazie!

Erklärung über die Eigenständigkeit der erbrachten wissenschaftlichen Leistung

Ich erkläre hiermit, dass ich die vorliegende Arbeit ohne unzulässige Hilfe Dritter und ohne Benutzung anderer als der angegebenen Hilfsmittel angefertigt habe. Die aus anderen Quellen direkt oder indirekt übernommenen Daten und Konzepte sind unter Angaben der Quelle gekennzeichnet.

Weitere Personen waren an der inhaltlichen materiellen Erstellung der vorliegenden Arbeit nicht beteiligt. Insbesondere habe ich hierfür nicht die entgeltliche Hilfe von Vermittlungs- bzw. Beratungsdiensten (Promotionsberater oder andere Personen) in Anspruch genommen. Niemand hat von mir unmittelbar oder mittelbar geldwerte Leistungen für Arbeiten erhalten, die im Zusammenhang mit dem Inhalt der vorgelegten Dissertation stehen.

Die Arbeit wurde bisher weder im In- noch im Ausland in gleicher oder ähnlicher Form einer anderen Prüfungsbehörde vorgelegt.

Osnabrück, im Januar 2020

Björn Bourdon